NORTHWESTERN UNIVERSITY

Fundamental Studies in the Design of Zirconium Metal–Organic Frameworks as Catalysts and Supports for the Conversion of Hydrocarbons and Biomass Feedstocks

A DISSERTATION

SUBMITTED TO THE GRADUATE SCHOOL

IN PARTIAL FULFILLMENT OF THE REQUIREMENTS

for the degree

DOCTOR OF PHILOSOPHY

Field of Chemistry

By

Kenton Eric Hicks

EVANSTON, ILLINOIS

September 2023

ABSTRACT

One of the greatest challenges in heterogeneous catalysis is the rational design and development of new catalytic systems, due to synthetic limitations in the design of solid catalysts and inhomogeneity of chemical sites at solid surfaces. This obfuscates understanding of catalyst behavior and slows improvements of processes. One approach to circumventing these challenges is the synthesis of well-defined, structurally tunable catalysts like Metal–Organic Frameworks (MOFs). MOFs are crystalline, porous coordination polymers, which are most useful for their structural tunability and molecular precision, allowing the optimization of catalytic performance through precise, structural modification and the elucidation of structure-reactivity relationships. Through a combination of chemical synthesis, materials characterization, catalytic testing, and computational modeling, this work studies zirconium MOFs (Zr-MOFs) for the development of structural parameters for optimizing conversion of hydrocarbon and biomass feedstocks. Chapter 1 introduces approaches towards and challenges in the rational design of solid catalysts. Chapter 2 details the study of the archetypal Zr-MOF, "NU-1000", as a catalyst support for organotantalum complexes in olefin and alkane metathesis. While the tantalum sites were inactive for these reactions due to over-coordination from the support, the serendipitous observation was made that NU-1000 heterolytically activates H_2, leading to 1-butene isomerization. Chapters 3 and 4, detail mechanistic investigations establishing structural parameters for H_2 activation and olefin hydrogenation and isomerization (OHI). Basic ligands adsorbed on the Zr_6O_8 nodes in Zr-MOFs cooperate with adjacent Zr^{4+} Lewis acid sites in heterolytic cleavage of H_2, leading to 1-butene hydrogenation and parallel hydride- and acid-catalyzed pathways for 1-butene isomerization. Increasing Brønsted acidity of protons formed in H_2 cleavage trends with increasing activity for 1-butene isomerization, and MOF topology is shown to control the orientation of co-adsorbates

during 1,2-insertion, affecting hydrogenation and isomerization activity. Finally, chapter 5 details effects of Zr-MOF topology upon performance in MPV reduction, where more accessible topologies lead to orders of magnitude differences in conversion at the expense of lower product selectivity with bulky substrates. These results are due to 1) more favorable formation of MPV transition states and 2) increases in the quantity of fruitful configurations of co-adsorbed substrates in more accessible topologies.

ACKNOWLEDGEMENTS

For this work, there are many people and entities I would like to acknowledge, both personal and professional. I owe many of my accomplishments to the support of my colleagues, friends, and families, and I'm not sure I would have succeeded without them. I will begin with the professional.

First, I would like to thank the centers that funded this work. This includes ICDC, or the Inorganometallic Catalyst Design Center, which helped to fund the majority of the work in chapters 2-4. After this, I would like to thank the Institute for Catalysis in Energy Processes at Northwestern. I'm not sure how much it directly funded my work, but I know it provided a large amount of funding for catalysis research at Northwestern. Finally, the work in chapter 5 was funded by the Catalyst Design for Decarbonization Center.

I also would like to thank the user facilities at Northwestern that contributed to this research, IMSERC, REACT, NUANCE, and Argonne National Lab—and any others that I may have used in passing that have escaped my mind.

I want to especially acknowledge Prof. Neil Schweitzer and Dr. Selim Alayoglu of REACT. Not only did I heavily use the facilities of REACT, but the two of them served as mentors for me in designing and conducting catalytic and spectroscopic studies. Also, they are just genuinely nice people. Additionally, the things I learned Neil's "Fundamentals of Heterogeneous Catalysis" class have been foundational in my development as a catalysis scientist, and I'm constantly thinking about and applying the things I learned from taking this course.

For the research and writing itself: For chapter 1, I would like to thank Prof. Sol Ahn, Prof. Omar Farha, and Prof. Justin Notestein. Many of the ideas in this chapter came from discussions

in writing a potential review, which never came to fruition. While the writing is my own, their suggestions and ideas have undoubtedly influenced the outcome.

For chapter 2, I would like to thank Dr. Alon Chapovetsky, who twice synthesized my tantalum precursor for me. While I ended up synthesizing some on my own, at a later point in time, his batches of precursor were used for the majority of the studies in chapter 2. Additionally, I would like to thank Dr. Evan Wegner and Dr. Massimiliano Delferro. Evan did some EXAFS for me on my material, although this did not reveal significant insights to us. And Max was the advisor of both Alon and Evan, and he collaborated with Omar and Justin to come up with the idea and funding of this initial project. I would also like to thank Dr. Bo Yang, Prof. Navneet Khetrapal, Prof. Don Truhlar, and Prof. Laura Gagliardi for the computational collaboration in the project. While this project never came to completion, I am grateful for the assistance of all these contributors, nonetheless.

For chapter 3, I would like to thank Dr. Andrew Rosen and Prof. Randy Snurr for their computational contributions to the project. They were extremely helpful for developing understanding of my catalytic and spectroscopic observations, and many of the hypotheses for chapter 4 were based upon these data. Additionally, Andrew has always been an incredibly encouraging, kind, and inspiring friend and colleague. I know he'll be a fantastic professor once he starts his own research group. I would also like to thank Zoha Syed, who helped give writing feedback and who was a very encouraging colleague and friend. Her help, scientific conversations, and friendship are always appreciated, and I'm sure she'll go on to do great things in her next steps as well.

For chapter 4, I would like to thank Andrew Rosen again, for aforementioned reasons, and Dr. Andrew Wolek. Drew (the latter) has also been a great and encouraging friend. I always enjoyed

the banter and teasing in the office and am excited to reconnect in the near future. Also, I'm grateful that he introduced me to curling, which has been a fun part of my time here in graduate school. I also would be remiss if I failed to acknowledge Neil and Selim again, who helped me establish methodology for testing catalytic behavior in both chapters 3 and 4. I would also like to give small acknowledgements to Dr. Xinyao Liu and Fanrui Sha, who I recall did me small favors like lending me a bit of sample to test and lumping in samples of mine with their PXRD reservations. Although small contributions, they are still appreciated.

For chapter 5, I would like to acknowledge Dr. Filip Formalik and Prof. Randall Snurr, for their computational assistance. I would like to thank Madeleine Gaidimas for collecting many SEM's for me. I would like to acknowledge Katie Chase, with whom many conversations and discussions helped me to develop the experimental methodology for catalytic testing in this chapter. She has been of great help. Finally, I would like to acknowledge Dr. Sylvia Hanna, who before leaving, lent me a bunch of MOF samples she no longer needed, so I didn't have to make them myself, saving me lots of time.

In general, I would like to thank colleagues in both research groups, from whom I've learned many things, big and small, and from whom I've found friendship and solidarity, when experiments weren't going my way. Members of these groups who helped serve as mentors early on in my graduate career and who deserve particular acknowledgement are Dr. Louis Redfern, Dr. Riki Drout, Dr. Lee Robison, Dr. Louisa Savereide, Dr. Scott Nauert, Dr. Alex Ardagh, Dr. Abha Gosavi, and Prof. Sol Ahn. I also don't want to leave out Dr. Mihir "Big Dawg" Baghat and Dr. Emily Cheng, but I suppose you were more friends than mentors. Still, you are appreciated.

For guidance in my research and my development as a scientist, I'd like to acknowledge Prof. Omar Farha, and Prof. Justin Notestein. The two of you have been a yin and yang in some

ways. I am the kind of person that likes to think deeply about science and other things, take my time reading and processing data, and coming up with new hypotheses and ideas. But sometimes I think I focus on these things too much, and there were many times where I had thought about a lot, but ultimately done very little. Science is empirical, and things need to be *done* at the end of the day. Perhaps your perspectives of yourselves are different from mine, but I see Omar as a real pusher, who always wanted to make sure I was doing *something* so that I had something to show for myself. I appreciate that and attribute many of my accomplishments to this pushing. At the same time, I think, while Justin pushes too, he has also always been more willing to indulge and encourage my ideas, allowing me to do and continue to grow in the aspects of science that I enjoy. Finding the right balance is crucial to success in pretty much everything, and I think the two of you have provided that to me as advisors. I could continue on about your expertise and individual influences in my thinking and research, but I wouldn't be telling you anything you don't know anyways. You guys have been nurturing, encouraging, and friendly advisors, and I appreciate that. Not everyone has advisors or mentors that they like in graduate school, so I'm lucky to have that.

I also should thank my committee, Prof. Brian Hoffmann, Prof. Ken Poeppelmeier, and Prof. Joe Hupp from my qualifying exam committee. Like what was said in the last paragraph, during my Qual, the three of you pointed out to me that while I had many hypotheses and ideas, knew the literature, and had done lots of structural characterization, I still had not actually gotten to the meat of my research—the catalysis. I remember being told that you did not want me to be here after four years, having learned very little about my central research questions. It was this impetus, and that from my advisors, that led me to screen many different substrates and conditions that summer, leading me to find that the tantalum catalyst was poor at pretty much everything I

was targeting. This also led me to the serendipitous finding of chapter 3, which was the foundation from which this entire dissertation is built, so I am grateful.

Outside of the professional realm, there are many people I would like to thank, as they have provided me with companionship and a home here at Northwestern. Often, graduate school has been challenging, and at times when my experiments weren't working and I was feeling down about myself, it was these people who gave me the support, encouragement, and relief I needed to keep going.

First, I'd like to acknowledge Dr. Tim "Timbalimbo" Goetjen and Dr. Craig "Curg" Laing. You guys were some of my first friends here and have been sources of friendship and support throughout my time at Northwestern. Living together was a blast, and I'll always think fondly of those years. To Tim, you also were a friend and colleague in the Farha Lab and a fellow catalysis scientist, and so your presence was always doubly appreciated. I know this is true for the entire Farha Lab, for which you took many burdens upon your big shoulders to help maintain lab organization and infrastructure.

I'd also like to acknowledge Dr. Peter "Pibbity-Pongo" Winegar. We had a lot of fun playing games, hanging out, chatting about nothing, etc. etc., and your presence is missed. Thanks for always being kind and encouraging, I'm sure you and Gertrude are doing great things out at Berkeley.

A part of this friend group, I'd also like to thank Waleed, Ward, Kaster, Luke, Corey, Jon, and Jenny, for being wonderful friends as well. Some of you I haven't seen for a while, but I still think fondly of the friendship you provided early on in graduate school, or still provide today.

In the Farha Lab, I'd like to thank Kira, Fanrui, Seryeong, Dr. Flo (not a rapper), Prof. Kent Kirlikovali, Julia, Zoha, and Xinyi. You guys have been a lot of fun and very helpful. Whether

going for drinks, eating out, talking about anime, going swing dancing, playing poker, or grinding together in the lab, you guys are part of the reason that working in the Farha lab has been enjoyable.

In the Notestein lab, I'd like to thank my bomboclaat sister Hiyab, Katie, Sarah, Lauren, and Jordy. You guys have been a lot of fun in the office and have provided me some of the goofiest scenes and stories from your incessant banter. Naturally, I call your banter "incessant" affectionately. It made the office a fun place to be. You are appreciated and will be missed.

I'd also like to acknowledge my friends Natalie, Adan, and Tony. You guys have all been encouraging in many ways, and although I don't see any of you that often anymore, you still played positive roles in my time here. Natalie, you were a lifeline during covid, and were one of the things that made grad school bearable at times, and a lot of fun at others. Adan, I always appreciate your random check in calls and your kind words of encouragement. I'm always happy to hear from you and hear what you've been up to. And Tony, bible studies with you during the weekends was often a nice reset.

To "Brotha" Mike, Courtney (Cool Chem-E Cour-Cour), and Madeleine (Big Chief/Big Bird), I think of the many folks I've mentioned, you guys have been special to me. In the last year or so, as I've been trying to finish up my graduate work, you guys have been a wonderful support network and set of friends, in and outside of the lab. You've always been encouraging and kind to me, and I'm lucky to have had you guys to lean on. Especially as some of the friends I started graduate school with have left, it's been a blessing to have friends like you around. I'll always remember some of the goofy activities we did together, and I'm a little sad I won't be around to do more with you. I can't wait to see what's next for you guys. You're all bright students and earnest people, and even though grad school's hard, you guys are doing great. I have faith you'll continue to do great.

Tim, Sylvie, Wassy, and Rodrigo. It's bittersweet that everybody seems to be parting ways, but you guys have been the core and consistent group of friends throughout my time here. Board games, food, drinks, swing dancing, concerts, you name it, it's without a doubt that you guys have made my time here special. In and outside of the lab. Between the big shoulders, good hair, and cat noises, you'll be missed! As we go our own ways, we'll have to make a point to stay in touch.

To my family: To all my aunts, uncles, grandparents, cousins, and everything in between, I love you all, and thank you for your constant encouragement. Not just through graduate school, but since I was baby. To my brother Sterling, I love you. And thank you for changing the password to my chess.com account so I would stop playing chess. I credit my finishing to you, sir. Thank you for your encouragement and faith in me, and I can't wait for little T.K. to arrive so I can give some of that same encouragement to him.

And to my parents, Glenda, and Timothy Hicks. Needless to say, without you, I wouldn't be here, and not just in the literal way. You guys have worked so hard to raise good young men, you have slaved and sacrificed, and it has been a blessing to have you as parents. Your unconditional love and faith in me have bolstered me and nurtured me into the man I am today, and I will always owe, so much to the two of you. You've given me so much. I could write pages on my love and gratitude for you, but this acknowledgements section is long enough, and my fingers are tired. And honestly, my words would probably inadequately capture the way I feel. So, I can just leave it at, I love you. And thank you to God. While getting this far does require hard work, I have so many blessings. From natural gifts and talents, to loving family, friends, and colleagues, needless to say, I have many blessings that I couldn't have done this without.

TABLE OF CONTENTS

LIST OF TABLES

LIST OF FIGURES

LIST OF SCHEMES

CHAPTER 1. Introduction to the Design of Molecularly Defined Heterogeneous Catalysts

1.1.Chapter Summary

Chemical approaches in rational design of heterogeneous catalysts primarily focus on novel and controlled synthetic strategies to make molecularly defined materials. These strategies include the anchoring of molecular complexes onto surfaces and the synthesis of extended, crystalline, molecularly defined materials, which can serve as catalysts or supports. This chapter provides motivation and context to these efforts, discusses their benefits, and challenges, and addresses how the work in this dissertation contributes towards the understanding and development of Metal–Organic Framework-based heterogeneous catalysts.

1.2 Introduction the Rational Design of Heterogeneous Catalysts

Chemical economy and infrastructure rely heavily upon industrial catalytic processes in order to produce fuels, pharmaceuticals, and agriculture, among various other products.[1, 2] Industrial catalytic processes primarily depend upon heterogeneous catalysts (or solid catalysts) due to favorable physical and chemical properties like thermal stability, facile recyclability, and amenability to flow processes, thus permitting use under harsh reaction conditions and facilitating catalyst and product separations. However, for many heterogeneous catalysts, one common drawback is difficulty in determining the relationship between catalyst structure and activity. This is in part due to the structural complexity and inhomogeneity of many solid materials, and in part due to synthetic limitations regarding precise modification of active site structure. [3-6] As an example, solid oxides show structural complexity by commonly possessing a range of acid, base, and/or redox sites at the surface of the lattice, affecting catalytic properties. Additionally, different phases, surface planes, and degrees of surface hydration can also significantly affect the catalytic performance or active site speciation, when using the oxide as a support. Finally, solid oxides can

also possess various kinds of defects like anionic and cationic vacancies, kinks, steps, and terraces, and these sites also tend to have varying degrees of reactivity.[5, 7-12] Challenges of structural complexity and inhomogeneity exist for many heterogeneous catalysts, typically making it difficult to build fundamental, structural, and mechanistic understanding, and thereby making it difficult to rationally improve existing catalysts and processes. As a result, much progress in heterogeneous catalysis has occurred empirically or through painstaking trial-and-error.

By comparison, molecular catalysts are typically well-defined and less technically challenging to structurally characterize than solid materials, and the well-developed synthetic toolboxes of organic and inorganic chemistry facilitate precise structural modifications of molecular catalysts.[3, 4, 6] As a result, many industrial and academic studies have effectively elucidated structure-activity relationships and mechanistic insights for molecular catalysts, resulting in iterative improvements in performance through increased activity, selectivity, and stability for various homogeneous catalysts and processes. (Famous examples of this include the many generations of Grubb's catalyst,[13] the Wacker Process,[14] olefin dimerization/oligomerization catalysts,[15, 16] etc.) Being able to achieve similar synthetic control and molecular understanding of heterogeneous catalysts has the potential to combine the benefits of heterogeneous and homogeneous catalysis, thus facilitating the synthesis, discovery, and rational development of well-defined, highly efficient, and practical heterogeneous catalysts and processes. (**Scheme 1.1.1.**) As a result, this has been the focus of much academic and industrial research over the last few decades, and many promising approaches and results have been proposed and investigated towards this endeavor.[3, 4, 6, 17-19]

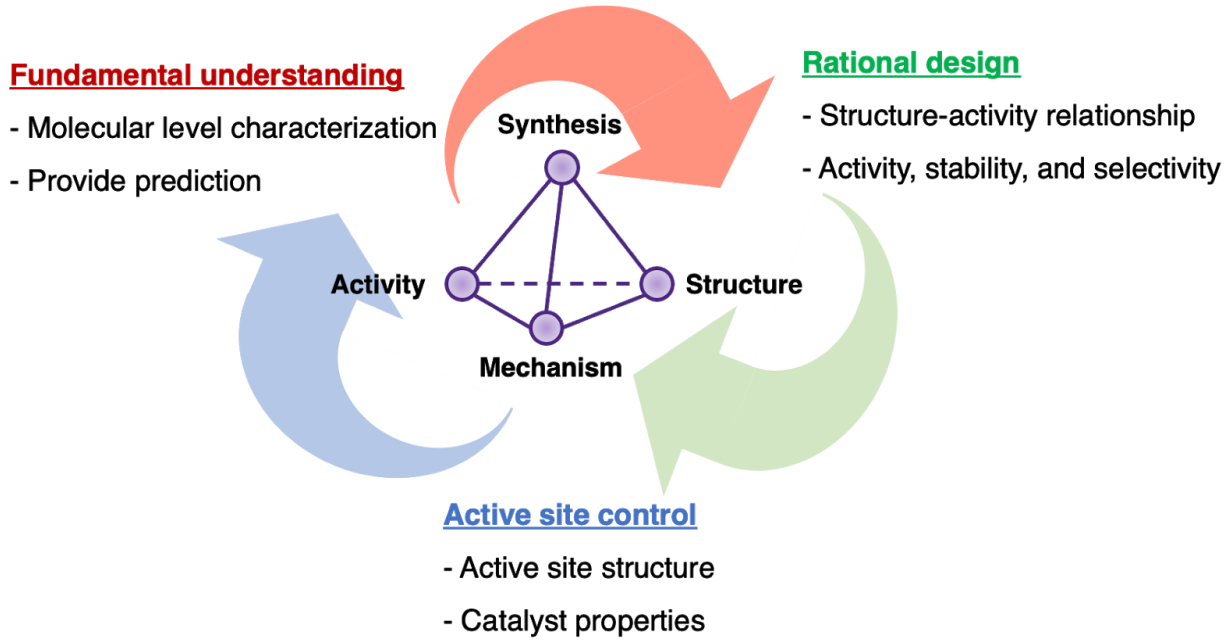

Scheme 1.1.1 Fundamental understanding of catalysts aids rational design. This, in turn, aids fundamental understanding.

Approaches towards greater understanding of heterogeneous catalysts and processes have generally focused on two strategies—the first being the development and utilization of methods for understanding complex catalytic systems. Experimental methods in this strategy include techniques like *in situ* and *in operando* spectroscopies and microscopies, to probe catalyst structure and behavior under reaction conditions, while computational methods like density functional theory and microkinetic modeling reveal insights into catalyst electronics and kinetic behavior.[20-24] While these methods can provide powerful insights into the behavior of many complex catalytic systems, they are also limited by uncertainties of whether what is measured or modeled corresponds to the sites most responsible for catalytic activity—often, small percentages of total surface sites.[25]

In contrast, approaches from a chemical paradigm towards understanding heterogeneous catalysts and processes have sought to synthesize well-defined or molecularly defined

heterogeneous catalysts as model systems and systems with precisely controlled properties. One approach to this is through the controlled grafting of discrete catalysts and precursors onto surface sites or into the pores of solid materials, thereby creating well-defined species that are more amenable to study and modification. In the strategy of surface organometallic chemistry (SOMC), for example, organometallic complexes are grafted to the surface of oxide supports with preserved and modifiable coordination spheres. Treating the support as a ligand in the coordination sphere of the organometallic active site, supports and other ligands can be selected or modified to optimize catalytic activity, much like in homogeneous catalysis. Naturally, heterogeneous catalysts made this way also more amenable to characterization techniques that are common for studying homogeneous catalysts, like ^{1}H and ^{13}C nuclear magnetic resonance spectroscopy and homogeneous molecular models.[3, 4, 6, 17]

Complementary to the grafting of discrete molecular complexes onto surface sites, synthetic chemists and materials scientists have sought to generate molecularly defined, extended materials as catalysts or supports, such as Metal–Organic Frameworks (MOFs) and zeolites. MOFs are crystalline, porous coordination polymers, while zeolites are porous, crystalline aluminosilicates. MOFs and zeolites, in contrast to traditional oxide catalysts and supports, have high crystallinity and periodicity, permitting the use of crystallographic characterizations and resulting in greater efficacy of bulk characterization techniques like solid state NMR and X-ray absorption spectroscopy in elucidating catalyst structure. This results in a high degree of structural definition and understanding of these materials relative to traditionally used, amorphous oxides and facilitates computational and theoretical studies. Not only can these advantages permit the molecular understanding of active site structure in extended materials, but they can also enable the understanding and rational design of relevant catalyst properties outside of active site speciation,

like pore diffusivity or size selectivity of substrates, especially in highly tailorable materials like MOFs.[17, 19, 26-36]

These synthetic approaches, and others,[37, 38] provide researchers with a theoretical framework and a wide degree of synthetic freedom when used together or separately for rational catalyst design and have great potential for providing insights and improving catalytic systems in the future. However, one of the limitations that faces the idea of rational catalyst design is that often, some of the most active sites are structurally complicated, poorly defined, and/or challenging to make in a rational/controlled way. Examples of such sites include surface defects in metals or metal oxides, sites with strained chemical bonds, sites at material interfaces, distorted mixed-metal oxide clusters, transient catalytic species, and many others.[10, 39-48] Sometimes some of the best catalysts are the most unstable chemical species. In other words, simply just because one has the synthetic tools to make catalysts with molecular definition and site uniformity, does not mean that one will make a highly active catalyst, and vice versa.

Despite these synthetic challenges, efforts towards making catalysts by design are inherently useful—and not just from the insights they provide. New synthetic strategies and catalyst compositions are ultimately exploratory, with the potential to create unique materials with unique and valuable properties that have not been observed before. For example, from surface organometallic chemistry, new forms of catalytic activity have been discovered, such as the single-site metathesis of alkanes, refining carbon chains into lower and higher molecular weight and branched homologues.[49] In zeolites, various forms of shape selectivity have been impactful in the refinement and conversion of hydrocarbon fuels and feedstocks, where channels and pores of the right size significantly influence selectivity in inherently unselective catalytic reactions.[50-54] And MOFs hold potential for shape selectivity and the precise special separation of active sites, which

can be useful for specific applications like tandem catalytic transformations.[35, 55, 56] Delving into new and unknown synthetic territories, exploring the properties of unique, catalytic materials, and yielding fundamental insights aids in the understanding of traditional systems, as well as accelerates the development of unique materials and catalytic processes.

1.2 Thesis Outline

The work in this dissertation contributes the research efforts of rational catalyst design, specifically in the development and study of Zirconium MOFs as catalysts and supports for reactions related to H_2 utilization, hydrocarbon conversion, and biomass conversion.

Chapter 2 begins with preliminary work studying Zr-MOFs as supports for surface organometallic chemistry, specifically examining grafting interactions of tantalum(V) trisneopentyl neopentylidene with the Zr_6O_8 secondary building unit in the MOF, NU-1000. The chapter reports characterization details and active site speciation and additionally examines preliminary reactivity studies for propane metathesis and 1-butene metathesis. Data show that the synthesized material is not active for propane metathesis or 1-butene metathesis under the tested reaction conditions, however activity for 1-butene isomerization was observed following catalyst pretreatment with H_2. Control experiments showed, though, that the support itself, NU-1000, was active for 1-butene isomerization without tantalum incorporation, laying the groundwork for chapters 3 and 4. Potential follow-up work and studies as how to make effective MOF-supported alkane metathesis catalysts are briefly discussed in the context of work has been published since the inception of this study.

Chapter 3 expands upon the observation of 1-butene isomerization over the Zr_6O_8 secondary building unit of NU-1000 through catalytic studies in a packed bed reactor, observing both hydrogenation and isomerization of 1-butene under reaction conditions. Additionally,

interactions of H_2 with the Zr_6O_8 node of NU-1000 are studied via spectroscopic and computational methods, finding that H_2 is heterolytically cleaved over adjacent Lewis acid and base sites, generating catalytically active proton and hydride pairs that are responsible for olefin conversion.

Chapter 4 expands the study from chapter 3 to additional Zr-MOFs sharing the same Zr_6O_8 building unit but varying in framework topology. Effects of thermal pretreatments on catalyst activity are also examined. Data show that catalytic activity in the series of MOFs does not trend with total quantity of open Lewis acid sites, but rather the nature of Lewis acid sites and H_2 cleavage pathways, as determined by framework topology and thermal pretreatment conditions. Spectroscopic and catalytic data, along with data reported in chapter 3, suggest that isomerization happens via parallel hydride- and acid-catalyzed pathways. As a result, data also show that thermal dehydration of the Zr_6O_8 cluster can lead to shifts in H_2 cleavage pathways (using bridging oxo ligands vs. terminal hydroxyl ligands as a base), which corresponds with shifts in isomerization selectivity due to differences in the Brønsted acidity of protons generated from H_2 cleavage. How these pathways shift varies between MOF topologies. Finally, MOF topology is also shown to dictate the orientation of substrate co-adsorption, with the *cis* orientation of substrates required for conversion. This study showed a complex interplay between catalyst structural parameters in performance for 1-butene hydrogenation and isomerization.

Finally, in chapter 5, the effects of MOF-topology on Lewis acid catalyzed reactions are directly studied on a geometrically constrained and sterically bulky reaction, Meerwein-Ponndorf-Verley (MPV) reduction. In a systematic study, computational and experimental results show 6-connected topologies are found to allow more favorable co-adsorption of substrates than 8-connected topologies, allowing more space for the bulky transition state to form. As a trade-off,

however, 6-connected topologies display less influence over product selectivity in MPV reduction of 4-*tert*-butylcyclohexanone, where the stereoselectivity of products has been shown to be influenceable by pore environment around the active site.

Ultimately, the findings in this dissertation reveal a versatility and complexity in Zr-MOF based catalysis and establish structural parameters for tuning catalytic performance in various acid-base catalyzed reactions.

CHAPTER 2. Preliminary Efforts in the Synthesis of Organotantalum Catalysts for Alkane Metathesis and Other Hydrocarbon Transformations

2.1. Chapter Summary

Single-site catalyzed alkane metathesis is a unique reaction, requiring multifunctional active sites to successively dehydrogenate alkanes, metathesize the resulting olefins, and then hydrogenate them, necessitating the use of highly reactive metal precursors such as organotantalum and organotungsten complexes. Through the utilization of surface organometallic chemistry (SOMC), these highly reactive compounds can be grafted and stabilized on oxide surfaces, resulting in molecularly defined heterogeneous catalysts of unique structure and reactivity. Challenges exist in this field however, with the use of traditional supports like SiO_2 and Al_2O_3, which typically have a range of surface sites, leading to inhomogeneity of grafted catalytic species. This chapter details early, unpublished work extending this approach to Metal–Organic Frameworks (MOFs) as supports for organometallic catalysts, with the aim of synthesizing well defined alkane metathesis catalysts. Specifically, tantalum(V) trisneopentyl neopentylidene was anchored onto the zirconium oxide node of the MOF, “NU-1000”, characterized using a range of techniques, and tested for propane metathesis. Characterization and reactivity studies show that, although tantalum neopentylidene is successfully incorporated into the MOF, interaction with the MOF node does not result in a competent alkane metathesis catalyst. Testing catalytic activity with olefins, however, showed the material was competent for 1-butene isomerization. Control experiments revealed that NU-1000 could perform this reaction after thermal treatment under an H_2 atmosphere—without tantalum incorporation—serendipitously revealing unreported activity of the Zr_6O_8 node and laying the groundwork for chapters 3 and 4 of this dissertation.

2.2 Introduction to Organotantalum Catalysts and Metal–Organic Frameworks

Heterogeneous catalysts (solid and solid-supported) are used nearly ubiquitously in industrial chemical processes due to their advantages over molecular catalysts such as higher thermal stability, recyclability, and straightforward separations from products.[3, 5, 6] However, they typically possess a broad distribution of chemical sites, with only a fraction of them being active for catalysis. This inhomogeneity makes it difficult to have a molecular understanding of their active sites and renders it difficult to build structure-activity relationships and rationally design new catalysts. As a result, improvements in the field of heterogeneous catalysis have mostly occurred by trial and error. With growing energy demands and environmental concerns, the rational design and discovery of new and more efficient catalysts is becoming more and more imperative.

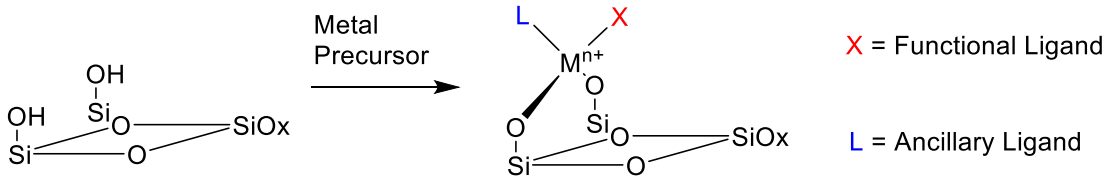

Scheme 2.2.1. Generic scheme of SOMC catalyst synthesis. Organometallic precursors can be grafted onto oxide surfaces. Ligand coordination sphere can be modified for various performance effects.

One powerful approach towards rationally designing heterogenous catalysts is surface organometallic chemistry (SOMC)[3, 4, 6], which involves anchoring coordination and organometallic compounds onto chemically controlled, well-defined supports, treating the support as a ligand. (**Scheme 2.2.1.**) By control of support-to-metal precursor reactivity, one can generate a narrower distribution of chemical sites with controlled and molecularly defined coordination spheres. Coordination spheres of catalytic and precatalytic species can further be controlled after grafting through thermal and chemical treatments (e.g., the generation of supported metal hydrides through treatment of supported organometallics under an H_2 atmosphere). Through the generation of molecularly defined sites and structure control, this approach facilitates the relation of a solid

catalyst's structure to its activity. Although typical SOMC supports are metal oxides with surface hydroxyls such as silica, alumina, or zirconia,[57-62] little of this approach has used functional materials such as MOFs for controlling active site activity.

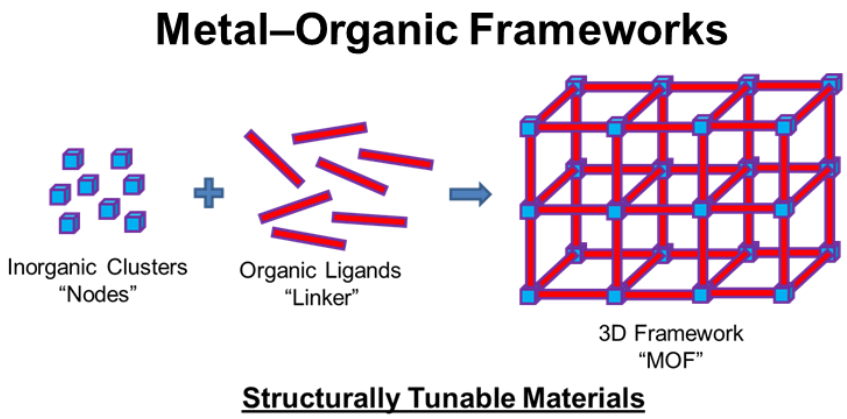

Scheme 2.2.2. Conceptual construction of Metal - Organic Frameworks.

Metal-organic frameworks (MOFs) are a class of functional materials gaining in academic interest for the rational design of heterogeneous catalysts.[35, 36] MOFs are comprised of metal clusters or ions (nodes) and multidentate organic linkers, which together assemble into crystalline, porous, coordination polymers. Depending upon choice of node, linker, synthetic conditions, and post-synthetic modifications, MOF chemical and physical properties can be precisely tuned for the design and optimization of heterogeneous catalysts and supports. As catalysts, MOFs can have catalytic acid sites or open coordination sites on the linkers and nodes,[63] and as supports, catalytic species have been post-synthetically incorporated into MOFs by encapsulation inside the pores,[55] anchored to MOF nodes[64-67], and tethered to organic linkers.[36, 68, 69] Given the periodicity and crystallinity of these materials, one can in principle design a well-defined, single-site catalyst, with active sites distributed uniformly throughout the structure, leading to even narrower distributions of chemical sites than with traditional catalyst supports like SiO_2 or Al_2O_3, which can have an inhomogeneous distribution of surface sites.[8, 9, 70, 71] With enhanced structural control

understanding of these catalysts, structure-reactivity relationships can ideally be delineated to propel the design of next generation catalysts for valuable chemical transformations.

One such chemical transformation is the metathesis of alkanes by silica and alumina supported organotantalum and tungsten species.[49, 57-61, 72, 73] Alkane metathesis involves the activation of C–C and C–H single bonds to transform alkanes into shorter and longer carbon chain homologues, e.g. propane conversion to ethane and butane, or butane to ethane, propane, and liquid hydrocarbon fuels. (**Scheme 2.2.3**) While this transformation has been reported using dehydrogenation catalysts and olefin metathesis catalysts in tandem,[74, 75] what makes organotantalum and tungsten catalysts unique is their capacity to do this transformation with a single site. Organotantalum and tungsten species have been shown to be multifunctional, consecutively performing alkane dehydrogenation, olefin metathesis, and olefin hydrogenation.[4, 6, 73, 76] As such, in addition to these reactions, these systems have also been studied for other unique and/or valuable chemical transformations such as alkane cross metathesis,[77] the non-oxidative coupling of methane,[78] ring-opening metathesis of cycloalkanes,[79] and the hydrogenolysis of paraffins, among others.[3, 6, 73, 76, 80] These conversions may be valuable in the refinement of petrol chemicals and shale gas to afford more efficient fuels and feedstocks.

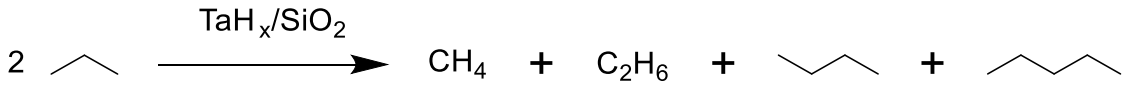

Scheme 2.2.3. Chemical equation for alkane metathesis. Supported tantalum hydrides can serve as catalysts.

Unfortunately, alkane metathesis catalysts have yet to realize any industrial application, in part because available catalysts exhibit inadequate activity, stability, and selectivity. Although displaying capabilities of C-H and C-C bond activation, supported organotantalum and tungsten complexes display low TON (<100) over the course of several days, deactivating as a function of time on stream. These catalysts are also highly air and moisture sensitive, limiting operating

conditions and synthetic methods. Additionally, these catalysts show little size selectivity, with olefin metathesis—and thereby alkane metathesis—being reversible and generally unselective with respect to the size of carbon chain, leading to statistical distributions of products.[81, 82]

With the catalytic potential and challenges of supported organotantalum and tungsten catalysts, this research sought to delve into unexplored territory (at the time)[80] of incorporating these catalysts into MOFs for fundamental studies regarding structure-reactivity relationships. Project aims were to 1) synthesize MOF-based alkane metathesis catalysts, 2) understand how activity and stability of supported organotantalum catalysts can be controlled through chemical modification of anchoring sites on the support, and 3) understand how selectivity of alkane metathesis may be influenced by the local pore environment surrounding the catalytic active site.

To approach these goals, tantalum(V) trisneopentyl neopentylidene, Ta(=Np)(Np_3), was incorporated into the zirconium MOF (Zr-MOF), "NU-1000", as a model system for MOF-supported organotantalum catalysts. Ta(=Np)(Np_3) was chosen as the organometallic precursor due to its ease of synthesis[83] and greater thermal stability relative to other precursors like pentamethyl tantalum ($TaMe_5$). Additionally, NU-1000 was chosen as the model support due to its thermochemical stability, its amenability towards controlled post-synthetic modification, and its structural relationship with other Zr-MOFs.[30, 84-87] NU-1000 is comprised of Zr_6O_8 cluster-based nodes and 1,3,6,8-tetrakis(p-benzoate) pyrene (TBAPy) linkers, forming mesoporous and microporous channels that form an extended Kagomi lattice (**Figure 2.2.1.**). Carboxylate-to-Zr^{4+} bonds between the linker and node yield thermally stable frameworks[88] (up to ~350°C) and the topology of NU-1000 yields uniformly 8-connected nodes, with 4 engineered, missing-linker defects. At these defects, hydroxyl ligands, water ligands, and bridging hydroxyl ligands coordinated to the node can provide anchoring sites for organometallic precursors.[66, 89, 90] Through

a range of thermal and chemical treatments,[91-97] identity and quantities of these anchoring ligands can be modified in NU-1000, providing a synthetic variability of anchoring sites within the system,

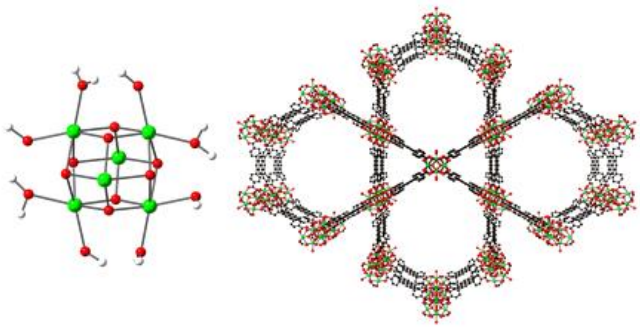

Figure 2.2.1. Zr_6O_8 node and extended Kagomi lattice of NU-1000. Zr atoms are in green and oxygen atoms in red.

in addition to the structural variability within the class of Zr-MOFs.[30] Thus incorporation, characterization, and study of Ta(=Np)(Np_3) in NU-1000 would provide a baseline from which structural variations could be synthesized and compared.

2.3 Catalyst Synthesis and Charcterization

2.3.1 Catalyst Synthesis:

A 5g batch of NU-1000 was synthesized and activated according to published procedures.[98] This same batch was used for all catalyst syntheses. 10 mg aliquots of NU-1000 were impregnated with Ta(=Np)(Np_3) using solvothermal deposition in MOFs (SIM).[66-68] In the general procedure, NU-1000 was added to a vial and soaked in heptane, while Ta(=Np)(Np_3) was dissolved in heptane. The dissolved tantalum solution was then transferred into the vial of NU-1000 at room temperature, agitated every hour for 3 hours, and then left overnight. The precursor solution was then solvent exchanged for fresh heptane three times and solvent exchanged three times with pentane to wash out any unbound precursor. Samples were activated under vacuum at 40℃ for 12 hours. Screened conditions of 2 eq, 4 eq, and 8 eq of Ta(=Np)(Np_3) dissolved in heptane (calculated on a per node

basis) show that tantalum loadings, using inductively coupled plasma-optical emission spectrometry (ICP-OES), are capped at about 1.2 tantalums per node (**Table 2.3.1.1.**). Since a theoretical maximum of 4 tantalums per node should be achievable, we investigated why loading stopped at approximately 1 tantalum per node. Digestion of NU-1000 in 0.1 M NaOD solution shows this batch of NU-1000 harbors approximately 2.5 formate ions per node, as detected by ^{1}H nuclear magnetic resonance spectroscopy (NMR). Formates ion can form as decomposition products of N,N-dimethylformamide during MOF synthesis; these ligands have been shown to cap open sites on zirconium nodes.[99] These data suggested, that the 2.8 sites along each node that tantalum did not anchor to are likely formate-capped, and that tantalum selectively binds to the sites capped with water and hydroxyl ligands and was a first suggestion of uniform, disperse tantalum sites. These data are also consistent with reports of grafting mechanisms of organotantalum complexes over silica and other traditional oxides, involving protonolysis of alkyl ligands of the precursor.[72, 78, 100, 101]

Ta(=Np)(Np_3)	Ta/Node
2 eq	0.79
4 eq	1.15
8 eq	1.19

Table 2.3.1.1. Tantalum loadings as measured by ICP-OES in NU-1000 as a function of precursor equivalents used in material synthesis. Loading maxes out around 1 Ta/Zr6 cluster, regardless of precursor equivalents.

2.3.2 Bulk Characterization

Upon obtaining these results, tantalum SIM was scaled up to 200mg of NU-1000 using 4 eq of Ta(=Np)(Np_3), yielding a ~200mg batch of Ta@NU-1000 with 1.08 Ta/node as determined with ICP-OES. BET analysis (**Figure 2.3.2.1.A**) shows a decrease in surface area per gram (~2100 m^2/g to ~1500 m^2/g) consistent with the incorporation of a heavy, bulky tantalum moiety into the

channels of NU-1000. The microporous and mesoporous steps in the nitrogen isotherm show porosity is maintained from the pristine NU-1000 to the tantalum impregnated NU-1000, suggesting all the tantalum should be accessible for reactants. Bulk characterization via powder x-ray diffraction shows that the long-range order of the framework does not change after tantalum incorporation (**Figure 2.3.2.1.B**), and there is no shift in the lattice peaks of NU-1000 as sometimes reported in other systems[102]. This suggests a gentle deposition, without any distortion of the framework. Scanning electron microscopy (SEM) (**Figure 2.3.2.2.**) and corresponding energy dispersive x-ray spectroscopy (EDS) (**Figure 2.3.2.3.**) also corroborate uniform and disperse tantalum in a crystalline framework. Elemental line scans show a uniform distribution of tantalum throughout the roughly 5 μm hexagonal crystallites of NU-1000. All bulk characterization methods suggest from a macroscopic level that the tantalum sites are uniform and evenly dispersed throughout NU-1000.

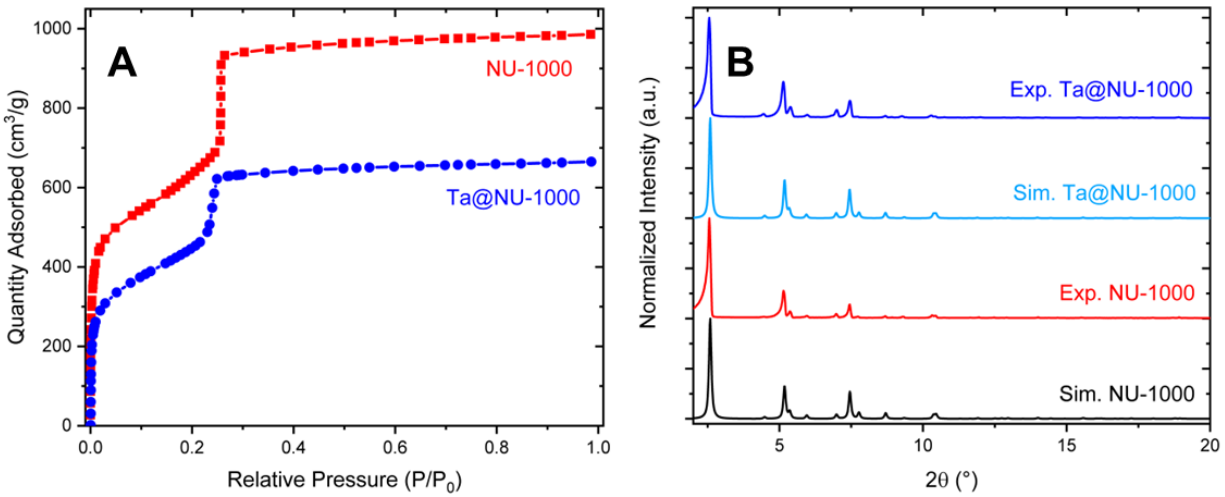

Figure 2.3.2.6. (A) N_2 Isotherms of NU-1000 (red) and Ta@NU-1000 (blue). (B) Experimental and simulated powder x-ray diffraction patterns for NU-1000 and Ta@NU-1000. From top down, Ta@NU-1000, Simulated Ta@NU-1000, NU-1000, and Simulated NU-1000. Data show a maintenance of porosity and crystallinity during synthesis of the materials, although tantalum grafting does lower total N_2 uptake.

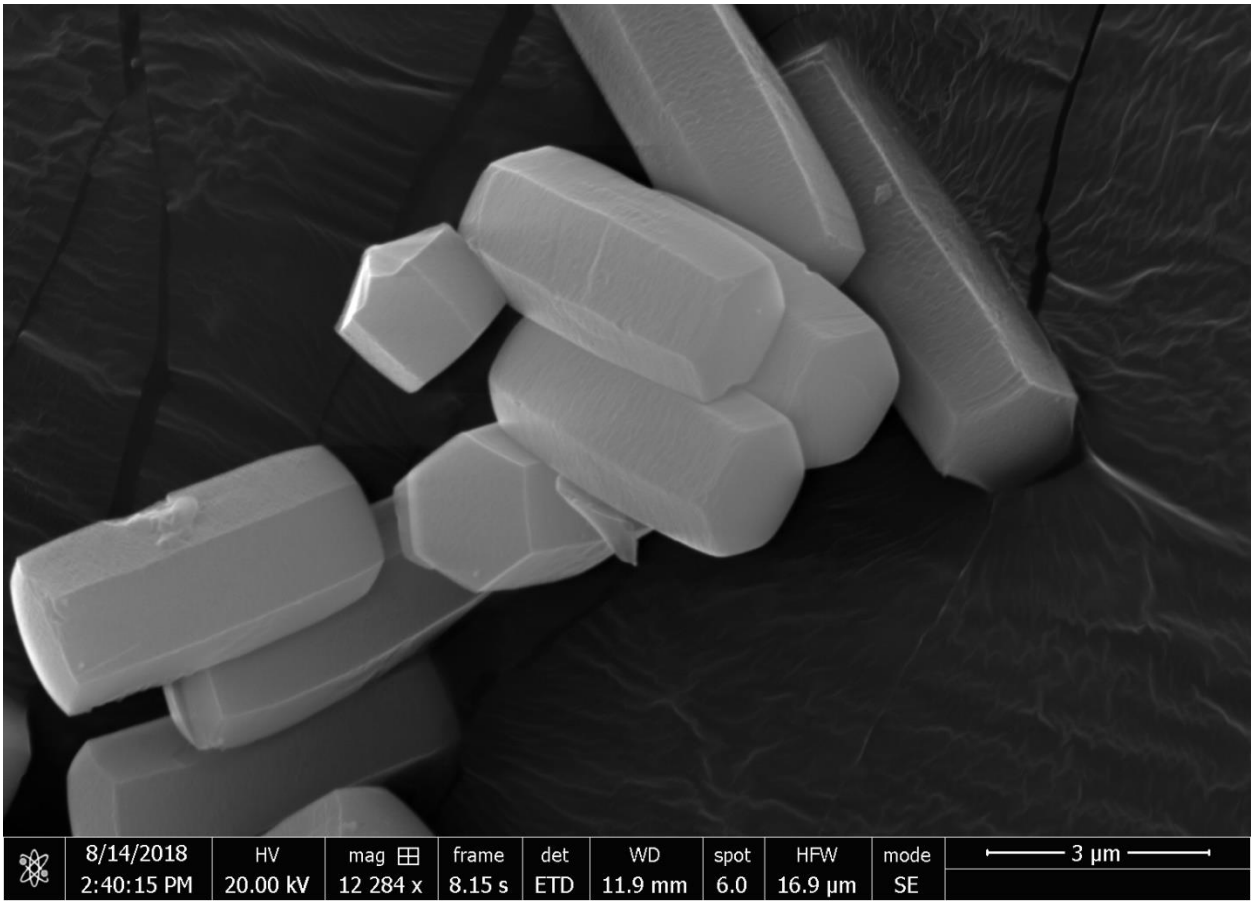

Figure 7.3.2.2 Scanning Electron Microscopy of Ta@NU-1000.

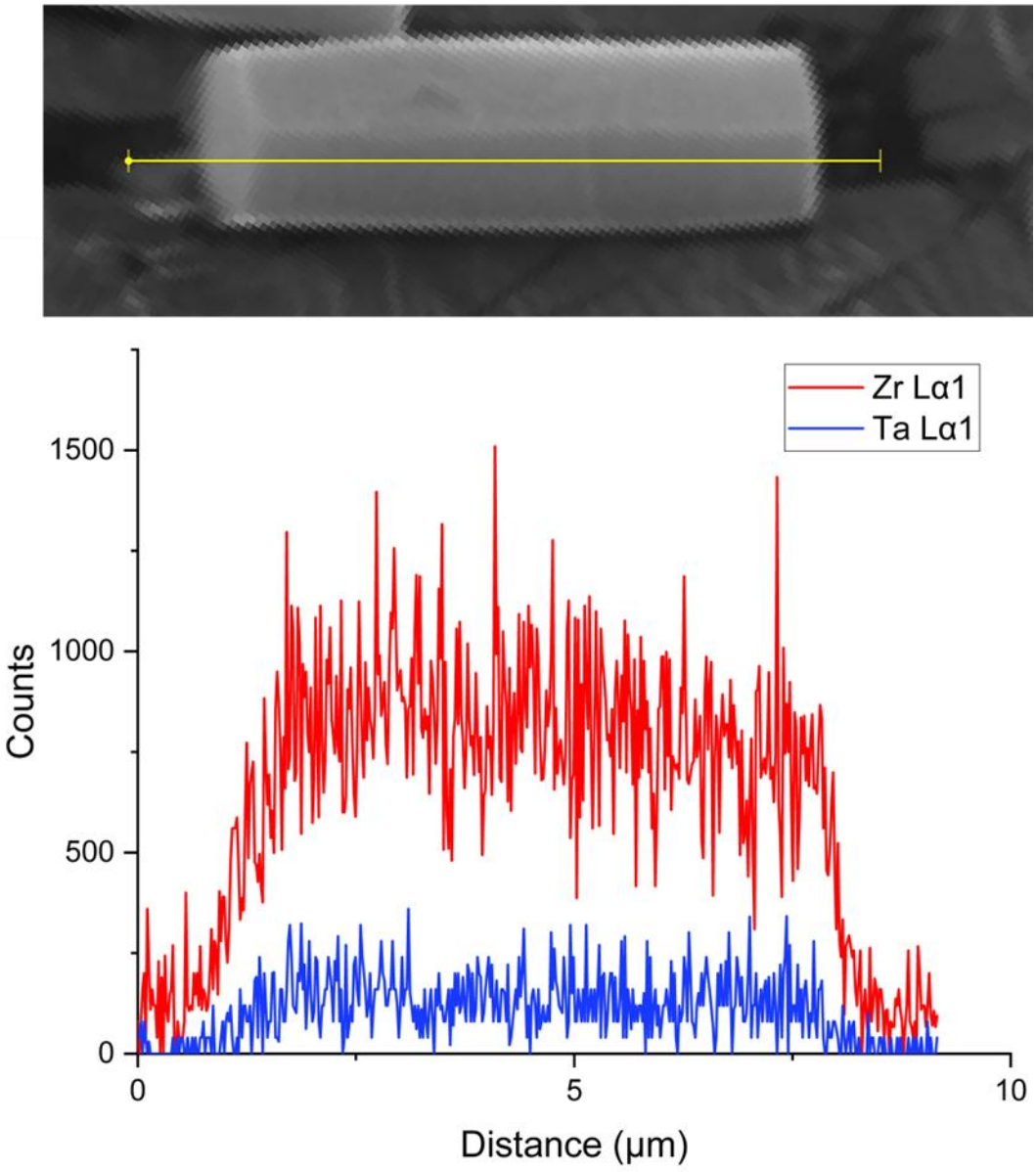

Figure 2.8.2.3. Energy Dispersive X-ray Spectroscopy line scan of Ta@NU-1000. Emission counts for Zr (red) and Ta (blue) are shown as a function of linear position in the crystallite.

2.3.3. Active-site Characterization

All characterization of Ta@NU-1000 involved use of air and moisture free conditions in an argon glovebox and in glassware on a N_2 atmosphere Schlenk line. Large single crystals of NU-1000, ~150 μm, were grown using a modified synthesis procedure[98] and post-synthetically impregnated with tantalum according to previously mentioned procedures. This yielded tantalum impregnated crystals with a loading of .25 Ta/node, despite using as high as 20eq during synthesis. The crystal structure obtained from single crystal x-ray diffraction (**Figure 2.3.3.1.**) indicates that tantalum binds to the node of NU-1000 in a 3-fold fashion, to both hydroxyl and water ligands, in both the mesoporous channel (A) and the orthogonal c-pore (B). The tantalum moieties found in the mesopore had an occupancy of 0.05 at each position, while the tantalum moieties in the c-pore had occupancies of 0.02 at each position. While this may suggest that there is a chemical preference

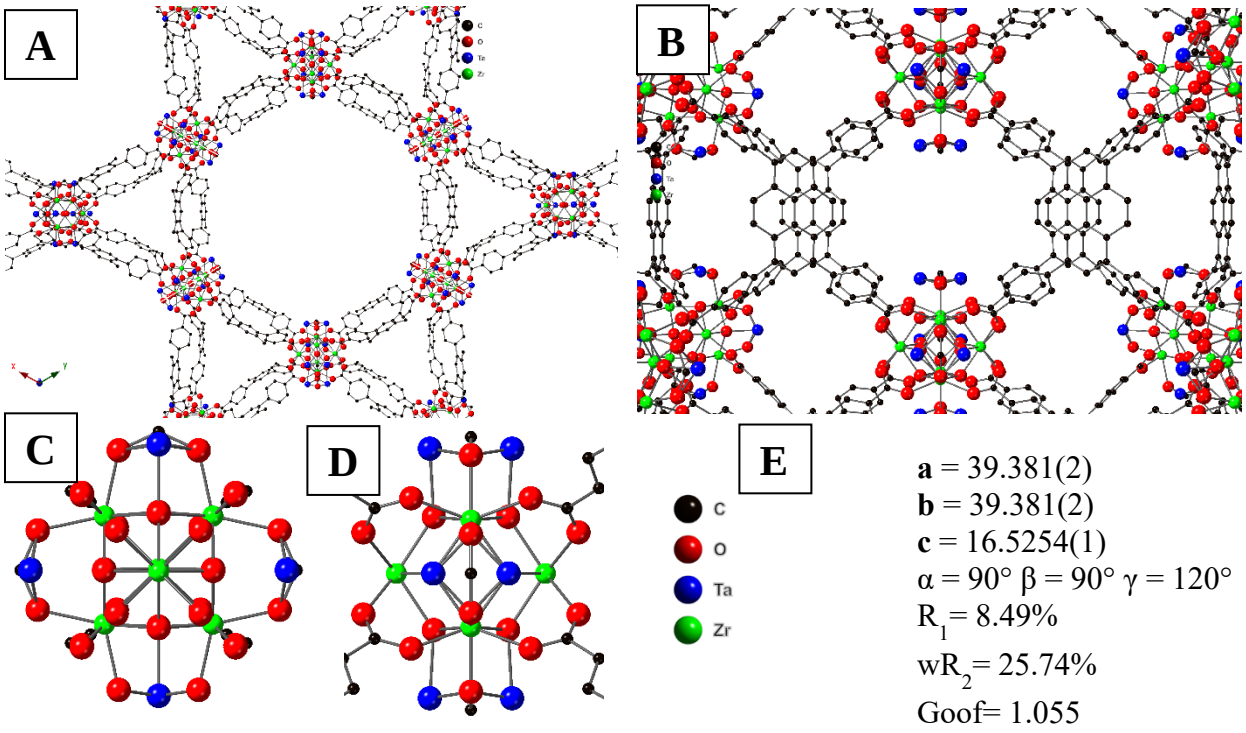

Figure 2.3.3.1. Ta@NU-1000 crystal structure. (A) Perspective of Ta in the Kagomi Lattice. (B) Perspective of tantalum in c-pore. (C&D) Views of Tantalum on NU-1000 node. Linkers omitted for clarity. (E) Crystal structure parameters

into which pore tantalum anchors, the likelier explanation is an uneven distribution of formate capping ligands on the node, given report of formates providing structural stability to NU-1000[92] and established protonolysis grafting mechanism for organotantalum precursors. Ultimately, crystallographic data show that tantalum precursors graft defects in the hexagonal pores and c-pores, resulting in sites with different pore environments. These steric differences may have potential for size-selective influence on catalytic performance, although this topic will not be investigated in this dissertation. Due to the low occupancy of the tantalum and the fluxionality, flexibility, and low molecular weight of the potential neopentyl ligands, we were unable to see the full coordination sphere of each tantalum site.

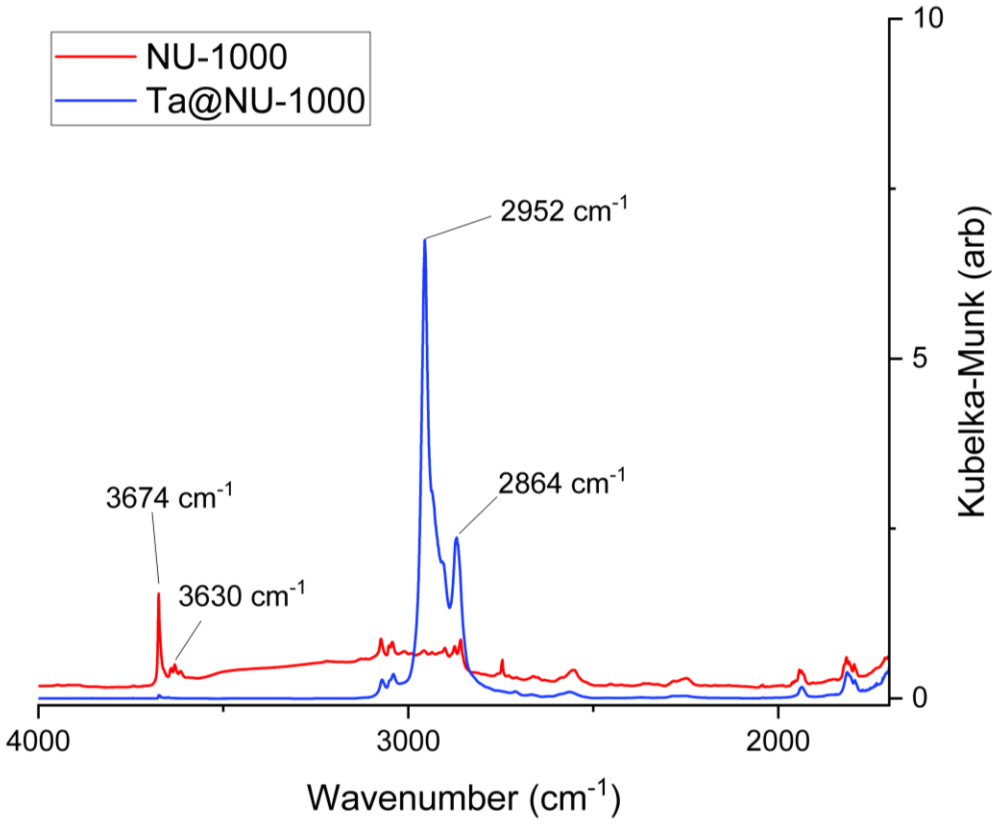

Figure 2.3.3.2 Diffuse Reflectance Infrared Fourier Transform Spectroscopy of NU-1000 (red) and Ta@NU-1000 (blue). C–H stretches can be seen from 2860-2952 cm^{-1} upon the incorporation of tantalum, in addition to a consumption of O–H stretches in NU-1000, located from 3600-3674 cm^{-1}.

To overcome this, the tantalum ligand sphere was probed using diffuse reflectance infrared Fourier transform spectroscopy (DRIFTS) and cross polarization magic angle spinning (CPMAS) solid state ^{1}H and ^{13}C NMR. Comparison of DRIFTS (**Figure 2.3.3.2.**) spectra for pristine NU-1000 and Ta@NU-1000, shows the appearance of strong C-H stretches from ~2952 cm^{-1} to ~2864 cm^{-1} which are consistent with the presence of tantalum neopentyl ligands, as seen in previously reported experiments.[57, 76] Further we see the disappearance of the strong O-H stretches at 3674 and 3630 cm^{-1}, assigned to the water and hydroxyl ligands on the node.[89] This is consistent with literature evidence that tantalum anchors to supports via the protonolysis of some of its neopentyl ligands, and low intensity of remaining OH stretches suggests a near complete consumption of node associated protons during the grafting process.[103] ^{1}H and ^{13}C CPMAS NMR data additionally corroborate the presence of neopentyl and neopentylidene ligands (**Figure 2.3.3.3.**). ^{13}C spectra of NU-1000 and Ta@NU-1000 show there is incorporation of a new, alkyl moiety at 30 ppm, consistent with methyl groups of neopentane ligands.[101] However, signals indicative of methylene and methylidene carbons are not visible. The α-methylene and methylidene carbons are very challenging to see without ^{13}C enrichment,[58, 59, 103] so this is not atypical. Even with ^{13}C enrichment, these peaks are usually broad and low intensity.

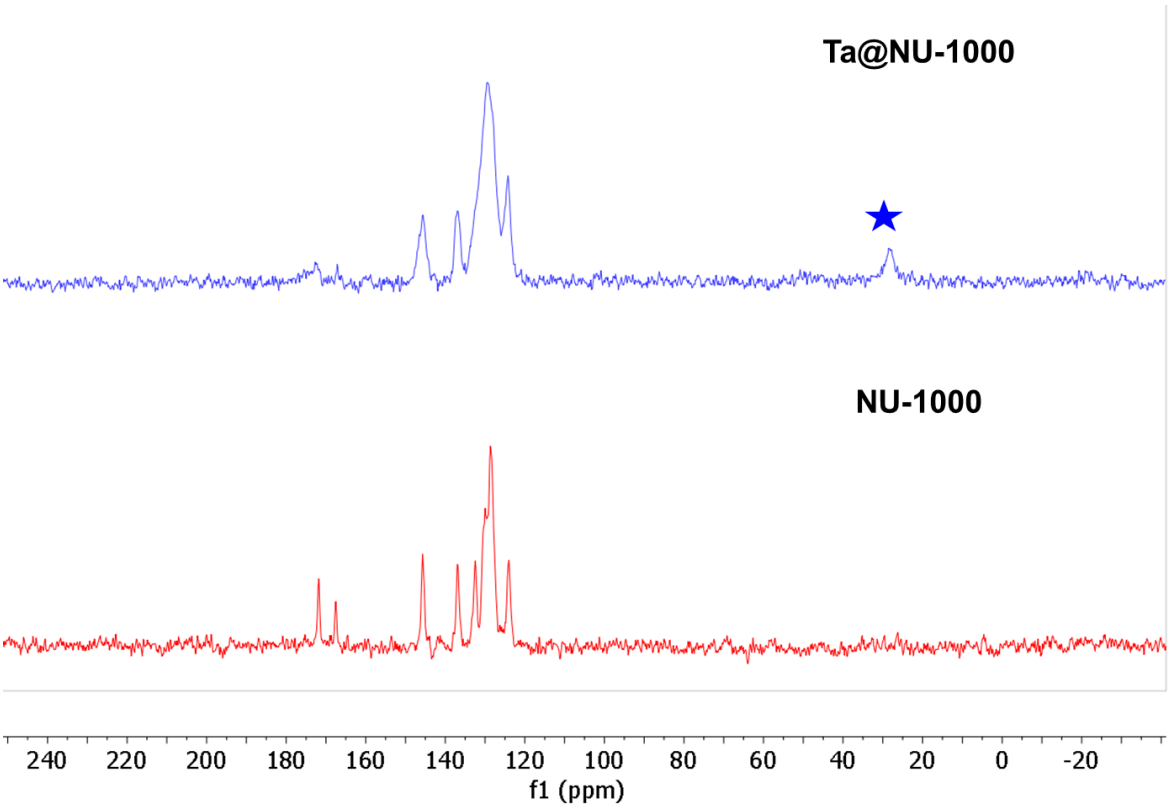

Figure 2.3.3.3 ^{13}C CP-MAS NMR of Ta@NU-1000 (top, blue) and NU-1000 (bottom, red). Blue star marks signal at 30 ppm consistent with methyl carbons of neopentyl and neopentylidene ligands.

Examination via ^{1}H-MAS NMR, however, shows the disappearance of peaks around 7.90 ppm and 2.54 ppm and the appearance of peaks at 5.23ppm, 0.77 ppm, and -0.68ppm, upon tantalum grafting (**Figure 2.3.3.4.**). The peaks at 7.90ppm and 2.54 ppm are assigned to hydroxyl and water protons, consistent with loss of protons from protonolysis of neopentyl ligands during precursor grafting.[80] The broad peaks at 5.23ppm and 0.77 ppm, however, strongly suggest the methylidene, methylene, and methyl moieties. Methyl peaks usually appear from 1.0-0.8[61, 71, 103] ppm in similar systems. While the peak is broad, the slight upfield shift in frequency may be consistent with methyl protons experiencing secondary fields from ring-current effects,[71] with the bulky *t*-butyl groups potentially placing methyl protons in proximity of the aromatic TBAPy linkers. Methylene protons also typically appear from 1.0ppm-0.8 ppm;[8,32, 34] thus, the broad

feature at 0.77 ppm may be consistent with the presence of both methylene and methyl species. Finally, methylidene protons have been reported around 4.4 ppm for similar systems.[61] While 5.23 ppm, is further downfield than one might expect, tantalum alkylidenes have not been studied on supports like NU-1000, which has increased Lewis acidity relative to SiO_2. Regarding the peak at -0.68 ppm, the moiety most likely belongs to residual heptane from catalyst synthesis that physisorbed in the pores of the material. This assignment is primarily due to the exceptional sharpness of the peak, which is not characteristic of solid-state, proton spectra. Overall, these data are consistent with a tripodal catalyst speciation, with either singular neopentylidene ligands or a pair of neopentyl ligands in the metal-coordination sphere.

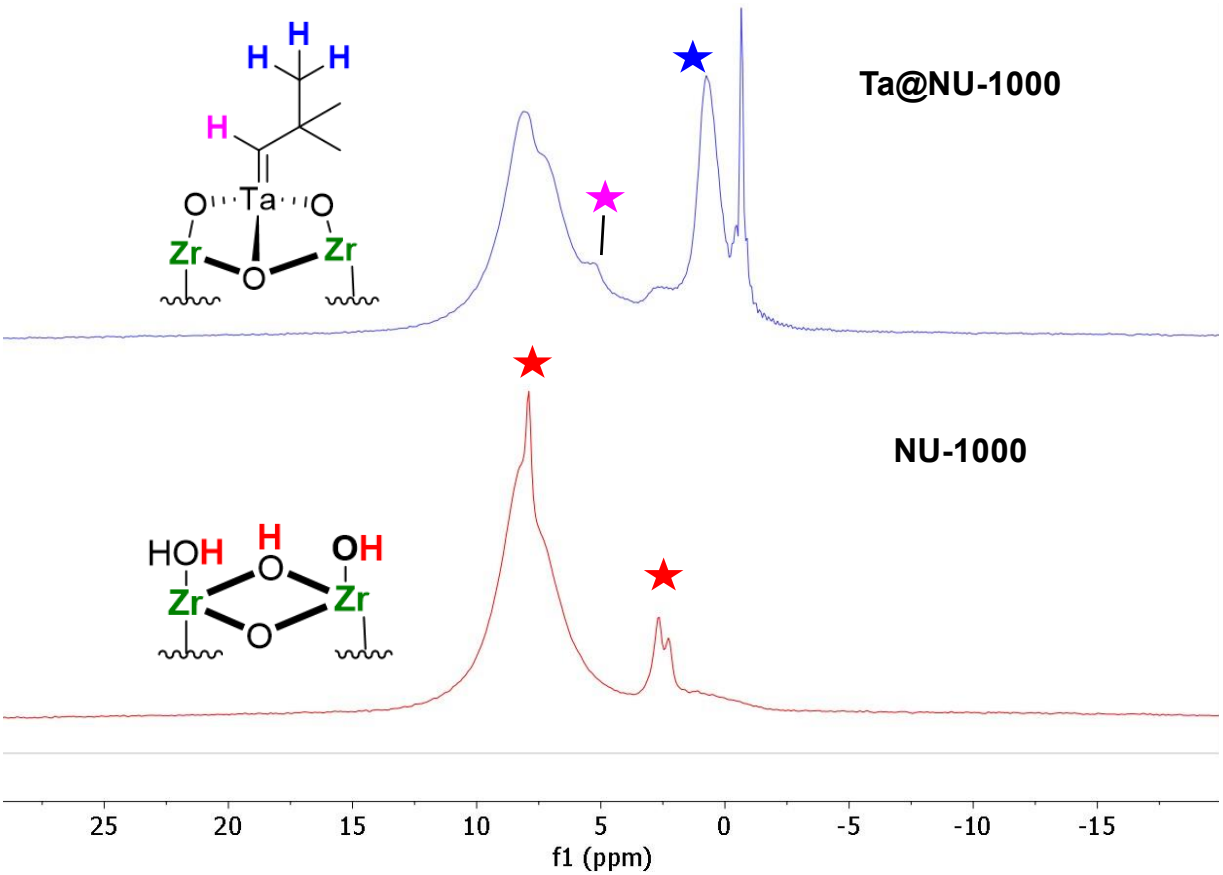

Figure 2.3.3.4. ^{1}H CP-MAS NMR of Ta@NU-1000 (top, blue) and NU-1000 (bottom, red). Red stars in the bottom spectra mark signals assigned to bridging O–H, H_2O, and terminal O–H protons on the Zr_6 node. Blue star in the top spectrum marks a feature consistent with methyl and methylene protons of neopentyl and neopentylidene ligands. Pink star marks new feature at 5.2 ppm, assigned to the methylidene proton of neopentylidene ligands.

2.4 Computational Study of Ta@NU-1000 Grafting and Structure

Density functional theory calculations in collaboration with the Gagliardi group corroborated the feasibility of these structural assignments. Calculations were done using basis set def2-SVP for carbon, hydrogen, and oxygen and basis set def2-TZVPP for zirconium and tantalum. The node of NU-1000 was modeled with acetate linkers to reduce computational load, with carbon atoms of acetate linkers frozen to mimic solid framework.

Results showed that Ta(=Np)(Np_3) can initially graft to water and hydroxyl ligands on the Zr_6O_8 node in a bipodal fashion (**Figure 2.4.1.**), containing a neopentyl and neopentylidene in a tetrahedral geometry. Following this, however, it is energetically favorable to undergo additional protonolysis with a bridging hydroxyl ligand, resulting in a tripodal tantalum species, with only a remaining neopentylidene ligand. These results suggested the material would be unlikely to display significant alkane metathesis activity, as it has been proposed that supported organotantalum and tungsten complexes require 3 alkyl ligands (or a functionally equivalent one alkyl ligand and one alkylidene) to observe catalytic activity.[4]

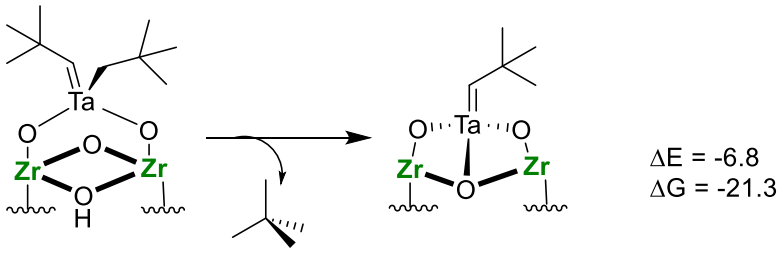

Figure 2.9.1. Structural calculations for reactivity of tantalum(V) trisneopentyl neopentylidene with the node of NU-1000. Node is truncated, and linkers omitted for visual clarity.

2.5 Tests of Reactivity Towards Alkanes and Olefins

2.5.1 Study of Reactivity of Ta-Np@NU-1000 (Np=Neopentyl) Towards Propane

Ta-Np@NU-1000 was subjected to ~10 p.s.i.g. of propane under various temperatures for time lengths up to a week to observe potential catalyst reactivity. Products for the reaction were identified and quantified via a combination of GC-FID and GC-MS.

Observed products upon the treatment of Ta-Np@NU-1000 under propane at 150-165℃ were methane, propylene, neopentane, isobutene, and heptane. Results are highlighted in **Table 2.5.1.1.** Analysis of Ta-Np@NU-1000 includes both old and fresh samples of the material, looking at potential effects of catalyst aging.

Batch of Catalyst	Temp.℃	Duration	Neopentanes lost per Ta (mol/mol)	Propylene per neopentane (mol/mol)	Isobutene per neopentane (mol/mol)
Old TaNp@NU-1000	160	12 h	0.048	N/a	N/a
		2-3 days	0.052	0.45	0.52
		6 days	0.049	0.22	0.21
		7 days	0.038	0.97	0.30
Fresh TaNp@NU-1000	160	1-2 days	.12	0.06	0.016
	250	1-2 days	.15-.50	0.18	0.077

Table 2.5.4.1. Summarized results of TaNp@NU-1000 reacting with propane. Moles of products were quantified using ideal gas law and FID peak areas relative to propane. Old catalyst was several months old.

Based on the product distribution and quantities under all conditions, Ta-Np@NU-1000 does not seem to be competent for propane metathesis. No expected propane metathesis products are observed, except neopentane and methane. All products are generated in low quantities. The most abundant product, neopentane, is released from the tantalum sites before propane metathesis occurs, based on a control experiment, heating the material to reaction temperature under an argon atmosphere. For an active catalyst, one would expect a loss of 2-3 neopentanes per tantalum.[57]

With Ta-Np@NU-1000, less than one neopentane per tantalum is observed across all experiments, maxing out at ~.5 neopentanes per tantalum at 250℃ with fresh catalyst. This suggests: 1) the tantalum sites are not sufficiently activated by heat and propane to conduct propane metathesis, and 2) the tantalum sites have fewer neopentyl and neopentylidene ligands than anticipated or required for catalytic conversion.

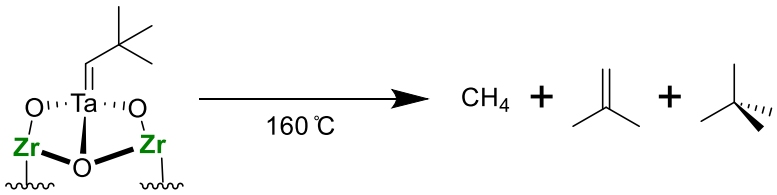

Scheme 2.5.1.5. Ligand loss and decomposition under thermal treatment.

The presence of other products can be explained through pathways other than alkane metathesis. Heptane was determined to be residual solvent remaining from material synthesis. Indeed, when fresh catalyst was made using only pentane, no heptane was observed. Isobutene is most likely the product of neopentyl fragmentation. Homolytic cleavage of one of the carbon-carbon bonds of a neopentyl ligand produces a tertiary radical, which may form isobutene if it loses another hydrogen. This fragmentation pathway is commonly observed in the thermal decomposition of t-boc protecting groups.[104] The corresponding tantalum bound methyl radical may be responsible for removing the other hydrogen, creating a tantalum-bound methyl ligand. This methyl ligand can be liberated from tantalum by obtaining a proton, which would create methane. Methane and isobutene peak areas are routinely found to be in a ratio close to 1:4 by GC-FID (signal is proportional to carbon number), giving credence to such a pathway.

The only promising product which may signify some reactivity is propylene, which indicates dehydration of propane. However, this also exists in small quantities; it never exceeds 0.05 moles of propylene per mole of tantalum. Furthermore, it is unclear by what pathway this molecule is produced. It may react with tantalum sites as in the first step of alkane metathesis, but

it is also possible that methyl, isobutyl, or other radicals may remove hydrogen from propane and result in the production of propylene.

Given this catalyst was inoperative for propane metathesis up to 250℃, we elected to try alternate treatments, substrates, and conditions.

2.5.2. Efforts in Liquid Phase Alkane Metathesis

To test if the catalyst was insufficiently heated due to the poor thermal conductivity of propane, Ta-Np@NU-1000 was put into liquid hexane in a pressure vessel with ~30atm of hydrogen at 165℃ to see if reaction would demonstrate increased reactivity for hexane metathesis or hexane hydrogenolysis. No products were observed in the gas phase, and no products were observed in the liquid phase. Only a small amount of dissolved neopentane was found in the reaction solution.

2.5.3. Tantalum-H_x@NU-1000

Tantalum hydrides and tungsten hydrides are more active than the corresponding neopentyl neopentylidene analogues.[49, 57] In attempt to spur reactivity, I treated my material between 150-165℃ under hydrogen for 16 hours, followed by exposure to propane. Again, negligible products were observed, with resulting products being primarily from neopentane loss/decomposition and reagent impurities. Additionally, investigation of H_2 treatment under *in situ* DRIFTS (**Figure 2.5.3.1.**) showed incomplete removal of alkyl ligands in the material. While there was a reduction in intensity corresponding to alkyl ligands from tantalum incorporation, this reduction was incomplete, even over the course of 48 hours, consistent with the sub-stoichiometric detection of neopentane evolved during reaction conditions. Additionally, tantalum hydride stretches were not detected, although if present, they would be obscured by overlapping stretches intrinsic to the framework linkers. (Under experimental conditions, we did observe a small growth in hydroxyl

stretches, although this was not understood at the time of the experiment and will be discussed in chapters 3 and 4. These stretches stem from heterolytic cleavage of H_2 across Zr–O acid base pairs, and potentially Ta–O acid base pairs.) Altogether, DRIFTS experiments and reactivity experiments show that H_2 pretreatment from 150-165 °C does not significantly improve the activity of Ta-Np@NU-1000 for alkane metathesis.

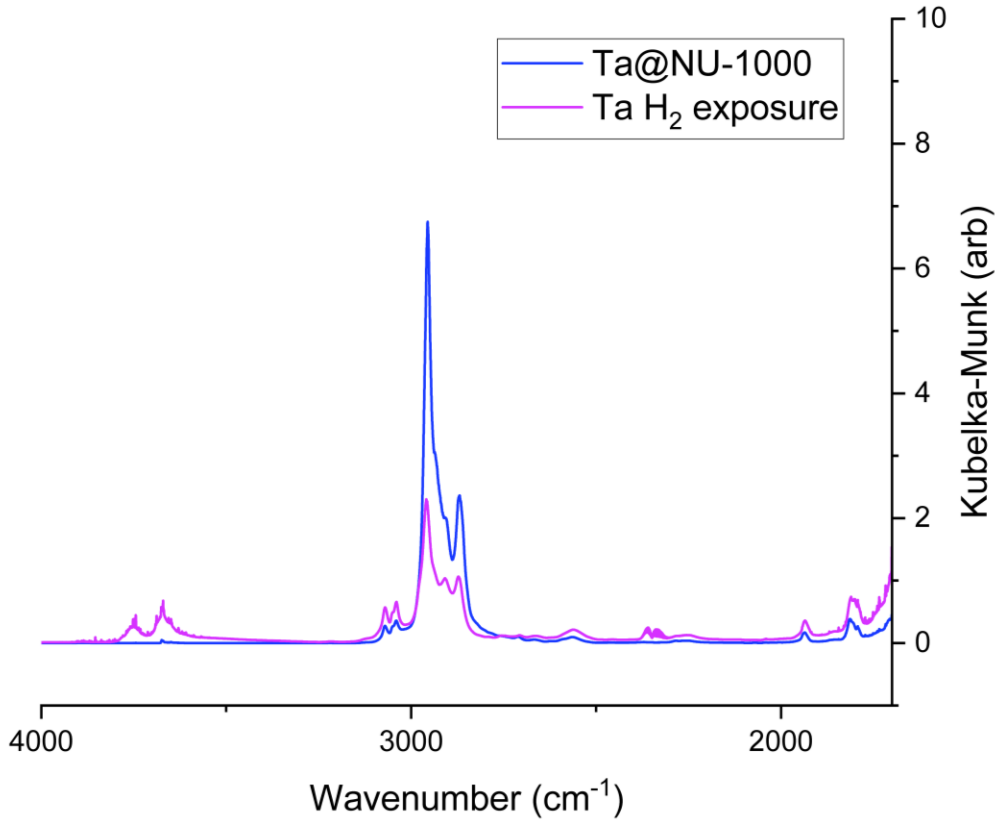

Figure 2.10.3.1. DRIFTS data for Ta@NU-1000 (blue) and Ta@NU-1000 after 24 hours of exposure to H_2 at 150 °C (pink). Data show H_2 exposure results in a partial loss of alkyl stretches (2950-2800 cm^{-1}) and a small growth on surface hydroxyl stretches at 3670 and 3744 cm^{-1}.

Ultimately, these results suggest that the tripodal Ta-Np@NU-1000 is too stable under reaction conditions to have significant activity towards alkanes from 150-250 °C. Most likely, the tantalum active site is too coordinatively saturated to effectively activate the C–H bonds of propane for productive reaction. As such we decided to test this material with more reactive substrates, such as olefins.

2.5.4. Catalytic Activity Towards Olefins

To start, testing was done for olefin metathesis and hydro-metathesis[105] of 1-butene. Experiments were done by pretreating the material with H_2 overnight at 200 °C, followed by exposure to psi of1-butene at 200 °C. After 6 hours under 1-butene exposure, ~6% of 1-butene was isomerized to *trans*- and *cis*-2-butene with 53% *trans* selectivity, showing that the material was active for 1-butene isomerization. No metathesis products were observed. Testing for the source of isomerization activity, given that olefin isomerization might also be catalyzed by acidic or basic sites on the Zr node,[28, 106-108] control experiments were run with unmodified NU-1000, with and without H_2 exposure. Interestingly, NU-1000 was inactive for 1-butene isomerization with a pretreatment at 200 °C under N_2, but active for 1-butene isomerization with a pretreatment at 200 °C under H_2 (~6% conversion at after 6.5 hours, 60% *trans* selectivity). These results show that NU-1000 can react with H_2 and 1-butene without tantalum incorporation, likely involving the generation of zirconium hydrides or new acid sites under H_2 exposure. Differences in trans/cis selectivity (53% vs. 60%) suggest that tantalum may have some influence on activity, but that activity cannot immediately be deconvoluted from the activity of NU-1000, which is clearly a non-innocent support.

These results indicated an importance for deeper understanding of zirconium MOF chemistry as catalysts and supports, given the unexpected propensity for H_2 activation. As a result, the research focus of this dissertation shifts away from supported tantalum catalysts to studying Zr-MOFs as catalysts. Those research findings will be discussed in subsequent chapters. However, opportunities and potential investigative avenues exist for continued work on alkane metathesis and SOMC in MOFs, and these will be briefly discussed in the closing sections of this chapter.

2.6. Conclusions and Outlook

Summarizing this chapter, tantalum(V) trisneopentyl neopentylidene was incorporated into the Zr-MOF, NU-1000, characterized, and tested for propane metathesis. Characterization using single crystal x-ray diffraction along with density functional theory calculations, suggested the tantalum formed a tripodal complex after protonolysis with water, terminal hydroxyl, and bridging hydroxyl protons on the node of NU-1000. Solid-state NMR spectroscopy, diffuse reflectance infrared Fourier transform spectroscopy, and density functional theory calculations suggested the coordination sphere of the tantalum was completed with a neopentylidene ligand.

Upon testing this species for alkane metathesis, no significant activity was observed under a range of pretreatments conditions, reaction conditions, and substrates, indicating that this material is not competent for alkane metathesis. Instead, small amounts of ligand decomposition are observed. Based on reactivity trends in literature-reported, tantalum-based alkane metathesis catalysts, this is likely due to support connectivity for tripodal species—with too few reactive alkyl ligands (minimum of 3 thought to be required) to catalyze alkane metathesis and too many oxygen containing ligands coordinated to the metal center. Despite the inactivity towards alkanes, experimental data do suggest these tantalum centers are active for olefin isomerization after pretreatment under H_2; although more experimentation will be needed to evaluate catalytic performance of Ta@NU-1000, deconvoluted from contributions to activity from the Zr-MOF node. Literature advances since the end of this preliminary work, however, suggest future potential for MOF-based alkane metathesis catalysts, and other SOMC derived systems.

One particular work, worth highlight, is the incorporation of tungsten(VI) trisneopentyl neopentylidyne into NU-1000, resulting in liquid phase and gas phase olefin metathesis.[80] For alkane and olefin metathesis SOMC-derived catalysts, tungsten catalysts have generally been more

active and stable with Lewis acidic oxide supports, suggesting tungsten precursor maybe more compatible with the Lewis acidic node of NU-1000. [57-60, 73, 77, 79] Additionally, tantalum complexes supported on Lewis acidic supports like Al_2O_3 have generally shown worse performance than when supported on SiO_2.[57, 61, 71, 73, 105] Given the Lewis acidity of the Zr_6O_8 node, precursors using metals other than tantalum will likely yield more fruitful results when bound to the node. The initial choice of working with the combination of tantalum and zirconium MOF supports may have been a strategic oversight in project semination.

One the other hand, for further study of MOF-supported tantalum catalysts, more active tantalum-based precursors may be employed, MOF anchoring sites may be modified, and substrates scope may be expanded. In terms of precursors and anchoring sites, some tantalum precursors have been shown to generate more active catalysts than others, e.g., pentamethyl tantalum yields more activity than tantalum(V) trisneopentyl neopentylidene. At the same time, node-based anchoring sites can be modified through a variety of thermal and chemical methods, and anchoring functionalities can also be incorporated onto MOF linkers, providing potential ways to control podality and Lewis acidity proximal to the active site. Finally, whether MOF-supported tantalum catalysts can be competent for alkane metathesis or not, they likely are competent for other reactions such as olefin metathesis,[73] oligomerization,[15] polymerization,[100] or hydrogenation.[76] Active tantalum catalysts have been reported for all these chemical transformations. Thus, there is potential and merit to further screening of catalyst syntheses and reactions conditions. Once active catalyst systems are discovered, a number of unique structure-activity relationships can be discovered or explored, e.g. size-selectivity and confinement effects upon olefin metathesis imparted by MOF pore structure,[82, 109] in addition to the potential structure reactivity relationships previously mentioned.

CHAPTER 3. Zr_6O_8 Node-Catalyzed Butene Hydrogenation and Isomerization in the Metal–Organic Framework NU-1000

3.1. Chapter Summary

Zirconium-based metal–organic frameworks (Zr-MOFs) have been increasingly studied over the last two decades as heterogeneous catalysts due to their synthetic tunability, well-defined nature, and chemical stability. In contrast to traditional zirconia-based heterogeneous catalysts, the community has assumed that Zr-MOFs are inert catalyst supports that do not participate directly in hydrocarbon transformations such as olefin hydrogenation and isomerization. Here, we report that the Zr-MOF NU-1000 is capable of catalyzing olefin hydrogenation and isomerization, without any post-synthetic modifications, under a hydrogen atmosphere. We probe H_2 activation over the nodes of NU-1000 via spectroscopic and computational techniques revealing that H_2 dissociation can occur heterolytically across coordinatively unsaturated Zr sites and proximal hydroxide and μ_3-oxo ligands. These results, along with catalytic experiments, suggest that H_2 activation results in node-supported zirconium hydrides capable of the hydrogenation and isomerization of 1-butene. When examining rate dependence on the partial pressure of H_2, we observe first-order dependence for hydrogenation and half-order dependence for isomerization. Half-order H_2 rate dependence is consistent with a mechanism where both fragments of cleaved H_2 are active for 1-butene isomerization, suggesting that heterolytic cleavage generates acidic protons resulting in parallel, acid- and hydride-catalyzed isomerization pathways. This work shows that Zr-MOFs have more diverse reactivity than the current literature may suggest and opens possibilities for ways in which Zr-MOFs can be used as heterogeneous catalysts and supports. The work in this chapter can also be found published in ACS Catalysis at the following URL: https://pubs.acs.org/doi/10.1021/acscatal.0c03579

3.2. Introduction to Zr-MOFs in Heterogeneous Catalysis

Metal–organic frameworks (MOFs), porous coordination polymers comprised of metal clusters (nodes) connected via multidentate organic ligands (linkers), have increasingly been studied as heterogeneous catalysts and catalytic supports over the past two decades. [17, 35, 110, 111] This is due to their structural diversity, synthetic tunability, and atomically defined nature. These traits enable precise structural characterization, computational modeling, and the elucidation of structure–activity relationships, thus aiding rational catalyst design.[17, 35, 110, 111]

Zirconium-based MOFs (Zr-MOFs) specifically have received significant attention as heterogeneous catalysts and supports due to their relatively high thermal and chemical stability.[30, 88, 112, 113] Most commonly, Zr-MOFs possess Zr_6O_8 nodes (**Figure 3.2.1.**) connected by carboxylate-terminated linkers, although zirconium oxide nodes of various sizes have been incorporated into MOFs.[30, 114-116] Depending on synthetic conditions,[96, 97, 99, 117] these nodes may possess Brønsted and Lewis acid sites, which have been shown to catalyze various reactions, including hydrolyses,[95] dehydrations,[99] and esterifications,[118] among others. [119-123] As supports, Zr-MOFs have hosted various catalyst active sites, engendering a wide array of reactivity. [18, 55, 102, 124-136] Two commonly investigated and valuable reactions in heterogeneous catalysis are olefin hydrogenation and isomerization (OHI). Both reactions are industrially important for the production and refining of hydrocarbon fuels and feedstocks, as well as for complex synthetic organic transformations.[28, 137]

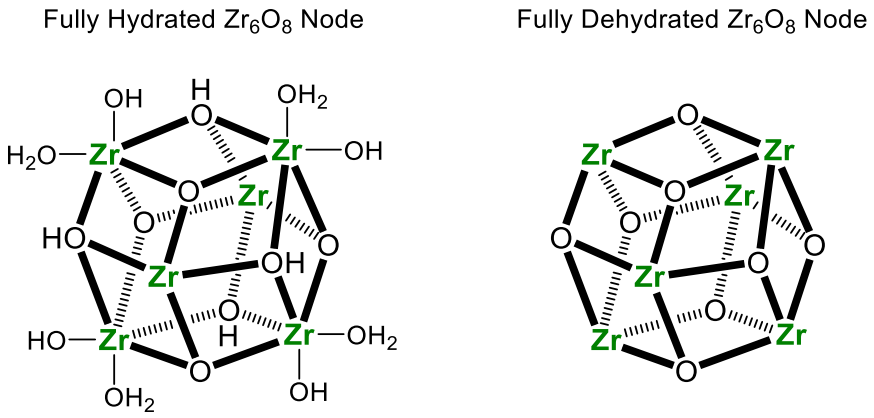

Figure 3.2.1. Hydrated and dehydrated Zr_6O_8 nodes, with MOF linkers omitted. Dehydrated and partially dehydrated nodes are commonly achieved through chemical and thermal treatments.

With regards to Zr-MOFs, design of OHI catalysts has focused on post-synthetic modification to install active sites. For hydrogenations, metal complexes,[125, 138-143] metal salts[22, 130, 144-146] and clusters[102, 126, 147, 148], and metal nanoparticles[148-153] have been supported on the nodes and linkers or encapsulated within pores of Zr-MOFs. In all cases, it has been proposed that the zirconium framework has improved catalytic activity through physical means, such as site isolation,[138, 146] nanoparticle size control,[150, 152, 154] and shape selectivity.[56, 155] However, to the best of our knowledge, no work has shown olefin hydrogenation activity intrinsic to the Zr-MOFs themselves. Fewer studies have focused on olefin isomerization in MOFs,[156, 157] and for Zr-MOFs, olefin isomerization has only been reported on sulfated nodes,[157] which possess strong Brønsted acid sites.[158, 159] Collectively, the current MOF catalyst literature suggests that the unmodified metal oxide nodes of Zr-MOFs are spectators or inactive in catalytic olefin transformations such as OHI.

Comparisons to bulk zirconia, however, suggest that Zr-MOFs may have much more diverse reactivity intrinsic to the framework itself. Zirconia has been reported to be a dynamic catalyst and support, possessing a combination of oxidizing, reducing, acidic, and basic sites.[107, 160, 161] This renders zirconia a competent catalyst for acid, base, and acid-base bifunctionally

catalyzed reactions.[28, 107, 160, 162] Zirconia can adsorb and dissociate H_2 both homolytically and heterolytically[20, 163-170] and is thought to be an active species and/or activity-enhancing support in many critical reactions. These include olefin hydrogenation[108, 163, 171, 172], isomerization[107, 108, 173], and dimerization,[171] alkane dehydrogenation,[174] carbon dioxide and monoxide hydrogenations,[45, 175-179] and many other reactions.[28, 161, 162, 176, 180-182]

Structural similarities between nodes of Zr-MOFs and the surface of bulk zirconia (i.e. the presence of Zr–OH, μ_3-OH, Lewis acidic Zr^{4+} ions, and Zr–O acid-base pair sites)[89, 90, 96, 97] suggest that Zr-MOFs should also be capable of dissociating H_2 and catalyzing many of the aforementioned reactions. These similarities also suggest Zr-MOF supports may have chemically relevant roles in some multi-component systems, e.g., H_2 dissociation and transfer of reactive species to or from the zirconium node. Understanding the interactions of H_2 and hydrocarbons with Zr-MOFs may yield valuable insights for the development of new and high-performance heterogeneous catalysts, as well as fundamental insights into related catalytic systems, like zirconia-supported metals, mixed metal oxides, and other families of MOFs.

Herein, we report and explore the reactivity of the Zr_6 nodes in NU-1000 for 1-butene OHI at 423 K and above. Catalytic, spectroscopic, and computational investigations were used to understand the H_2 activation that is required for both hydrogenation and isomerization over these catalysts. Zirconium hydrides on the node are identified as critical intermediates, which suggests that exposed and coordinatively unsaturated sites in Zr-MOFs, like NU-1000, are catalytically competent for hydrocarbon transformations, such as olefin hydrogenation and isomerization.

3.3. Experimental

3.3.1. Materials

For NU-1000 linker and MOF synthesis, 1,3,6,8-tetrabromopyrene, (4-(ethoxycarbonyl)phenyl)boronic acid, tetrakis(triphenylphosphine) palladium(0), tripotassium phosphate, zirconyl chloride octahydrate, and benzoic acid were purchased and used as received from Sigma Aldrich. Hydrochloric acid, acetone, and *N*,*N*-dimethylformamide were purchased from Fisher Scientific and used as received.

For catalytic studies, 2% 1-butene balance argon, N_2 Ultra-High Purity (UHP, 99.999%), and H_2 UHP (99.999%) were purchased from Airgas. A calibration tank containing 2% ethane, 2% ethene, 2% propane, 2% propylene, 2% *n*-butane, 2% 1-butene, 2% *trans*-2-butene, and 2% *cis*-2-butene (balance Ar) was also purchased from Airgas. Quartz sand (trace-metals grade) was purchased from Sigma Aldrich.

For *in situ* Diffuse Reflectance Infrared Fourier Transform Spectroscopy (DRIFTS), 5% H_2 in balance argon and UHP N_2 were purchased from Airgas. Deuterium gas (D 99.8%, D_2 99.6% and HD 0.4%) was purchased from Cambridge Isotope Laboratories. Restek super-clean gas filters (triple model) were used to further purify and remove hydrocarbons, water, and O_2 from H_2 in balance Ar and UHP N_2. No additional purification was used for D_2. KBr (spectroscopic grade) was purchased from Sigma Aldrich.

3.3.2. NU-1000 Synthesis

A 5 g batch of NU-1000 was synthesized and characterized according to previously published protocols.[183, 184] All MOF samples used for catalytic and characterization experiments came from the same batch.

3.3.3. Catalyst Characterization

Catalyst characterization can be found in section **3.6.1. Additional Information** (Figures 3.6.1.1-3.6.1.3, Figure S11). N_2 adsorption isotherms were collected on a Tristar II 3020 (Micromeritics) at 77 K using 65 mg of sample after evacuation at 393 K for ~16 hours on a SmartVacPrep (Micromeritics). The Brunauer-Emmett-Teller (BET) area was calculated in the relative pressure region P/P_0 = 0.005–0.05.

Powder X-ray Diffraction (PXRD) data were collected at room temperature on a STOE-STADI-P powder diffractometer equipped with an asymmetric curved Germanium monochromator (CuKα1 radiation, λ = 1.54056 Å) and one-dimensional silicon strip detector (MYTHEN2 1K from DECTRIS). The line focused Cu X-ray tube was operated at 40 kV and 40 mA. NU-1000 was packed in an 8 mm metallic mask and sandwiched between two polyimide layers of tape. Intensity data from 0 to 20 degrees two theta were collected over a period of ~10 mins. The instrument was calibrated against a NIST silicon standard (640d) prior to the measurement.

Scanning Electron Microscopy (SEM) images were collected with a Hitachi SU8030 microscope in the EPIC/NUANCE core facility at Northwestern University. The sample was coated with 8 nm OsO_4 before imaging to prevent charging.

X-ray photoelectron spectra were collected at Keck-II/NUANCE facility at Northwestern University using a Thermo Scientific ESCALAB 250Xi (Al Kα radiation, 1486.6 eV). All measurements were performed with an electron flood gun and were calibrated to C1s peak at 284.8 eV. When probing for potential node reduction, 5 mg of NU-1000 were treated under ~10 psig of UHP H_2 for 12 hours at 473 K in a sealed parr reactor. The parr reactor was then transferred into a

glovebox, where the sample was then transferred into an air-free transfer chamber for analysis without exposure to air.

3.3.4. In situ H_2-D_2 Diffuse Reflectance IR Fourier Transform Spectroscopy

The experiment was carried out in the Reactor Engineering and Catalyst Testing (REACT) core facility at Northwestern University. NU-1000 was diluted and ground with spectroscopic grade KBr (3 wt% NU-1000) and sealed into the praying mantis cell of a Thermo-iS50 infrared spectrometer. The sample was pretreated under nitrogen flow (30 sccm) at 473 K. Loss of adsorbed H_2O was observed, and spectra were recorded at 473 K for an hour or until the acquired spectra had stabilized. The final spectrum at 473 K under nitrogen was then used as the background for all difference spectra. The catalyst was then exposed to H_2 at 473 K, and difference spectra were recorded until there was no noticeable change from spectrum to spectrum. Then, the H_2 treated sample was exposed to D_2 at 473 K. Again, difference spectra were recorded until there was no noticeable change from spectrum to spectrum. Afterwards, the sample was retreated with H_2 to observe reversibility.

3.3.5. Reactivity Studies

All reactivity studies were carried out using a packed bed reactor in the REACT core facility at Northwestern University. In a typical reaction, ~40 mg of catalyst (NU-1000) was diluted with 1 g of quartz sand (trace metals grade) and packed in a quartz tube. The height of the bed was approximately 1 inch. Pretreatments with UHP H_2 or UHP N_2 were carried out at 473 K for 2 hours with flow rates of 25 sccm. Pressure in the reactor was controlled to be ~10 psig using a back-pressure regulator directly downstream from the reactor.

After pretreatment in UHP N_2 or UHP H_2 for 2 hours at 473 K, reactant gases were then flowed over the sample without cooling the reactor system. Reactant gases were 2% 1-butene

diluted in Ar and UHP H_2. Reactants were analyzed via Gas Chromatography-Flame Ionization Detection (GC-FID) and gas phase products were separated using a GS-Gaspro column (Agilent, 30 m length, 0.32 mm diameter). C4 gas phase species *n*-butane, 1-butene, *trans*-2-butene, and *cis*-2-butene were identified using calibration standards, *vide supra*. Isobutane and isobutene identities were inferred from retention times of identified species and reference chromatograms for the gs-Gaspro and separate gas chromatography mass spectrometry.

The 2% 1-butene in Ar tank had small quantities of C4 impurities; isobutane, *n*-butane, and isobutene made up approximately 0.3%, 0.4%, and 0.04% of the total hydrocarbon content, respectively. Because *n*-butane is the hydrogenation reaction product, the isobutane area in each injection was used as a reference for the *n*-butane area resulting from impurities. The average n/iso ratio for each injection at zero conversion was 1.3, so to find the area of *n*-butane produced in each injection, the isobutane area was multiplied by 1.3 and then subtracted from the total *n*-butane area.

When calculating conversion, X, the following equation was used:

$$X = \frac{A_{\text{butane}} + A_{trans} + A_{cis}}{A_{\text{butane}} + A_{trans} + A_{cis} + A_{\text{1-butene}}} \tag{3.3.5.1}$$

where A is the area for each subscripted product, the butane area being the area of only the butane produced, as previously mentioned. Selectivity for each product was calculated by dividing the area of each product respectively by the area sum of all the products.

The turnover frequency (TOF) for 1-butene conversion was calculated by multiplying the molar flow rate (2×10^{-5} mol/min) by the conversion under each reaction condition and then normalizing to the moles of NU-1000 (mol 1-butene/mol node of NU-1000). For H_2 co-feeding experiments, the average rate was calculated using time points after the first 30 min at reaction conditions, to allow the system to reach stable conversion.

3.3.6. DFT Calculations

DFT calculations were carried out using Gaussian 16, Rev. A03.[185] A cluster model of the inorganic node of NU-1000 was adopted from prior work[97] with the favored "mix-S" proton topology.[89] The chemical formula of the unmodified NU-1000 cluster model is $Zr_6(\mu_3\text{-}O)_4(\mu_3\text{-}OH)_4(OH)_4(H_2O)_4(C_2H_3O_2)_8$ where ($C_2H_3O_2$) are acetate capping ligands in place of the MOF linkers. Using this model as a starting point, a single terminal H_2O molecule was removed to explore different H_2 adsorption and activation pathways. The M06-L/def2-TZVP level of theory[186, 187] was adopted for all atoms, in addition to the SDD[188] effective core potential for Zr. The positions of all atoms were relaxed except the C and H atoms of the capping acetate groups, which were held fixed to mimic the bulk constraints of the NU-1000 framework. A pruned (99,590) "UltraFine" integration grid was used, and no symmetry constraints were applied. All stationary points in the potential energy surface were confirmed via analytical vibrational frequency calculations. Intrinsic reaction coordinate calculations were used to confirm that the identified transition states connect the proposed reactants and products. All structures were modeled in the closed-shell singlet state except for the product of the reductive homolytic cleavage pathway, which was modeled in the triplet spin state. Thermochemical corrections were calculated at 473 K and 1 atm using GoodVibes v.3.0.1.[23] The ideal gas, rigid-rotor, particle-in-a-box, and harmonic oscillator approximations were applied with a vibrational frequency scale factor of 0.976,[189, 190] a frequency cutoff of 100 cm^{-1}, and quasi-harmonic corrections to both the enthalpy and entropy.[24, 191]

3.4. Results and Discussion

3.4.1. Catalytic Testing of NU-1000 for 1-butene Hydrogenation and Isomerization

Gas phase kinetics demonstrate that H_2 is required for NU-1000 to react with 1-butene, even for isomerization, which does not stoichiometrically consume H_2 (**Figure 3.4.1.1.**). No OHI

activity is observed when the catalyst is pretreated under N_2 at 473 K, then the flow is switched to 1-butene. When the catalyst is pretreated under H_2, followed by a switch to 1-butene, there is some

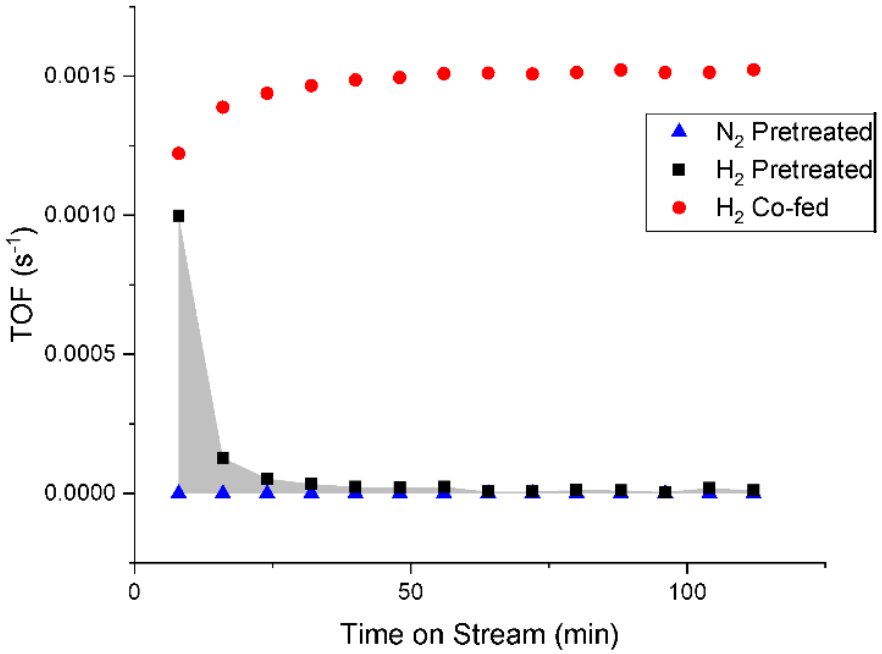

Figure 3.4.1.1. Turnover frequency for 1-butene conversion as a function of time on stream for ~40 mg of NU-1000 at 473 K. 25 sccm 2% 1-butene after a N_2 pretreatment at 473 K (blue triangles). 25 sccm 2% 1-butene/Ar after an H_2 pretreatment at 473 K (black squares). Cofeeding of 25 sccm H_2 and 25 sccm 2% 1-butene/Ar after an H_2 pretreatment at 473 K (red circles).

initial conversion corresponding to a rate of 0.001 turnovers per second, but the rate decays to zero in < 30 min time on stream. Integrating over the life of the catalyst shows (shaded area in **Figure 3.4.1.1.**) the material can convert ~0.4 moles of 1-butene per mole of Zr_6 nodes absent a continuous flow of H_2. The initial selectivity is approximately 20% *n*-butane, 45% *trans*-2-butene, and 35% *cis*-2-butene, indicating that both 1-butene hydrogenation and isomerization occur.

H_2:C_4 ratio	psi 1-butene	psi H_2	Conversion	TOF ($mol_{1\text{-}butene}/mol_{node}/s$)	Butane	*trans-*	*cis-*	*trans-* : *cis-*
10	0.41	4.09	3.5%	0.63×10^{-3}	36%	36%	28%	1.3
30	0.31	9.21	6.7%	1.22×10^{-3}	48%	30%	23%	1.3
50	0.25	12.4	8.3%	1.51×10^{-3}	52%	27%	21%	1.3
100	0.17	16.5	10%	1.81×10^{-3}	57%	25%	19%	1.3

Table 3.4.1.1. Isomerization and hydrogenation rates and selectivities at various partial pressures of hydrogen and 1-butene. Partial pressures were modulated by changing flow rates of reactant gases.

In contrast, stable rates and different selectivities, *vide infra*, are observed when H_2 and 1-butene are co-fed (**Figure 3.4.1.1.**). In a final experiment, the catalyst is pretreated with H_2 at 473 K, purged with N_2 for 2 hours, then the flow is switched to 1-butene. No butene conversion is observed under these conditions but reintroducing an H_2 cofeed immediately leads to OHI activity that steadily increases over 2 hours (**Figure 3.6.2.1.**).

Overall, these results suggest that OHI sites are reversibly created in the presence of H_2. A rapid switch from H_2 to 1-butene gives some residual activity but purging the system with N_2 eliminates all active sites. A continuous flow of H_2 is required for stable activity, even for olefin isomerization, which does not consume H_2.

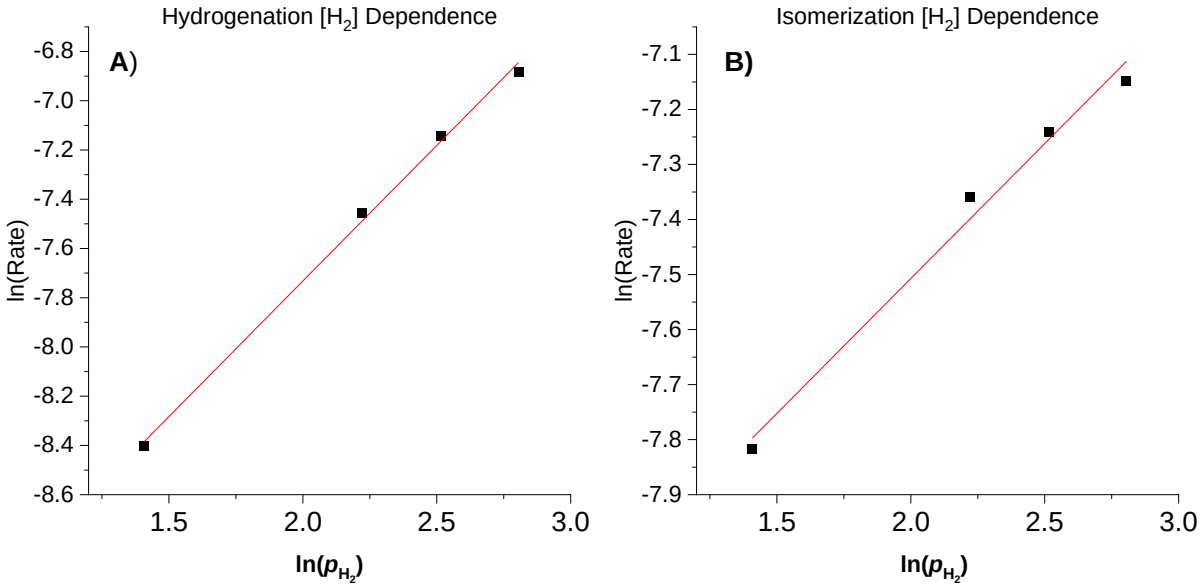

Figure 3.4.1.2. Log plots examining 1-butene hydrogenation and isomerization as a function of H_2 partial pressure. Slopes of each plot indicate apparent reaction order in [H_2]. A) Natural log of 1-butene hydrogenation TOF (s^{-1}) vs. natural log of H_2 partial pressure (psi). Best fit line: $y = 1.1017x - 9.9355$ with an R^2 of 0.9975. B) Natural log of 1-butene isomerization TOF (s^{-1}) as a function of the natural log of H_2 partial pressure (psi). Best fit line: $y = 0.4902x - 8.4876$ with an R^2 of 0.9868.

Under steady state conditions, increasing the H_2 partial pressure increases the rates of both hydrogenation and isomerization (**Table 3.4.1.1.**). Hydrogenation rates have a first-order dependence on H_2 partial pressure, while isomerization has an apparent half-order H_2 dependence

(**Figure 3.4.1.2.**). This difference in H_2 dependence results in increasing hydrogenation selectivity at higher H_2 partial pressures (**Table 3.4.1.1.**). We also observe that the *trans/cis* selectivity is unaffected by H_2 partial pressure, with a constant *trans/cis* ratio of 1.3, which is less than the thermodynamic equilibrium at 473 K, ~1.6,[192-194] but greater than hydride-catalyzed isomerization over Zr/SiO_2, 1:1.[195] Slight deviation from thermodynamic equilibrium may suggest a slight destabilization of the transition state leading to the *trans*-olefin (or stabilization of the transition state leading to the *cis*-olefin) by the bulk of the framework.

Our observed rates also show a zero-order dependence on 1-butene partial pressure, which is consistent with previously reported hydrogenation studies over ZrO_2.[163] This may suggest that 1-butene saturates catalytic sites across the experimentally tested pressures at 473 K. These results yield empirical rate laws of:

$$Rate_{\mathrm{Hyd}} = k_{\mathrm{obs}}[\mathrm{H_2}]^1[\text{1-butene}]^0 \quad (3.4.1.1)$$

and:

$$Rate_{\mathrm{Isom}} = k_{\mathrm{obs}}[\mathrm{H_2}]^{0.5}[\text{1-butene}]^0 \quad (3.4.1.2.)$$

Altogether, we have demonstrated that H_2 activation and cleavage are essential to 1-butene hydrogenation and isomerization in NU-1000.

Reaction Temperature	Relative Rates
423 K	1.4
473 K	2.0
523 K	1.5
573 K	1.0

Table 3.4.1.2. Comparison of 1-butene OHI over NU-1000 at various temperatures. Relative rate is the TOF (s^{-1}) of 1-butene conversion at temperature, T, relative to the TOF of 1-butene conversion at T= 573 K.

We also investigated the effects of temperature on 1-butene conversion (**Table 3.4.1.2.**)**.** In our experiments, maximum rates were observed at 473 K, with temperatures below (423 K) and above (523–573 K) being 50–75% slower, with little change in product selectivity. Maximum rates at an intermediate temperature may indicate a balance between kinetic and thermodynamic effects.

At lower temperatures, the rate may be limited by smaller rate constants, whereas at higher temperatures, there may be lower surface concentrations of 1-butene, rendering the partial pressure of olefin kinetically relevant. Additionally, changes in reaction pathways or node structure may occur with increasing temperature— both possibilities are discussed, *vide infra*.

To further understand the H_2-dependent OHI activity, we investigated H_2 interactions with NU-1000 computationally and spectroscopically. H_2 dissociation over ZrO_2 surfaces at high temperatures has been observed homolytically and heterolytically.[20, 166, 168, 169, 178, 196] At high temperatures (> 273 K), homolytic dissociation occurs reductively, producing pairs of zirconium hydroxides and reduced metal centers, and heterolytic dissociation occurs over coordinatively-unsaturated zirconium-oxygen pairs, producing a zirconium hydride-hydroxide pair. As temperature increases, reductive homolytic cleavage becomes favored over heterolytic cleavage.

3.4.2. Spectroscopic and Computational Investigation of H_2 Cleavage Pathways over the Zr_6O_8 Cluster

DFT calculations at the M06-L/def2-TZVP level of theory[186, 187] were used to explore the feasibility of several H_2 dissociation pathways over the Zr_6 node of NU-1000. The most thermodynamically favorable pathway is predicted to be heterolytic cleavage of H_2 over a terminal Zr–OH species and an adjacent, coordinatively unsaturated Zr site (**Figure 3.4.2.1.**, Additional information **Figure 3.6.3.1**). The activation free energy, ΔG_{a}, of H_2 cleavage via this mechanism is predicted to be 60 kJ/mol after H_2 adsorption to yield Zr–H and Zr–OH_2 sites. Due to the late nature of the transition state (Additional information, **Figure 3.6.3.1.c** and **3.6.3.1.d**), the calculated ΔG_{rxn} is nearly identical in energy (for further details, refers to **Table 3.6.3.1.**). The analogous H_2 dissociation mechanism over a single Zr site is predicted to be significantly less favorable with a ΔG_{a} and ΔG_{rxn} of 147 kJ/mol and 114 kJ/mol, respectively (**Figure 3.4.2.1.**,

additional information **Figure 3.6.3.2.**). Heterolytic H_2 cleavage across a μ_3-O site and coordinatively unsaturated Zr species is predicted to have similar reaction energetics, with a ΔG_a and ΔG_{rxn} of 146 kJ/mol and 128 kJ/mol, respectively (**Figure 3.4.2.1.**, additional information **Figure 3.6.3.3.**). We also considered reductive homolytic cleavage across adjacent μ_3-O sites (additional information, **Figure 3.6.3.4.**) but found this process to be highly endergonic with a ΔG_{rxn} of 294 kJ/mol such that it is unlikely to be thermodynamically or kinetically feasible (Table S1).

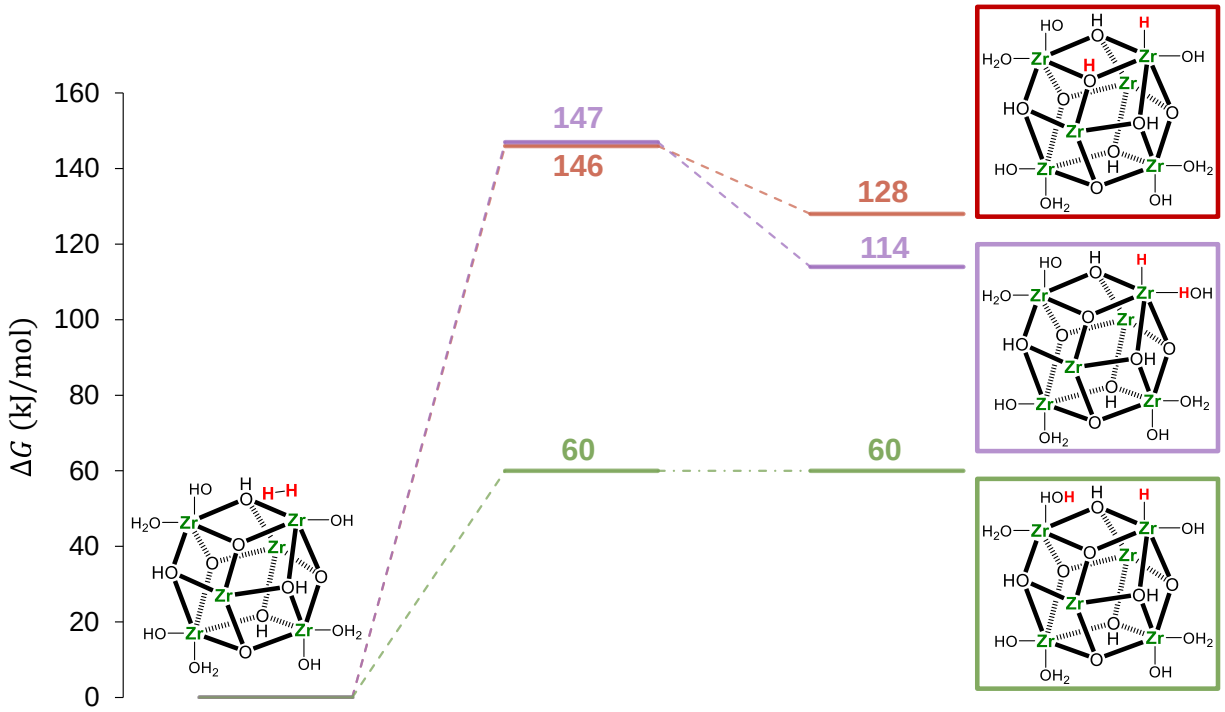

Figure 3.4.2.1. DFT-computed Gibbs free energy diagram for heterolytic H_2 dissociation over the Zr_6 node of NU-1000. Each color represents a different pathway for H_2 dissociation over a coordinatively unsaturated Zr site and a μ_3-O species (red), terminal –OH species at the same Zr site (purple), or terminal –OH species at an adjacent Zr site (green). Only a relevant portion of the node is shown for clarity.

Supporting our calculations, infrared characterization of NU-1000 upon exposure to H_2 and D_2 at 473 K provides evidence for dissociative H_2 adsorption over the zirconium node. Difference spectra of NU-1000 upon exposure to H_2 show the production of a Zr–OH stretch at 3671 cm^{-1} (**Figure 3.4.2.2. A**), consistent with bridging and terminal hydroxyl stretches reported over bulk

zirconia[20, 166, 168-170] and hydroxyls in Zr-MOFs,[89, 97, 99] at 3668 cm^{-1} and 3674–3672 cm^{-1}, respectively. Concomitantly, a small stretch at 1564 cm^{-1} appears (**Figure 3.4.2.2. B**), consistent with reported surface zirconium hydrides on zirconia (1565–1562 cm^{-1}).[166, 169, 170, 178] Reported surface hydrides on bulk zirconia typically display weak intensity at 473 K,[166, 169, 170, 178] consistent with our data. In addition, a broad feature, representative of hydrogen-bonded O–H moieties (~3600-3100 cm^{-1}), grows in, consistent with the presence of new H_2O ligands and a greater extent of node protonation.

Subsequent D_2 exposure produces a negative feature at 3668 cm^{-1}, indicating a net loss in bridging and terminal hydroxyl species, and a large Zr–OD stretch at 2700 cm^{-1} (**Figure 3.4.2.2. C**). Additionally, the hydrogen-bonded O–H feature is entirely consumed, while a broad, hydrogen-bonded deuteroxide stretch appears from ~2600-2300 cm^{-1}. The putative Zr–H stretch at 1564 cm^{-1} disappears upon exposure to D_2 (**Figure 3.4.2.2. D**). However, we do not observe a corresponding Zr–D stretch, expected around 1120 cm^{-1}. We expect this is due to obscuring of the stretch by the high absorbing background of NU-100 in this region and/or other structural changes to the framework at reaction conditions. Upon a second exposure to H_2, the Zr–OH and Zr–H features reappear (additional information **Figure 3.6.4.1.**). These spectroscopic results confirm dissociative adsorption over the node of NU-1000 and indicate the reversible nature of H_2 and D_2 dissociative adsorption.

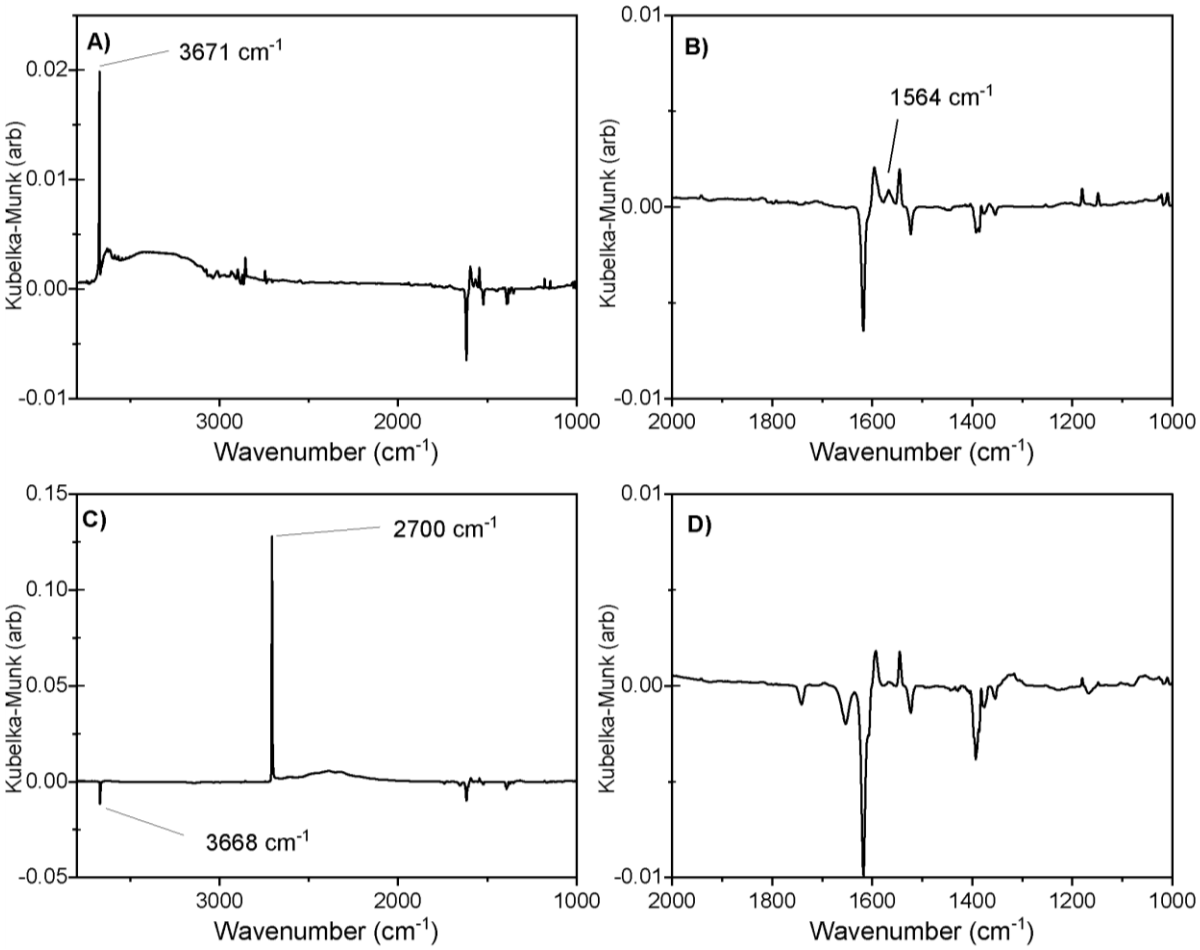

Figure 3.4.2.2. DRIFTS difference spectra of NU-1000 upon exposure to H_2 and D_2 at 473 K. NU-1000 pretreated under N_2 at 473 K was subtracted from each spectrum, and the sample was exposed to H_2 first and then subsequently exposed to D_2. (A) NU-1000 difference spectrum after exposure to H_2 (5% H_2 balance Ar) at 473 K. A clear growth in Zr–OH is observed at 3671 cm^{-1}. (B) Magnified difference spectrum of NU-1000 upon exposure to H_2 showing putative Zr–H stretch at 1564 cm^{-1}. (C) NU-1000 difference spectrum upon subsequent exposure to D_2 (D 99.8%, D_2 99.6% and HD 0.4%). A negative Zr–OH feature is observed at 3668 cm^{-1} along with a positive Zr–OD feature at 2700 cm^{-1}. (D) Magnified difference spectrum of NU-1000 shows disappearance of putative Zr–H feature upon exposure to D_2.

3.4.3. Mechanistic Discussion

Overall, computational and spectroscopic data render plausible the existence of zirconium hydrides on the node of NU-1000, helping to explain the observed 1-butene OHI activity. At temperatures above 423 K, water and hydroxyl ligands begin to desorb as water from the Zr_6 node,[21] generating coordinatively unsaturated Zr-μ_3-O and Zr-hydroxyl pairs, which can dissociatively adsorb H_2 through heterolytic cleavage, generating active sites for 1-butene conversion *in situ*. DFT calculations predict that several heterolytic cleavage pathways exist, and it is plausible that all these pathways are active at 473 K. Sites generated from differing pathways would likely have varying reactivity towards 1-butene, and the relative abundance of these sites would change as a function of temperature, based upon their relative ΔG_{rxn} values. This helps to potentially explain the previously observed, non-Arrhenius effects of reaction temperature on 1-butene conversion. Additionally, at higher temperatures, hydroxyl ligands further desorb as water from the node,[21] which would decrease the abundance of Zr-hydroxyl pairs for H_2 cleavage, favoring the energetically less-favorable cleavage at Zr-μ_3-O sites. Finally, high temperatures have also been shown to cause distortions in Zr_6 nodes[21]—potentially altering the free energy landscape

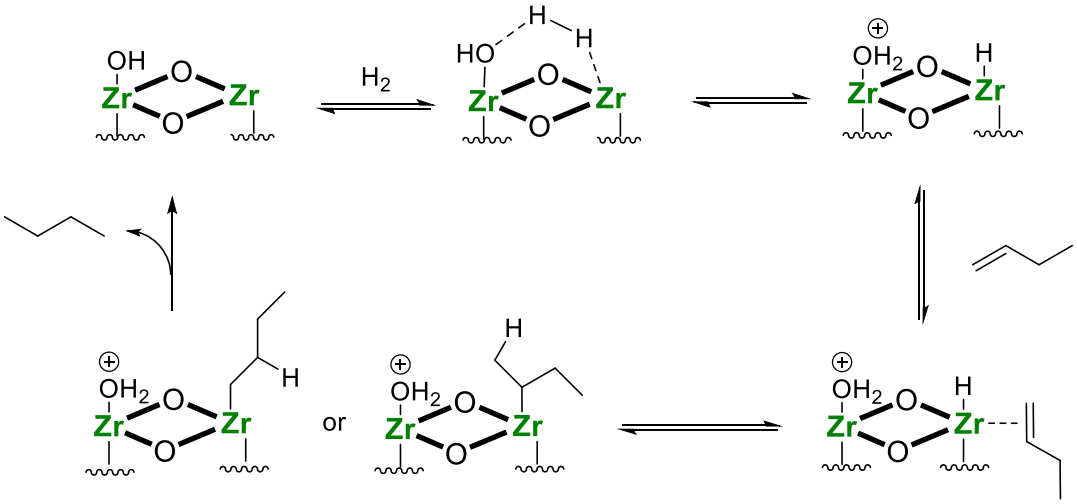

Scheme 3.4.3.1. Potential Mechanism for 1-Butene Hydrogenation

of H_2 cleavage—via simultaneous shrinking and lengthening of Zr-Zr distances and the shrinking of Zr-O distances. Further experimental and computational investigations will be needed to fully understand the complexities of this system and which of these sites are involved in the observed butene hydrogenation and isomerization.

For butene hydrogenation, we propose that *in situ*-generated zirconium hydrides react with adsorbed butene, creating a Zr-alkyl species, followed by alkyl protonation to create *n*-butane (**Scheme 3.4.3.1.**). This reaction mechanism is consistent with first-order dependence on H_2 and goes through a pathway like those proposed for other metal-oxide based hydrogenation and dehydrogenation catalysts.[11, 197] Apparent zero-order rate dependence on concentration of olefin indicates 1-butene has no kinetic relevance under the tested reaction conditions, and it is consistent with previous studies over zirconia.[108, 163] We propose it indicates non-competitive adsorption sites for 1-butene (e.g. favorable π-bond coordination),[198, 199] which remain saturated across experimental reactant pressures, and indicates an abundance of adsorbed butene relative to *in situ*-generated hydrides at the Zr_6 node.

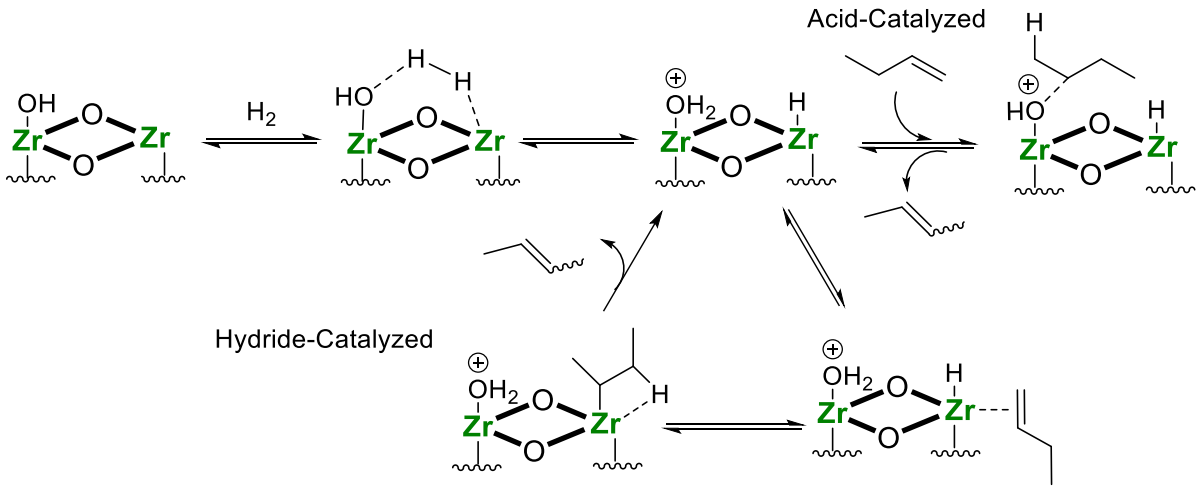

Scheme 3.4.3.6. Potential Mechanisms for 1-Butene Double-bond Isomerization

Alternate pathways for olefin hydrogenation exist as well. Instead of protonating a zirconium alkyl to liberate *n*-butane, H_2 may be activated and added directly across the double bond of the adsorbed olefin, with both H atoms being 'instantaneously' incorporated as proposed by Kondo and coworkers.[199] This would also be consistent with first-order dependence upon H_2. In addition, Zr(IV) organometallic complexes have been reported to exchange ligands via σ-bond metathesis.[200, 201] Such a pathway would also liberate *n*-butane as a product and would show first-order H_2 dependence.

For 1-butene isomerization, half-order H_2-dependence suggests that two active sites are generated per mole of H_2 cleaved. We propose that the protons produced via heterolytic cleavage are more acidic than those intrinsic to NU-1000 and are active for 1-butene isomerization, resulting in parallel, acid- and hydride-catalyzed pathways (**Scheme 3.4.3.2.**). Alternatively, the possibility exists of sites not accounted for in our models capable of homolytic H_2 cleavage, (e.g. sites resulting from node distortions);[21] however, we believe this much less likely, given the high ΔG_{rxn} predicted for reductive homolytic cleavage and a lack of evidence for Zr(III) in the XPS spectrum of NU-1000 after H_2 exposure at 473 K (Additional information **Figure 3.6.4.2.**). Therefore, our observations are best explained by the generation of catalytically active hydrides and protons via heterolytic cleavage of H_2 at the zirconium node, although it is unclear whether newly generated Zr–OH_2 sites, newly generated μ_3-OH sites, or both, are active for acid-catalyzed pathways.

3.5. Conclusion

We have reported evidence of reversible H_2 dissociation on the Zr_6O_8 node of NU-1000, resulting in olefin hydrogenation and isomerization reactivity. These findings demonstrate a greater chemical versatility than previously thought for zirconium MOFs. Although many MOF-

based olefin hydrogenation catalysts have been reported, none have been reported possessing a zirconium node as the catalytic site.

In practical terms, these findings indicate that in modified Zr-MOFs, exposed zirconium sites may contribute to overall observed OHI rates and selectivity. A cursory comparison to MOF-supported catalysts suggests that rates of OHI over unmodified NU-1000 are generally similar to or slower than in modified systems.[65, 125, 126, 140, 141, 143, 148] However, due to many inconsistencies in reaction substrates and conditions, more thorough investigations are necessary before making conclusions.

When comparing our observed rates of olefin conversion per gram of zirconia to previously reported studies,[108, 163] the Zr_6 node of NU-1000 performs similarly to bulk and aerogel zirconia ($\sim 10^{-6}$ mol/g/s ZrO_2). However, it is worth noting that all literature samples were pretreated under very different conditions (i.e., vacuum at 700 and 900 K) and rates and selectivities were sensitive to these pretreatment conditions. Our observed rates and selectivities for NU-1000 were sensitive to sample activation as well (Figure S5), and studies over bulk ZrO_2 show that formate and methoxy ligands slow the rate of H_2 activation and H/D exchange.[168] Formate ligands are commonly found in Zr-MOFs synthesized in *N*,*N*-dimethylformamide, further indicating the importance of synthesis and pretreatment conditions.

We believe these findings have the potential to advance the design of MOF catalysts as well as yield fundamental insights into related catalytic systems. Many ZrO_2-based heterogeneous catalysts are proposed to possess synergistic effects, such as reaction at material interfaces, the transfer of adsorbed species from nanoparticles to the support, and vice versa.[45, 179] MOF catalysts are being designed to mimic and study these effects in valuable reactions, like CO_2 hydrogenation to methanol,[127, 133, 202-204] and understanding the H_2 interactions with zirconium nodes and surfaces

can help to provide insights into tailoring catalyst properties and performance. MOF ligands can be judiciously chosen to tune the properties of zirconium clusters,[205] and zirconium clusters can be modulated in shape and size to potentially tune H_2 interactions.[115, 116, 120] Thus, Zr-MOFs may provide powerful insights into improving zirconia catalyzed-reactions and discovering new facets of reactivity for ZrO_2-based materials.

3.6 Additional Information

3.6.1. NU-1000 Characterization

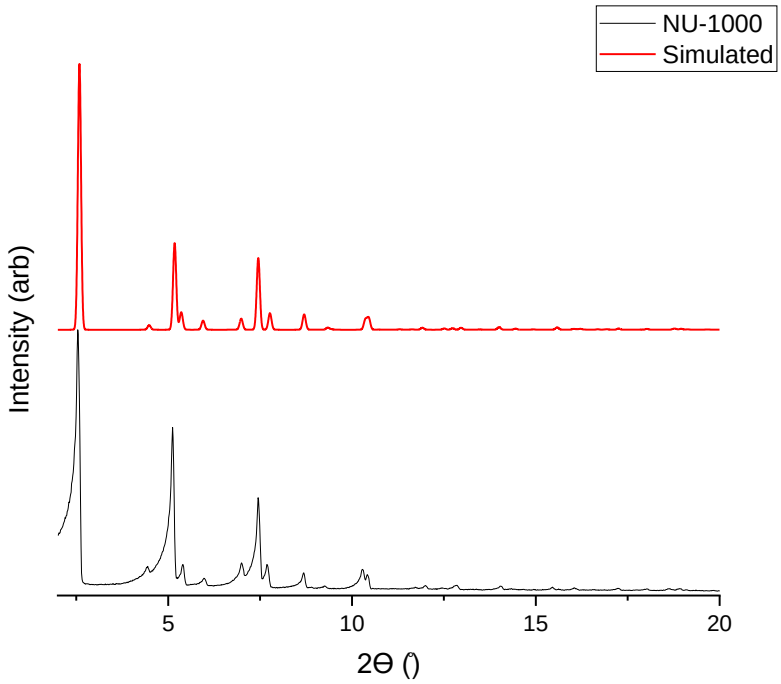

Figure 3.6.1.1. Powder X-ray Diffraction pattern of NU-1000 (black) and simulated pattern from NU-1000 crystal structure[1] (red).

Nitrogen Isotherm

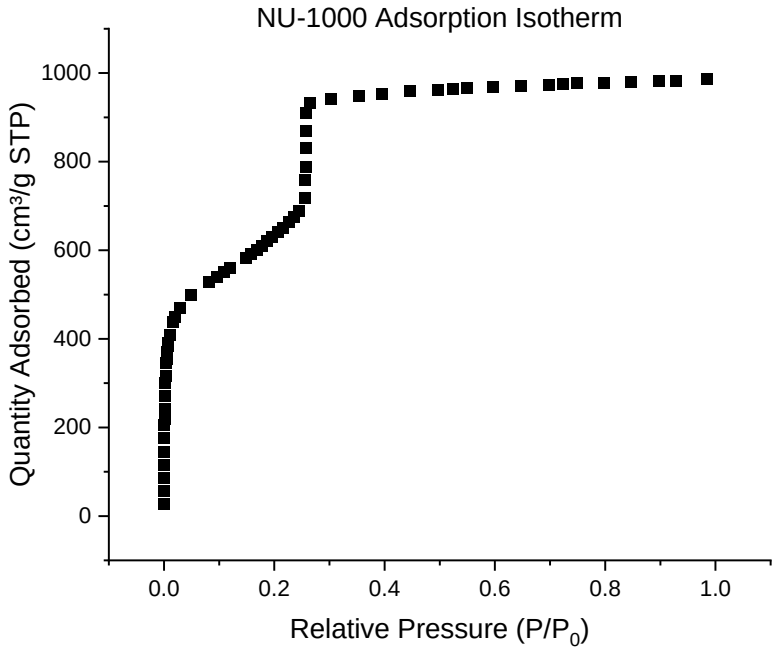

Figure 3.6.1.2. N_2 adsorption isotherm of NU-1000 at 77 K. BET calculated surface area = 2135 m^2/g

Scanning Electron Microscopy

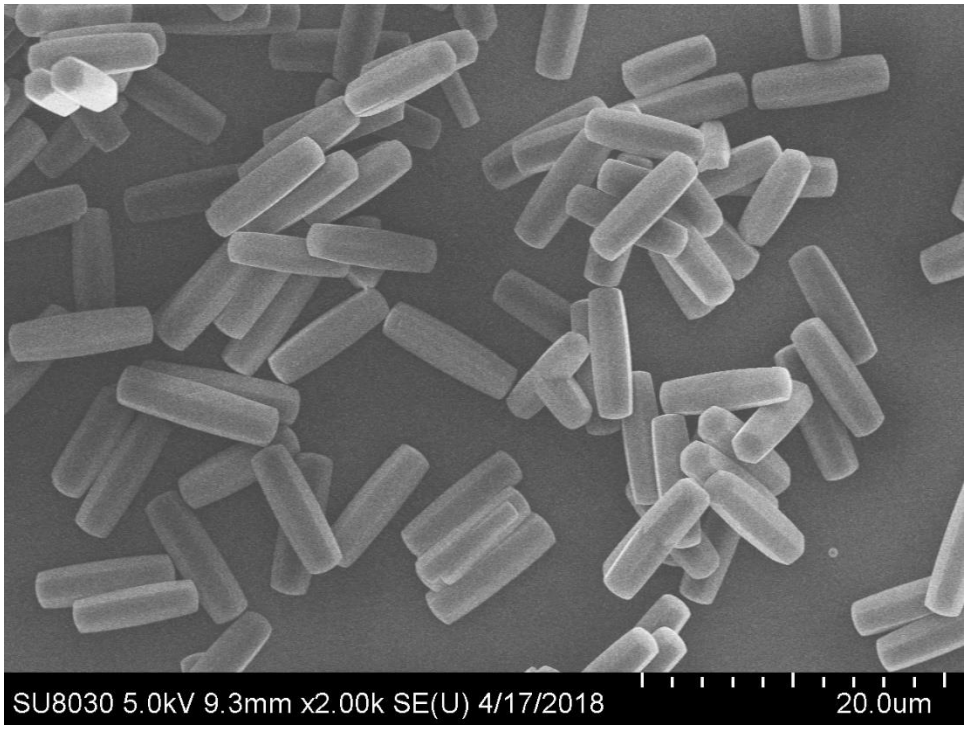

Figure 3.6.1.3. SEM of NU-1000 Crystallites. Particles are approximately 9 μm long and 2.5 μm wide.

3.6.2. Reaction Studies

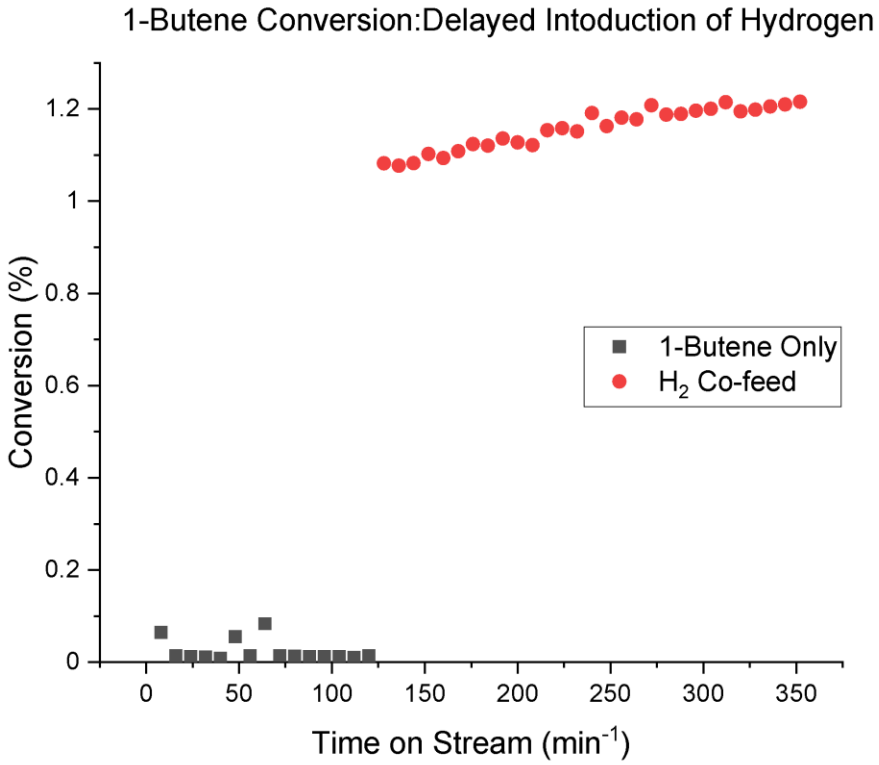

Figure 3.6.2.1. 1-Butene conversion over time after delayed H_2 introduction at 473 K, 10 psig total pressure. 25 sccm 1-butene (black squares). 25 sccm 2% 1-butene and 25 sccm H_2 (red circles). Rate can be seen steadily increasing over time, potentially due to generation of coordinatively unsaturated Zr atoms under reaction conditions.

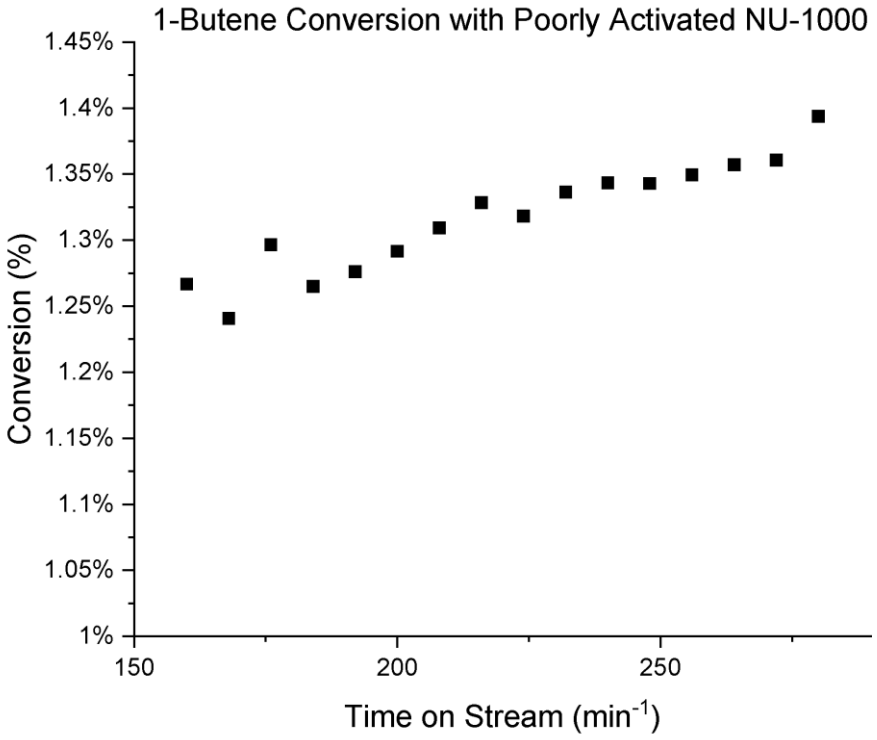

Figure 3.6.2.2. 1-butene conversion using a sample of NU-1000 with incomplete activation. Sample was activated according to conditions mentioned in the main text; however, > 0.5 g of sample was activated at once, without increasing treatment time under heat and vacuum, resulting in less solvent removal. Identical reaction conditions (40 mg catalyst, 473 K, 25 sccm 2% 1-butene and 25 sccm H_2 after ~2 hours pretreatment with H_2) resulted in ~8% conversion for better activated samples. Product selectivity was observed to be 22% n-butane, 47% trans-2-butene, and 31% cis-2-butene.

3.6.3. Density Functional Theory (DFT) Results

The DFT-optimized structures are shown in **Figures 3.6.3.1.–3.6.3.4**. **Figure 3.6.3.1.** shows the H_2 dissociation process over a terminal Zr–O species and coordinatively unsaturated Zr site to yield terminal Zr–H and Zr–OH_2 species. **Figure 3.6.3.2.** shows the analogous H_2 dissociation process but at a single Zr site rather than two adjacent Zr sites. **Figure 3.6.3.3.** shows the heterolytic dissociation of H_2 over a μ_3-O site and coordinatively unsaturated Zr site. The aforementioned processes are modeled using the "mix-S" proton topology for the Zr_6 node with one terminal H_2O molecule removed from the Zr atom at the top right of the image. Figure S9 shows the proposed H_2 dissociation pathway at two adjacent μ_3-O species. For this mechanism, we considered a slightly modified starting proton topology to yield two neighboring μ_3-O species that are otherwise not present in the "Mix-S" topology. This alternate proton topology is 109 kJ/mol less favorable than the Mix-S proton topology in terms of Gibbs free energy, as expected based on prior work.[2] In all cases, H_2 adsorption is consistent with physisorption behavior (ΔH = –16 kJ/mol and –18 kJ/mol for the processes in **Figures 3.6.3.1.–3.6.3.3**. and **Figure 3.6.3.4.**, respectively).

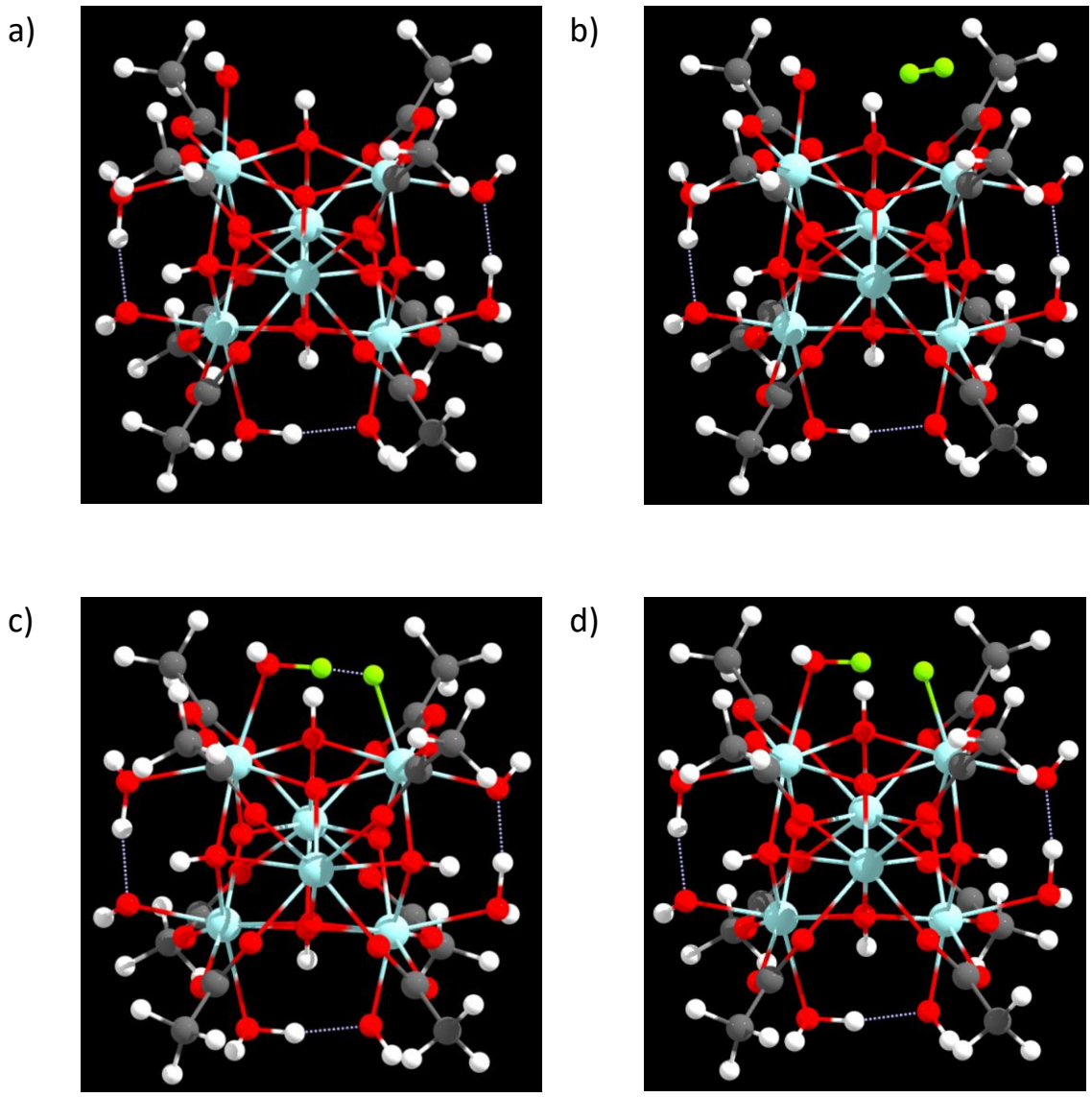

Figure 3.6.3.1. Mechanism for H_2 dissociation via a terminal Zr–OH species and adjacent, coordinatively unsaturated Zr site. DFT-optimized structures are shown for a) NU-1000 (mix-S topology), b) adsorbed H_2, c) transition state for heterolytic H_2 cleavage, d) product of heterolytic H_2 cleavage. Color key: Zr (teal), O (red), C (gray), H (white), $H_{adsorbed}$ (green).

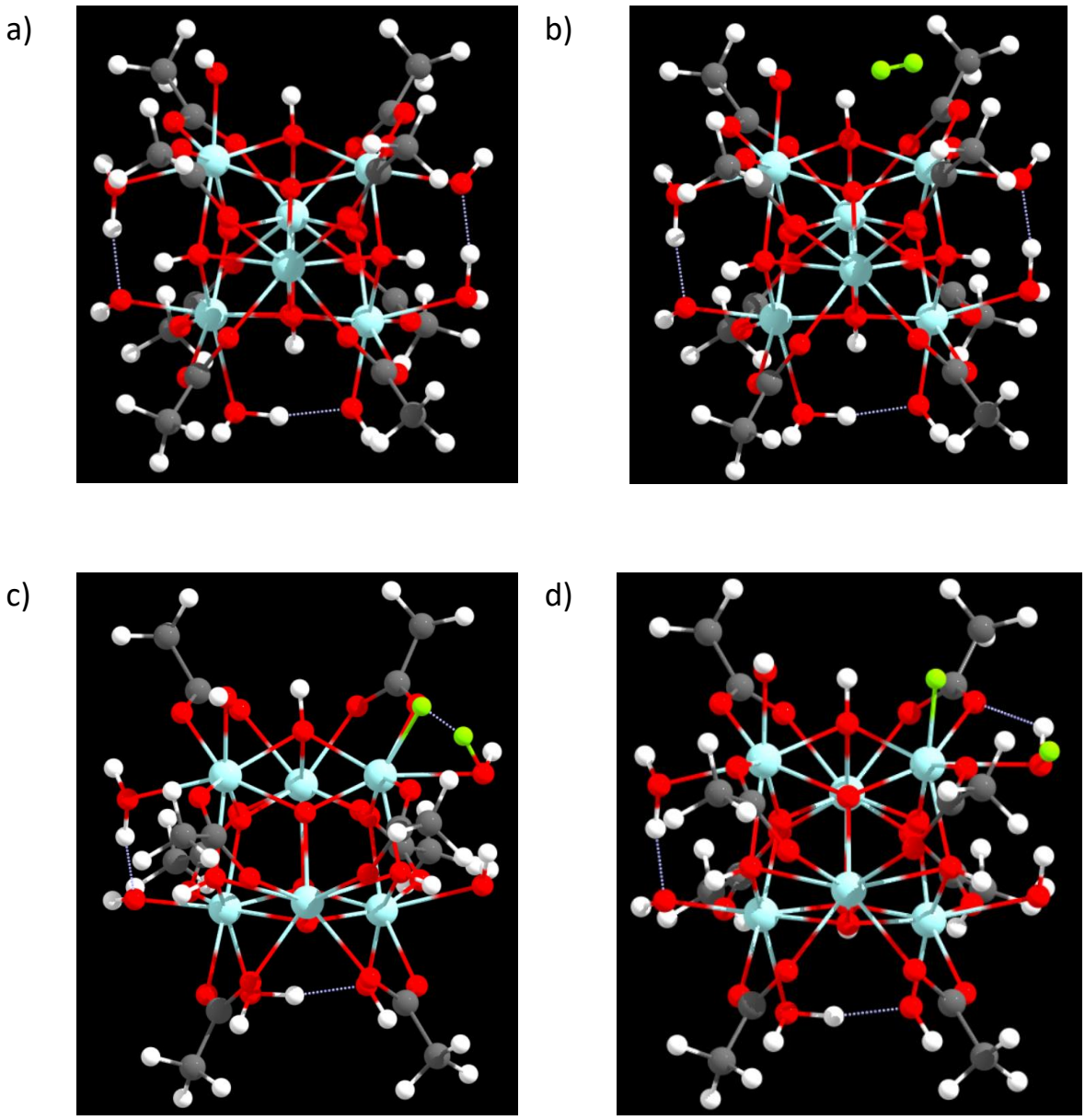

Figure 3.6.3.2. Mechanism for H_2 dissociation via an accessible Zr site with terminal OH group. DFT-optimized structures are shown for a) NU-1000 (mix-S topology), b) adsorbed H_2, c) transition state for heterolytic H_2 cleavage, d) product of heterolytic H_2 cleavage. Color key: Zr (teal), O (red), C (gray), H (white), $H_{adsorbed}$ (green).

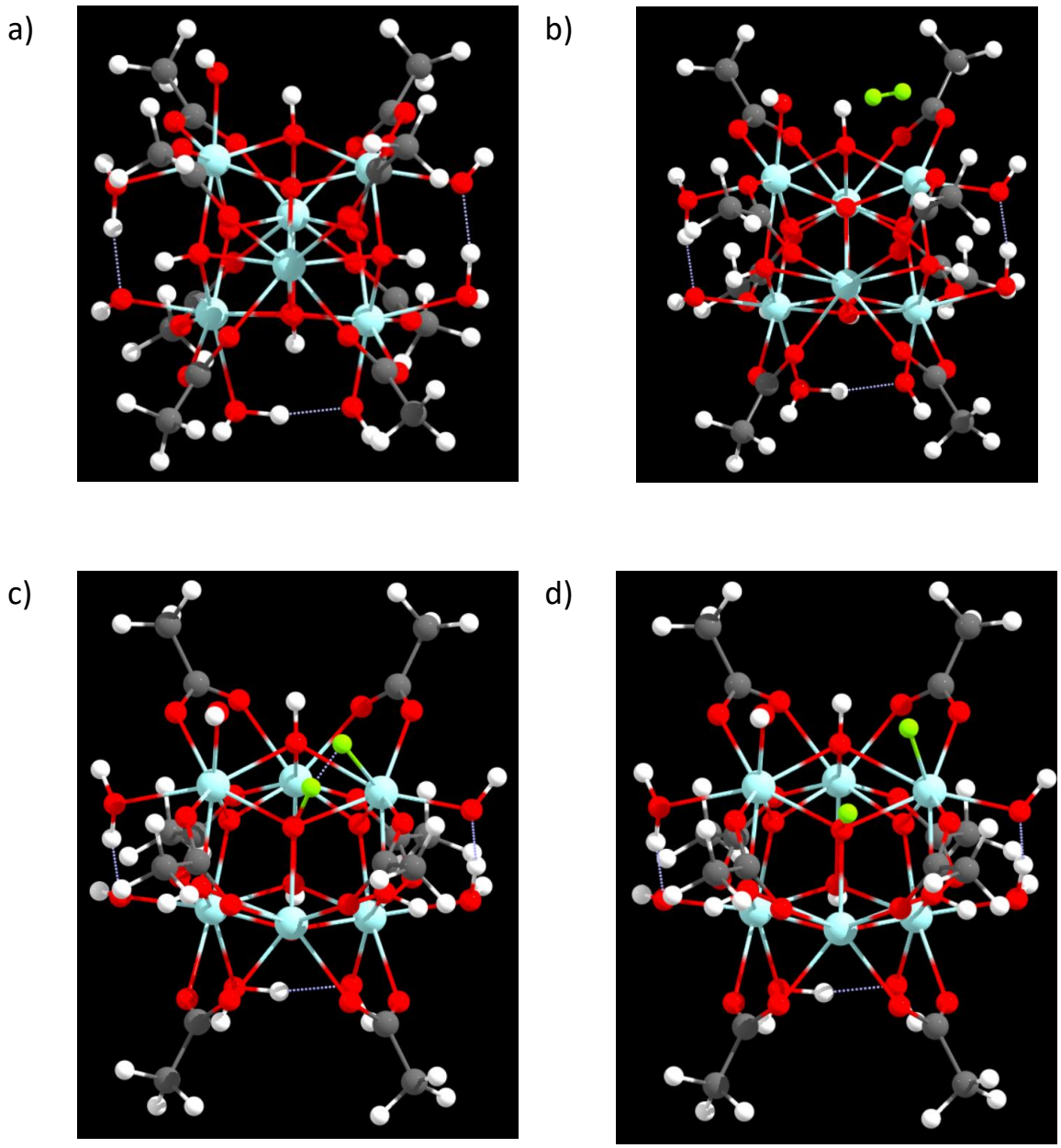

Figure 3.6.3.3. Mechanism for H_2 dissociation over a μ_3-O species and coordinatively unsaturated Zr site. DFT-optimized structures are shown for a) NU-1000 (mix-S topology), b) adsorbed H_2, c) transition state for heterolytic H_2 cleavage, d) product of heterolytic H_2 cleavage. Color key: Zr (teal), O (red), C (gray), H (white), $H_{adsorbed}$ (green).

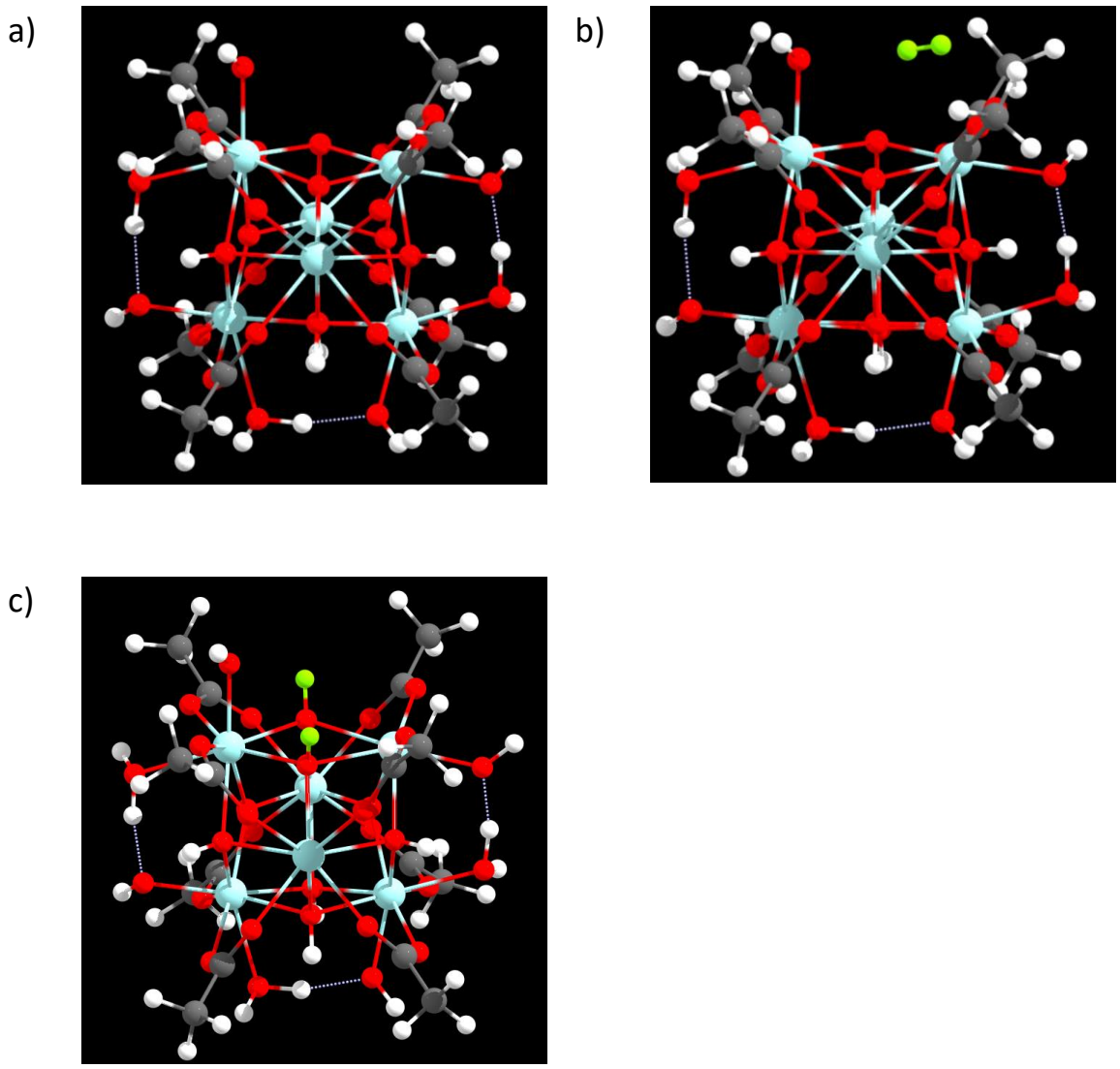

Figure 3.6.3.4. Mechanism for H_2 dissociation over two adjacent μ_3-O groups. DFT-optimized structures are shown for a) NU-1000 (alternate proton topology), b) adsorbed H_2, c) product of homolytic H_2 cleavage. Color key: Zr (teal), O (red), C (gray), H (white), $H_{adsorbed}$ (green).

Structure	ΔE (kJ/mol)	ΔH (kJ/mol)	ΔG (kJ/mol)
S6a	0	0	0
S6b	–24	–16	37
S6c	22	24	97
S6d*	19	31	100
S7a	0	0	0
S7b	–24	–16	37
S7c	124	126	184
S7d	86	100	151
S8a	0	0	0
S8b	–24	–16	37
S8c	118	119	183
S8d	94	106	165
S9a+	0	0	0
S9b	–26	–18	32
S9c	258	279	326

Table 3.6.3.1. Relative electronic energies, ΔE, enthalpies (473 K), ΔH, and Gibbs free energies (473 K, 1 atm), ΔG, for the species shown in **Figures 3.6.3.1.–3.6.3.4.** All energies are reported with respect to the starting reagents in the respective "a" subpanels of **Figures 3.6.3.1.–3.6.3.4.** (i.e., infinitely separated Zr_6 node and H_2). Absolute energies can be found in the supporting data files.

*Due to the late nature of the transition state in **Figure 3.6.3.1. c**, the electronic energy is only marginally higher than that of the product. As a result, the Gibbs free energy (and enthalpy) of the transition state ends up being slightly lower than that of the product, in large part due to the loss of a single 896 cm^{-1} vibrational mode. For the sake of clarity, in Figure 4, we display the Gibbs free energy of the product to be essentially identical to that of the transition state.

+Due to the altered proton topology, the structure shown in **Figure 3.6.3.4.** a is 117 kJ/mol, 114 kJ/mol, and 109 kJ/mol uphill in energy based on electronic energy, enthalpy, and Gibbs free energy, respectively, than the structure shown in Figure S6a with the "Mix-S" proton topology.

3.6.4. Additional Spectroscopic Characterization of H_2 Interaction With NU-1000

Infrared Difference Spectrum of NU-1000 Upon Exposure to H_2 After Exposure to D_2

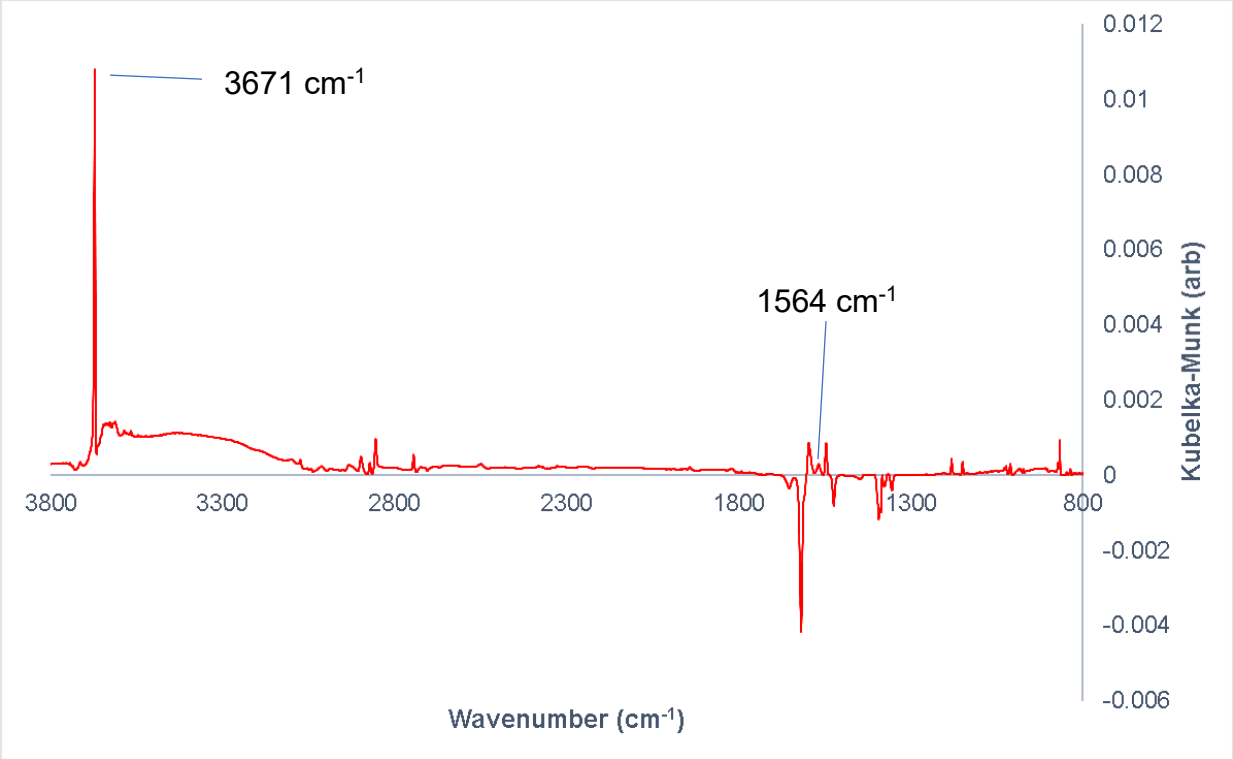

Figure 3.6.4.1. DRIFTS spectrum of NU-1000 upon exposure to H_2 at 473 K after exposure to D_2 as seen in **Figures 3.4.2.2. C** and **3.4.2.2. D**. The reappearance of Zr–OH (3671 cm^{-1}) and Z–H (1564 cm^{-1}) stretches are highlighted. Hydrogen bonded Zr–OH stretches are also observed from ~3600-3000 cm^{-1}.

X-ray Photoelectron Spectra of NU-1000

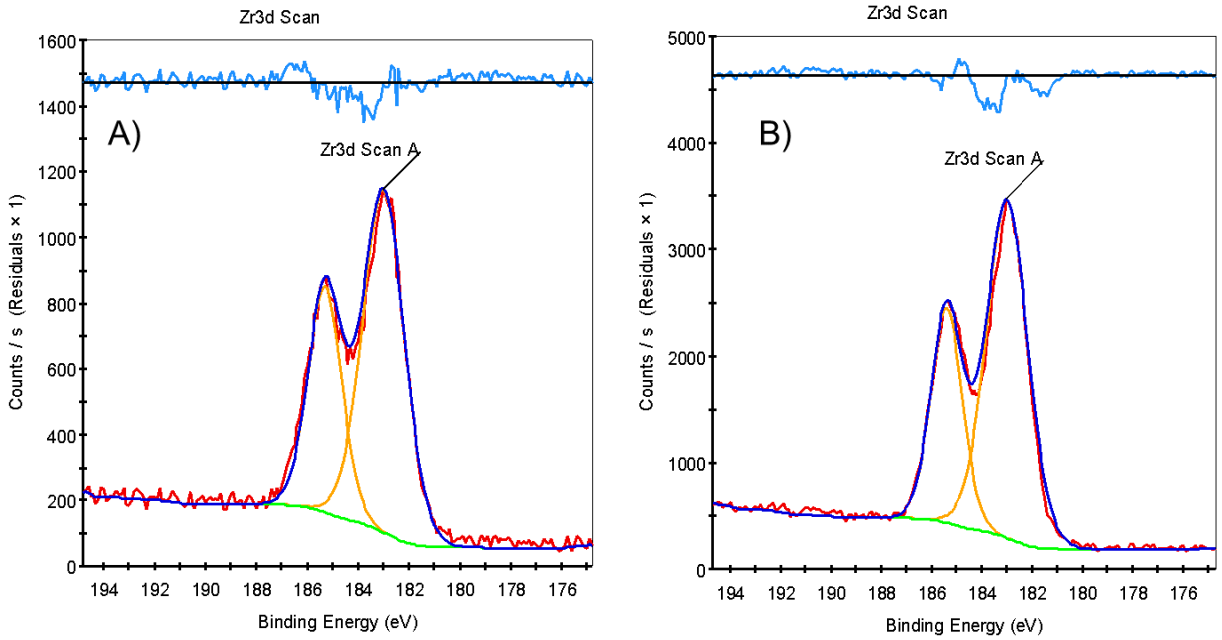

Figure 3.6.4.2. XPS spectra of NU-1000 in the Zr 3d region. A) NU-1000 before exposure to H_2. Zr $3d_{3/2}$= 183.0 eV, Zr $3d_{5/2}$ =185.3 eV based on best fit peaks. B) NU-1000 after exposure to ~10 psig of H_2 at 473 K for 12 hours. Sample was transferred to XPS chamber without exposure to air, as described in main text. Zr$d_{3/2}$=183.0 eV, Zr $3d_{5/2}$=185.4 eV based on best fit peaks. (Red) Collected data, (Dark blue) Best fit spectrum, (Yellow) Peak contributions to best fit, (Green) Baseline, (Light blue at the top) Residual for best fit spectrum. Data show no reduction of zirconium.

Chapter 4. The Dependence of Olefin Hydrogenation and Isomerization Rates on Zirconium Metal–Organic Framework Structure

4.1 Chapter Summary

Zirconium metal–organic frameworks (Zr-MOFs) are a structurally diverse and well-defined class of materials studied in heterogeneous catalysis. Previously, we showed that partial dehydration of the Zr_6O_8 node in NU-1000 results in heterolytic H_2 cleavage over adjacent Lewis acid and base sites, leading to catalytic conversion of 1-butene. In this chapter, given the ubiquity of the Zr_6O_8 node as a secondary building unit (SBU) in Zr-MOFs, with many different potential MOF topologies and capping ligands surrounding the cluster, we study the influence of thermal pre-treatments and MOF topology (MOF-808, NU-1000, UiO-66, and NU-1000-NDC) on the activity of the Zr_6O_8 cluster for H_2 activation and 1-butene hydrogenation and isomerization. Diffuse reflectance IR in the presence of H_2 and pyridine show that both thermal pre-treatment and MOF topology affect the Brønsted acidity of protons generated from H_2 activation and their resulting activity for olefin conversion. High isomerization activity of dehydrated NU-1000 is correlated with the formation of μ_3OH species after H_2 activation. Additionally, catalytic studies show that the geometry of open coordination sites on individual Zr_6O_8 nodes influences butene hydrogenation. For this reason, MOF-808 gives anomalously low hydrogenation activity, despite its relatively high total number of open coordination sites, as calculated either from its crystal structure or from NH_3 adsorption. These results reiterate the importance of pre-treatment in defining MOF catalytic activity and demonstrate that MOF topology, outside of simply affecting node accessibility, influences reactivity at individual nodes. The work in this chapter can also be found in ACS Catalysis at the following URL: https://pubs.acs.org/doi/10.1021/acscatal.2c04303

4.2. Introduction and Review of Zr-MOFs in Heterogeneous Catalysis

Zirconium-based metal-organic frameworks (Zr-MOFs) are among the most studied MOF-based catalysts due to their structural diversity and high thermal and chemical stability compared to other MOFs.[17, 30, 111, 112] Typically, these materials are composed of zirconium oxide-based clusters, called 'nodes' or 'secondary building units' (SBU), combined with multitopic carboxylate-based ligands referred to as 'linkers', which together make well-defined, 3D, porous lattices. The resulting materials are potentially useful and tunable catalysts and supports for fundamental study and the building of structure-reactivity relationships.[30, 91, 95, 97, 112, 206, 207]

For heterogeneous catalysis using Zr-MOFs, the most common strategy is to leverage open coordination sites in the material for catalytic activity, where sites may be uniformly or randomly dispersed throughout the structure.[91, 97, 120, 204, 205, 208, 209] Missing linker defects can expose Lewis acid sites on the node,[35, 96, 118, 208, 210] where catalysis can occur, and additionally, water and hydroxyl ligands capping these sites can act as anchors for metal ions, clusters, and complexes.[86, 129, 147, 206, 211] As such, controlling the chemistry at and around open coordination sites has been shown to be important for controlling the performance of Zr-MOFs as both intrinsic catalysts and catalyst supports.[92, 94, 97, 99, 184, 205, 212, 213]

Approaches towards controlling the catalytic properties of open coordination sites have primarily focused on controlling the identity of capping ligands present, as well as the node connectivity in the MOF structure. In the former case, chemical and thermal methods have been used to replace or remove capping ligands, such as hydroxyl, water, formate, alkoxy, chloride and other ligands, which modulate Lewis and/or Brønsted acidity.[92-94, 97, 99, 157-159] In the latter case, MOFs with identical SBUs but varying linker structure can change the node connectivity within the material (**Figure 4.2.1.**). Missing linker defects can also decrease the effective node

connectivity. In these cases, decreasing the node connectivity typically corresponds with increased bulk reactivity.[95, 203, 207] In some cases, higher concentrations of defects have also been reported to lead to more favorable substrate interactions when the resulting open coordination sites are closely oriented to one another. [99]

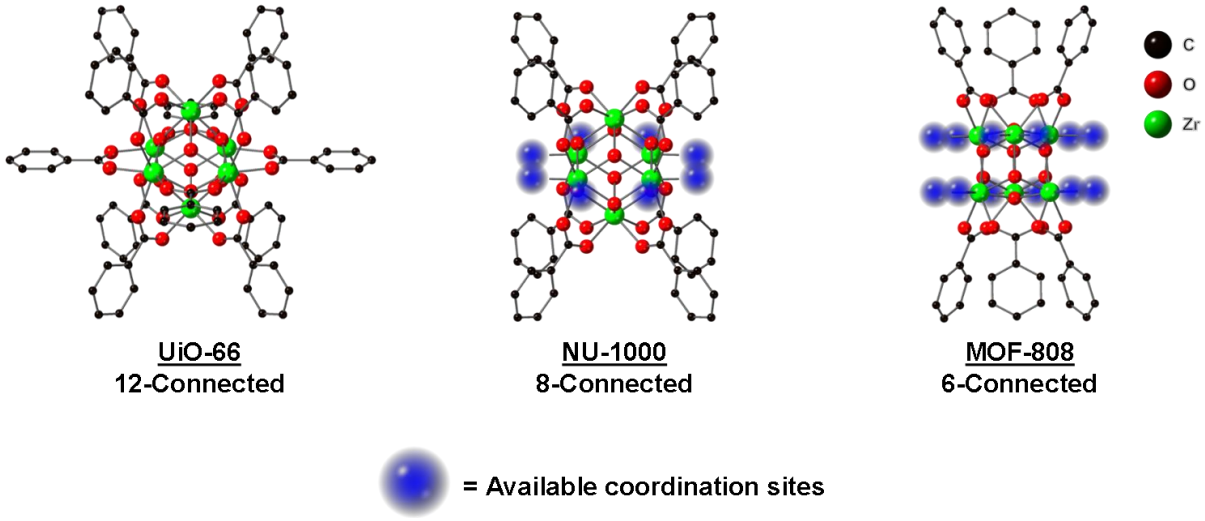

Figure 4.2.1. Examples of Zr-MOFs sharing the same Zr_6O_8 cluster but with varying connectivity. Connectivity refers to the total number of linkers bound to the node. Changes in connectivity result in different quantities and orientations of open coordination sites (represented as blue spheres), which may be occupied by ligands such as water, hydroxyls, and formates or left unoccupied, exposing Lewis acid sites. Coordination sites are unavailable for the 12-connected UiO-66 but are available in the 8-connected NU-1000 and 6-connected MOF-808. In NU-1000, these sites are oriented in-plane along the equator of the Zr_6 octahedron, while sites are oriented in two parallel planes around the edges of the Zr_6 octahedron. Representations were generated from crystal structures reported in the cited references.[184, 212, 213] Linkers are truncated, and hydrogen atoms are removed for clarity.

Recently, we reported that partial dehydration of the Zr-MOF NU-1000 leads to heterolytic cleavage of H_2, resulting in catalytic hydrogenation and isomerization of 1-butene.[214] This heterolytic cleavage was endothermic and reversible, according to DFT calculations and *in situ* infrared experiments with H_2 and D_2, and multiple potential H_2 activation sites were identified on the Zr_6O_8 cluster (**Scheme 4.2.1.**). Homolytic cleavage pathways were also investigated computationally and experimentally but were deemed unfavorable. Kinetic analysis of 1-butene hydrogenation and isomerization over NU-1000 demonstrated that the *in situ*-formed Zr–H and

Zr–OH species were responsible for reactivity at the MOF node. Different reaction orders with respect to H_2 were observed for hydrogenation and isomerization, suggesting that hydrides were responsible for hydrogenation, while both hydrides and protons could contribute to isomerization. In this work, we expand upon those initial findings and investigate the effects of changing the ligand sphere around the Zr_6O_8 cluster on H_2 activation and 1-butene conversion via thermal pretreatment. Additionally, we study the performance of Zr-MOFs (MOF-808, NU-1000, NU-1000-NDC, and UiO-66) that possess the same node structure but different orientations and numbers of connecting ligands around the cluster.

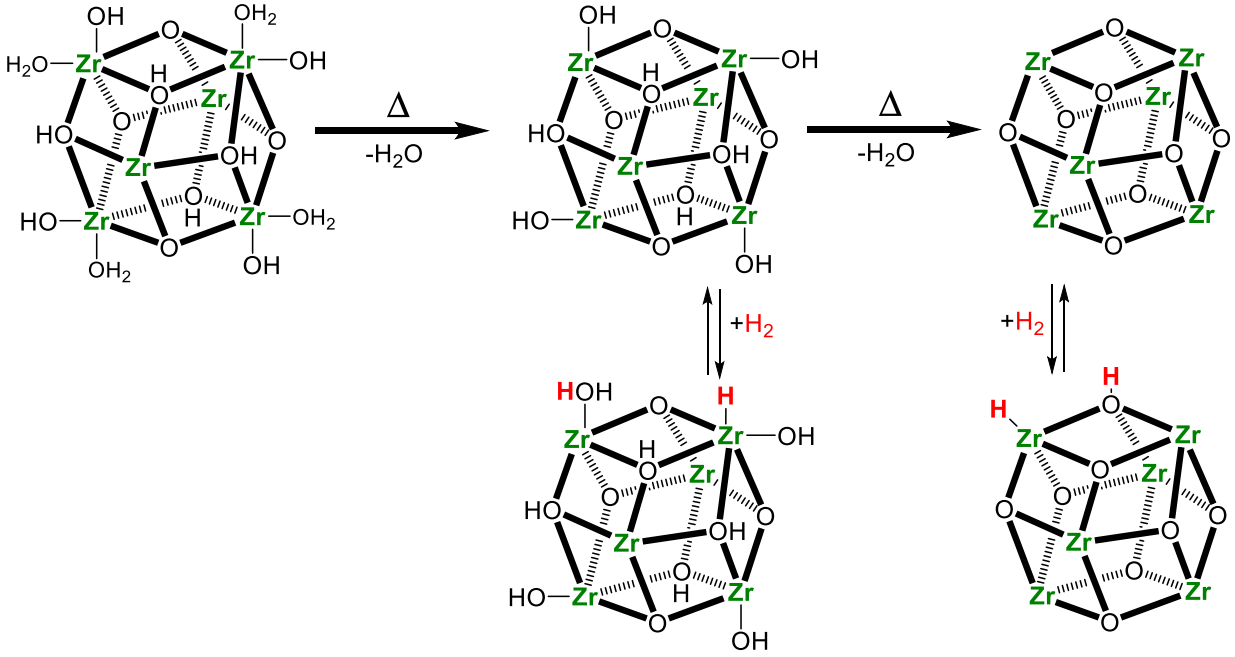

Scheme 4.2.1.1. Extended, higher-temperature pretreatments can dehydrate Zr_6O_8 nodes (top). Heterolytic H_2 activation was previously calculated to occur with the involvement of terminal OH groups (left) more prevalent with lower-temperature pretreatment and with a lower free energy of formation from bridging oxo groups (right) more prevalent following higher pretreatment temperatures.

4.3. Experimental Section

Additional details regarding materials and methods for experiments can be found in the **Additional Information**. Brief descriptions of each experiment are provided here.

4.3.1. Materials Syntheses

NU-1000, NU-1000-NDC, and Dehydrated NU-1000

NU-1000 was synthesized from $ZrOCl_2$ and 1,3,6,8-tetrakis benzoic acid pyrene (TBAPy) according to previously reported literature procedures on a 5g scale.[183, 184] NU-1000-NDC and Dehydrated NU-1000 were both produced from the same 5g batch of NU-1000 to keep reactivity comparisons between the 3 materials internally consistent. NU-1000-NDC was synthesized on a 100 mg scale through Solvent-Assisted-Ligand-Incorporation (SALI) of naphthalene dicarboxylic acid into NU-1000 according to reported procedures.[86] Dehydrated NU-1000 was produced through thermal treatment on a Micromeritics ASAP 2420 at 573 K, under vacuum at 1 x 10^{-6} Torr, overnight.

MOF-808 Synthesis and Dehydration

MOF-808 was synthesized from $ZrOCl_2 \cdot 8H_2O$ and trimesic acid in DMF on a 500 mg scale, using formic acid as the modulator, according to reported procedure.[215] Dehydration of MOF-808 was done by heating at 573 K under vacuum overnight on a Micromeritics ASAP 2420. Additionally, *in-situ* dehydrations were studied by heating MOF-808 under H_2 flow initially at 473 K for 2 hours, followed by heating at 523 K for 2-12 hours, depending on the experiment, then rates for butene conversion were measured at 473 K.

UiO-66 Synthesis and Dehydration

UiO-66 was synthesized using $ZrCl_4$ and terephthalic acid, with HCl as the modulator, on a 2 g scale according to the reported literature procedure.[117] Dehydration experiments were conducted identically to those for NU-1000, with heating under vacuum at 573 K overnight on a Micromeritics ASAP 2420.

4.3.2. Characterization

General bulk characterizations of PXRD, BET, and SEM were done for each MOF sample as detailed and shown in the supporting information (**additional information, section 4.6.2.**). Thermogravimetric analysis (TGA) of UiO-66 was done on a Mettler-Toledo TGA/DSC 1 Star System, where the sample was heated to 873 K at 10°C/min and held at 873 K for 12 hours under a 20% O_2 atmosphere, bal. N_2.

NH_3-TPD was conducted for each material with an AMI-200. ~Approximately 50 mg of MOF catalyst was loaded into a u-tube reactor with quartz sand packed above and below the reactor. Once connected to the reactor, samples were then ramped at 10°C/min up to 473 K under UHP H_2 where it was held for 2 hours. Sample was then cooled to 373 K under argon, and then 10% NH_3 was allowed to flow and adsorb for 1 hour at 373 K. After this, the sample was ramped up to 873 K at 10°C per minute under argon to desorb ammonia, with fragments detected via mass spectrometry.

4.3.3. Catalyst Testing

Experiments were conducted in the Reactor Engineering and Catalyst Testing (REACT) core facility at Northwestern University. Catalytic studies were done identically to those reported in our previous study.[214] Full details of experiments can be found in the section **4.6.1.** Briefly, 30-40 mg of MOF catalyst was diluted with ~1g of quartz sand (trace metal basis) and loaded into a quartz tube reactor tube with a bed height of approximately 1 inch. Sample was then pretreated with UHP H_2 (Ultra-High Purity, 99.999%) for 2 hours at 473 K (or 523 K for *in situ* dehydrated MOF-808) followed by exposure to 2% 1-butene balance argon and UHP H_2. Products were detected via GC-FID and conversion was calculated according to the areas of n-butane, *trans*-2-butene, and *cis*-2-butene relative to 1-butene, as detailed in the Supporting Information.

4.3.4. In situ H_2 Diffuse Reflectance IR Fourier Transform Spectroscopy

Experiments were conducted in the Reactor Engineering and Catalyst Testing (REACT) core facility at Northwestern University. MOF sample was diluted and ground with spectroscopic grade KBr (3-10 wt% MOF, depending on the optimal signal) and sealed into the *in situ* praying mantis cell of a Thermo-iS50 infrared spectrometer. The sample was pretreated and monitored under argon flow (60 s.c.c.m.) at 473 K for a minimum of 2 hours or until no further changes were observed in the spectra. The final spectrum of the material under argon at 473 K was used as the background for difference spectra under H_2 exposure of each respective sample. The catalyst was then exposed to 10% H_2 blend argon at 473 K, and difference spectra were recorded until there was no noticeable change from spectrum to spectrum. H_2 atmosphere was then exchanged with argon to observe reversibility/stability of changes due to initial H_2 exposure.

In the case of D-MOF-808, sample pretreatment involved an additional pretreatment under argon at 323 K for ~16 hours after initial pretreatment at 473 K. The sample was then cooled back down to 473 K before the collection of background and difference spectra.

4.3.5. Pyridine DRIFTS and Catalytic Studies

NU-1000 was dehydrated overnight on a Micromeritics ASAP 2420, followed by transfer to a dry, 25 mL Schlenk flask which was immediately placed under vacuum. The flask was then placed into an oil bath kept at 433 K. Approximately 6 μL of pyridine (4 eq) were added to 40 mg of dehydrated NU-1000 under static vacuum. The sample was allowed to sit at 433 K for 2 hours. Sample was then removed from the Schlenk line and prepared for collection of IR spectra.

~ 20mg of pyridine-treated sample was then loaded neat into the *in situ* praying mantis cell of a Thermo-iS50 infrared spectrometer, and spectral data were collected at room temperature under argon, using a background from neat KBr. We also measured a sample of untreated,

dehydrated NU-1000, from the same batch used to make the pyridine-treated sample, for comparison. Sample was then heated to 473 K before exposure to 3% H_2 bal. argon overnight. Sample was allowed to cool back down to room temperature before subsequent spectroscopic measurement.

The remainder of the pyridine treated sample and untreated D-NU-1000 were allotted for catalytic studies, which were conducted according to procedures described *vide supra*.

4.4. Results and Discussion

4.4.1. Effects of Thermal Dehydration and NDC insertion in NU-1000

Previous quantum chemical calculations suggested that terminal hydroxyl and μ-O ligands in a Zr_6O_8 cluster could independently function as bases for heterolytic cleavage of H_2 (**Scheme 4.2.1.**) resulting in distinct proton-hydride pairs and with different free energies of formation. From this, changes to the relative populations of sites through thermal or chemical treatments should shift activity and selectivity in 1-butene hydrogenation and isomerization. Higher temperature pretreatments dehydrate Zr_6O_8 nodes and remove other adventitious ligands, exposing Lewis sites. Continued pretreatment eliminates Zr–OH groups, leaving only μ-O ligands for H_2 activation. The latter sites have higher DFT-predicted free energies of H_2 activation.[214] Thus, we hypothesized the following upon high-temperature pretreatment of NU-1000: 1) increased overall rates of butene conversion due to the increase in Lewis sites, 2) increased apparent barriers of 1-butene conversion by leaving only μ-O ligands for H_2 activation, 3) increased isomerization activity due to the different Brønsted acidity of *in situ*-generated protons.

First, *in situ* DRIFTS was conducted under H_2 at 473 K, showing a change in population of H_2 activation sites upon thermal pretreatment. Difference spectra[199] (**Figure 4.4.1.1. A**) for as-synthesized NU-1000 show features at 3670 cm^{-1} and 3619 cm^{-1} after H_2 exposure, as well as a

broad feature at lower wavenumbers consistent with physisorbed water. The feature at 3670 cm^{-1} is most consistent with Zr–OH/H_2O stretches newly generated from H_2 activation via cleavage with terminal OH ligands, based on assignments in the hydroxyl region of NU-1000 and other Zr-MOFs.[89, 93, 97, 216] We assign the feature at 3619 cm^{-1} to the generation of μ_3-OH species from H_2 activation over bridging oxo ligands, based upon the feature's redshifted position relative to that at 3670 cm^{-1} and consistent with stretching observations over ZrO_2 surfaces.[20, 166, 168-170, 178] Redshifted OH stretches indicate weaker O–H bonds and more acidic protons, anticipating a reactivity difference between the two different acid sites. Together, these stretches suggest two pathways for H_2 activation, with cleavage across terminal hydroxyl ligands being the primary pathway for activation in the as-synthesized material. Comparing these data to those for the thermally pretreated material (D-NU-1000, **Figure 4.4.1.1. B**) shows different relative proportions of the surface features. H_2 exposure over D-NU-1000 initially yields three Zr–OH features appearing at 3770 cm^{-1}, 3670 cm^{-1}, and 3619 cm^{-1}, with the feature at 3619 cm^{-1} being much larger and sharper than in the as-synthesized material. Stretches at 3770 cm^{-1} are assigned to isolated, terminal Zr–OH stretches next to Lewis acid sites in Zr-MOFs,[92, 99] while stretches at 3670 and 3619 cm^{-1} remain as previously assigned. After an hour of H_2 flow at 473 K, the feature at 3670 cm^{-1} decreases in intensity, primarily leaving the features at 3770 and 3619 cm^{-1}. Additionally, shoulders are observed at 3720 cm^{-1} and 3648 cm^{-1}, suggesting subpopulations of protonated species on the dehydrated node due to node distortions. The appearance of new stretches and the increase in relative abundance of the redshifted, more acidic μ_3-OH species supports the hypothesis that H_2 activation over the thermally pretreated MOF primarily occurs over bridging oxo ligands, rather than terminal OH species for the as-synthesized material and predicts changes in reactivity for 1-butene conversion.

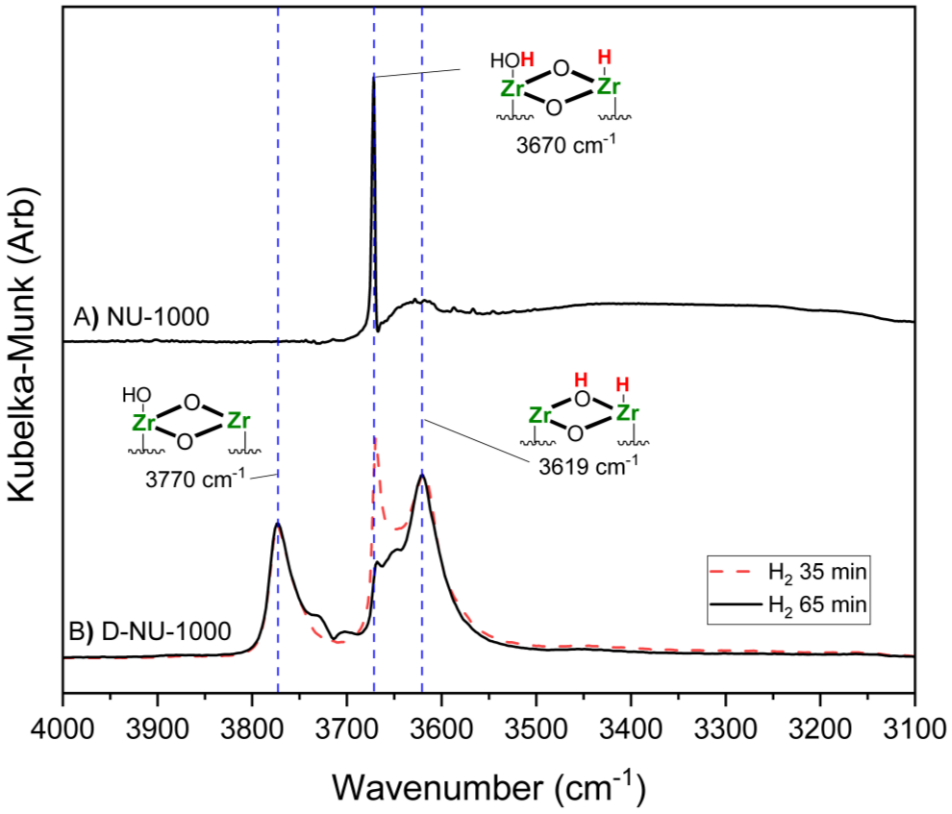

Figure 4.4.1.1. Difference DRIFTS of A) NU-1000 and B) pretreated D-NU-1000 after 1hr H_2 exposure at 473 K. Background spectra recorded at 473 K under (A) N_2 and (B) Ar. Full spectra in the additional information (**4.6.4.**) A) Positive features at 3770 cm^{-1}, 3670 cm^{-1} and 3619 cm^{-1} are assigned to newly generated Zr-OH, Zr-OH_2 and μ_3OH sites, respectively. Dashed curve acquired after 30 min under H_2.

Additionally, *in situ* DRIFTS of D-NU-1000 was collected after exposing the sample to 4 eq. of pyridine per node and to H_2 showing the generation of Brønsted acidity upon H_2 activation. It should be noted that vibrations of the MOF linkers overlap with typical bands of adsorbed pyridine, making those features more complex to interpret than for a bulk oxide. When pyridine-loaded D-NU-1000 is exposed to H_2, a new feature appears at 1546 cm^{-1} and features grow at 1523 cm^{-1} and 1446 cm^{-1} (**Figures 4.4.1.2. A** and **4.4.1.2. B**). At the same time, a feature at 1370 cm^{-1}, attributed to weakly adsorbed pyridine, disappears after exposure to H_2. In comparison, when pyridine-free D-NU-1000 is exposed to H_2, features are found at 1523 cm^{-1}, 1446 cm^{-1} and 1420 cm^{-1}, presumably due to perturbations of the linker (**Figure 4.4.1.2. C**). Notably, the feature at

1446 cm^{-1} is of lower intensity in the spectrum of pyridine-free D-NU-1000, consistent with pyridine adsorbed at Lewis acid sites. Additionally, the new feature at 1546 cm^{-1} is completely absent from the pyridine-free spectrum, and the region from 1550-1540 cm^{-1} has been previously associated with pyridinium ions adsorbed on Brønsted acid sites in ZrO_2.[41, 107, 217] We also observe a broad shoulder centered around 1490 cm^{-1}, consistent with a Brønsted/Lewis combination band (**Figures 4.4.1.2. A** and **4.4.1.2. B)**. Therefore, these spectra provide evidence that H_2 activation over D-NU-1000 dynamically generates Brønsted acidic protons that are accessible to chemical species like pyridine.

Next, the reaction of 1-butene in the presence of H_2 was studied at 473 K. Representative TOS data are presented in **Figure 4.4.1.3**. **Table 4.4.1.1** shows an increase in 1-butene steady state rates, normalized per Zr_6O_8 node, over NU-1000 following a dehydration pretreatment. This was due to a 5-fold increase in the isomerization rate, that more than compensated for a small decrease in hydrogenation rate. The apparent barriers (see supporting information, S26-S28) for hydrogenation and isomerization are both ~40 kJ/mol after dehydration. This is an increase from 28 kJ/mol for the hydrogenation sites, and a decrease from ~50 kJ/mol for the isomerization sites. One explanation for this change is a shift in H_2 activation sites from terminal ZrOH to bridging oxo ligands after dehydration, as observed in the DRIFTS difference spectra under H_2. The DFT-computed free energies of formation of hydride-proton pairs are higher over bridging oxo ligands than over terminal hydroxyl sites,[214] decreasing the surface coverage of hydrides at steady state. However, this would also result in stronger Brønsted acidity of the newly formed μ_3OH protons, which could be responsible for the higher isomerization rates.

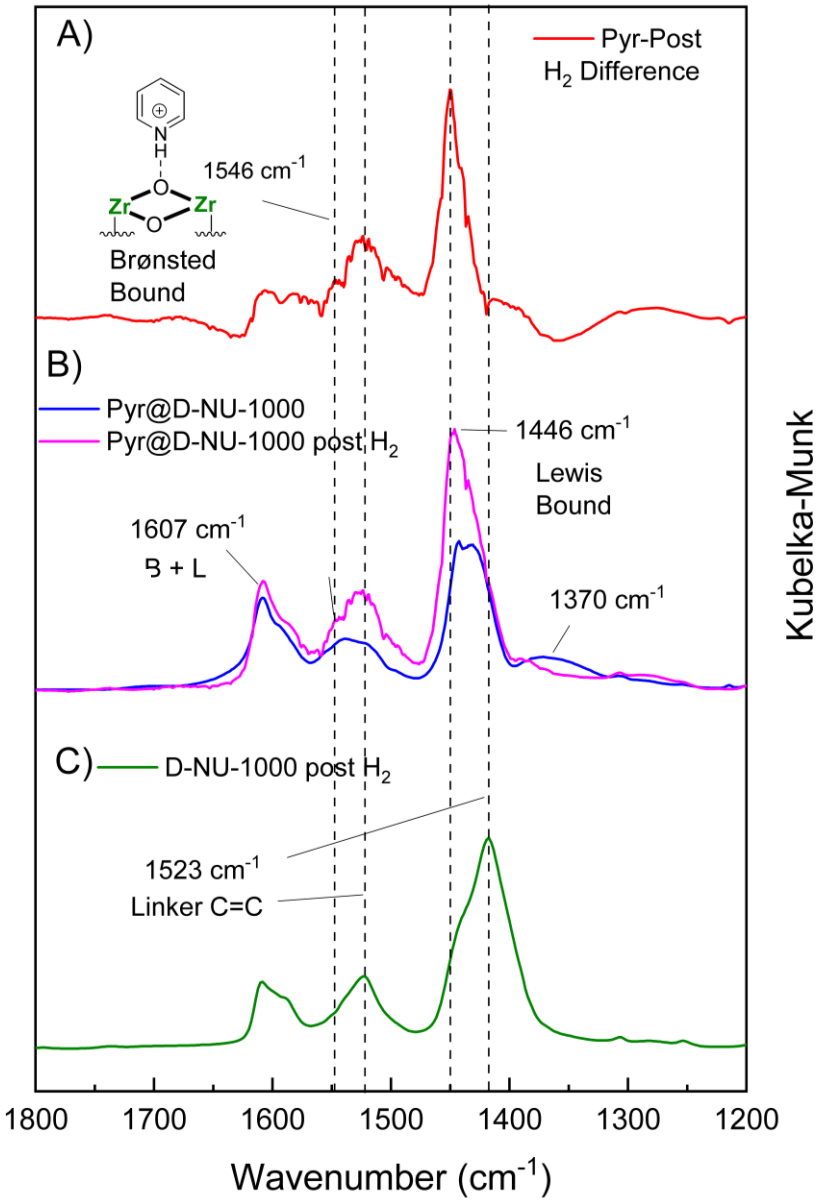

Figure 4.4.1.2. DRIFTS spectra of D-NU-1000 in the aromatic ring vibration region. Full spectra can be found in the additional information (**4.6.2.14-15**). A) Pyridine-treated D-NU-1000, before exposure to H_2 (before), after exposure (pink) and the difference (red). B) Spectra for D-NU-1000 after H_2 exposure (green). C) Spectrum for dehydrated NU-1000 after exposure to H_2. The 1546 cm^{-1} feature is unique to pyridine- and H_2-treated D-NU-1000, and it is consistent with formation of Bronsted acid sites.

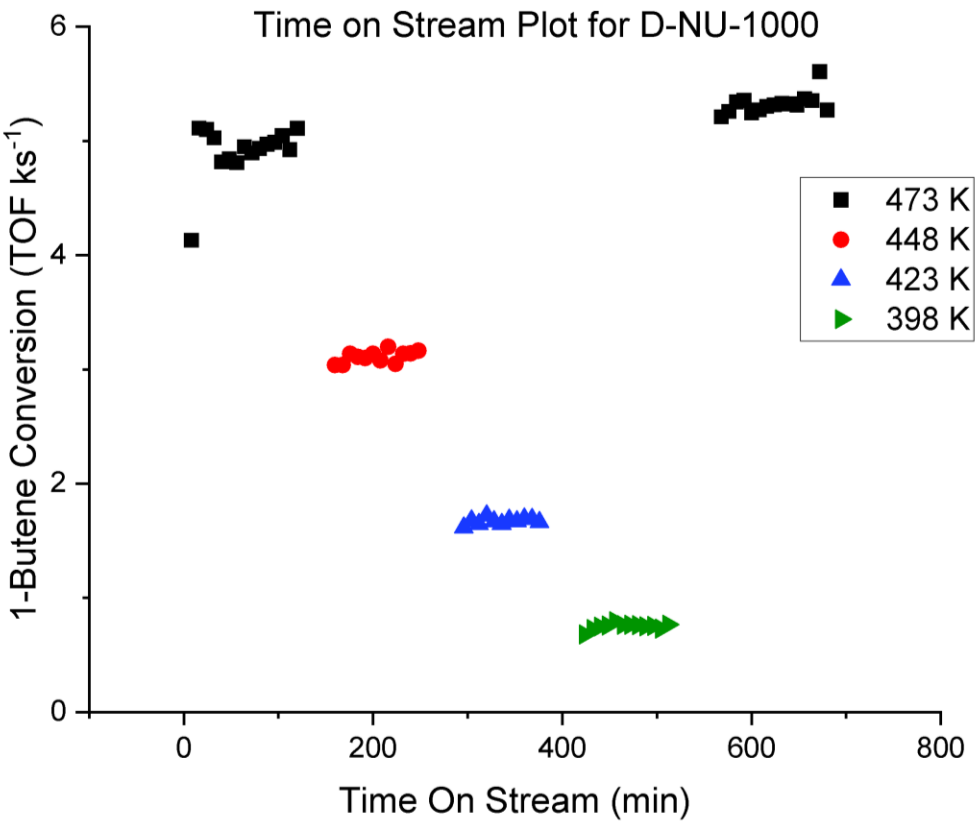

Figure 4.4.1.3. Example time-on-stream plot from a typical experiment. Shown, D-NU-1000 under 25 s.c.c.m. UHP H_2 and 25 s.c.c.m. 2% 1-butene balance argon with ~10 P.S.I.G. total pressure, at a variety of bed temperatures. Apparent steady state rates at temperatures from 473-398 C were used to calculate apparent activation energies for this sample. Each condition lasts approximately 2 hours with approximately 16 injections per condition. Injections included in the average apparent rate at each condition (as listed in **Table 4.4.1.1.**) was determined by the overall stability of conversion from injection to injection.

Next, we examined 1-butene conversion over D-NU-1000 that was pretreated with 4 eq. pyridine per node (**Table 4.4.1.1., entry 3**). Pyridine addition to the dehydrated material depressed all butene conversion rates, with a disproportionate impact on isomerization rates. We attribute this to pyridine effectively titrating the Brønsted acid sites as they are generated dynamically by H_2 activation, while leaving hydrides generated at Lewis sites available. Thus, H_2 forms hydrides that participate in hydrogenation, but newly formed Brønsted sites are immediately titrated away, suppressing isomerization rates. Overall, these DRIFTS and reactivity studies demonstrate that

changes to the Zr_6O_8 node caused by thermal pretreatments change the nature of the H_2 activation sites, resulting in changes to the hydrogenation and isomerization activity. Next, we investigated whether changes to the MOF topology, while maintaining the same Zr_6O_8 node, would have similar effects.

	Rate ($mol_{1\text{-butene}}/ks/mol_{node}$)			**Selectivity**		
MOF	Total	Hyd.	Isom.	butane	2-butene	*trans/cis*
NU-1000[a]	1.4 ± 0.4	0.7±0.2	0.7±0.2	51 %	49%	1.3
D-NU-1000[a]	4.0 ± 0.9	0.4±0.1	3.7±0.8	10 %	90%	1.5
Pyr@D-NU-1000[b]	0.5	0.07	0.4	23%	77%	1.6
NU-1000-NDC[b]	0.25	0.13	0.12	52%	48%	1.3

Table 4.4.1.1. Comparison of apparent rates in as-synthesized, dehydrated, pyridine-treated NU-1000, and NU-1000-NDC. Conditions for experiments with each sample were 25 s.c.c.m. UHP H_2 and 25 s.c.c.m. 2% 1-butene balance argon with ~10 P.S.I.G. total pressure at 473 K. All reactivity data come from one batch of NU-1000. TOFs for NU-1000 and D-NU-1000 are averaged from apparent rates at steady conversion across multiple catalytic experiments at 473 K, in triplicate or more. Error bars reflect the calculated standard error, $\frac{\sigma_{TOF}}{\sqrt{n}}$, where σ_{TOF} is the standard deviation and n is the total number of sample points, and where each sample point is the average apparent rate at steady state conversion in a given catalytic run.[a] Catalytic conversion exceeded 10% in some catalytic runs. [b]Data comparing NU-1000-NDC and Pyridine@D-NU-1000 are from steady state data of single catalytic runs.

4.4.2. Effect of MOF topology

The effect of MOF topology on catalytic performance was initially tested by incorporating naphthalene dicarboxylic acid (NDC) into NU-1000 using previously reported protocols.[86] One NDC ligand bridges two nodes of NU-1000 through the c-pore, which is orthogonal to the hexagonal and triangular channels of NU-1000. When incorporated throughout the framework, open coordination sites are systematically blocked in the c-pore and left open in the hexagonal

channels, changing the framework from an 8-connected to a 10-connected material and blocking off 2 out of 4 open coordination sites at the Zr node. (**Figure 4.4.2.1.**). In our synthesis, NMR showed the incorporation of ~0.8 NDC linkers per node of NU-1000 (Additional information, **Figure 4.6.2.13**), blocking ~80% of Lewis acid sites within the c-pore, or ~40% of total open coordination sites in the framework.

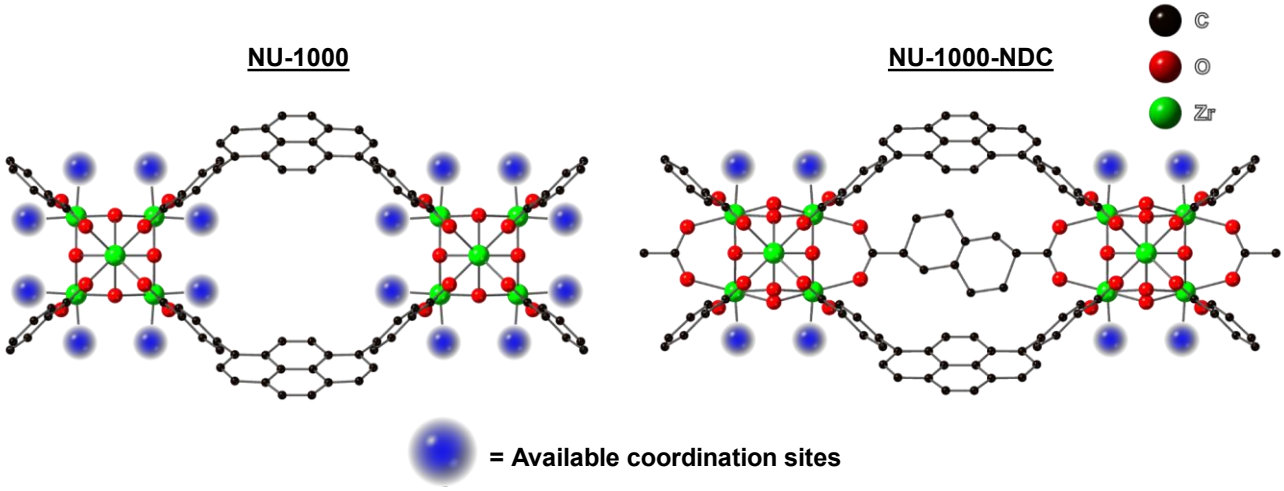

Figure 4.4.2.1. Representations of c-pore in NU-1000 (Left) and NU-1000-NDC (right). Comparison of crystal structures shows the bridging of nodes by NDC ligand. Open coordination sites (represented as blue spheres) are unavailable in the c-pore of NU-1000-NDC.

As seen in **Table 4.4.1.1.**, entry 4, NDC incorporation reduced the rate of olefin conversion by ~80% when compared to NU-1000 (Entry 1). This value corresponds to the fraction of sites blocked within the c-pore, but also to the number of Zr sites that have an open coordination site within the hexagonal channel as well as an adjacent site in the c-pore. Only this arrangement can accommodate cis-coordination of reactive intermediates, such as the olefin and hydride as required for 1,2-insertion mechanisms[218, 219] (**Scheme 4.4.2.1.**). While the precise origin of the change in reactivity will need further research and modeling, the large reactivity loss after NDC incorporation indicates that rates are sensitive not only to the total number of open coordination sites, but also their structure.

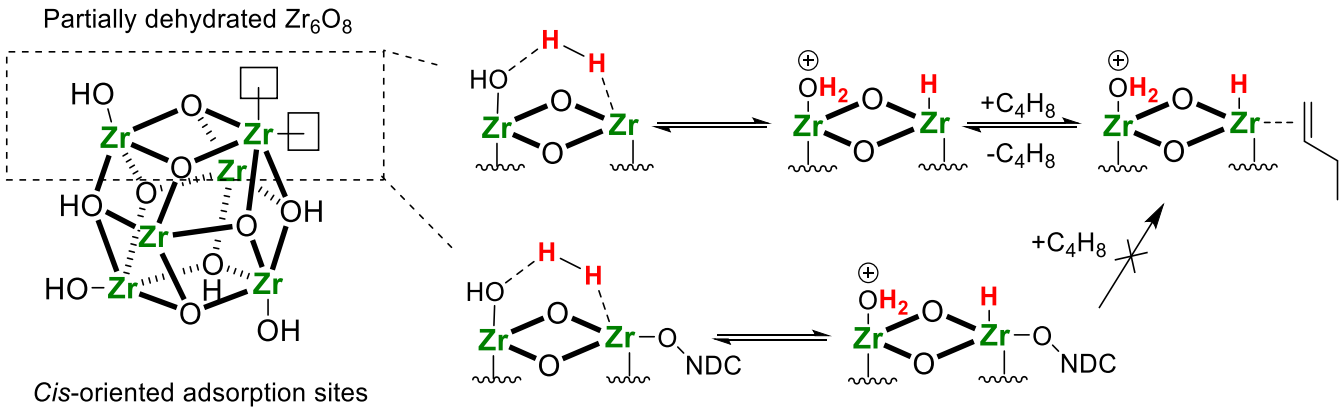

Scheme 4.4.2.1. Cis-oriented open coordination sites on partially dehydrated nodes (left) are important for activity in 1-butene hydrogenation and isomerization. Proposed mechanism (right) of how NDC ligand blocks sites for 1-butene hydrogenation and isomerization. Nodes are truncated along one edge of the Zr_6O_8 octahedron for simplicity in representation. Linkers are omitted for clarity.

Starting from the observations of reactivity decreases for NU-1000-NDC, we expanded our study to additional MOFs with differing connectivity in terms of both number and orientation of coordination sites, MOF-808 and UiO-66. MOF-808 has a lower, 6-connected structure when compared to the 8-connected NU-1000, while pristine UiO-66 is 12-connected (**Figure 4.2.1.**). The latter would indicate no available open coordination sites, but various synthesis procedures for UiO-66 yield materials with missing linkers, creating undercoordinated nodes of different quantities. Literature regarding Zr-MOF catalysis has shown that lower connected nodes typically perform better for catalytic reactions due to greater proportions of available Lewis acid sites.[30, 88, 95, 204, 207-209, 220] Here, we used an HCl-modulated synthesis[117] to provide a defective UiO-66 for reactivity studies, for which thermogravimetric analysis (TGA) measured an average of ~8-connected clusters in the material (**Figure 4.6.2.7**), resulting in an overall connectivity trend of UiO-66≥NU-1000>MOF-808 across the materials studied. NH_3-temperature programmed desorption was then conducted on the materials after an H_2 pretreatment at 473 K. UiO-66, NU-1000, and MOF-808 gave 0.047, 0.049, and 0.14 total mol NH_3/Zr_6O_8, respectively (**Figure**

4.6.2.12.). The order of magnitude of these values is consistent with previous reports of NH_3 adsorption in Zr-MOFs,[93] and the values are inversely correlated with the average connectivity, as expected. From these results, one would expect a trend in reactivity of MOF-808>NU-1000≥UiO-66 if H_2 activation and 1-butene conversion are insensitive to topological differences among the materials.

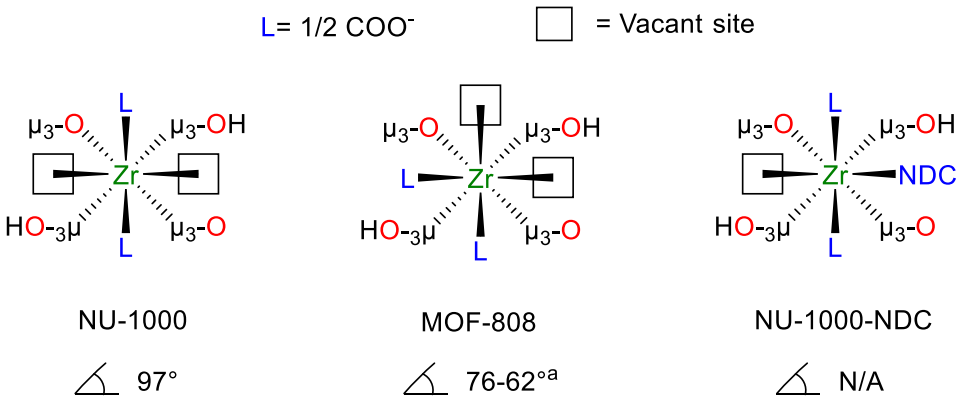

Scheme 4.4.2.2. Projections of environment around a single Zr-atom of the Zr_6O_8 cluster in different MOF topologies. Projections look down a single vertex of the Zr_6 octahedron, where μ_3-oxo/hydroxyl ligands in the Zr_6O_8 cluster extend into the page while MOF linkers and available coordination sites extend out of the page. Under reaction conditions, 'vacant sites' are created from the desorption of hydroxyl and aquo ligands, resulting in open coordination sites for the adsorption of hydrides and olefins. Angles between these sites are reported below each projection, as measured from the bond angles between capping ligands in the crystallographic information files[184, 212] of each structure. [a]Depending on the capping ligand used in measurement (multiple ligands and conformations were observed due to symmetry and disorder), bond angles between ligands were as high as 76° and as low as 62°.

However, these materials also differ in the arrangement of open coordination sites on the Zr_6O_8 cluster. For example, examination of the respective crystal structures of MOF-808 and NU-1000 (**Figure 4.2.1.**) shows that open sites in NU-1000 are arranged in a plane along the equator of the Zr_6 octahedron, while open sites sit along 6 of the 8 faces in MOF-808. Focusing on a single Zr atom in a cluster, the O-Zr-O bond angles with capping ligands are ~100° for NU-1000[184] vs. ~70° for MOF-808[212] (**Scheme 4.4.2.2.**). After thermal pretreatment to remove the capping ligands, these become potential reactant adsorption sites, and the different geometries may impact the energetics of H_2 activation sites and/or butene activation barriers. Presumably, defective UiO-66

has some mixture of these sites, given the disorder induced in the structure from missing linkers. These topological differences, therefore, suggest that there can also potentially be reactivity trends beyond those expected from differences in numbers of open coordination sites.

H_2 activation over the different materials was first studied via *in situ* DRIFTS (**Figure 4.4.2.2.**). In this section, NU-1000 and UiO-66 were pretreated at 573 K under vacuum while MOF-808 was pretreated at 523 K under vacuum, to remove the influence of residual capping ligands. Experiments were tried pretreating MOF-808 at 573 K under vacuum, but a significant loss in reactivity was observed (Additional information **Table 4.6.3.1.**), so pretreatments were limited to a maximum temperature of 523 K under argon thereafter. Spectra and reactivity data of the as-synthesized materials are found in the supporting information (Additional information, section **4.6.4.**). As shown in **Figure 4.4.1.1.** and **Figure 4.4.2.2. C**, H_2 activation over D-NU-1000 leads to hydroxyl features at 3770, 3670, 3619 cm^{-1}, and shoulders at 3640 and 3730 cm^{-1}. After extended exposure to H_2, the dominant features are at 3770 and 3619 cm^{-1}. For D-MOF-808, the peak at 3770 cm^{-1} is present, but relatively weaker, while there is a sharp and persistent peak at 3670 cm^{-1}. In D-UiO-66, the peak at 3770 cm^{-1} is much weaker, and the spectrum is dominated by the peak at 3670 cm^{-1}. In neither D-MOF-808 nor D-UiO-66 is there a significant peak at 3619 cm^{-1}. Above, we assigned this peak to Brønsted acidic μ_3OH species, implying weaker Brønsted acidity of sites generated from H_2 activation in D-MOF-808 and D-UiO-66. Previous studies have shown that node distortions and bridging ligand losses upon thermal dehydration are dependent on MOF structure,[21, 114] and it is reasonable that this would then influence subsequent H_2 activation pathways.

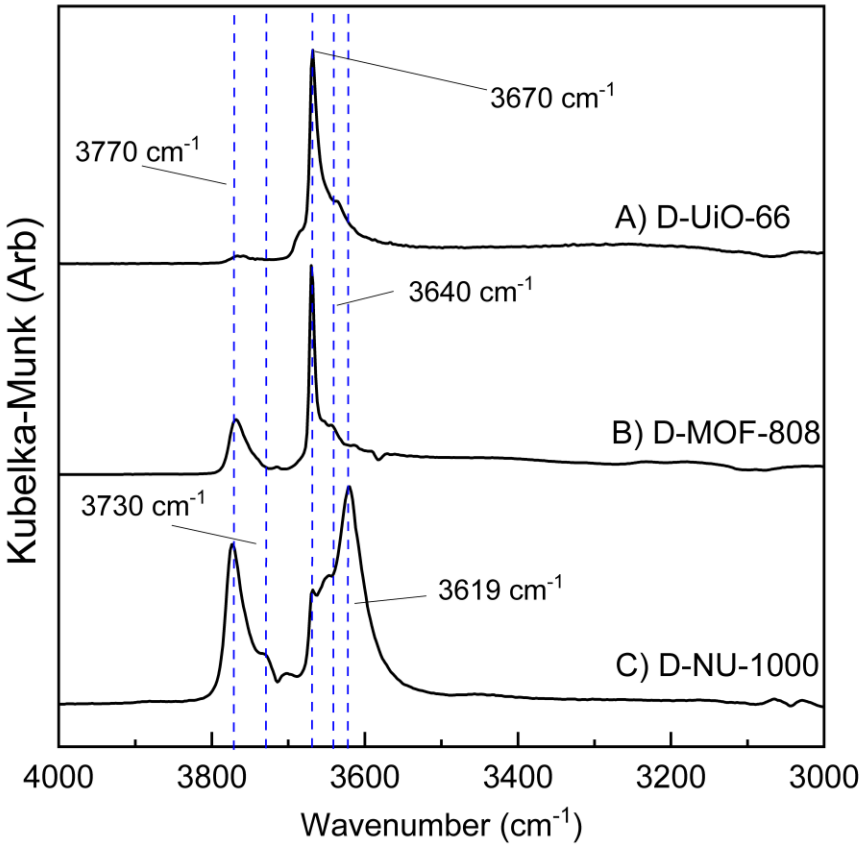

Figure 4.4.2.2. DRIFTS difference spectra under H_2 exposure (10% balance Ar) at 473 K for dehydrated UiO-66 (top), MOF-808 (middle), and NU-1000 (bottom). Full spectra can be observed in the SI. Stretches at 3770 cm^{-1} are assigned to newly generated terminal hydroxyls, while stretches at 3670 cm^{-1} are consistent with $ZrOH_2$ and μ_2OH ligands. As previously mentioned, stretches at 3619 cm^{-1} have been assigned to newly generated μ_3OH.

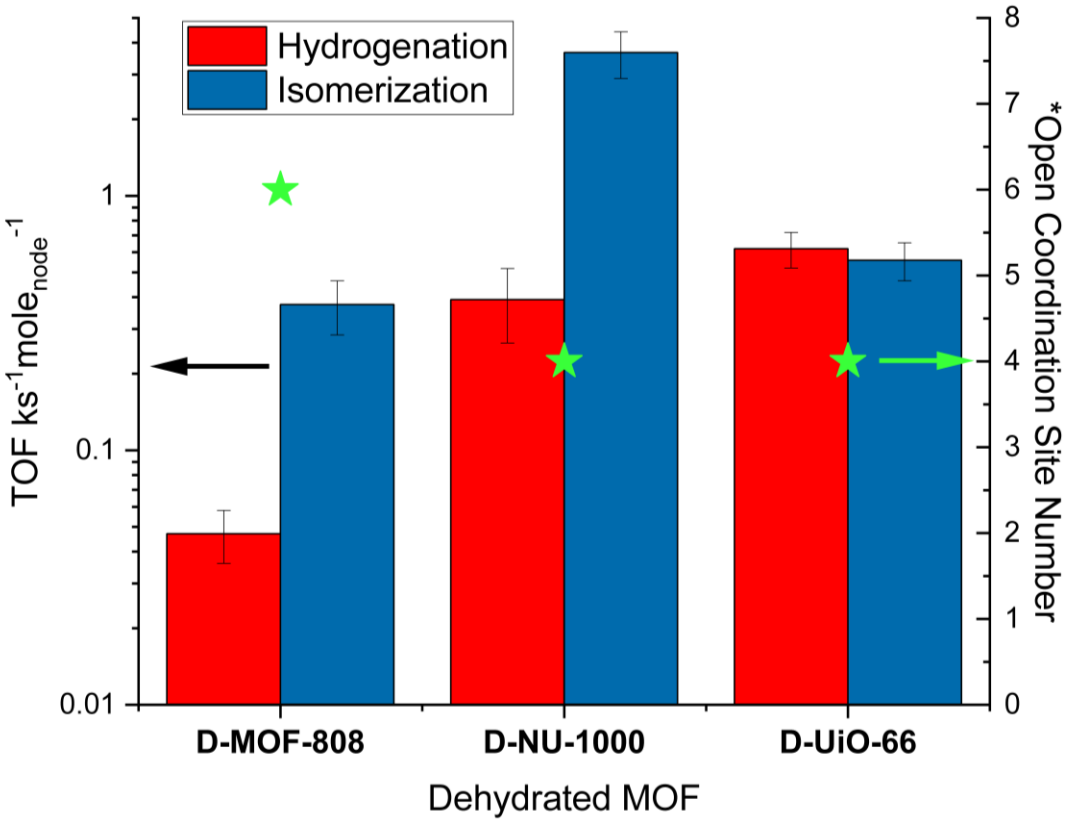

Figure 4.4.2.3. (Left axis) Comparison of apparent rates for 1-butene hydrogenation and isomerization, respectively, in dehydrated MOF-808, NU-1000, and UiO-66. All reactivity data comes from the same starting batches of MOF. TOFs are averaged from apparent rates at steady conversion across multiple catalytic experiments at 473 K. Error bars reflect the calculated standard error, $\frac{\sigma_{TOF}}{\sqrt{n}}$, where σ_{TOF} is the standard deviation and n is the total number of sample points, and where each sample point is the average apparent rate at steady state conversion in a given catalytic run. Catalytic conversion exceeded 10% in some catalytic runs of dehydrated NU-1000. Additional details about these experiments can be found in the methods section. (Right axis) Relative quantities of adsorption sites in each material, as defined relative to linkers coordinated around the Zr_6O_8 node. *Values for MOF-808 and NU-1000 are determined from the respective crystal structures of each material, while the value for UiO-66 is determined from the node linker ratio as measured via TGA. All values are on a per mole basis of the Zr_6O_8 cluster. Data are qualitatively consistent with adsorption sites as measured via NH_3-TPD.

1-butene isomerization and hydrogenation rates, normalized per node, over the different materials are shown in **Figure 4.4.2.3**. First looking at hydrogenation rates, these trend as D-UiO-66 ≥ D-NU-1000 >> D-MOF-808, opposite the trend in open coordination sites as determined by either NH_3 adsorption or their average chemical compositions. This shows an apparent influence of local structure at the Zr_6O_8 node. Literature on homogeneous catalysis with Zr-H complexes has

shown that barriers for 1,2-insertion and β-hydride elimination are higher for more crowded metal centers.[218] Thus, the low hydrogenation rates of D-MOF-808, in spite of the high number of total open coordination sites, may be due to the lower bond angles between open coordination sites in MOF-808 than for NU-1000 (Scheme 3), increasing the barriers of steps relevant to butene hydrogenation. Because open coordination sites in UiO-66 are generated by random defects, the material is also expected to possess some nodes with high bond angles between open coordination sites, enabling high rates. Next, node-normalized butene isomerization rates trend as D-NU-1000 >> D-UiO-66 ≥ D-MOF-808. Here, the activity of D-NU-1000 is anomalously high. Because Brønsted acidity can contribute to butene isomerization, we assign the high reactivity of D-NU-1000 to its stronger Brønsted acidity upon H_2 activation, as manifested in the μ_3-OH stretch at 3619 cm^{-1} in the *in situ* DRIFTS. These data suggest that the nature of H_2 activation sites in these materials is critical for determining catalytic activity for 1-butene isomerization, even on compositionally identical Zr_6O_8 nodes. Importantly, this trend in reactivity also goes against observed trends in Zr-MOFs for other catalytic reactions, where lower-connected materials typically perform best. Because the *nature* of the active site will have an exponential influence on rate via the apparent reaction barrier, while the *number* of active sites only has a linear dependance, these results show how changes in the linkers surrounding the node can have an additional influence on rates, well beyond connectivity numbers.

4.5. Conclusion

Altogether, catalytic and spectroscopic data of MOF-808, NU-1000, and UiO-66 show that rates of 1-butene hydrogenation and isomerization do not correlate with node connectivity but suggest the existence of distinct H_2 and olefin activation sites within each material despite each containing the same Zr_6O_8 node. In the case of isomerization, different H_2 cleavage sites produce

protons of varying degrees of catalytic activity, yielding significantly different rates for 1-butene isomerization across materials and thermal pretreatments. Likewise, MOF topology affects the orientation with which substrates can meet on the node surface, impacting both hydrogenation and isomerization rates at the newly generated hydride sites. The effect of MOF topology is geometric, dictating the relative orientation of open coordination sites on the nodes and the specific bond angles of those coordination sites, but it may also exert influence electronically, due to different numbers and types of carboxylates attached to the node, for which direct participation in H_2 activation cannot be ruled out, meriting further investigation. Importantly, the sensitivity of product selectivity to pretreatments and the small size of the butene reactant make it unlikely that sterics or transport through the pores are determining factors in the rate differences.

These results show that MOF topology is important for reasons beyond determining node accessibility, and at least for some reactions, other factors should be taken into consideration when choosing or comparing Zr-MOF catalysts. Future work should consider methods for controlling the orientation and proximity of open coordination sites, to achieve desired reactivity within a given MOF system. Extensive future research will be needed to understand reaction mechanisms over such materials, including the use of quantum chemical models that may need to include more of the active site structure beyond the Zr_6O_8 node.

4.6. Additional Information

4.6.1. Fully Detailed Materials and Methods

Materials

Reagents for MOF and linker syntheses, zirconyl chloride octahydrate, zirconium chloride, trimesic acid, terephthalic acid, and naphthalene dicarboxylic acid, 1,3,6,8-tetrabromopyrene, (4-

(ethoxycarbonyl)phenyl)boronic acid, tetrakis(triphenylphosphine) palladium(0), tripotassium phosphate, and benzoic acid were purchased and used as received from Sigma Aldrich. Additionally, hydrochloric acid, trifluoroacetic acid, formic acid, ethanol, acetone, and *N*,*N*-dimethylformamide were purchased from Fisher Scientific and used as received.

For catalytic studies, 2% 1-butene balance argon, N_2 Ultra-High Purity (UHP, 99.999%), and H_2 UHP (99.999%) were purchased from Airgas. A calibration tank containing 2% ethane, 2% ethene, 2% propane, 2% propylene, 2% *n*-butane, 2% 1-butene, 2% *trans*-2-butene, and 2% *cis*-2-butene (balance Ar) was also purchased from Airgas. Quartz sand (trace-metals grade) was purchased from Sigma Aldrich.

For *in situ* Diffuse Reflectance Infrared Fourier Transform Spectroscopy (DRIFTS), 10% H_2 in balance argon and UHP Argon were purchased from Airgas. Restek super-clean gas filters (triple model) were used to further purify and remove hydrocarbons, water, and O_2 from H_2 in balance Ar and UHP N_2. KBr (spectroscopic grade) was purchased from Sigma Aldrich.

Ammonia TPD studies were done using 10% NH_3 balance Ar, H_2 UHP, He UHP purchased from Airgas. Pyridine used in pyridine adsorption studies was purchased from Fischer Scientific and used as received. Base digestion of MOFs was done using 40 wt% NaOD/D_2O purchased from Cambridge Isotopes, and D_2O (99.9 atom%) from Sigma Aldrich.

Catalyst Synthesis

NU-1000, NU-1000-NDC, and Dehydrated NU-1000

NU-1000 was synthesized from $ZrOCl_2$ and 1,3,6,8-tetrakis benzoic acid pyrene (TBAPy) according to previously reported literature procedures on a 5g scale.[183, 184] NU-1000-NDC and Dehydrated NU-1000 were both produced from the same 5g batch of NU-1000 to keep reactivity comparisons between the 3 materials internally consistent. NU-1000-NDC was synthesized on a

100 mg scale through Solvent-Assisted-Ligand-Incorporation (SALI) of naphthalene dicarboxylic acid into NU-1000 according to reported procedures.[86] Dehydrated NU-1000 was produced through thermal treatment on a Micromeritics ASAP 2420 at 300 °C, under vacuum at 1 x 10^{-6} Torr, overnight.

MOF-808 Synthesis, and Dehydration

MOF-808 was synthesized from $ZrOCl_2 \cdot 8H_2O$ and trimesic acid in DMF on a 500 mg scale, using formic acid as the modulator, according to reported procedure.[215] Dehydration of MOF-808 was done by heating at 300 C under vacuum overnight on a Micromeritics ASAP 2420. Additionally, *in-situ* dehydrations were studied by heating MOF-808 under H_2 flow initially at 200 °C for 2 hours, followed by heating at 250 °C for 2-12 hours, depending on the experiment, then rates for butene conversion were measured at 250 °C.

UiO-66 Synthesis and Dehydration

UiO-66 was synthesized using $ZrCl_4$ and terephthalic acid, with HCl as the modulator, on a 2 g scale according to the reported literature procedure.[117] Dehydration experiments were conducted identically to those for NU-1000, with heating under vacuum at 300 °C overnight on a Micromeritics ASAP 2420.

Characterization

N_2 adsorption isotherms were collected on an ASAP 2420 (Micromeritics) at 77 K using 50-70 mg of sample after evacuation at 120 °C (MOF-808 and NU-1000) or 150 °C (UiO-66) for ~16 hours on the ASAP 2420. The Brunauer-Emmett-Teller (BET) area was calculated in the relative pressure region $P/P_0 = 0.005–0.05$.

Powder X-ray Diffraction (PXRD) data were collected at room temperature on a STOE-STADI-P powder diffractometer equipped with an asymmetric curved Germanium

monochromator (CuKα1 radiation, λ = 1.54056 Å) and one-dimensional silicon strip detector (MYTHEN2 1K from DECTRIS). The line focused Cu X-ray tube was operated at 40 kV and 40 mA. NU-1000 was packed in an 8 mm metallic mask and sandwiched between two polyimide layers of tape. Intensity data from 0 to 40 degrees two theta were collected over a period of ~10 mins. The instrument was calibrated against a NIST silicon standard (640d) prior to the measurement.

Scanning Electron Microscopy (SEM) images were collected with a Hitachi SU4800 microscope in the EPIC/NUANCE core facility at Northwestern University. The samples were coated with 8 nm OsO_4 before imaging to prevent charging.

Thermogravimetric analysis (TGA) of UiO-66 was done on a Mettler Toledo TGA/DSC 1 Star System. Sample was heated to 873 K at 10°C/min and held at 873 K for 12 hours under a 20% O_2 atmosphere, bal. N_2.

NH_3-TPD was conducted with an AMI-200. ~approximately 50 mg of MOF catalyst was loaded into a u-tube reactor with quartz sand packed above and below the reactor. Once connected to the reactor, samples were then ramped at 10 C/min up to 200 C under UHP H_2 where it was held for 2 hours. Sample was then cooled to 100 C under argon, and then 10% NH_3 was allowed to flow and adsorb for 1 hour at 100 C. After this, sample was ramped up to 600 C at 10 C per minute, under Ar, to desorb ammonia, with fragments detected via mass spectrometry.

In situ H_2 Diffuse Reflectance IR Fourier Transform Spectroscopy

The experiment was carried out in the Reactor Engineering and Catalyst Testing (REACT) core facility at Northwestern University. MOF sample was diluted and ground with spectroscopic grade KBr (3-10 wt% MOF) and sealed into the *in situ* praying mantis cell of a Thermo-iS50 infrared spectrometer. The sample was pretreated and monitored under argon flow (60 sccm) at

473 K for a minimum of 2 hours or until no further changes were observed in the spectra. The final spectrum of the material under argon at 473 K was used as the background for difference spectra under H_2 exposure of each respective sample. The catalyst was then exposed to 10% H_2 blend Ar at 473 K, and difference spectra were recorded until there was no noticeable change from spectrum to spectrum. H_2 atmosphere was then exchanged with argon to observe reversibility/stability of changes due to initial H_2 exposure.

In the case of D-MOF-808, sample pretreatment involved an additional pretreatment under argon at 323 K for ~16 hours after initial pretreatment at 473 K. The sample was then cooled back down to 473 K before the collection of background and difference spectra.

Pyridine DRIFTS and Catalytic Studies

NU-1000 was dehydrated overnight on a Micromeritics ASAP 2420, followed by transfer to a dry, 25 mL Schlenk flask which was immediately placed under vacuum. The flask was then placed into an oil bath kept at 433 K. Approximately 6 μL of pyridine (4 eq) were added to 40 mg of dehydrated NU-1000 under static vacuum. The sample was allowed to sit at 160 for 2 hours. Sample was then removed from the Schlenk line and prepared for collection of IR spectra.

~ 20mg of pyridine-treated sample was then loaded neat into the *in situ* praying mantis cell of a Thermo-iS50 infrared spectrometer, and spectral data were collected at room temperature under argon, using a background from neat KBr. We also measured a sample of untreated, dehydrated NU-1000, from the same batch used to make the pyridine-treated sample, for comparison. Sample was then heated to 473 K before exposure to 3% H_2 bal. argon overnight. Sample was allowed to cool back down to room temperature before subsequent spectroscopic measurement.

The remainder of the pyridine treated sample and untreated D-NU-1000 were allotted for catalytic studies, which were conducted according to procedures described *vide infra.*

Catalytic Testing

Reactivity studies were conducted by similar procedures previously reported using a packed bed reactor in the REACT core facility at Northwestern University. Catalytic experiments were done similarly to those previously reported. Briefly, 30-40 mg of catalyst was diluted in 1g of quartz sand (trace metals grade) and packed in a quartz tube with a bed height of approximately 1 inch. Sample was then pretreated with UHP H_2 at 473 K for 2 hours with a flow rate of 25 sccm. Pressure in the reactor was controlled to be ~10 psig using a back-pressure regulator directly downstream from the reactor.

After pretreatment in UHP H_2 for 2 hours at 473 K, 2% 1-butene diluted in Ar and UHP H_2 were flowed over the catalyst. Products were analyzed via Gas Chromatography-Flame Ionization Detection (GC-FID) and separated using a GS-Gaspro column (Agilent, 30 m length, 0.32 mm diameter). C4 gas phase species *n*-butane, 1-butene, *trans*-2-butene, and *cis*-2-butene were identified using calibration standards, *vide supra*. Isobutane and isobutene identities were inferred from retention times of identified species and reference chromatograms for the gs-Gaspro and separate gas chromatography mass spectrometry.

The 2% 1-butene in Ar tank had small quantities of C4 impurities; isobutane, *n*-butane, and isobutene made up approximately 0.3%, 0.4%, and 0.04% of the total hydrocarbon content, respectively. Because *n*-butane is the hydrogenation reaction product, the isobutane area in each injection was used as a reference for the *n*-butane area resulting from impurities. The average n/iso ratio for each injection at zero conversion was 1.3, so to find the area of *n*-butane produced in each injection, the isobutane area was multiplied by 1.3 and then subtracted from the total *n*-butane area.

When calculating conversion, X, the following equation was used:

$$X = \frac{A_{\text{butane}} + A_{trans} + A_{cis}}{A_{\text{butane}} + A_{trans} + A_{cis} + A_{\text{1-butene}}} \quad (4.6.1.1.)$$

where A is the area for each subscripted product, the butane area being the area of only the butane produced, as previously mentioned. Selectivity for each product was calculated by dividing the area of each product respectively by the area sum of all the products.

The turnover frequency (TOF) for 1-butene conversion was calculated by multiplying the molar flow rate (2×10^{-5} mol/min) by the conversion under each reaction condition and then normalizing to the moles of NU-1000 (mol 1-butene/mol node of NU-1000). For H_2 co-feeding experiments, the average rate was calculated using time points after the first 30 min at reaction conditions, to allow the system to reach stable conversion.

4.6.2. Sample Characterization

PXRD

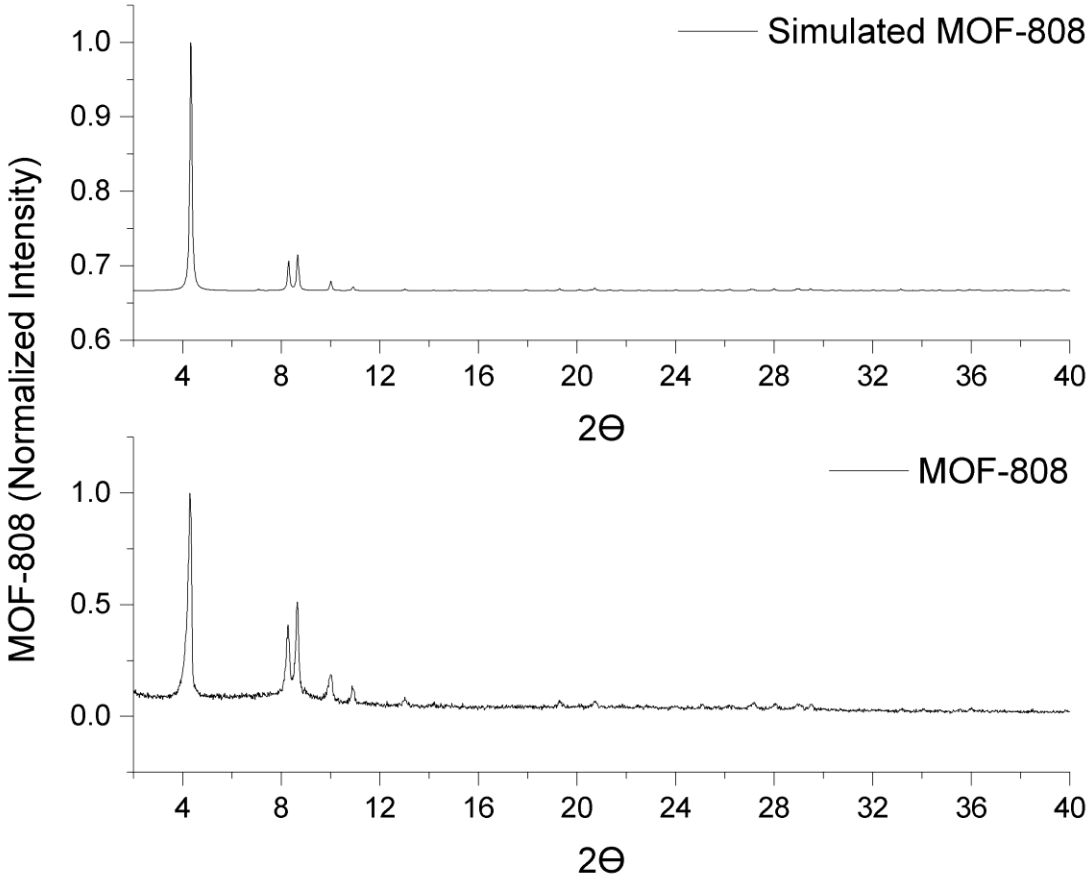

Figure 4.6.2.1. Powder X-ray diffraction pattern of MOF-808. (TOP) Simulated pattern from crystal structure. (Bottom) measured diffraction pattern from sample synthesized.

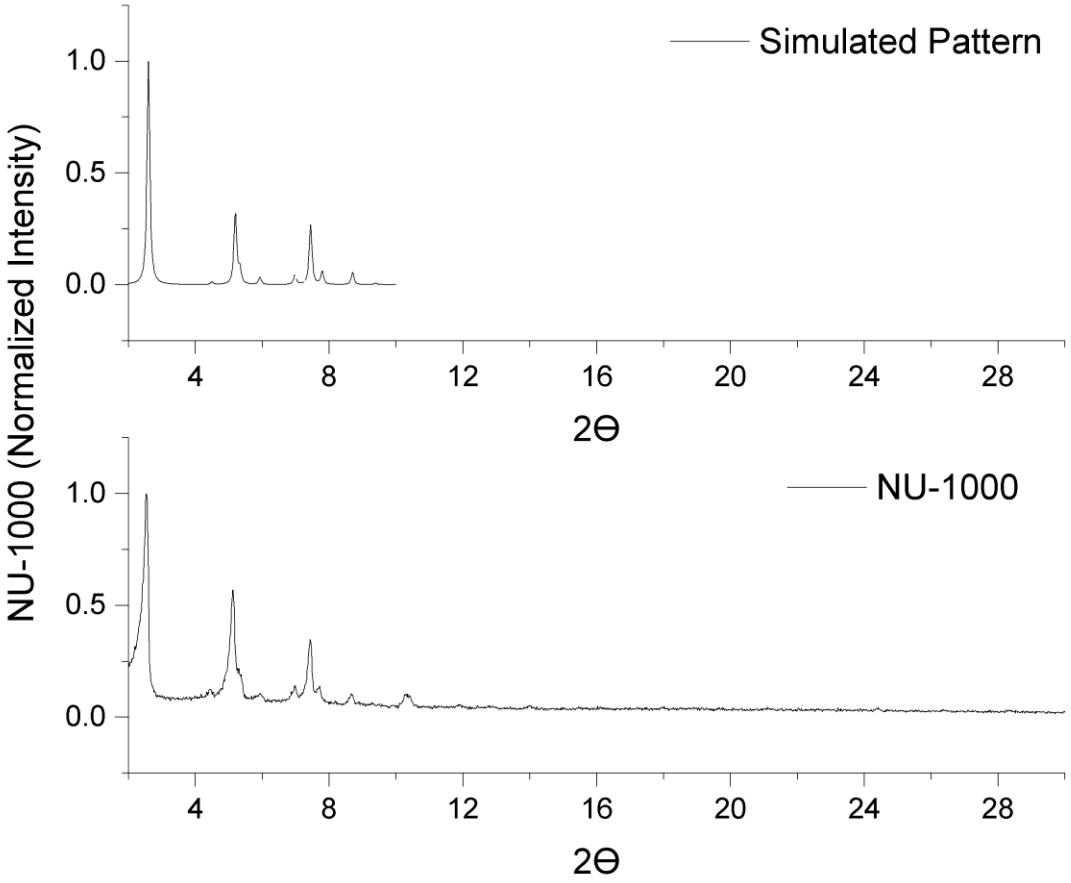

Figure 4.6.2.2. Powder X-ray diffraction pattern of NU-1000. (TOP) Simulated pattern from crystal structure. (Bottom) measured diffraction pattern from sample synthesized.

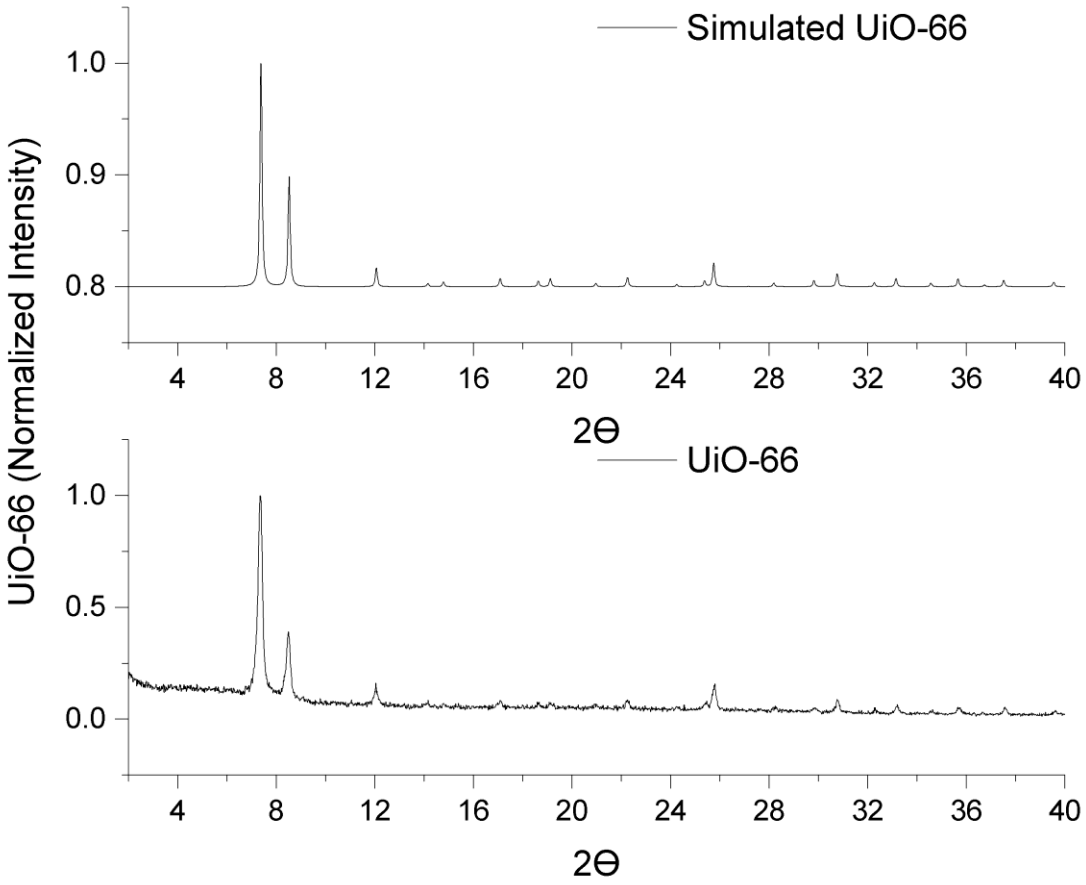

Figure 4.6.2.3. Powder X-ray diffraction pattern of UiO-66. (TOP) Simulated pattern from crystal structure. (Bottom) measured diffraction pattern from sample synthesized.

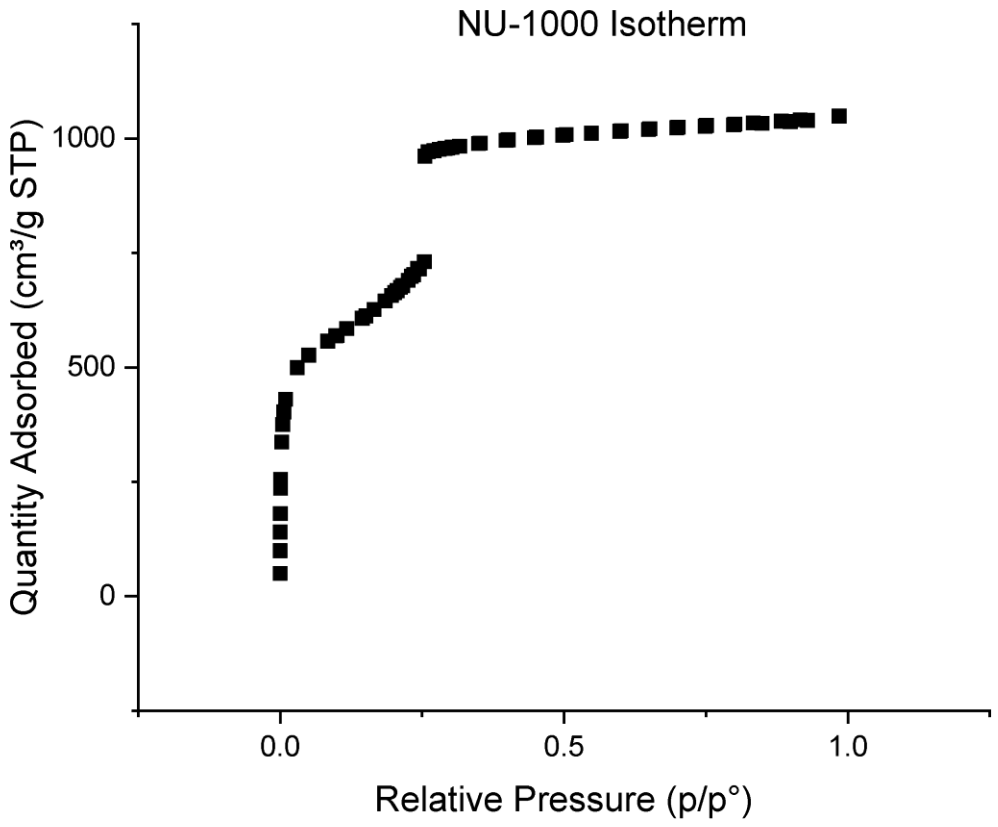

Figure 4.6.2.4. N_2 adsorption isotherm of NU-1000 at 77 K. BET calculated surface area = 2135 m^2/g

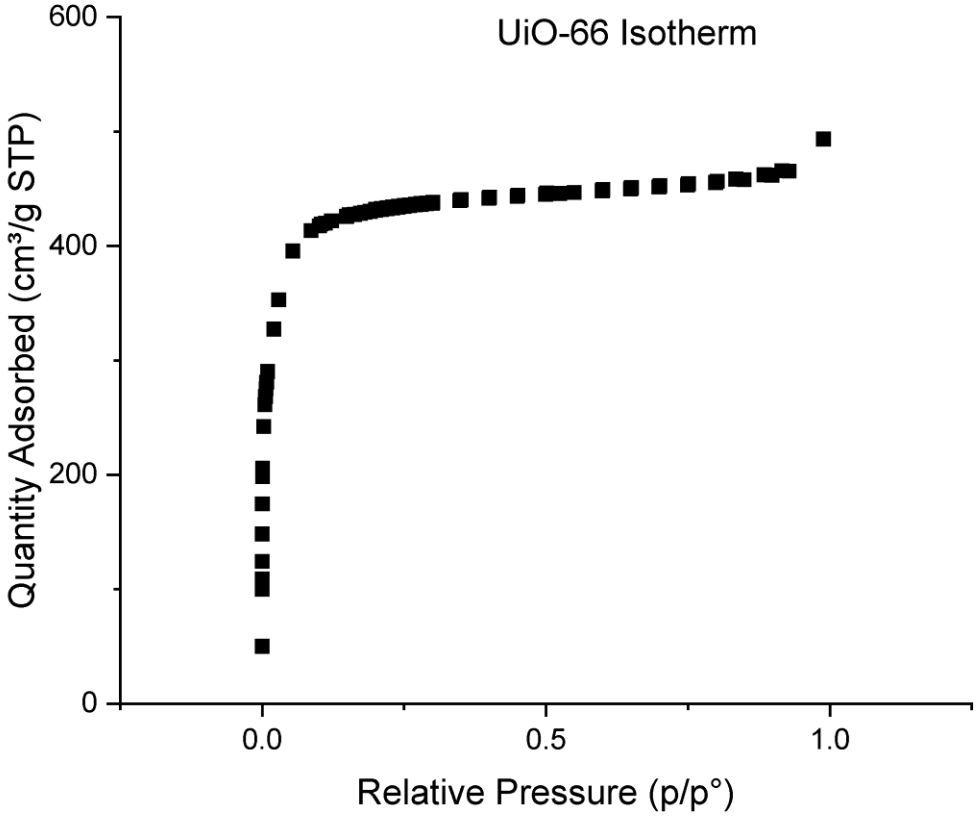

Figure 4.6.2.5. N_2 adsorption isotherm of UiO-66 at 77 K. BET calculated surface area = 1700 m^2/g

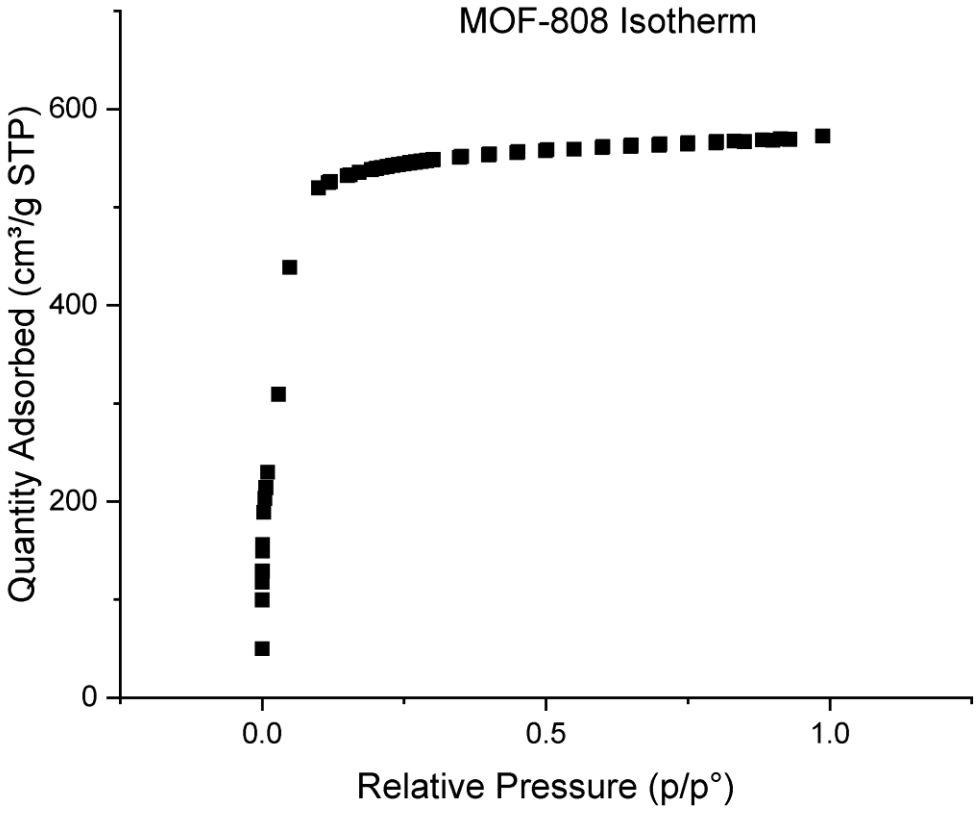

Figure 4.6.2.6. N_2 adsorption isotherm of MOF-808 at 77 K. BET calculated surface area = 2000 m^2/g

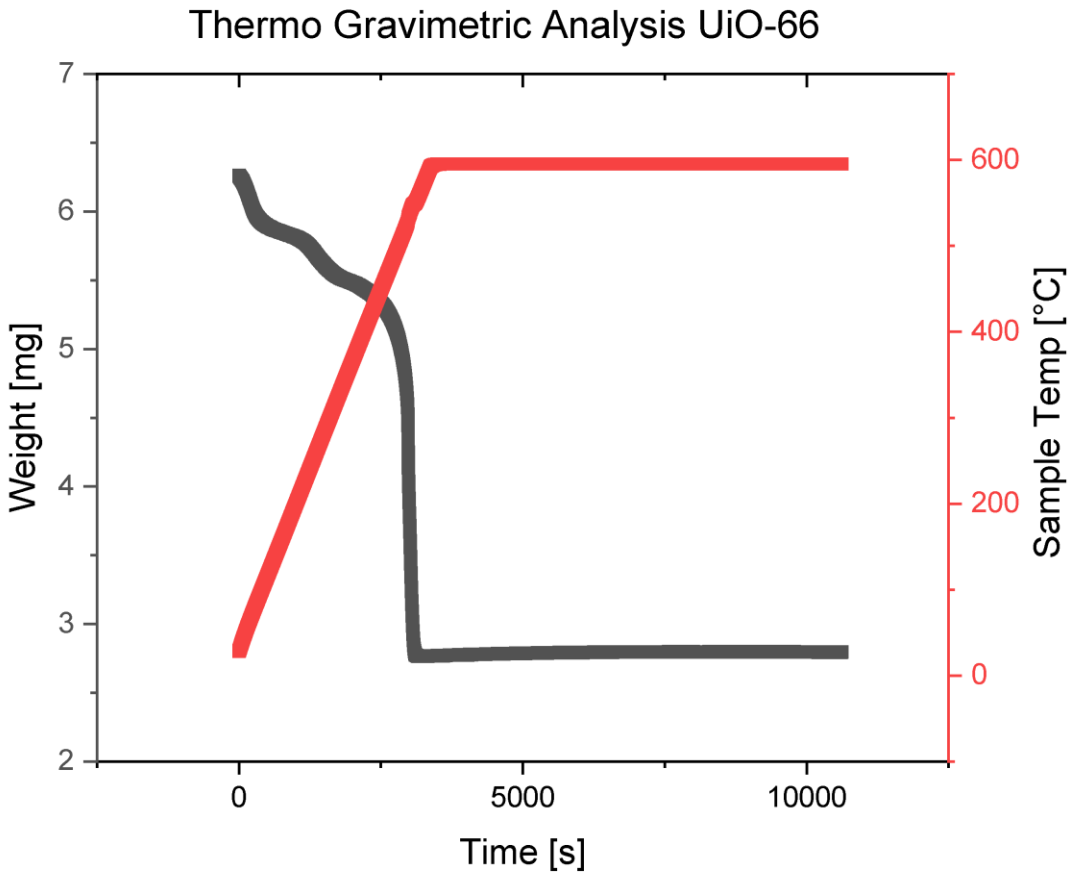

		mass%	MW	mg*mol/g	linker/node
linker	2.685	0.492661	164.116	0.01636	3.995932
node	2.765	0.507339	675.336	0.004094	

Figure 4.6.2.7. Thermogravimetric analysis under 20% O_2 of UiO-66 and corresponding calculations. (Black) Sample mass curve. (Red) Sample temperature. Ramped at 10°C/min. Shows loss of mass due to moisture followed by the burning of linkers starting at ~400 °C. Mass at plateau corresponds to the remaining mass at 600 C, assumed to be solely ZrO_2. Mass of organic vs. inorganic materials were converted to moles using molecular weights of linker and node to get approximate linker/node ratio.

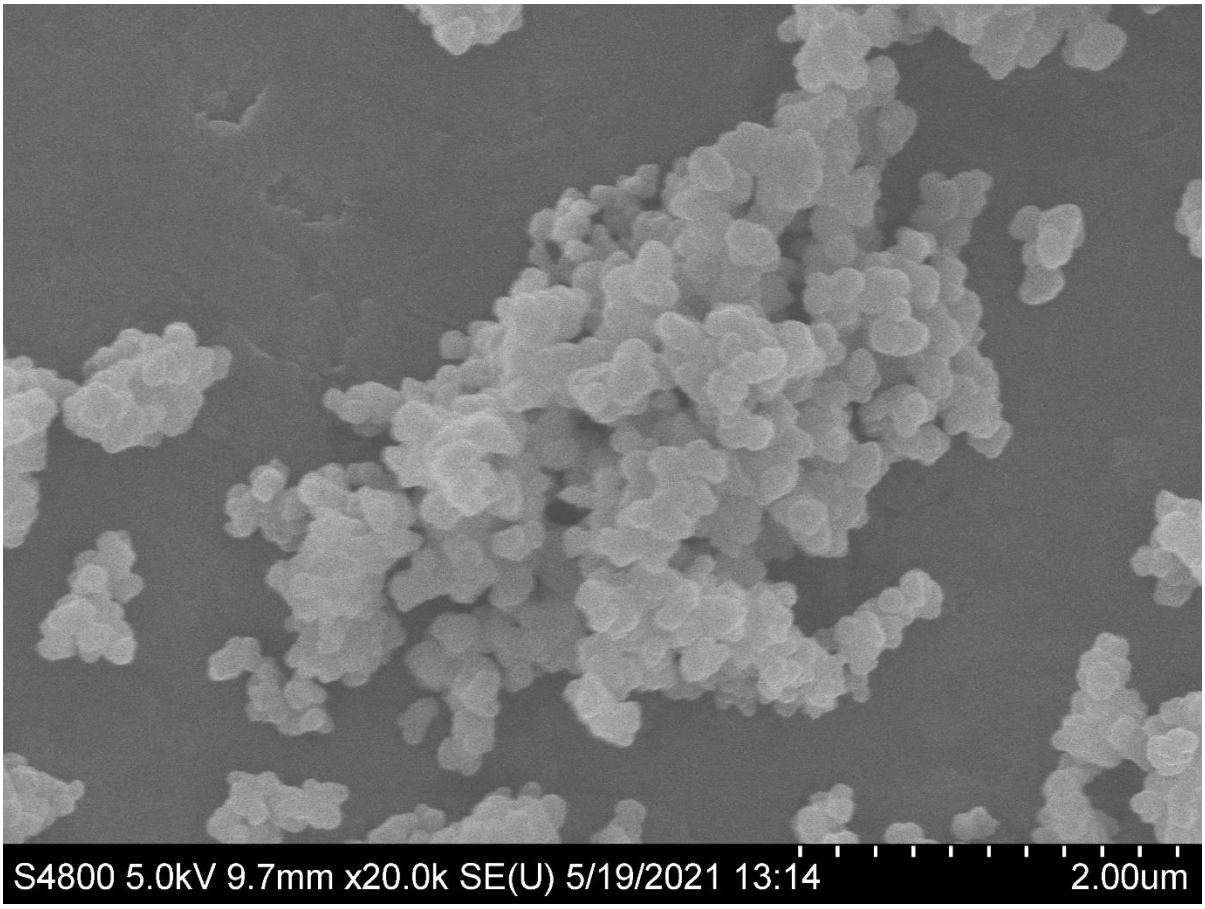

Figure 4.6.2.8. Scanning Electron Microscopy (SEM) image of UiO-66

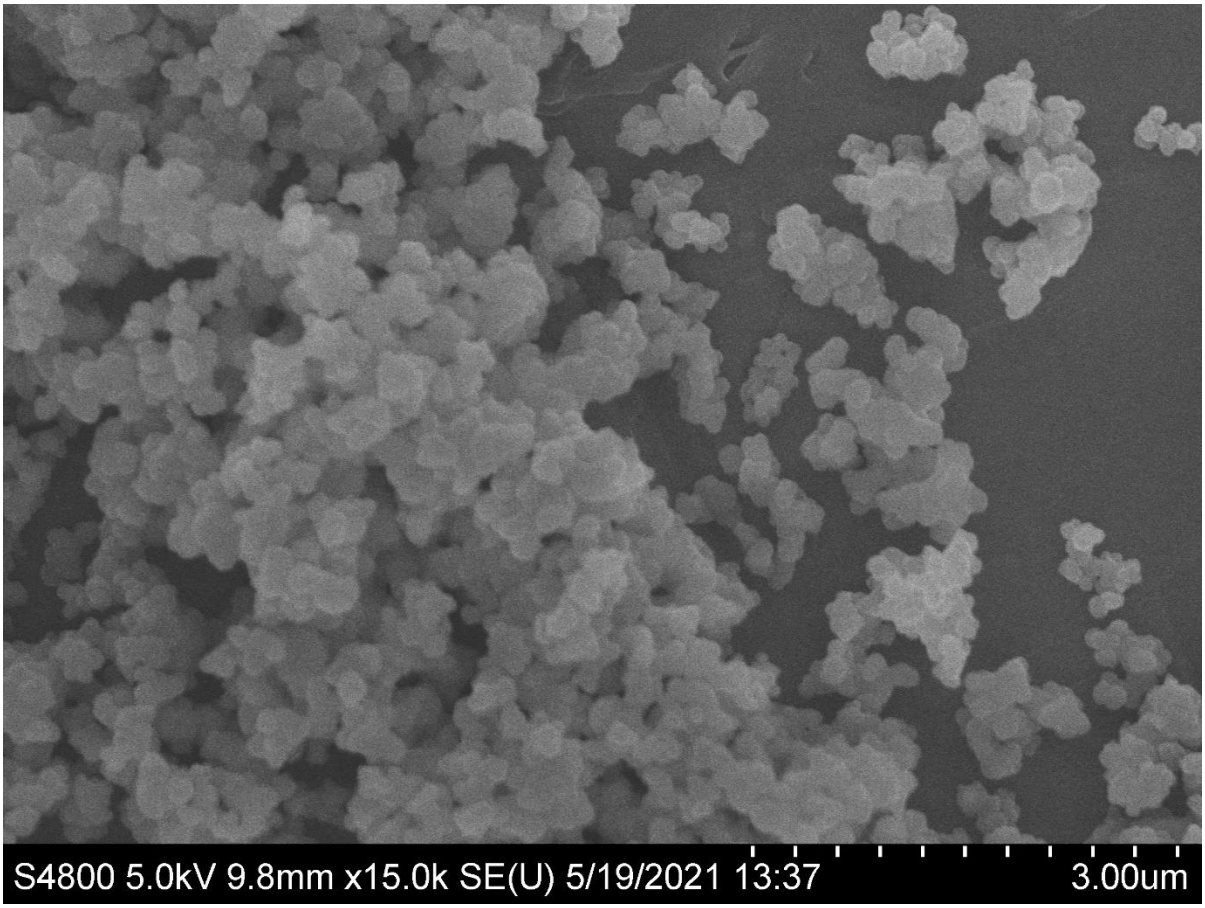

Figure 4.6.2.9. Scanning Electron Microscopy (SEM) image of UiO-66

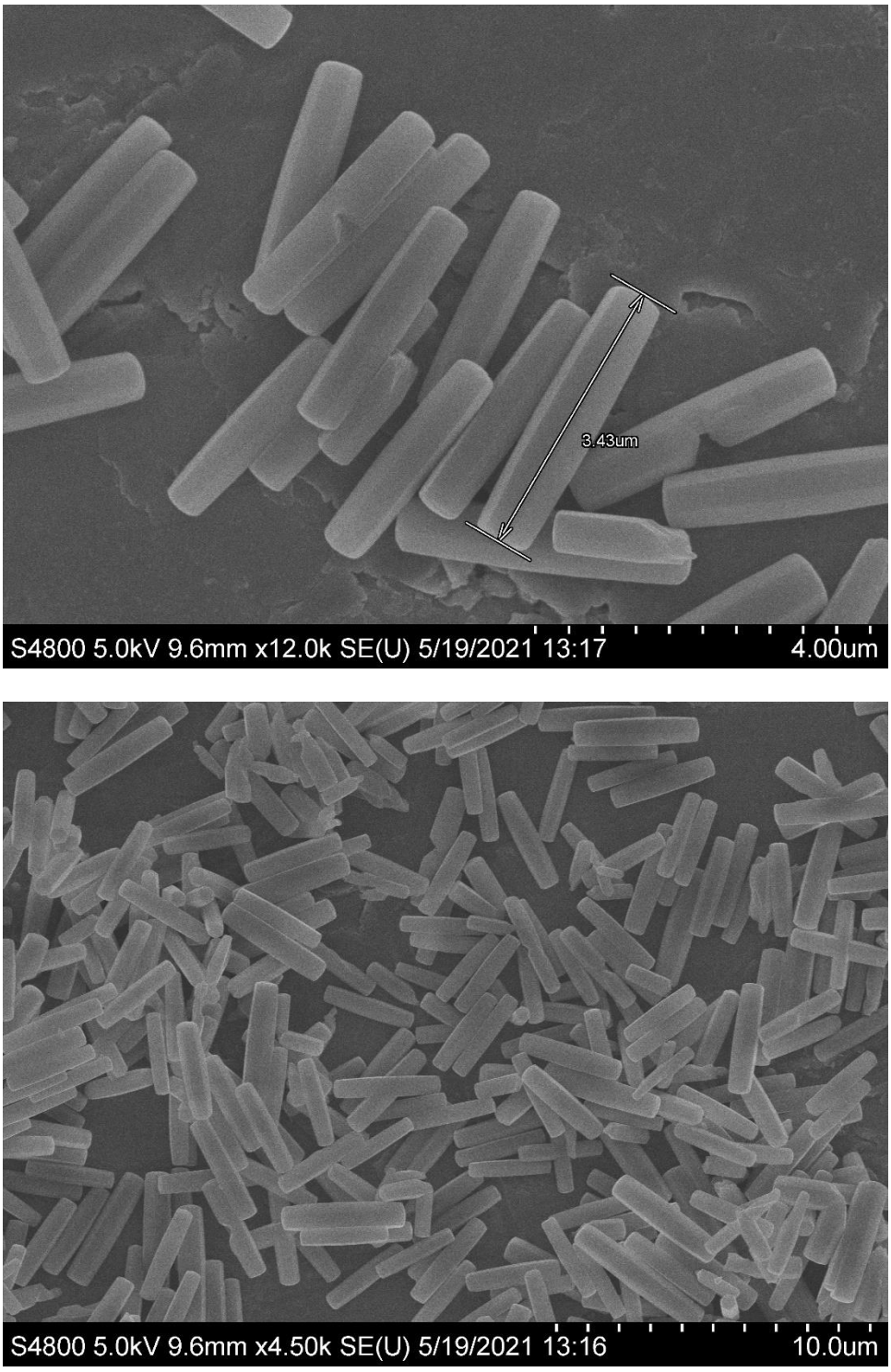

Figure 4.6.2.10. Scanning Electron Microscopy (SEM) images of NU-1000

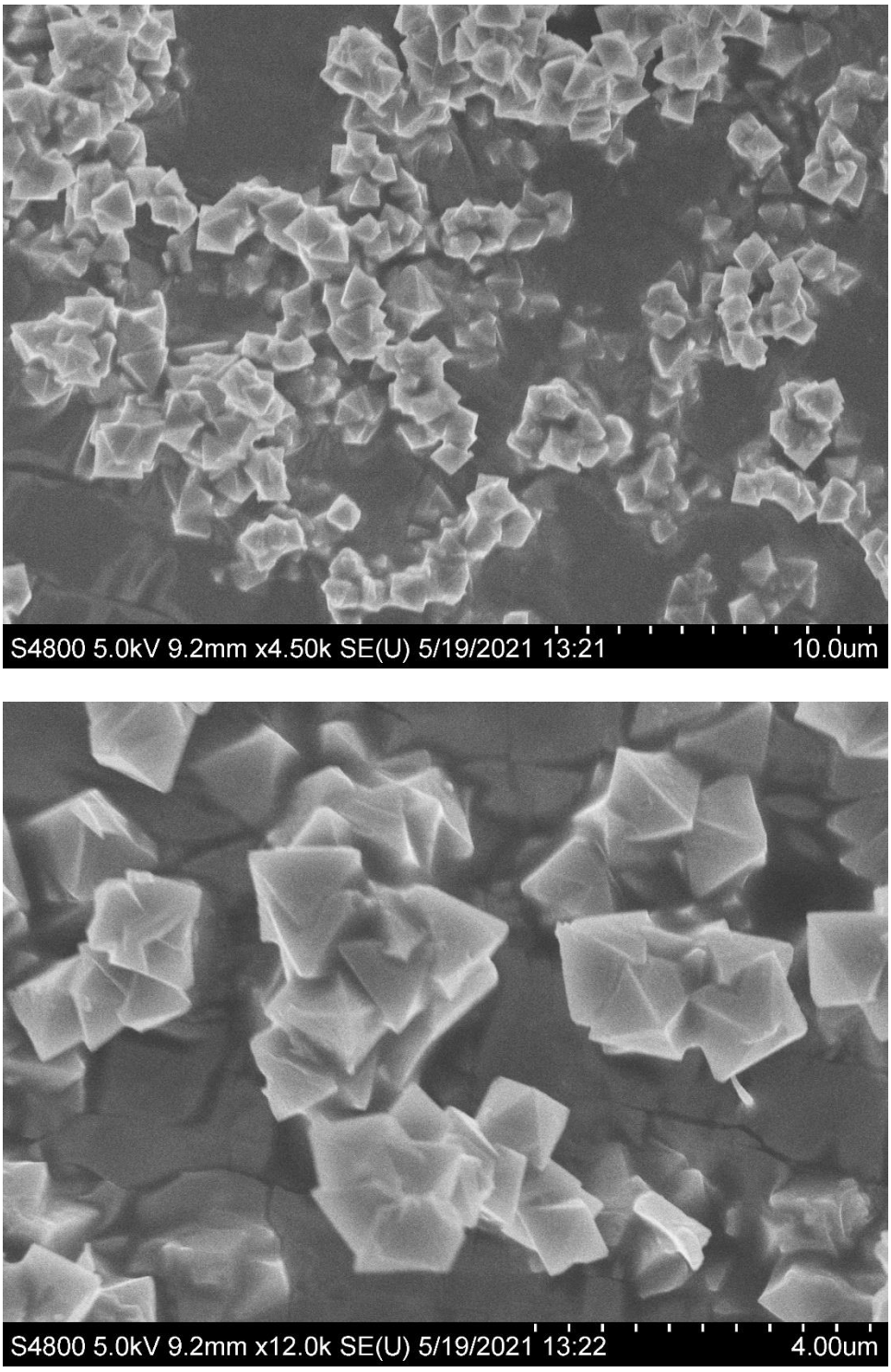

Figure 4.6.2.11. Scanning Electron Microscopy (SEM) images of NU-1000

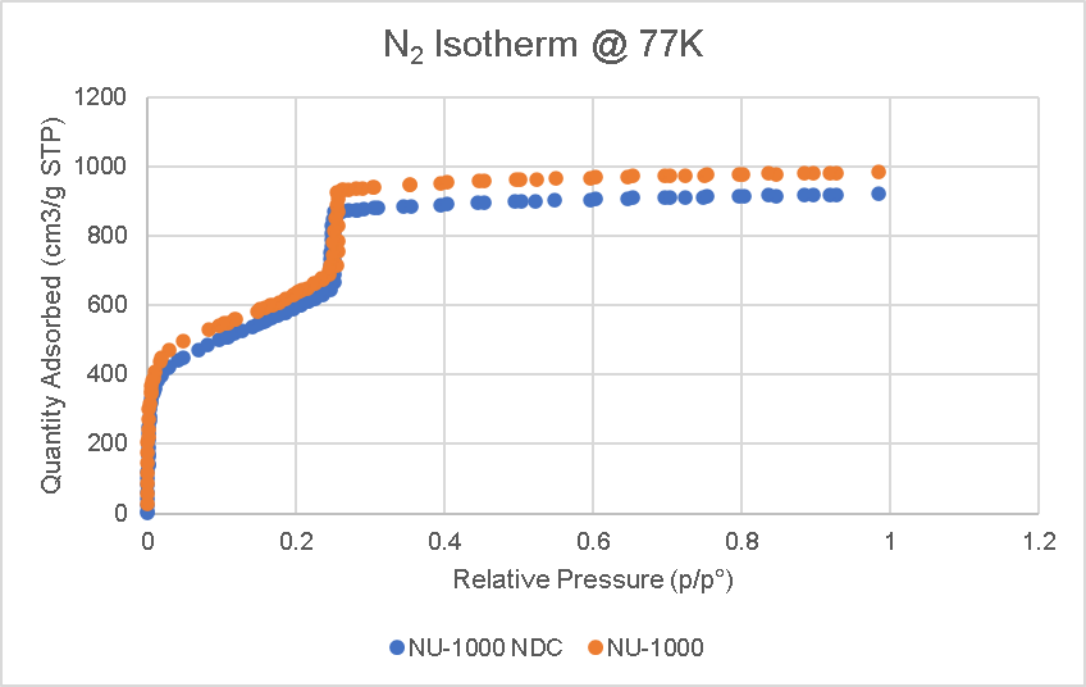

Figure 4.6.2.12. N_2 adsorption isotherm of NU-1000-NDC (Blue), with NU-1000 as comparison (Orange), at 77 K. BET calculated surface area = 1900 m^2/g

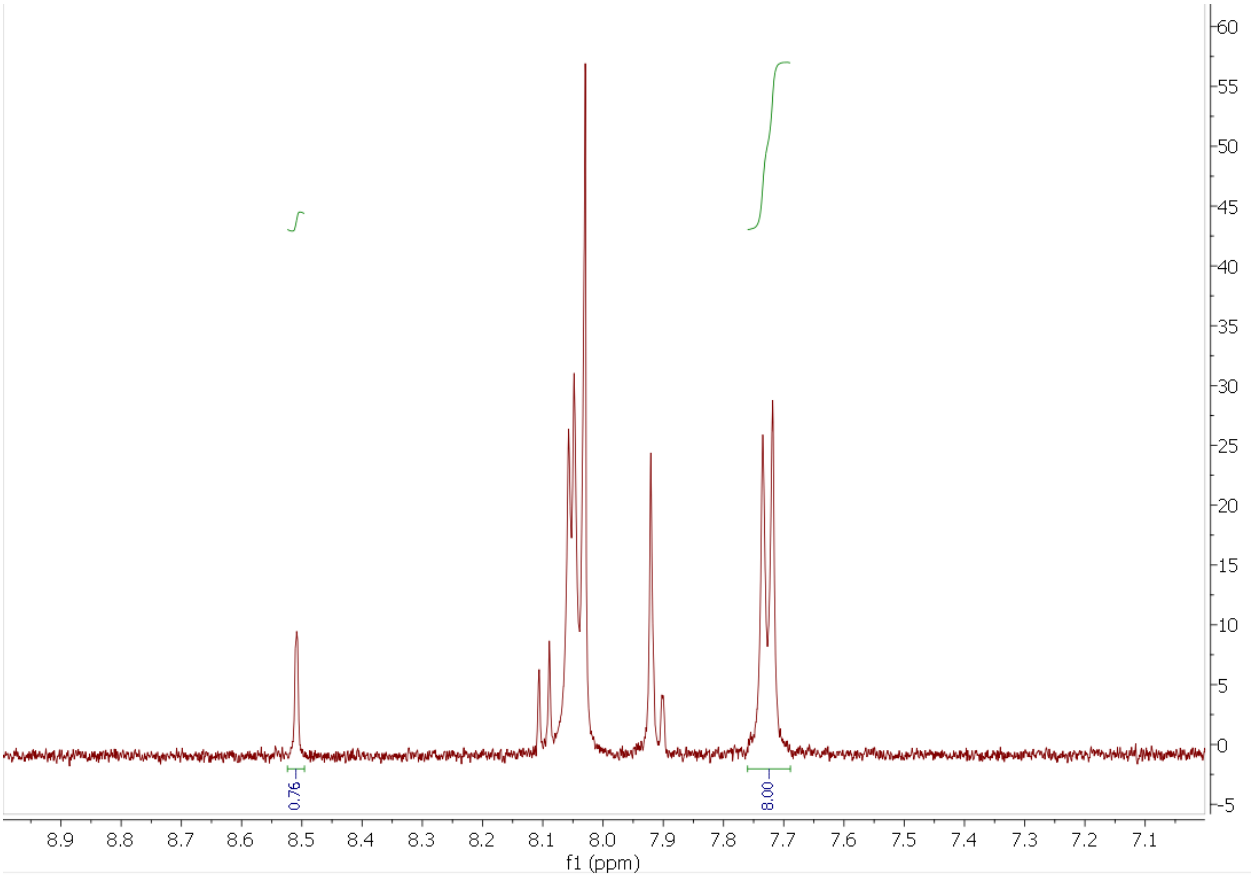

Figure 4.6.2.13. NMR of NU-1000-NDC digested in D_2SO_4 and diluted in DMSO-d6. Peak at ~8.5 ppm represents carboxylic acid protons of naphthalene dicarboxylic acid. Integration of protons suggests ~0.8 NDC linkers per Zr_6O_8 node. This calculation was done using the stoichiometry of NU-1000 (2 TBAPy linkers/Zr_6O_8 node), where all peaks were normalized to the 8 benzyl, ortho protons of TBAPy (~7.7 ppm). This calculation yields 0.38 NDC linker per TBAPy and therefore, 0.76 NDC per node.

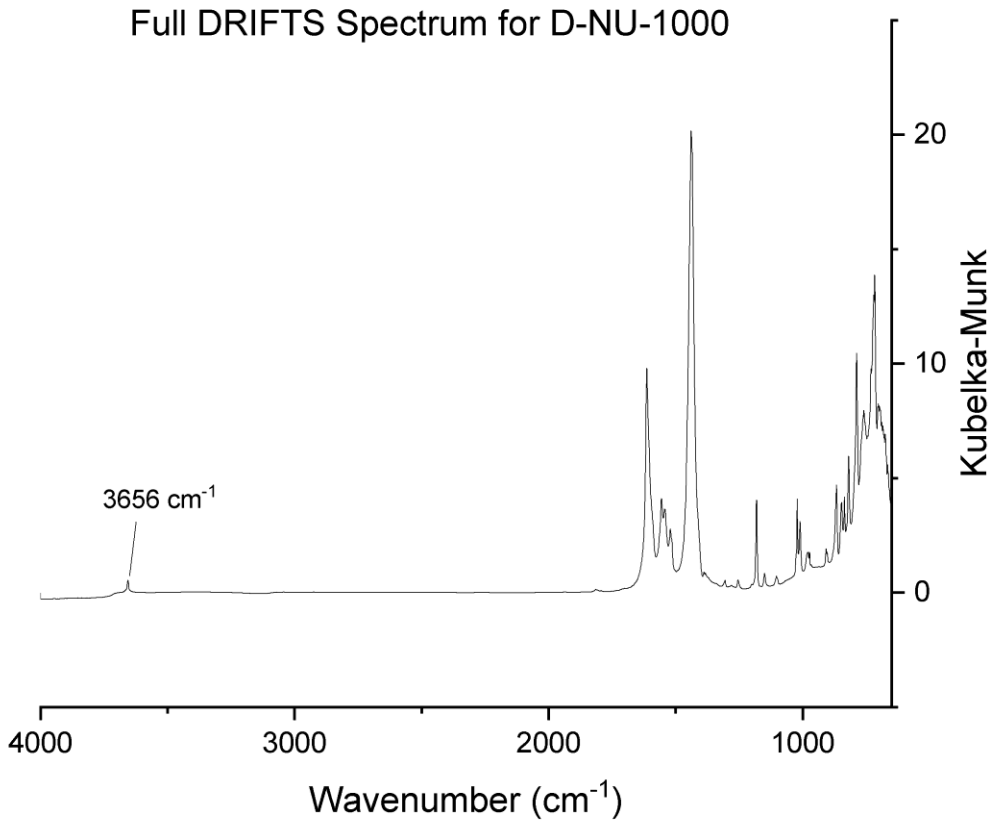

Figure 4.6.2.14. Full DRIFTS Spectrum for D-NU-1000 used for pyridine adsorption experiments. Spectrum was recorded with sample neat using a KBr background. Peaks in the region of ~1600-1400 cm^{-1} are as shown in Figure 3C of the main text. Briefly, a small Zr-OH stretch can be observed at 3656 cm^{-1}. Aromatic linker stretches can be observed at 1613 cm^{-1} and 1438 cm^{-1}.

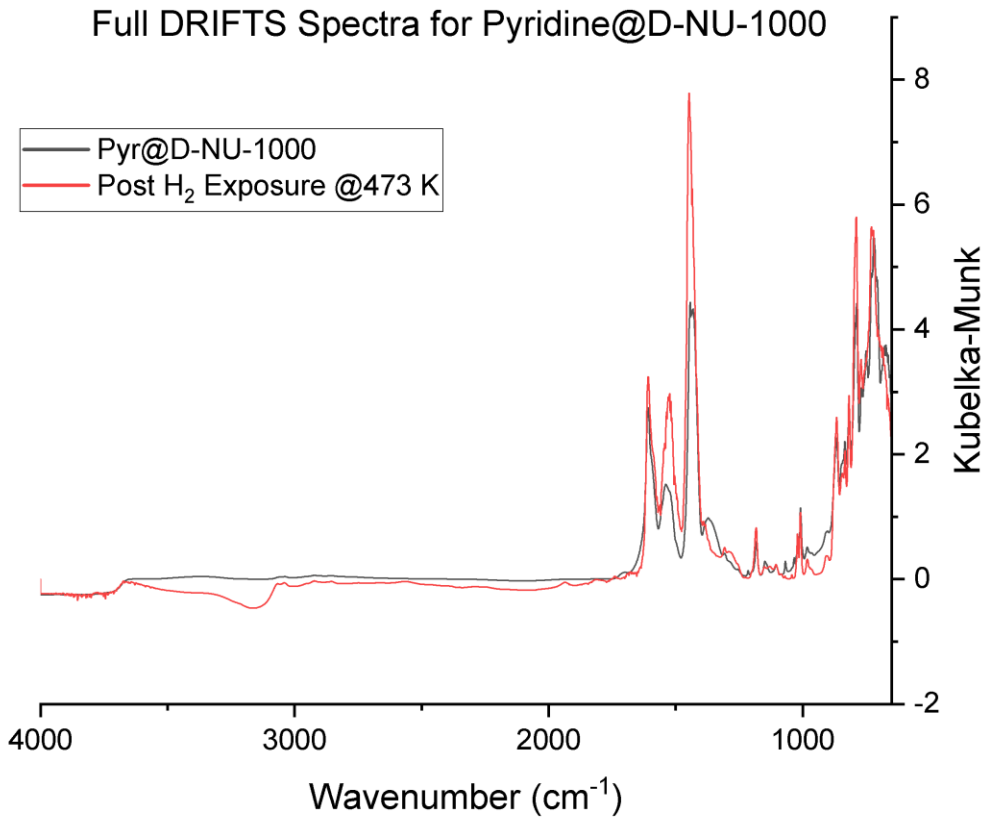

Figure 4.6.2.15. Full DRIFTS Spectra for Pyridine@D-NU-1000 (black) neat and (red) after exposure to 3% H_2 overnight at 473 K. Spectra were recorded at RT using a KBr background. Peak at 3656 is gone after pyridine adsorption when compared to the full spectrum of D-NU-1000. Details of spectral differences are discussed and highlighted in Figure 3 of the main text. Briefly, H_2 exposure at 473 K results in growth stretches in the region of pyridine adsorption at Brønsted sites (1550-1540 cm^{-1}) and Lewis acid sites ~1440 cm^{-1}. Additionally, a broad feature at 1370 cm^{-1} disappears upon H_2 exposure. Results are consistent with the migration of weakly adsorbed pyridine to Brønsted and Lewis acid sites under thermal conditions and H_2 exposure.

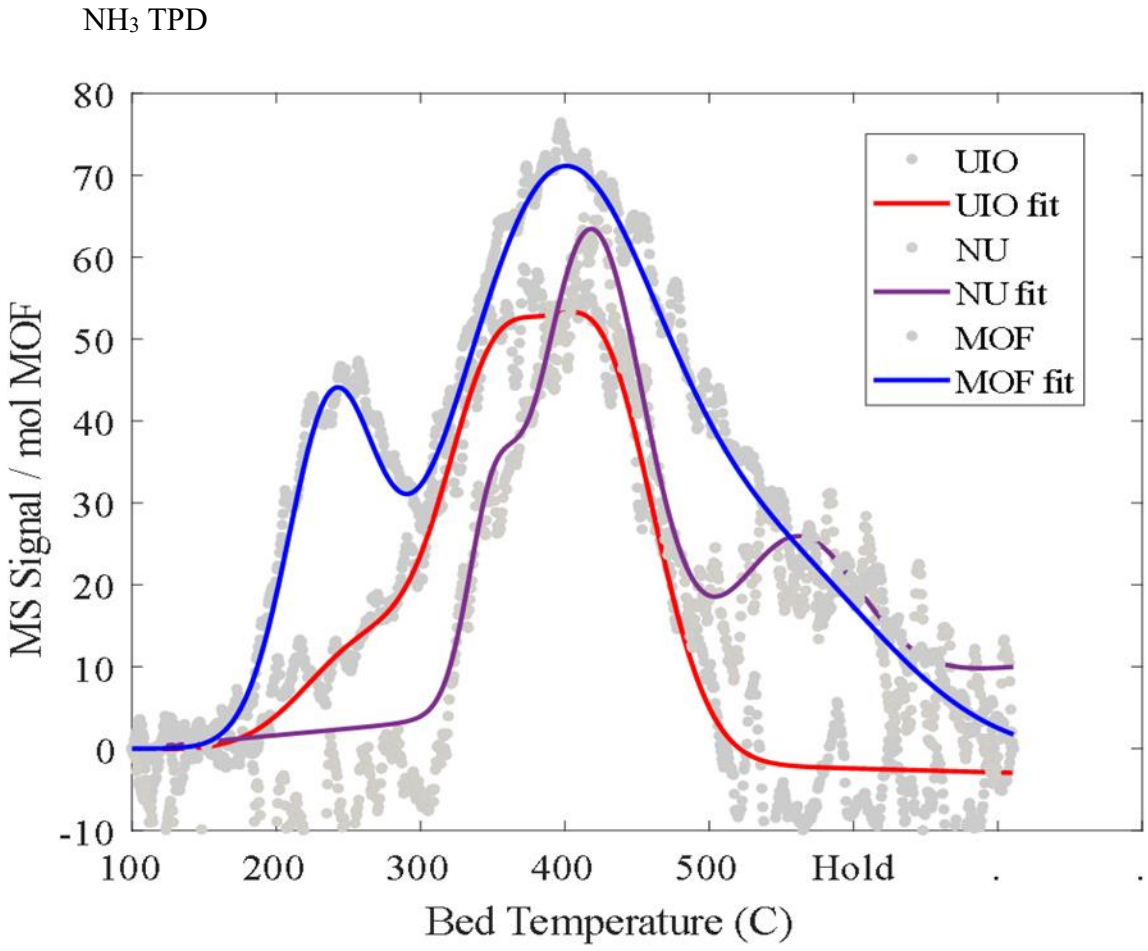

	Amounts(mol_{NH3}/mol_{node})				
Peak Positions	230-270 C	340-400 C	400-425 C	540-560 C	Total
MOF-808	2.10×10^{-2}	8.54×10^{-2}	N/A	3.24×10^{-2}	0.14
NU-1000	N/A	4.65×10^{-3}	3.25×10^{-2}	1.19×10^{-2}	0.049
UiO-66	7.16×10^{-3}	1.75×10^{-2}	2.28×10^{-2}	N/A	0.047

Figure 4.6.2.16. Ammonia TPD result for MOF-808, NU-1000, and UiO-66. NH_3 adsorption was done at 100°C after a pretreatment in UHP H_2 at 200°C for 2 hours. Ramp rate for both pretreatment and desorption steps was 10°C/min. Results show different relative amounts of NH_3 adsorbed in each sample. Quantitative results correlate well with expected results based on missing linker defects in each material. Additionally, samples show a range of adsorption sites, with different desorption temperatures across the series. Suggests differences in the kinds of adsorption sites in each material, not just quantity.

4.6.3. Supplementary Reaction Data

MOF	**TOF ($mol_{1\text{-}butene}/ks/mol_{node}$)**			**Selectivity**		
	Total	Hyd.	Isom.	butane	*trans*-butene	*cis*-butene
NU-1000	1.4 ± 0.4	0.7 ± 0.2	0.7 ± 0.2	51 %	28 %	21 %
MOF-808	0.3 ± 0.07	.02 ± 0.003	0.3 ± 0.07	7%	55%	38%
UiO-66	0.1 ± 0.01	0.02 ± 0.002	0.1 ± 0.001	13 %	51%	36%
D-NU-1000[a]	4.0 ± 0.9	0.4 ± 0.1	3.7 ± 0.8	10 %	54 %	36 %
***In situ* D-MOF-808 (523 K)**	0.4 ± 0.1	0.05 ± 0.01	0.4 ± 0.09	11%	53%	35%
D-UiO-66	1.2 ± 0.1	0.6 ± 0.1	0.6 ± 0.1	53%	28%	19%
D-MOF-808 (573 K, vac)[b]	0.02 ± 0.003 10^{-5}	0.004 ± 0.0003 x 10^{-6}	0.02 ± 0.002 x 10^{-5}	20%	46%	34%

Table 4.6.3.1. Comparison of apparent rates of 1-butene hydrogenation and isomerization in hydrated and dehydrated MOF-808, NU-1000 and UiO-66. All reactivity data comes from the same starting batch of Each MOF. TOFs for NU-1000 and D-NU-1000 are averaged from apparent rates at steady conversion across multiple catalytic experiments at 473 K, in triplicate or more. Error reflects the calculated standard error, $\frac{\sigma_{TOF}}{\sqrt{n}}$, where σ_{TOF} is the standard deviation and n is the total number of sample points, and where each sample point is the average apparent rate at steady state conversion in a given catalytic run.[a] Catalytic conversion exceeded 10% in some catalytic runs. [b]Sample activated under similar conditions to dehydrated NU-1000 and dehydrated UiO-66, under vacuum. Data show vacuum at 573 K is too harsh for MOF-808, with over an order of magnitude lower activity than the in situ dehydrated (523 K under H_2 flow) MOF-808. Value not averaged over several runs, but within a single run, although other runs showed similar loss in activity.

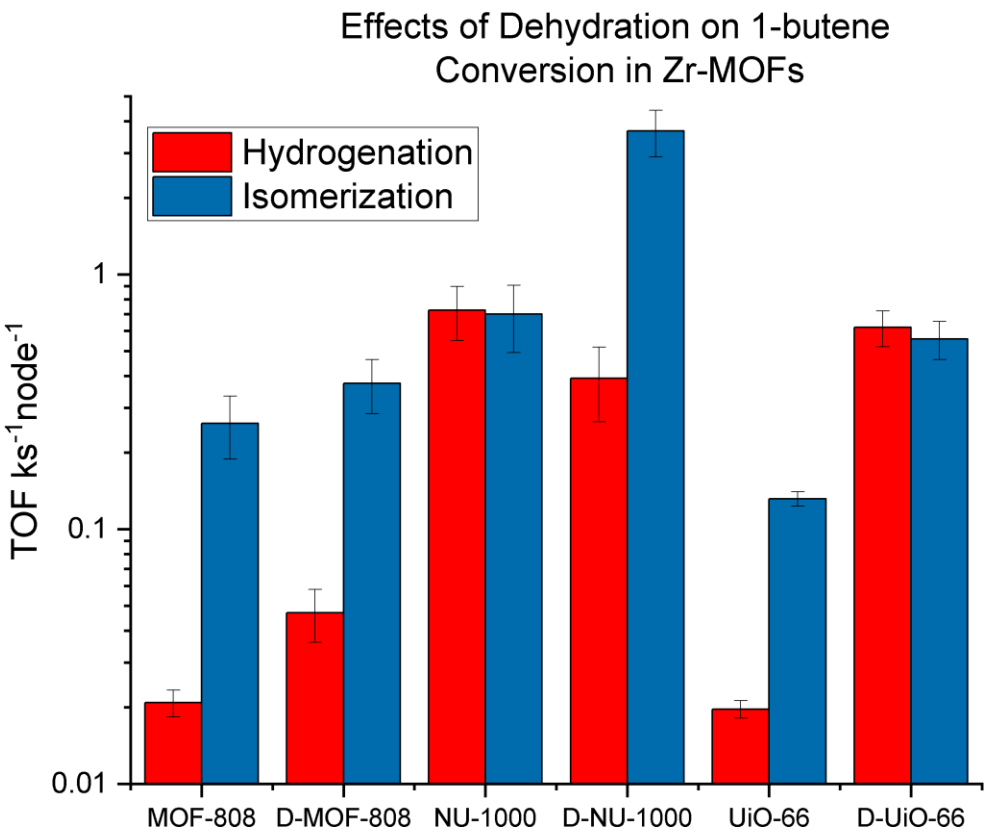

Figure 4.6.3.1. Graphical comparison of apparent rates for hydrogenation and isomerization of 1-butene in hydrated and dehydrated MOF-808, NU-1000 and UiO-66, as in table S1. All reactivity data comes from the same starting batch of Each MOF. TOFs for NU-1000 and D-NU-1000 are averaged from apparent rates at steady conversion across multiple catalytic experiments at 473 K, in triplicate or more. Error bars reflect the calculated standard error, $\frac{\sigma_{TOF}}{\sqrt{n}}$, where σ_{TOF} is the standard deviation and n is the total number of sample points, and where each sample point is the average apparent rate at steady state conversion in a given catalytic run. Data show that dehydration increases conversion across Zr-MOFs, although selectivity changes very depending on the starting MOF. Dehydrated MOFs are prepared as previously described, under heat and vacuum (NU-1000 & UiO-66) or heat and H_2 (MOF-808), while hydrated MOFs were loaded into the reactor after vacuum activation at 120 C, followed by a 2h pretreatment under H_2 at 200 C, as described in the methods section.

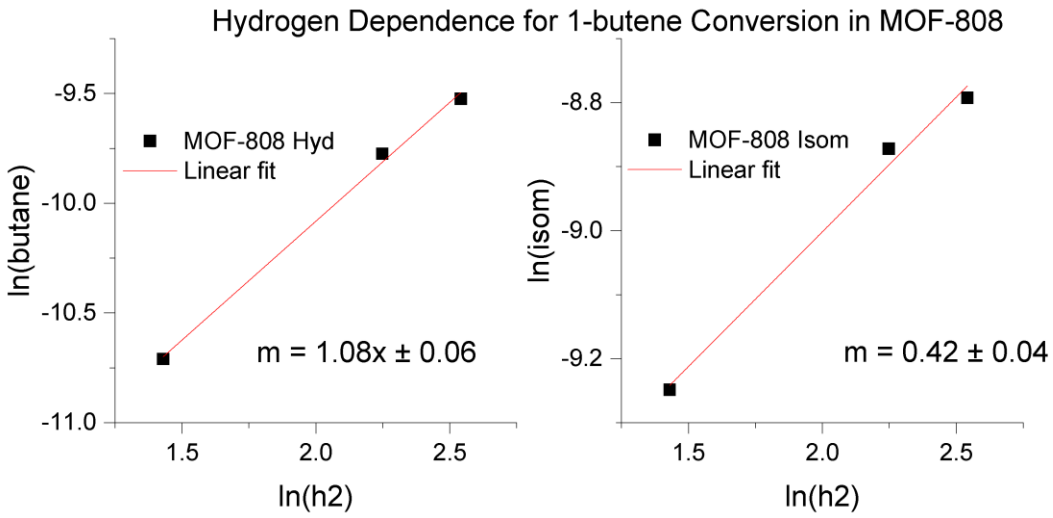

Figure 4.6.3.2. Dependence of 1-butene hydrogenation and isomerization on H_2 partial pressure in MOF-808 at 473 K. (Left) Log plot of apparent hydrogenation rate as a function of H_2 partial pressure. Slope of best fit line ≈1, suggesting a first order dependence, similar to observations for NU-1000.[214] (Right) Log plot of apparent isomerization rate as a function of H_2 partial pressure. Slope of best fit line ≈0.4, suggesting a half order dependence upon H_2 for isomerization, also similar to previous observation sin NU-1000.

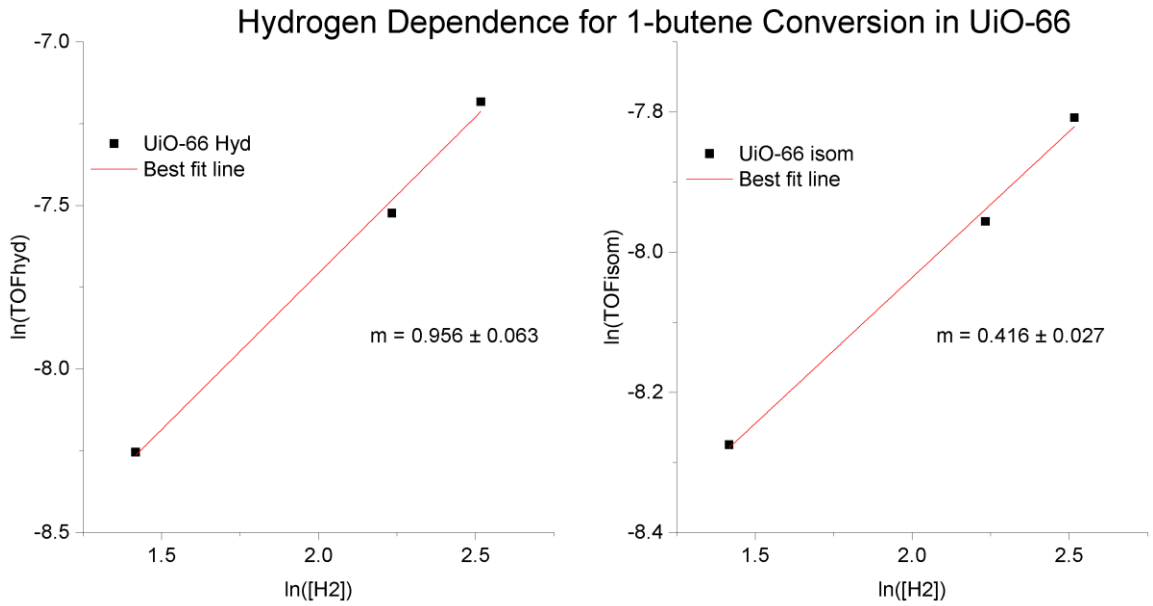

Figure 4.6.3.3. Dependence of 1-butene hydrogenation and isomerization on H_2 partial pressure in MOF-808 at 473 K. (Left) Log plot of apparent hydrogenation rate as a function of H_2 partial pressure. Slope of best fit line ≈1, suggesting a first order dependence, similar to observations for NU-1000.[214] (Right) Log plot of apparent isomerization rate as a function of H_2 partial pressure. Slope of best fit line ≈0.4, suggesting a half order dependence upon H_2 for isomerization, also similar to previous observation sin NU-1000.

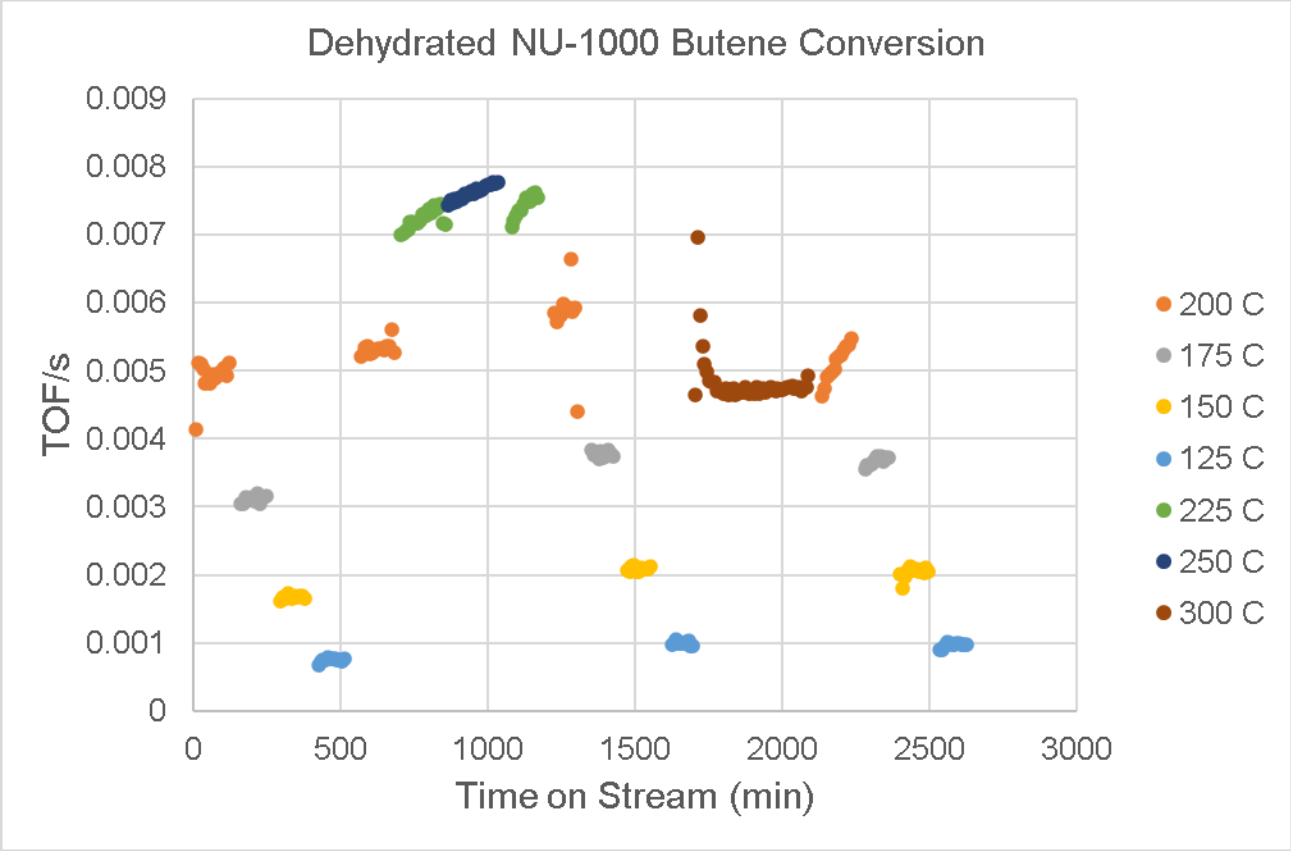

Figure 4.6.3.4. Example time-on-stream plot from a typical experiment. Shown, D-NU-1000 under 25 sccm UHP H_2 and 25 sccm 2% 1-butene balance argon with ~10 P.S.I.G. total pressure, at a variety of bed temperatures. Apparent steady state rates at temperatures from 200-125 C were used to calculate apparent activation energies for this sample. Each condition lasts approximately 2 hours with approximately 16 injections per condition. Injections included for the average apparent rate of each condition was determined by the overall stability of conversion from injection to injection.

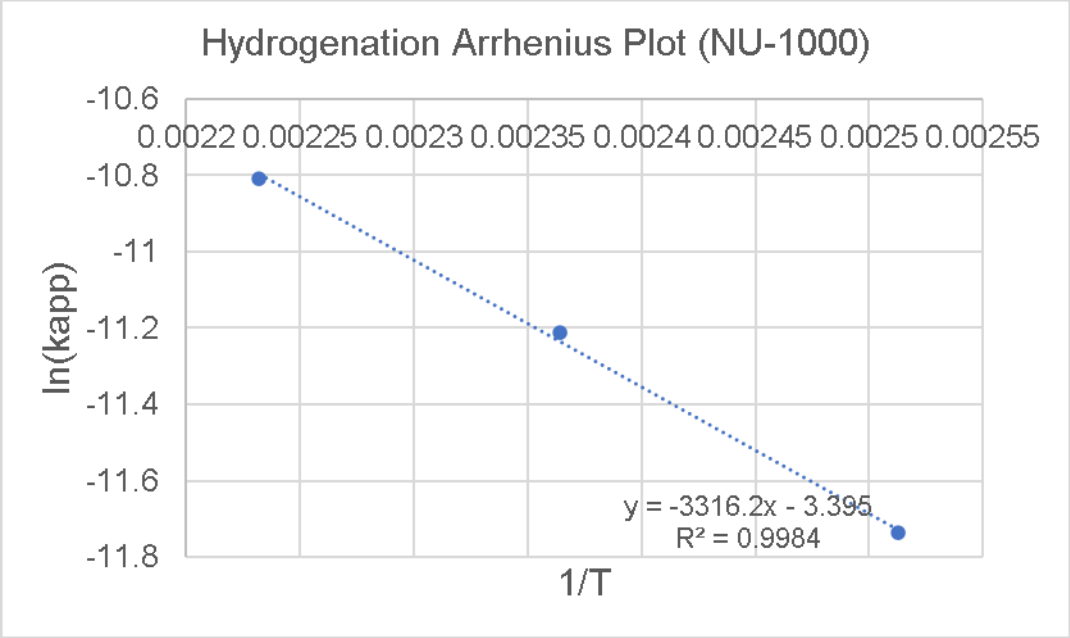

Figure 4.6.3.5. Arrhenius plot for 1-butene hydrogenation in NU-1000. 25 sccm UHP H_2 and 25 sccm 2% 1-butene balance argon with ~10 P.S.I.G. total pressure. Temperatures used, 125, 150 and 175 °C. ln(kapp) was calculated using the empirical rate law: rate=$k_{app}[H_2]^1[1\text{-butene}]^0$. Slope corresponds to an Ea_{app} of 28 kJ/mol.

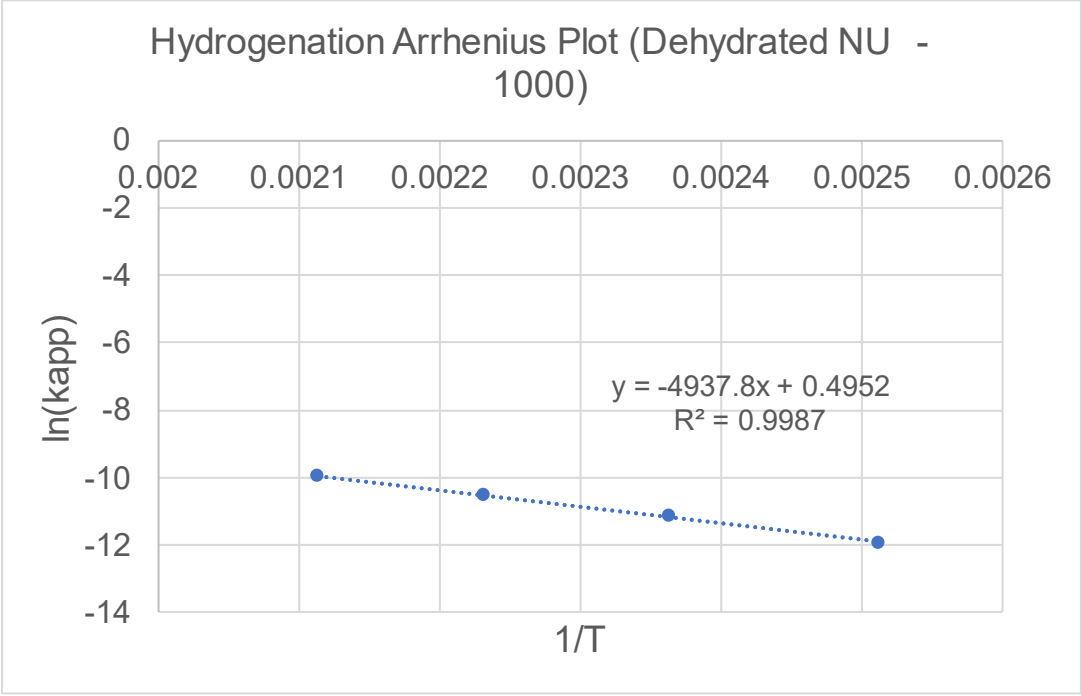

Figure 4.6.3.6. Arrhenius plot for 1-butene hydrogenation in D-NU-1000. 25 sccm UHP H_2 and 25 sccm 2% 1-butene balance argon with ~10 P.S.I.G. total pressure. Temperatures used, 125, 150, 175, and 200 °C. ln(kapp) was calculated using the empirical rate law: rate=$k_{app}[H_2]^1[1\text{-butene}]^0$. Slope corresponds to an Ea_{app} of 41 kJ/mol.

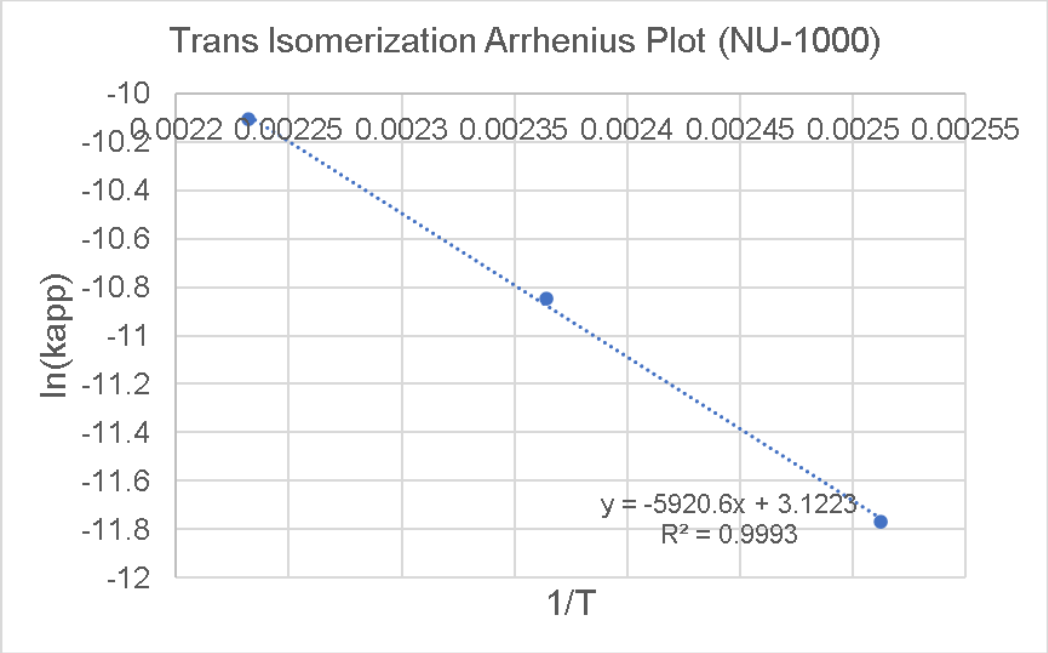

Figure 4.6.3.7. Arrhenius plot for 1-butene isomerization in NU-1000. 25 sccm UHP H_2 and 25 sccm 2% 1-butene balance argon with ~10 P.S.I.G. total pressure. Temperatures used, 125, 150 and 175 °C. ln(kapp) was calculated using the empirical rate law: rate=$k_{app}[H_2]^{0.5}$[1-butene]^0. Slope corresponds to an Ea_{app} of 49 kJ/mol.

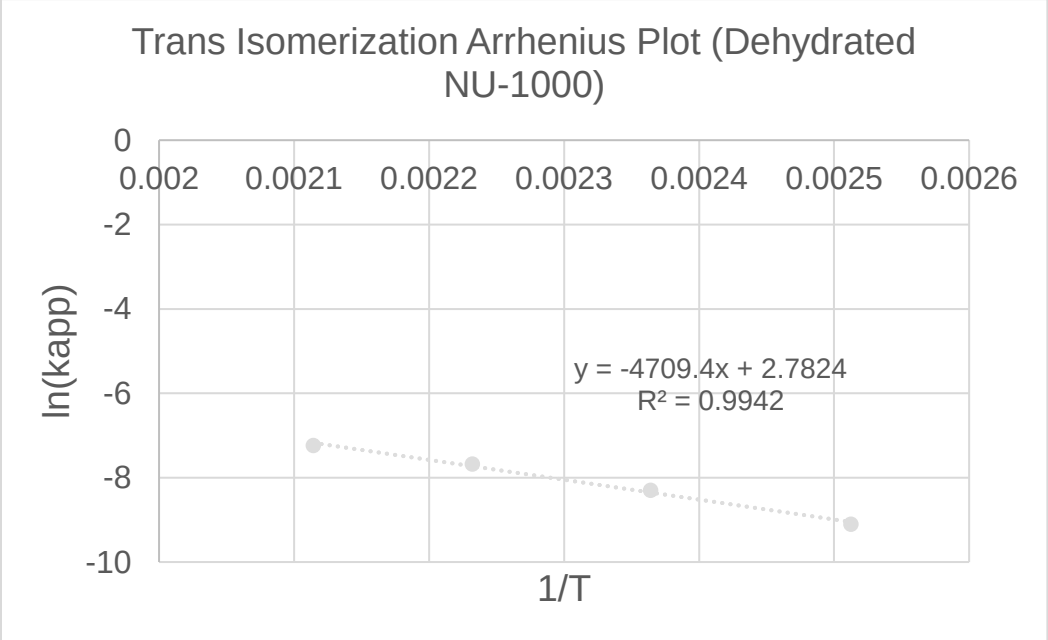

Figure 4.6.3.8. Arrhenius plot for 1-butene isomerization in D-NU-1000. 25 sccm UHP H_2 and 25 sccm 2% 1-butene balance argon with ~10 P.S.I.G. total pressure. Temperatures used, 125, 150, 175, and 200 °C. ln(kapp) was calculated using the empirical rate law: rate=$k_{app}[H_2]^{0.5}$[1-butene]^0. Slope corresponds to an Ea_{app} of 39 kJ/mol.

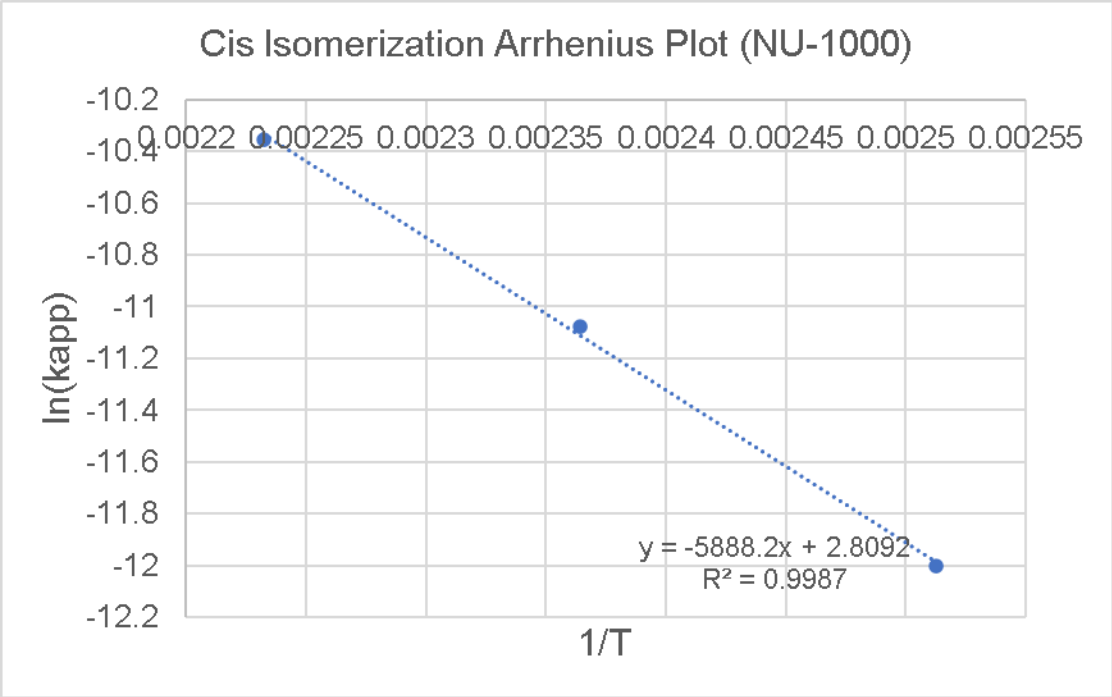

Figure 4.6.3.9. Arrhenius plot for 1-butene isomerization in NU-1000. 25 sccm UHP H_2 and 25 sccm 2% 1-butene balance argon with ~10 P.S.I.G. total pressure. Temperatures used, 125, 150 and 175 °C. ln(kapp) was calculated using the empirical rate law: rate=$k_{app}[H_2]^1[1\text{-butene}]^0$. Slope corresponds to an Ea_{app} of 49 kJ/mol.

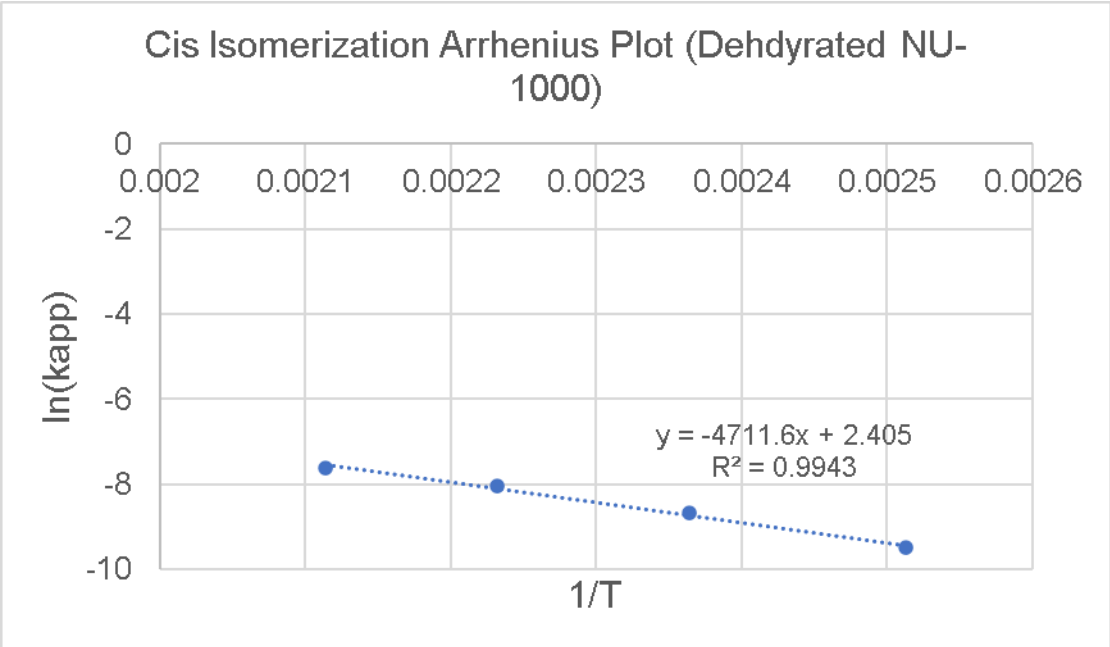

Figure 4.6.3.10. Arrhenius plot for 1-butene isomerization in D-NU-1000. 25 sccm UHP H_2 and 25 sccm 2% 1-butene balance argon with ~10 P.S.I.G. total pressure. Temperatures used, 125, 150, 175, and 200 °C. ln(kapp) was calculated using the empirical rate law: rate=$k_{app}[H_2]^{0.5}[1\text{-butene}]^0$. Slope corresponds to an Ea_{app} of 39 kJ/mol.

Discussion of reactivity in the as-synthesized/hydrated Zr-MOFs

Catalytic studies in the as-synthesized materials showed similar results to the dehydrated materials, as discussed in the main text, displaying rates of 1-butene hydrogenation and isomerization at 473 K that vary by up to an order of magnitude on a per-cluster basis across the materials: NU-1000: 1.4 x $10^{-3}s^{-1}$ > MOF-808: 2.8 x $10^{-4}s^{-1}$ ≥ UiO-66: 1.5 x $10^{-4}s^{-1}$ (**Table 4.4.3.1.**, **Figure 4.6.3.1**) with NU-1000 being the most active catalyst. Similar to with the dehydrated MOFs, these results are contrary to expectations from previous literature studies, which have shown that increasing defect concentration and lowering node connectivity leads to greater catalytic activity in Zr-MOFs.

Variation of H_2 and 1-butene partial pressures at 473 K yields similar results for MOF-808 and UiO-66 as reported for NU-1000, with approximate 1st-order H_2-dependence for hydrogenation and half-order H_2-dependence for 1-butene isomerization (**Figures 4.6.3.2.** and **4.6.3.3.**), with apparent zero-order 1-butene dependence observed for both reactions. These results suggest similar catalytic pathways in each material, where H_2 cleavage appears to generate one active species involved in olefin hydrogenation, a zirconium hydride, and two active species for isomerization, a hydride and proton each, as previously proposed from experimental and computational observations with NU-1000. Additional similarities are observed in terms of the effects of thermal dehydration. As discussed in sections **4.4.** and **4.5.**, thermal dehydration at 573 K, under vacuum, results in increased 1-butene conversion for both NU-1000 and UiO-66, consistent with previous reports regarding CWA degradation.[96] In the case of MOF-808 however, dehydration decreases activity of 1-butene conversion by an order of magnitude, potentially indicating conditions too harsh for the lowest-connected, least stable framework. Partial dehydration at milder conditions (*in situ* 523 K, 12 p.s.i.g H_2, 25 s.c.c.m.), however,

increases 1-butene conversion, similar to the effects of vacuum dehydration observed in NU-1000 and UiO-66. These observations show similarities among MOF-808, NU-1000, and UiO-66, and suggest that Zr-MOFs, in general, should be active for heterolytic cleavage of H_2 and olefin hydrogenation and isomerization in the presence of H_2.

Similar to the dehydrated materials, selectivity varies between the as-synthesized MOFs, with NU-1000 > UiO-66 > MOF-808 in terms of hydrogenation selectivity, which is different from that observed in the dehydrated materials UiO-66 > MOF-808 > NU-1000. Notably, while isomerization selectivity goes up for NU-1000, it goes down for both MOF-808 and UiO-66. These results support the finding that pretreatment conditions are important for controlling active site speciation, since dehydration changes the presence of ligands that may be capping the node, and they also indicate that the catalytic performances of materials can change differently, upon thermal pretreatments, depending on the starting material. These results suggest that careful attention should be paid to the ligands present at the node from materials synthesis if as-synthesized or non-dehydrated materials are being used for some catalytic studies. In this regard, we also noticed a certain degree of batch-to-batch variability in control experiments with NU-1000. Briefly, while 1-butene conversion was similar across the as synthesized materials ~1-3 ks^{-1}, hydrogenation/isomerization selectivity varied depending on the batch. Consistent with findings from DRIFTS experiments and reactivity studies discussed in the main text, we suspect this variability has to do with slight, unforeseen variations in starting materials or synthesis conditions between batches, resulting in differences in adsorbed ligands around the node. More work into the syntheses of these materials and controlling the concentrations of capping ligands may be useful.

4.6.4. H_2 DRIFTS Spectra

Full DRIFTS spectra and additional spectra for the as-synthesized materials can be found in the following section. All spectra are probing changes in the materials upon exposure to H_2 under reaction conditions. Briefly, DRIFTS for the as-synthesized materials shows H_2 activation in each material, with differences in active site speciation even before dehydration. All materials show a primary peak at ~3670 cm^{-1}, while NU-1000 and Ui-66 show additional red shifted peaks at 3619 cm^{-1}, and 3650 and 3630 cm^{-1} respectively. These results suggest differences in the speciation of sites in each material even before thermal dehydration.

In the full spectra of dehydrated and hydrated materials, we were unable to see hydride stretches like in our previous reported study. While stretches were observed in the general region (1600-1300 cm^{-1}) of Zr-H stretches, these features were better assigned to perturbation of ligands on the MOF-node, such as formate ligands and MOF-linkers. We also experimented with stopping H_2 flow and replacing with an argon atmosphere. Results showed that species generated from H_2 activation stick around for some time, with total concentration of reactive intermediates slowly decreasing over the course of an hour.

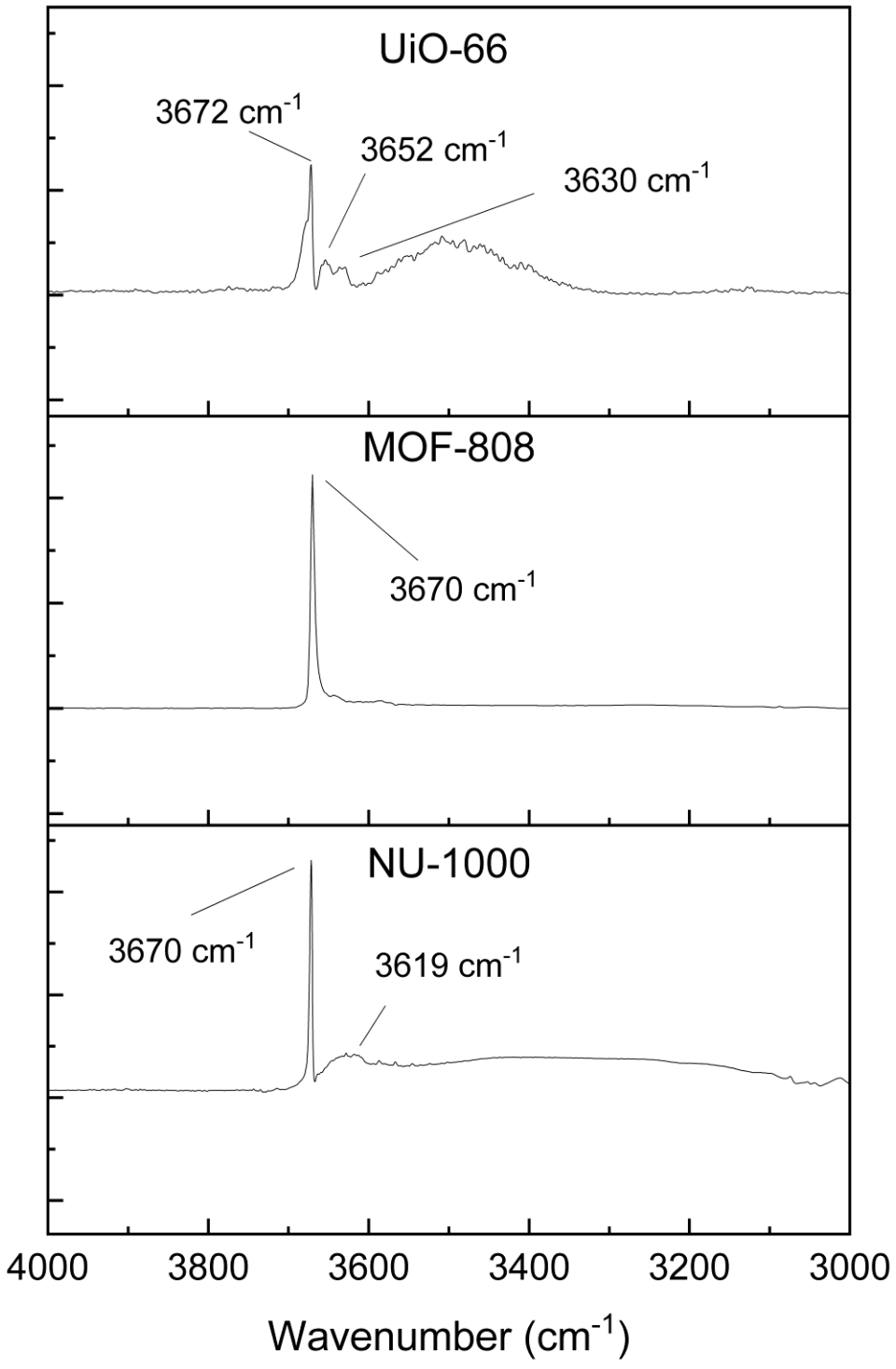

Figure 4.6.4.1. Comparison of H_2 DRIFTS spectra for the as-synthesized materials. All materials show a primary peak at ~3670 cm^{-1}, while NU-1000 and Ui-66 show additional red shifted peaks at 3619 cm^{-1}, and 3650 and 3630 cm^{-1} respectively. These results suggest differences in the speciation of sites in each material even before thermal dehydration.

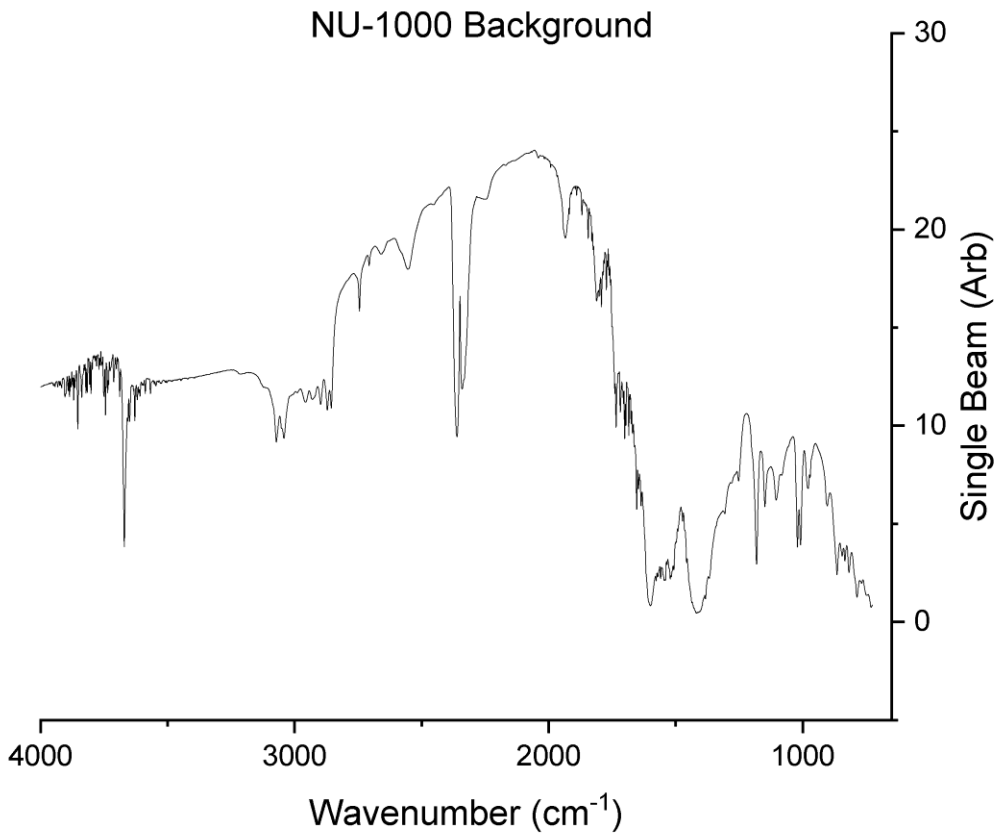

Figure 4.6.4.2. Background spectrum used in H_2 DRIFTS experiment for NU-1000 as reported in.[214] Spectrum shows 5 wt% NU-1000 in KBr after 1h thermal pretreatment at 473 K under N_2. Hydroxyl peak can be observed at 3670 cm^{-1}, indicating a partially hydrated node under these conditions.

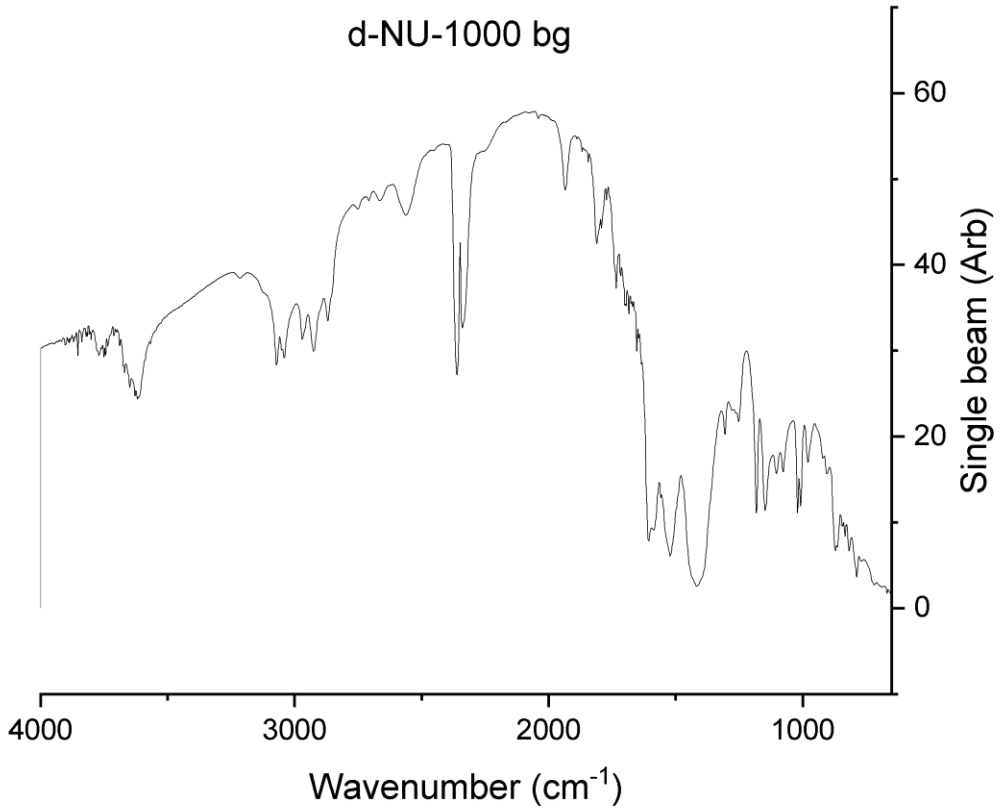

Figure 4.6.4.3. Background spectrum used for H2 DRIFTS experiment with dehydrated NU-1000 (D-NU-1000). Spectrum shows 5 wt% D-NU-1000 in KBr after ~4 h thermal pretreatment at 473 K under Ar flow (~50 sccm). Background spectrum shows a reduction and broadening of hydroxyl peaks in D-NU-1000 relative to NU-1000 (**Figure 4.6.4.4.**), with the most intense feature showing up around ~3619 cm-1. Data show changes in the hydroxyl/oxo population of the material.

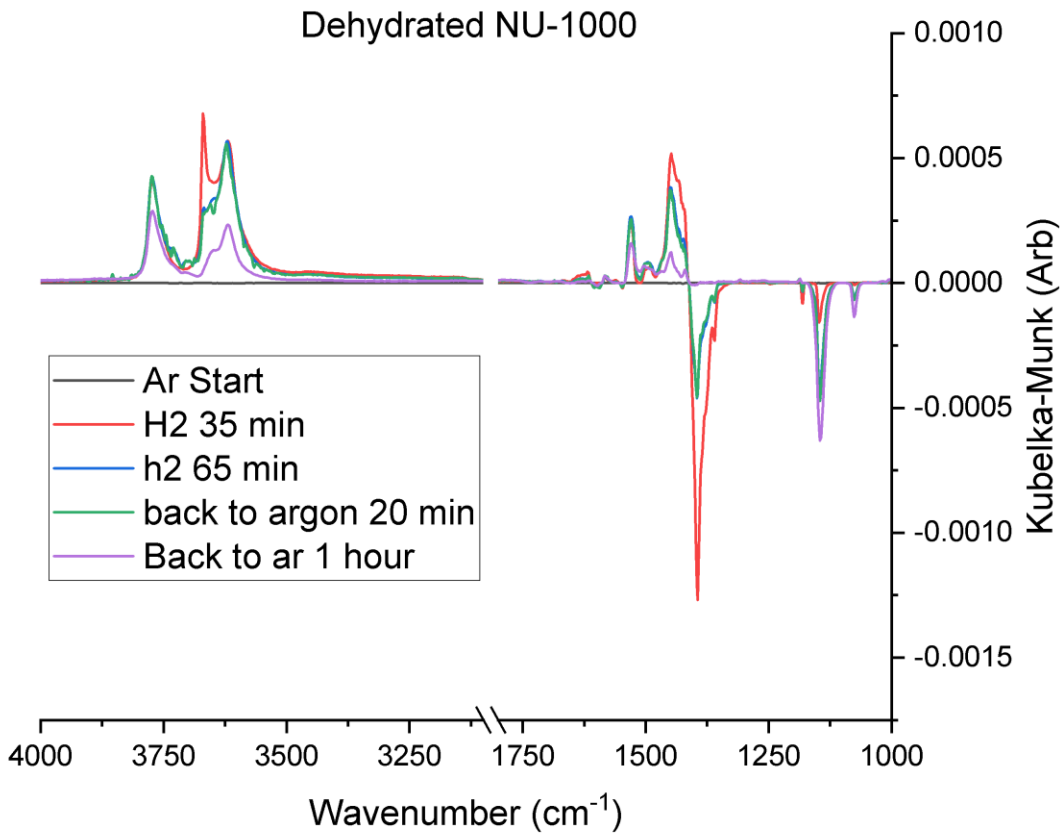

Figure 4.6.4.4. Full difference spectra for D-NU-1000 under H_2 exposure at 473 K over time. (Black) Initial recorded spectrum for D-NU-1000 after taking background, with the sample still under argon. Spectra in general show the reversible activation of H_2 leading to the production of node bound protons. No hydride stretches are observed in the sample, however, stretches in the regions are consistent with linker perturbations, which may obscure any hydride stretches. (Red) 35 min after switching to H_2; 3 hydroxyl peaks are observed at 3770, 3670, and 3619 cm^{-1} respectively. (Blue) 65 min after switching to H_2; peaks at 3770 and 3619 cm^{-1} stay the same, while features at 3670 cm^{-1} are reduced to shoulders. These data suggest a predominant presence of the former two peaks under reaction conditions. (Green) The same sample, after stopping H_2 flow and replacing with argon. No clear change is observed among the peaks, suggesting that species generated from H_2 activation remain on the node for at least some time. (Purple) Sample after 1 hour of argon flow. Data show a reduction in the features generated from H_2 activation, indicating a gradual decrease in the amount of cleavage products present at the node in the absence of an H_2 atmosphere.

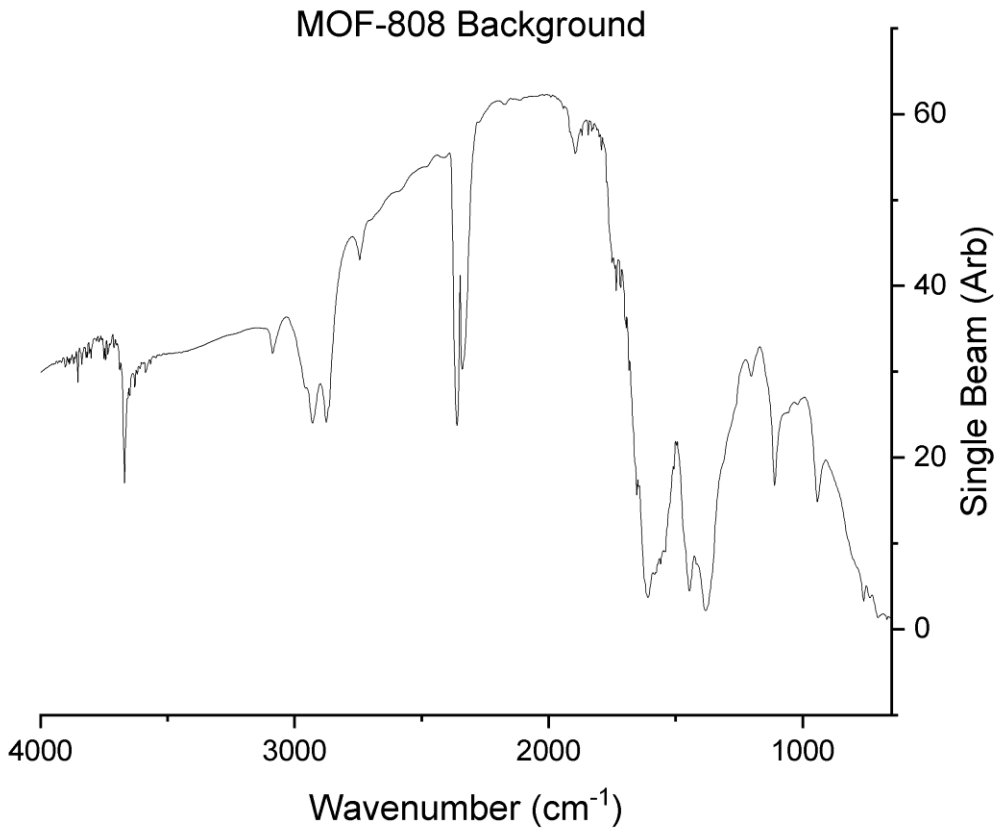

Figure 4.6.4.5. Background spectrum used for H_2 DRIFTS experiment with MOF-808. Spectrum shows 5 wt% MOF-808 in KBr after ~4 h thermal pretreatment at 473 K under Ar flow (~50 sccm). Hydroxyl peak can be observed at 3670 cm^{-1}, indicating a partially hydrated node under these conditions.

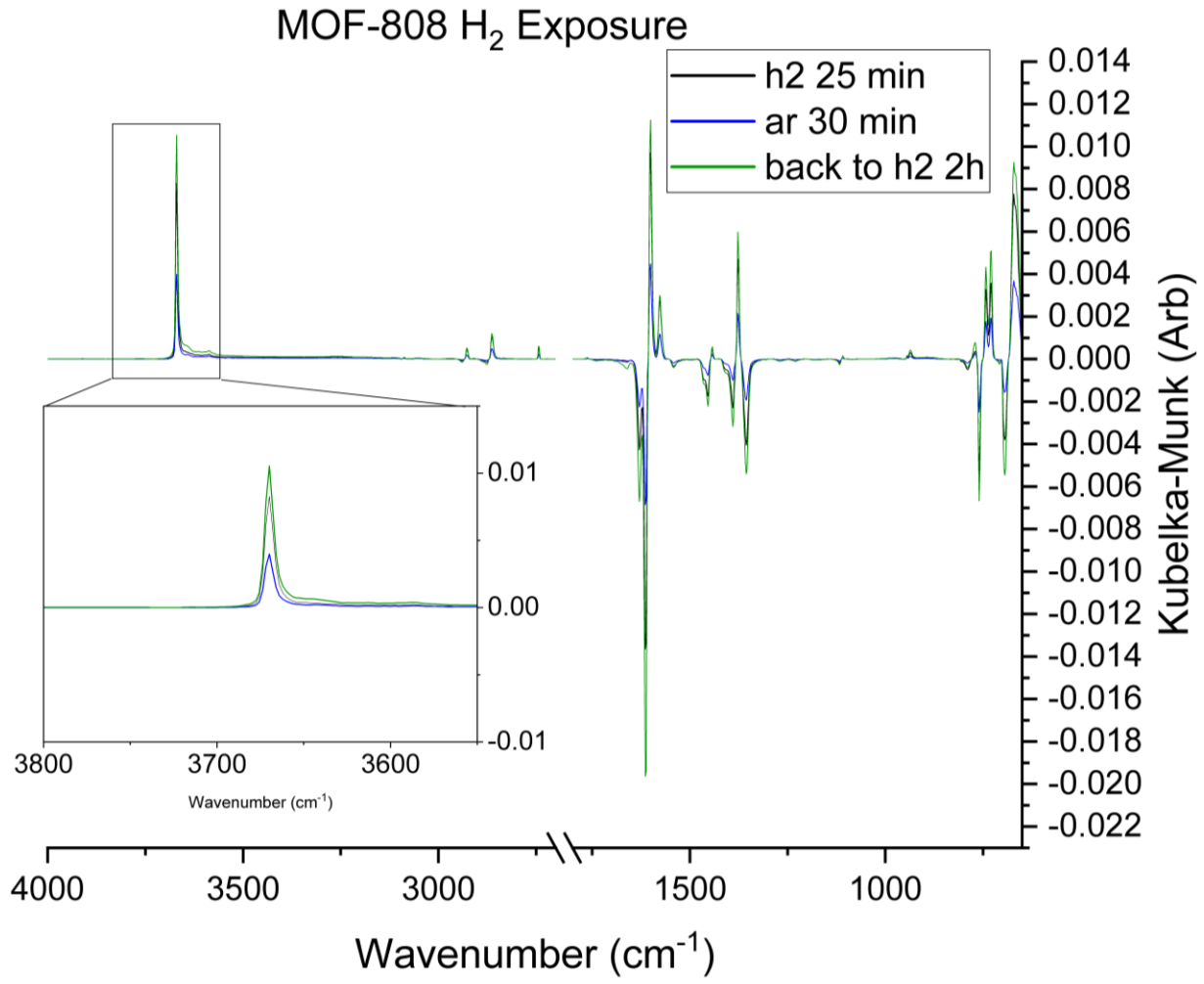

Figure 4.6.4.6. Full difference spectra for H_2 DRIFTS experiment with MOF-808. Spectra show the growth of hydroxyl species at 3670 cm^{-1} in addition to perturbation of linkers and node-capping ligands from 1800-1300 cm^{-1}. (Black) Difference spectrum of MOF-808 upon H_2 exposure after 25 min. (Blue) Difference spectrum for MOF-808 after replacement of H_2 atmosphere with argon after 30 min. A reduction in hydroxyl intensity is observed. (Green) 2 hours after switching back to H_2 flow shows increased intensity in H_2 stretch.

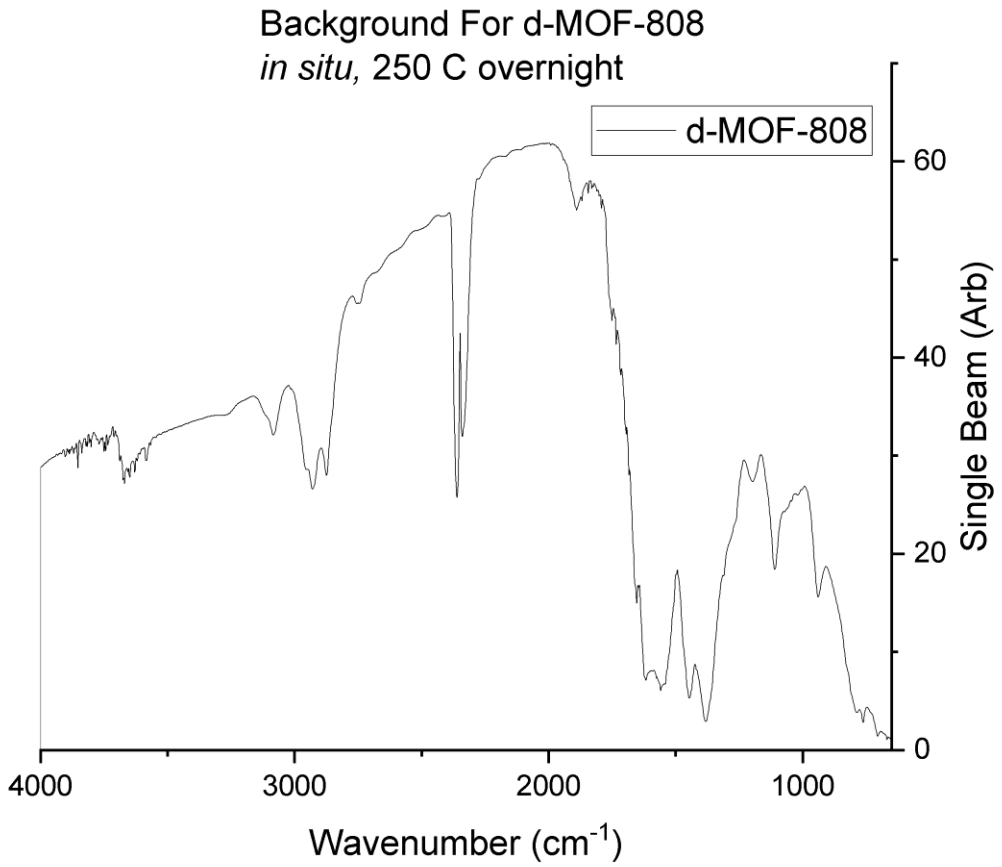

Figure 4.6.4.7. Background spectrum used for H_2 DRIFTS experiment with *in situ* dehydrated MOF-808 (D-MOF-808). Spectrum shows 10 wt% D-NU-MOF-808 in KBr at 473 K under argon after an overnight thermal treatment at 523 K under Ar flow (~50 sccm). Background spectrum shows a reduction and broadening of hydroxyl peaks in D-MOF-808 relative to MOF-808 (**Figure 4.6.4.6.**), with the most intense feature showing up around ~3670 cm^{-1}. Data show changes in the hydroxyl/oxo population of the material under pretreatment conditions.

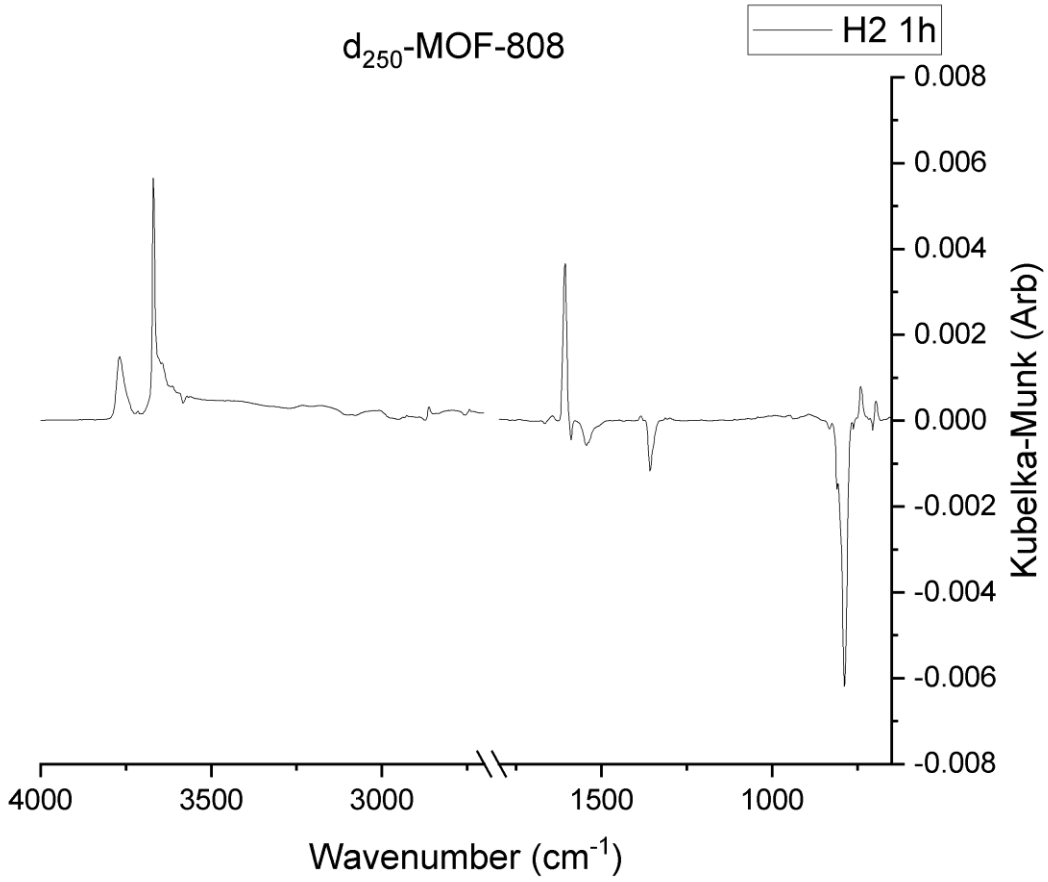

Figure 4.6.4.8. Full difference spectrum of H2 DRIFTS experiment for in situ dehydrated MOF-808 (D-MOF-808). Spectrum shows hydroxyl stretches generated at 3770 cm-1 and 3670 cm-1. Fewer spectral changes are observed in the region from 1800-1300 cm-1 than for MOF-808 (Figure 4.6.4.6.), with a sharp peak at 1608 cm-1; however, features are still challenging to assign with specificity.

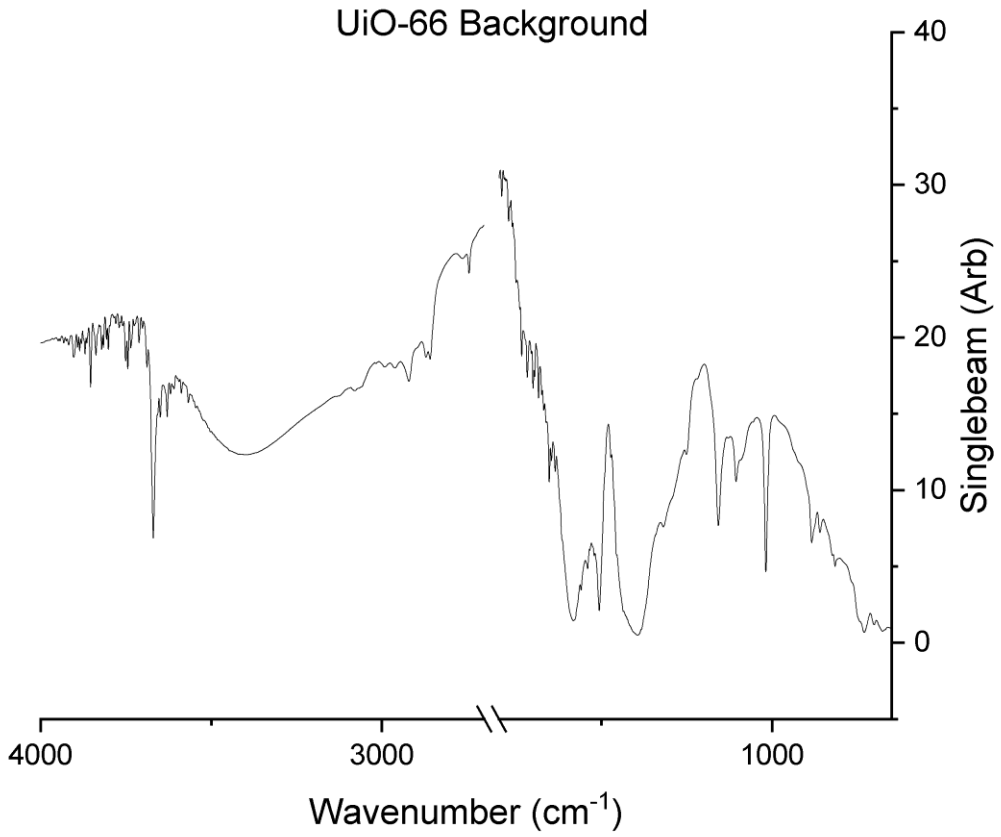

Figure 4.6.4.9. Background spectrum used for H2 DRIFTS experiment with UiO-66. Spectrum shows 5 wt% UiO-66 in KBr after ~4 h thermal pretreatment at 473 K under Ar flow (~50 sccm). Hydroxyl peak can be observed at 3670 cm^{-1}, indicating a partially hydrated node under these conditions. Additionally, a broad peak is associated with moisture in the material.

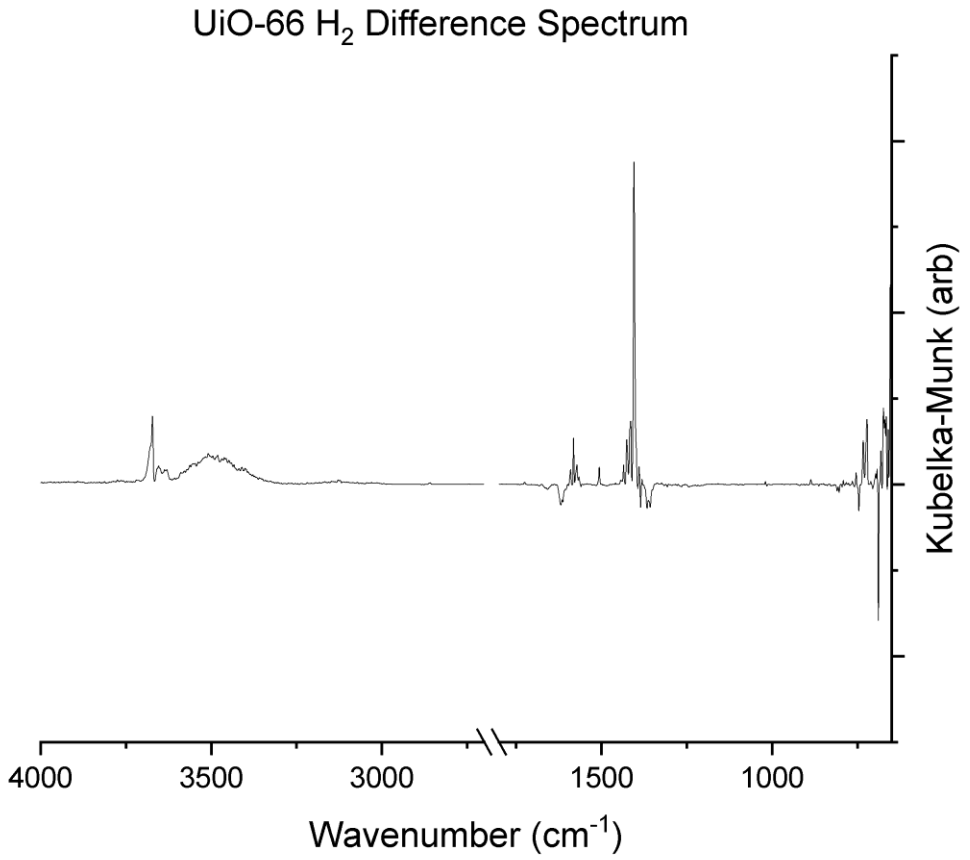

Figure 4.6.4.10. Difference spectrum for H_2 DRIFTS experiment with UiO-66. Similar to other experiments, spectrum shows the growth of hydroxyl peaks around 3670, though in this case with some additional moisture. Additionally, some features are observed in the region from 1800-1300 cm^{-1}consistent with perturbations of linkers/node-capping ligands.

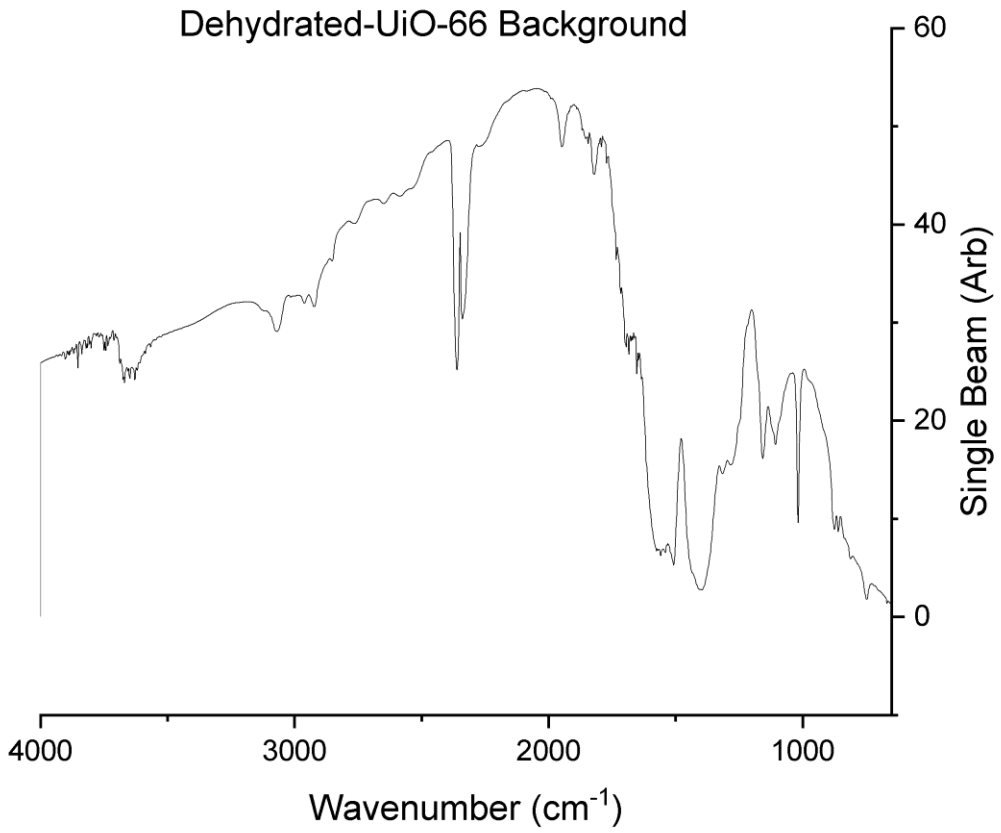

Figure 4.6.4.11. Background spectrum used for H_2 DRIFTS experiment with dehydrated UiO-66 (D-UiO-66). Spectrum shows 5 wt% D-UiO-66 in KBr at 473 K under argon (~50 sccm). Background spectrum shows a reduction and broadening of hydroxyl peaks in D-UiO-66 relative to UiO-66 (Figure S30), with the most intense feature showing up around ~3670 cm^{-1}. Data show changes in the hydroxyl/oxo population of the material under pretreatment conditions.

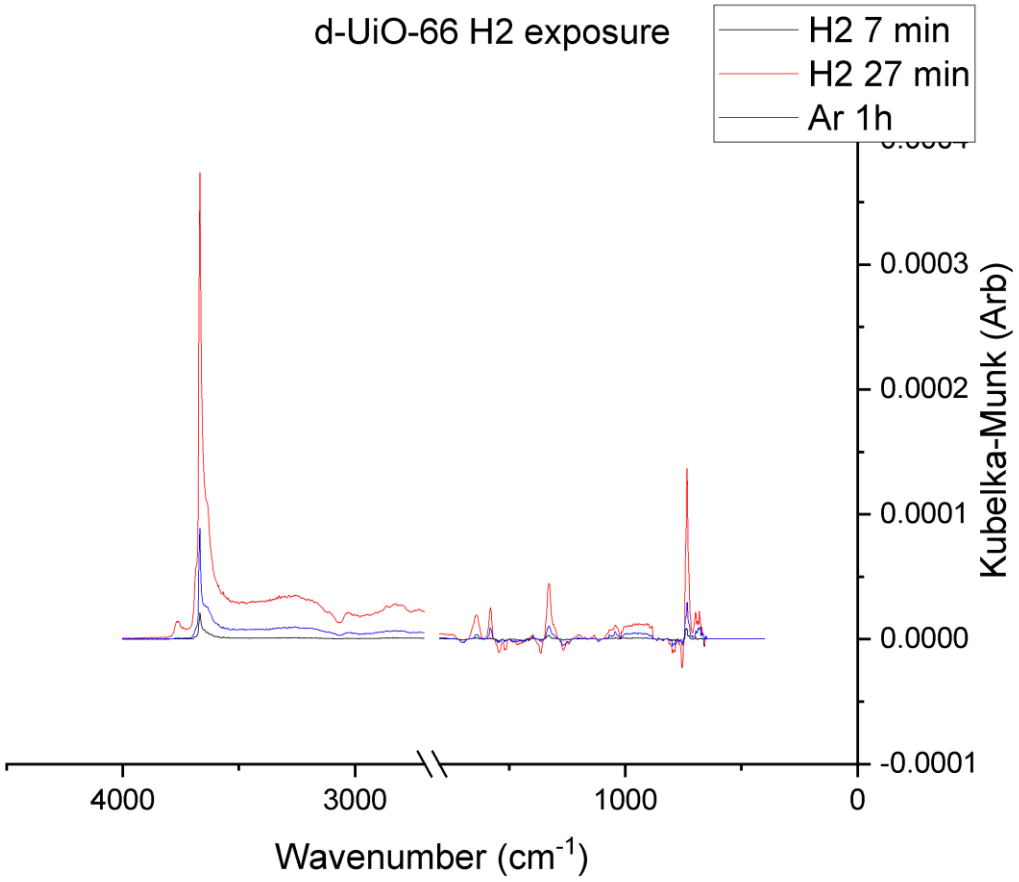

Figure 4.6.4.12. Full difference spectra of 5 wt% D-UiO-66 in KBr after H_2 Exposure at 473 K. Hydroxyl peak can be observed at 3670 cm^{-1}, with an additional, small feature at 3770 cm^{-1}. (Black) Initial changes from H_2 activation after 7 min of exposure. (Red) Spectral changes from H_2 activation at 27 min. (Blue) Exchange of H_2 atmosphere with argon results in a substantial decrease in hydroxyl features after 1 hour.

CHAPTER 5. Topological constraint and influence over Merweein-Ponndorf-Verley Reduction in Zr-MOF catalysts

5.1. Chapter Summary

In this final chapter, the influence of MOF topology upon catalytic activity of the Zr_6O_8 cluster is studied for the geometrically sensitive reaction, Merweein-Ponndorf-Verley (MPV) Reduction. MPV reduction is the transfer hydrogenation of ketones and aldehydes using a secondary alcohol as a H_2 source, and is relevant for the conversion of renewable, biomass-based feedstocks and the production of fine chemicals. The reduction of these ketones and aldehydes using an alcohol as a co-reactant requires co-adsorption of the substrate and alcohol at the same Zr-atom or adjacent Zr atoms, which then must form a large and geometrically constrained transition state to produce products. In a systematic study of MOF catalysts that vary in topology and pore size, data show MOF catalysts with more topologically open or accessible adsorption sites at the Zr_6O_8 clusters display orders of magnitude greater catalytic activity for ketone and aldehyde reductions than MOF catalysts with less accessible topologies. As a trade-off however, employing slower, more geometrically constrained MOF catalysts permits greater control over selectivity in ketone/aldehyde reductions where multiple possible products of varying size may be formed during the reaction. Experimental and computational data suggest that differences in catalytic yields for MPV reduction are attributable to a combination of factors, 1) total accessible Zr atoms, as determined by cluster connectivity, 2) differences in intrinsic barriers of MPV reduction on a per Zr basis due to destabilization of MPV transition states by proximal linkers and reactant bond angles, and 3) greater configurational entropy of adsorbed reaction intermediates in 6-connected topologies, where more surface configurations of substrates can lead to fruitful catalytic activity than in 8-connected MOFs. These results suggest controlling the rates and

selectivity of ketone/aldehyde reductions in Zr-MOF catalysts requires a fine balance and control over structural parameters in Zr-MOFs, and these fundamental findings provide insights into potential challenges and advantages in the use of MOF catalysts for ketone/aldehyde reductions, as well as other, related catalytic processes.

5.2 Lewis acid catalyzed reactions in Zr-MOFs

Zirconium Metal–Organic Frameworks (Zr-MOFs) have been studied for a wide range of Lewis acid and base catalyzed reactions, particularly receiving attention for their structural stability, structural tunability, and catalytic modularity. Typically composed of Zr_6O_8 clusters and carboxylate ligands, these materials possess strong node-to-linker bonds, providing thermal and chemical stability under a range of pH and temperature conditions. Additionally, Zr_6O_8 building units possess Zr^{4+} Lewis acid sites which can be leveraged for catalysis, while organic linkers can be functionalized with acidic or basic functionalities.[30, 95, 207]

Strategies for optimizing the performance of Zr-MOFs for Lewis acid catalyzed reactions have primarily focused on control over topology and electronics of the material. In terms of topology, strategies typically focus on maximizing the quantity of missing-linker defects or exposed Lewis acid sites for substrate activation. Reports for a wide range of Zr-MOF-catalyzed reactions generally show that decreasing cluster connectivity, whether by defect engineering or topological design, increases activity per Zr.[95, 118, 207, 209] In terms of electronics, strategies typically aim to modify Lewis acidity at defect sites and coordination sites through thermal and chemical removal of capping ligands and modulators.[94, 96, 221] Additionally, electronic modification has also been achieved through the incorporation of withdrawing groups, such as nitro groups and sulfates, on structural linkers of the MOF or at the MOF node increasing overall Lewis acidity of the Zr_6O_8

cluster.[119, 210, 222, 223] Tuning of these structural parameters has led to the development, understanding, and improvement of Zr-MOFs as Lewis acid catalysts.

What is understudied is how MOF topology and defect density may be leveraged to influence Lewis acid catalysis through geometric constraint. Many Lewis acid catalyzed reactions (and other surface reactions) require the co-adsorption of substrates for fruitful reactivity, and often, these substrates must meet in specific proximities and orientations to one another.[224-227] In addition to total quantity of coordination sites, MOF-topology has been shown to influence the relative orientation of coordination sites at the Zr_6O_8 cluster, thereby dictating the ways in which substrates can co-adsorb on the MOF node.[228-230] Despite this, to the best of our knowledge, only a couple of studies have specifically examined the influence of defect orientation on catalytic activity. In a study of ethanol dehydration in UiO-66 and UiO-67 by Yang et al.,[99] increasing defect density was shown to not only increase turnover frequency (on a per Zr_6O_8 basis) for the reaction, but also decrease the reaction barrier for ethanol dehydration. In this study, computational and experimental data suggested that missing-linker defects randomly adjacent to one another led to favorable co-adsorption and reaction of substrates through allowed stabilizing H-bonds, resulting in increased selectivity for diethyl ether over ethylene. Additionally, in our recent work studying hydrogenation and isomerization, incorporation of 1,6- naphthalene dicarboxylic acid into NU-1000 topologically modified the material, systematically eliminating the *cis* adjacency of coordination sites on the Zr_6O_8 cluster. In turn, this resulted in a titration of olefin hydrogenation and isomerization activity, which required the *cis* coordination of hydride and olefin for 1,2-insertion and β-hydride elimination, at the Zr^{4+} Lewis acid site.[230] (**Scheme 5.2.1.**) However, in this system, full understanding of the effects of MOF-topology were challenging, due to the additional influence of H_2 activation pathways and Brønsted acid-catalyzed pathways upon olefin conversion.

Nevertheless, these examples demonstrate a greater complexity to topological effects on MOF node chemistry than the mere quantity of missing-linker defects or engineered coordination sites and therefore, suggest an underexplored route for tuning catalytic activity of Zr-MOFs.

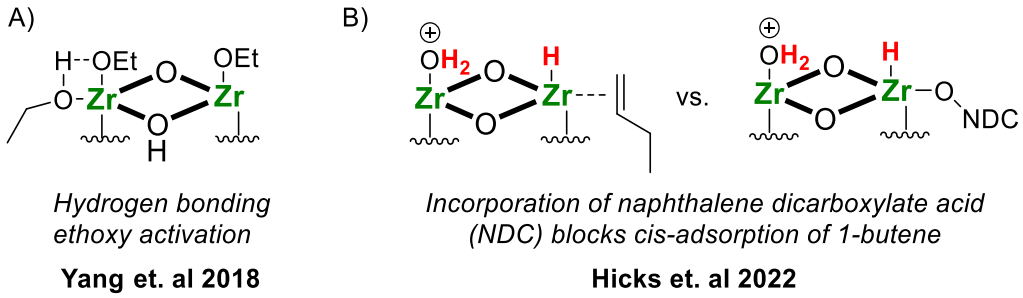

Scheme 5.2.7. Examples of *cis* adsorption sites on Zr_6O_8 node. Node is truncated for simplicity. Hydrogen bonding from ethanol adsorbed at adjacent defect site assists in ethoxy activation in ethanol dehydration (left). Naphthalene dicarboxylic acid blocks *cis* adsorption of hydride and 1-butene, hindering 1,2-insertion mechanisms.

One reaction that is likely sensitive to the geometric effects of MOF topology is Meerwein-Ponndorf-Verley Reduction (MPV), which is the transfer hydrogenation of a carbonyl, typically using a secondary alcohol like isopropanol as a hydrogen source and producing a new alcohol and carbonyl. This reaction has useful applications in the production of pharmaceuticals and fragrances, as well as applications in the conversion of biomass feedstocks (e.g. reduction furfural to furfuryl alcohol, and MPV is a step in ethanol conversion to sustainable aviation fuel).[123, 231-235] But MPV reduction is of particular interest in probing effects of MOF topology due to its mechanistic pathway. In Lewis acid-catalyzed MPV reduction, substrates co-adsorb at a single Lewis acid site, followed by a hydride transfer that goes through a bulky, 6-membered ring transition state.[52, 226, 231, 236] Additionally, over bulk Lewis acids like ZrO_2, it has been proposed that substrates can coordinate at adjacent Lewis acid sites, forming 7 or 8-membered rings during the hydride transfer step.[237] (**Scheme 5.2.2.**) Given the necessity of substrate co-adsorption and the bulky nature of the transition state, we hypothesized that MOF-topology would determine the allowed orientations of substrate co-adsorption having significant effects transition state favorability and catalytic

performance. Additionally, we also hypothesized that in MPV reductions with products of varying shape and size, MOF pore environment or the steric effects of nearby structural linkers could also affect transition-state and influence product selectivity, as consistent with studies regarding MPV in zeolites.[52, 238]

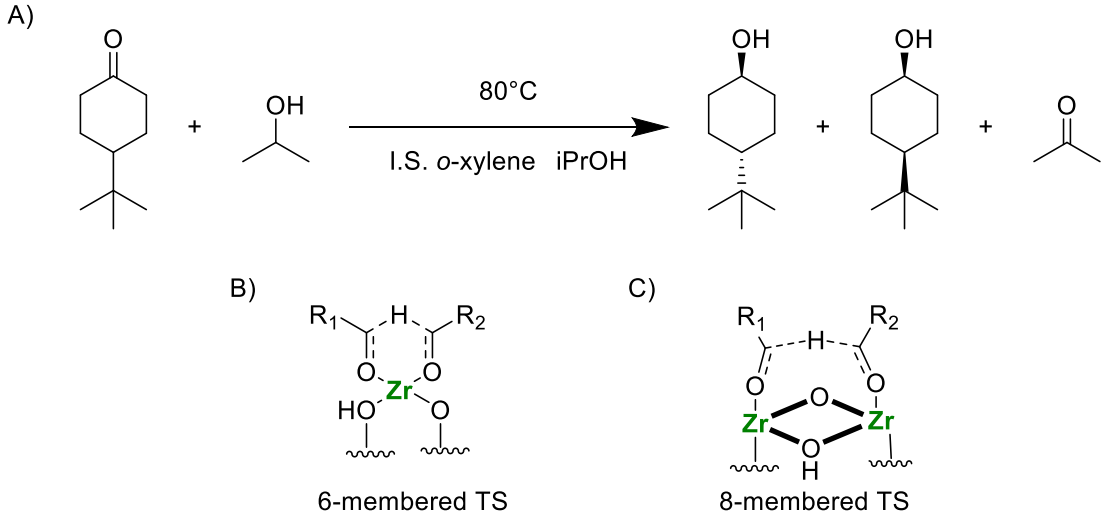

Scheme 5.2.8. MPV reduction of typical substrate 4-*tert*-butylcyclohexanone (A). Proposed of transition states of substrates co-adsorbed at the same Lewis acid site (B) and adjacent Lewis acid sites (C)

While MPV reduction has been studied in Zr-MOFs, studies have primarily focused on the structural parameters of cluster connectivity, site accessibility, and electronic influence from linker substituents. These studies found that lowering cluster connectivity, like for many other reactions, increases the quantity of substrate adsorption sites, and removal of capping ligands can significantly improve conversion at mild reaction temperatures (<40 °C).[220, 239-242] Additionally, incorporation of electron withdrawing groups onto structural linkers increases the Lewis acidity of the Zr active site.[122, 234, 239, 243] Other studies have investigated the incorporation of Zr-MOFs into composite materials for MPV reduction, but these studies do not provide insights into differences between MOF structures.[121] To the best of our knowledge, no work has directly investigated the influence of MOF topology or cluster connectivity upon mechanistic pathways and catalytic

parameters intrinsic to the active sites, such as catalytic barriers or selectivity—ultimately showing a gap in the knowledge and potential usage of these materials as heterogeneous catalysts.

To investigate these hypotheses regarding the effects of topology upon Zr-MOF performance in MPV reduction, we herein conducted a systematic study of MPV reduction with substrates of different sizes in a series of MOFs with different topologies and cluster connectivity. Focusing on MOF-808 (6-connected), NU-1000 (8-connected), and defective UiO-66 (~8-connected), and MOFs of similar connectivity, we examined the effects of Zr_6O_8 connectivity upon rates, barriers, and selectivities for this reaction.

5.3. Results and Discussion

5.3.1. Screening of MPV 6-8 connected Zr-MOFs

Considering the proposed mechanism of MPV reduction, we began our studies with an experimental screening using the three MOFs, MOF-808, NU-1000, and UiO-66. These MOFs were chosen not only because of differences in their coordination site densities, but also because of the orientations of their coordination sites in each structure. Representing the shared Zr_6O_8 node between the three MOFs as an octahedron, where each Zr atom is a vertex of the octahedron, MOF-808's *spn*, 6-connected topology has six edges, along two of the six faces of the structure, coordinated by structural linkers, thereby leaving six edges along the rest of the faces open for reactant adsorption. (**Figure 5.3.1.1.**) This leaves a very open space for substrate adsorption, with room for *cis* coordination of substrates at each vertex. In contrast, from the *csq*, 8-connected topology of NU-1000, structural connectivity leaves four edges of the octahedron, around the equator of the structure, for reactant adsorption. While each vertex still has space for the *cis*-coordination of reactant intermediates, we hypothesized that structural linkers from the MOF would leave less room for favorable reactivity, leading NU-1000 to be disproportionately slow.

In the case of UiO-66, which has an *fcu*, 12-connected topology, we synthesized a missing-linker defective material using established literature procedures,[117] yielding a nominally 7- or 8-connected material (~7.4 connected via TGA). (**Additional Information, Figure 5.5.2.3.**) While quantitatively close in connectivity to NU-1000, this material is notably different in that the orientation of its defects are randomly distributed throughout the crystal, yielding a distribution of clusters with varying connectivity. As a result, we predicted the material to have coordination sites like both NU-1000 and MOF-808, as well as some isolated defects that would not facilitate the *cis* adsorption of reactant intermediates.

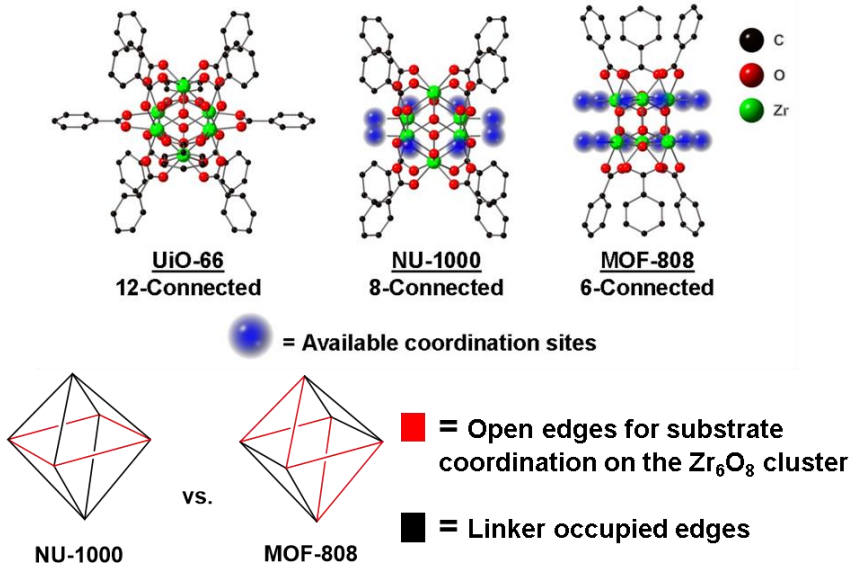

Figure 5.3.1.1. Top, crystal structural representations of the Zr_6O_8 cluster in UiO-66, NU-1000, and MOF-808. Linkers are truncated for clarity, with H atoms omitted. Bottom, representations of the Zr_6O_8 cluster as an octahedron. Zr atoms are located at vertices, and O atoms are located at each face, but omitted for clarity. Edges are highlighted to represent the presence (black) of carboxylate linkers or the absence (red) of carboxylate linkers, leaving space for the coordination of reactants.

Screening these catalysts for MPV reduction with a variety of substrates showed drastic differences between the materials. Of potential substrates, we used cyclohexanone and 4-*tert*butyl-cyclohexanone, which are commonly studied for this reaction, 2-butanone due to its small size, and furfural, which is commonly studied as a biomass feedstock. Isopropanol was used as solvent and excess reductant, and reactions were conducted at 80°C. Across the series of substrates,

screening results consistently showed MOF-808 outperforms UiO-66 and NU-1000 by up to 2 orders of magnitude, with UiO-66 also consistently outperforming NU-1000, although to a significantly lesser degree. (**Table 5.3.1.1.**)

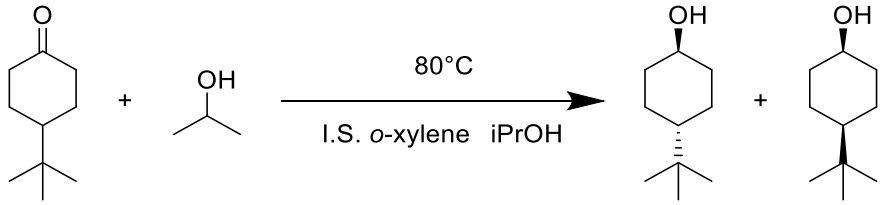

		MOF-808		UiO-66		NU-1000	
Substrate	Time (hours)	Conversion	T.O.N.[a]	Conversion	T.O.N.[a]	Conversion	T.O.N.[a]
Cyclohexanone[b]	24 h	99%	125(21)	9%	11.0(2)	0.4%	1(0.3)
4-*tert*butyl-cylcohexanone[c]	3 h	67%	39(7)	1%	1(0.2)	0.4%	0.3(0.1)
2-butanone[d]	3h	9%	5(1)	<1%	N/A*	<1%	N/A*
Furfural[e]	3h	88%	73(12)	15%	13(3)	6%	7(2)

Table 5.3.5.1. Initial reaction screening for MOFs and substrates. Values rounded to the nearest digit. All reactions were done parallel in 1.5-dram vials with reaction volumes of 2.5 ml on a heated aluminum block shaker plate. Reactions were heated at 80°C and 500 rpm of shaking. *O*-xylene was used as the internal standard for all reactions, and 5-6 mg of catalyst were added to each vial. [a]T.O.N. presented on a per Zr_6O_8 basis and accessible Zr atom basis in parentheses. Accessible Zr atoms are estimated, based on crystal structure, or measured defect density, to be 6, 4.6, and 4 for MOF-808, UiO-66, and NU-1000, respectively. [b]Reaction done in triplicate, all errors <5% total conversion. Zr/cyclohexanone/iPrOH molar ratio of 1/210/14000. [c, d, e]Single experimental screenings. Molar ratios for Zr/substrate/iPrOH are [c]1/16/2100, [d]1/10/2100, [e]1/21/2100. *No signal detected via GC-FID.

These initial results point to intrinsic differences between the catalytic sites of each material, despite all of them sharing the same Lewis acidic Zr_6O_8 cluster. If open coordination sites were chemically equivalent in activity across the materials, turnovers on a per cluster basis would not differ by orders of magnitude, where missing linker defects only range from 4-6 per cluster. Additionally, differences persisting across a range of substrate sizes suggests that these results are

not representative of diffusion phenomena, consistent with other reports of MPV in Zr-MOF catalysts.[242] In substrates of all sizes, NU-1000 has the lowest activity; both 2-butanone and 4-*tert*-butylcyclohexanone (the largest substrate, 6.4 x 5.8 x 9.6 Å, Corey–Pauling–Koltun model)[244] should be able to access the large pores of NU-1000 (13 & 30 Å).[98] By comparison the defective pores of UiO-66 are 11.5 & 16 Å[117] and the pores of MOF-808 are 18 Å, both accessible for all of the substrates. Given the pore sizes of these materials and catalytic trends, data suggest that diffusion limitations are an unlikely explanation for differences in activity.

Running a control experiment, (**Figure 5.3.1.2.**) we also found that catalytic differences are not solely attributable to differences in the quantity of defect-capping ligands left over from MOF-synthesis. Comparing MPV reduction of 4-*tert*-butylcyclohexanone in MOF-808 capped with and without formic acid/formate modulators showed capping ligands may cause slight induction periods, but otherwise do not significantly affect rates of MPV reduction at reaction temperature (80°C). These results are consistent with reported post synthetic modification procedures, where formate ions can be removed when soaking Zr-MOFs in alcohol at temperatures as low as 60°C.[97, 242] Our reaction conditions occur in neat isopropanol at 80°C, so formates loss appears to occur quickly under reaction conditions (10 min), only limiting initial conversion rates, but not explaining the orders of magnitude difference between materials over longer timeframes. Supporting these conclusions, post catalysis base digestion and characterization of MOF-808 and NU-1000 via ^{1}H NMR showed the loss of formates under reaction conditions (**Additional information**, **Figures 5.5.3.1** and **5.5.3.2.**). Finally, other studies of MPV reduction in Zr-MOFs indirectly suggested reaction insensitivity to defect-capping ligands, consistent with our observations.[245]

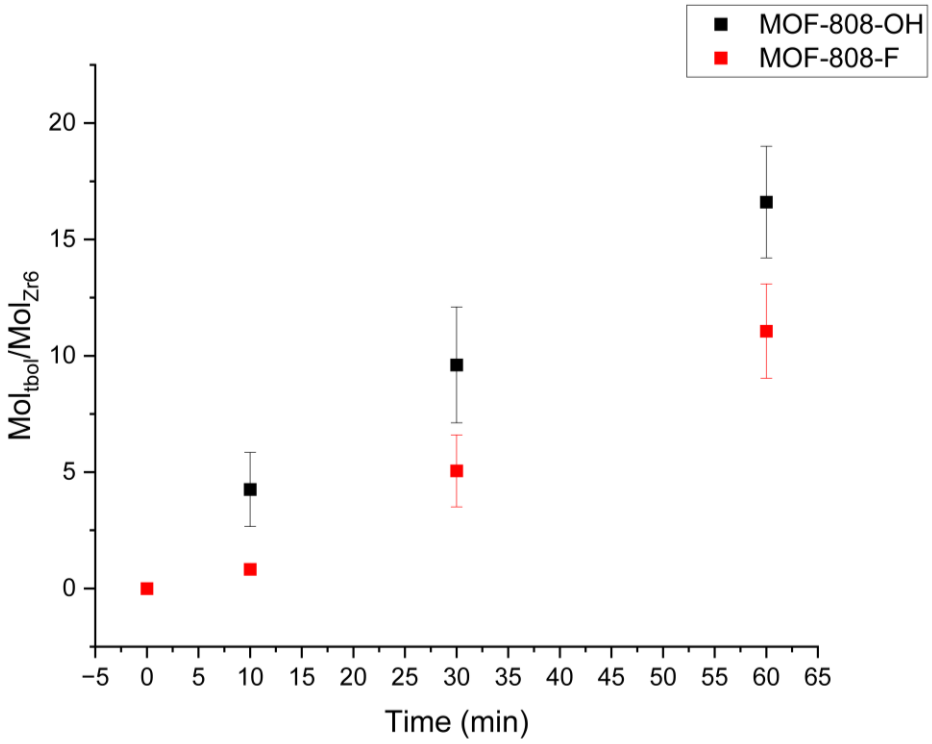

Figure 5.3.1.2. Kinetic comparison of formate containing MOF-808 (red) and formate-free MOF-808 (black). Y-axis shows moles of *trans*- and *cis*-4-*tert*butyl-cyclohexanol produced on a per Zr_6O_8 basis. Kinetic curves suggest differences between catalysts are primarily due to an induction period, rather than intrinsic rates of active sites in each material. Reaction done in triplicate, temperature = 80°C, 500 rpm shaker plate. Zr/tbutyl-cyclohexanone/iPrOH molar ratio of 1/16/2100. Conversion between 0-30%.

Based on these observations, we hypothesized that 8-connected topologies like observed in NU-1000, provide poor catalytic sites for MPV reduction, likely due to the relative orientation of adsorption sites to one another and to lack of space from structural linkers. Validating these hypotheses, we extended our reactivity studies to additional 6 and 8-connected MOFs, focusing primarily upon the conversion of cyclohexanone and 4-*tert*-butylcyclohexanone. When testing the additional 8-connected MOFs, NU-901 (*scu*, 8-connected) and NU-1200 (*the*, 8-connected), experimental results showed that both materials were poor catalysts for MPV reduction. (**Table 5.3.1.2., Figure 5.3.1.3.**) Although varying in topology, each MOF shares the same cluster connectivity as NU-1000, with coordination sites along the equator of the Zr_6O_8 octahedron. Catalytic results for both cyclohexanone and 4-*tert*-butylcyclohexanone showed MOF-808 and

UiO-66 outperformed all the 8-connected MOFs, with NU-901 and NU-1200 being similarly poor to NU-1000 (MOF-808>>UiO-66≥NU-901>NU-1000>NU-1200). While MOF-808 reached near quantitative conversion after 16 hours, NU-901 only achieved 35% conversion (34 T.O.N.) after 96 hours. Performing the worst, NU-1200 only achieved 1.7% conversion (1.5 T.O.N.) after 96 hours. These data indicate that regardless of the MOF-topology, 8-connected cluster geometries are suboptimal for MPV reduction.

	Reaction Time (h)	*Cis*-Selectivity	Conversion	T.O.N.[a]
MOF-808	16	7%	99.7%	62(10)
UiO-66	96	15%	49%	37(8)
NU-901	96	22%	36%	34(9)
NU-1000	96	30%	16%	15(4)
NU-1200	96	18%	2%	2(0.4)
ZrO2[b]	48	4%	9%	(0.6-0.4)

Table 5.3.1.6. Screening of activity for additional 8-connected MOFs NU-901 and NU-1200 for reduction of 4-*tert*-butylcyclohexanone in isopropanol, compared to MOF-808, UiO-66, NU-1000 and Bulk ZrO_2. Values rounded to the nearest digit. All reactions were done parallel in 1.5-dram vials with reaction volumes of 2.5 ml on a heated aluminum block shaker plate. Reactions were heated at 80°C and 500 rpm of shaking. *O*-xylene was used as the internal standard for all reactions, and 5-6 mg of catalyst was added to each vial. [a]T.O.N. presented on a per Zr_6O_8 basis and accessible Zr atom basis in parentheses. [b] Commercially purchased t-ZrO_2 (20-30 nm^2) was used as a comparison for *cis*-selectivity in MPV reduction. T.O.N. was calculated on a per Zr basis using estimated surface density of tetragonal ZrO_2 as reported in Gonell et al.[237]

By contrast, study of Hf-MOF-808 (isostructural to Zr-MOF-808 except with Hf instead of Zr) and UiO-67 (structurally analogous to UiO-66 but with longer linkers and larger pores, 8.4 connected as measured by TGA, additional information **Figure 5.5.2.21.**) yields similar catalytic performances to their structural analogues, unilaterally outperforming NU-1000. (**Figure 5.3.1.3.**) In the case of Hf-MOF-808, rates of conversion are increased with the increased Lewis acidity of the Hf_6O_8 node,[241, 246, 247] (39 turnovers per Zr_6O_8 vs. 58 turnovers per Hf_6O_8, after 3 hours), while

conversion in UiO-67 is slightly increased relative to UiO-66 (0.8 turnovers for UiO-66 vs. 1 turnover for UiO-67 after 3 hours), showing negligible improvement but maintained, better performance relative to NU-1000. Together, these results indicate that catalytic performance in MPV reduction is significantly determined by cluster connectivity in MOFs sharing the M_6O_8 structural motif.

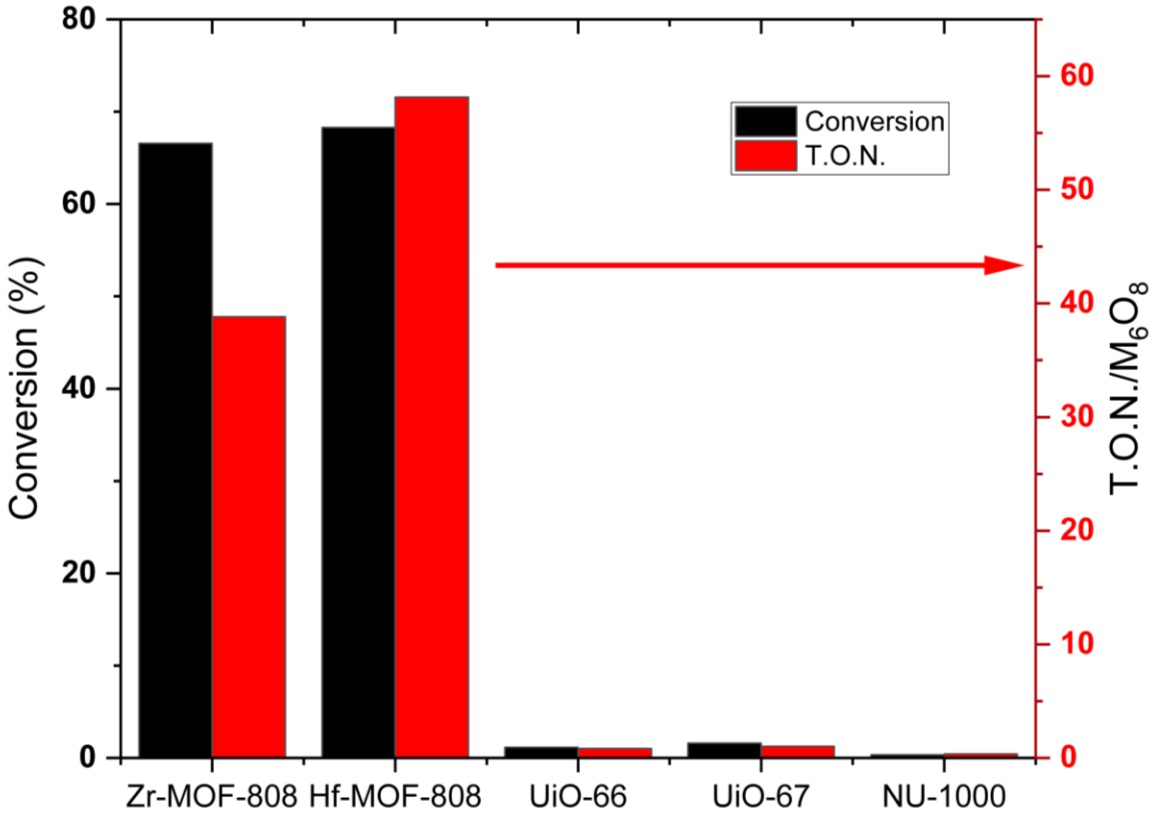

Figure 5.3.1.3. Catalytic comparison of *spn* and 8-connected *fcu* analogues Hf-MOF-808 and UiO-67 with other Zr-MOFs via conversion (black, left axis) and T.O.N. (red, right axis) in MPV reduction of 4-*tert*-butylcyclohexanone. Reaction time 3 hours, temperature 80°C, 500 rpm. Reactions done in parallel using same stock reaction solution.

Differences in performance between MOFs of similar connectivity can potentially be understood through additional structural and topological motifs. Experimental data may be consistent with NU-901 being the best 8-connected MOF due to its flexibility, as studies have shown the diamond shaped pores of the *scu* topology allows for greater flexibility of the framework than in *csq* and *the* topologies.[248] Most likely, this allows for easier accommodation of the bulky

transition state for MPV reduction in NU-901. In contrast, NU-1200's sodalite-like *the* topology is achieved via steric constraints introduced to the linker to force out-of-plane phenyl rotations.[249] Likely, barriers for the rotation of phenyl rings next to defects are higher for NU-1200, inhibiting flexibility to accommodate MPV reduction. These structural details may explain why of the 8-connected MOFs, NU-1200 performs the worst while 901 performs the best.

5.3.2. Influence of MOF-Topology upon Selectivity in reduction of 4-tert-butylcyclhexanone

Focusing on topological influence of selectivity in MPV reduction, selectivity in reduction of 4-*tert*-butylcyclohexanone appears to show that 8-connected MOFs generally exert more influence on product selectivity, as a trade-off to catalytic activity. (**Table 5.3.1.2., Figure 5.3.2.1.**)

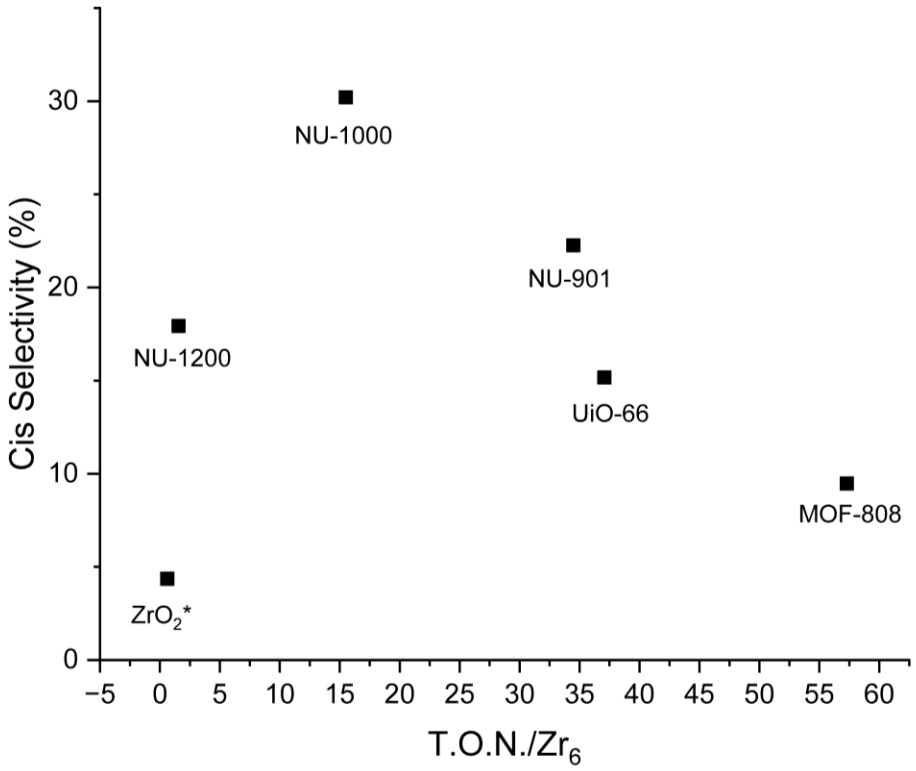

Figure 5.3.2.1. Selectivity for *cis*-4-*tert*-butylcyclohexanol in the MPV reduction of 4-*tert*-butylcyclohexanone in Zr MOFs as a function of relative catalytic activity on a per Z_6O_8 basis. Data appear to show more constrained, less active MOF topologies generally lead to higher *cis* product selectivity. *ZrO_2 is included as reference for selectivity. T.O.N. is on a per Zr atom basis, rather than Zr_6.

In MPV reduction of 4-*tert*-butylcyclohexanone, *trans*-4-*tert*-butylcyclohexanol is the thermodynamically preferred isomer due to the stability of ring substituents; however, some pore environments in zeolites have been shown to destabilize the transition state for the *trans* isomer, leading to high selectivity (>95%) for the *cis* isomer.[52, 238] 8-connected MOFs are shown to increase selectivity for the *cis* product up to 30% from 10% in MOF-808 and 4% in non-porous low surface area ZrO_2. These results demonstrate that more crowded linker geometries around the active site generally exert influence over selectivity as a tradeoff for rates of conversion in stereoselective MPV reduction. The slight exception to this observation is NU-1200, which displays less steric influence than NU-1000 and NU-901, but significantly slower rates. We suspect this material may be so slow that activity is dominated by defect sites within the material, rather than topologically engineered coordination sites. However, it still shows greater *cis* selectivity than the non-8-connected MOFs.

5.3.3. Density Functional Theory Investigation (DFT) of MPV Mechanistic Pathways in 6- and 8-connected Topologies

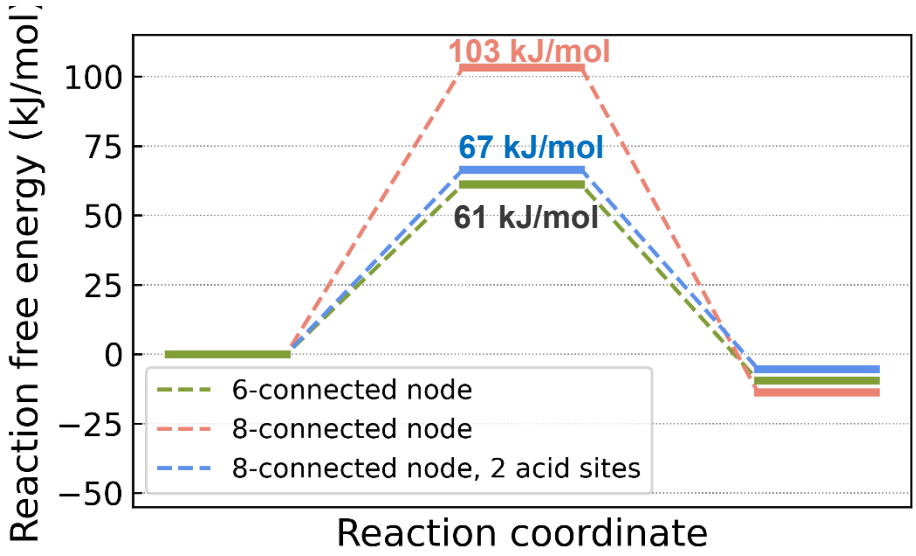

Figure 5.3.3.1. Reaction diagram for 8- and 6-connected Zr nodes. Barriers calculated via DFT.

Computationally testing the hypothesis that topology influences the kinetic favorability of MPV reduction, we collaborated with the Snurr group to model MPV reduction of cyclohexanone by isopropanol over 6-connected and 8-connected cluster models. In our calculations we modeled the 1-acid site pathway, where isopropanol and cyclohexanone adsorb on the same Zr site, forming an intermediate, comprised of alcohol, ketone, and the Lewis acid (Zr). Following this, co-adsorbed substrates go through a hydride transfer from alcohol to ketone, forming a six-membered ring transition state, in line with the model proposed by Komanoya et al.[226] We additionally modeled the 2-site pathway for the 8-connected cluster, where reactants adsorb at adjacent Lewis acids, forming an 8-membered ring transition state. Modeling of the 2-site pathway for the 6-connected cluster is still in progress.

Initially examining co-adsorption of reactants at the same Zr atom, our findings reveal that the 1-site reaction is energetically downhill, as demonstrated by the Gibbs free energy, ΔG, of the product being lower than that of the reactant by 9 and 14 kJ/mol for the 6 and 8-connected nodes, respectively. (**Figure 5.3.3.1.**) Strikingly, the 1-site pathway on the 6-connected node is significantly more favorable than on the 8-connected node, with an energy barrier of 61 kJ/mol vs. 103 kJ/mol for the 8-connected model. We attribute this kinetic favorability to the lesser degree of bend required in the $O_{alcohol}$-Zr-O_{ketone} angle during the reaction within the 6-connected node scenario. The angle changes from 72° to 70° for the 6-connected node, and from 101° to 79° for the 8-connected node. This less pronounced deformation results in a reduced energy penalty. (**Figure 5.3.3.2.**) Additionally, the effective distance of proton translation (assuming the transition state geometry) in the more kinetically favored scenario is shorter by 0.06 Å, further contributing to a lower transition state energy. Finally, structural data show that hydride transfer on the 8-connected node occurs through a pore window of the MOF, requiring structural linkers to rotate

and distort to accommodate the steric bulk of the transition state, and thereby giving mechanistic plausibility to the influence of linker geometry and flexibility upon product selectivity.

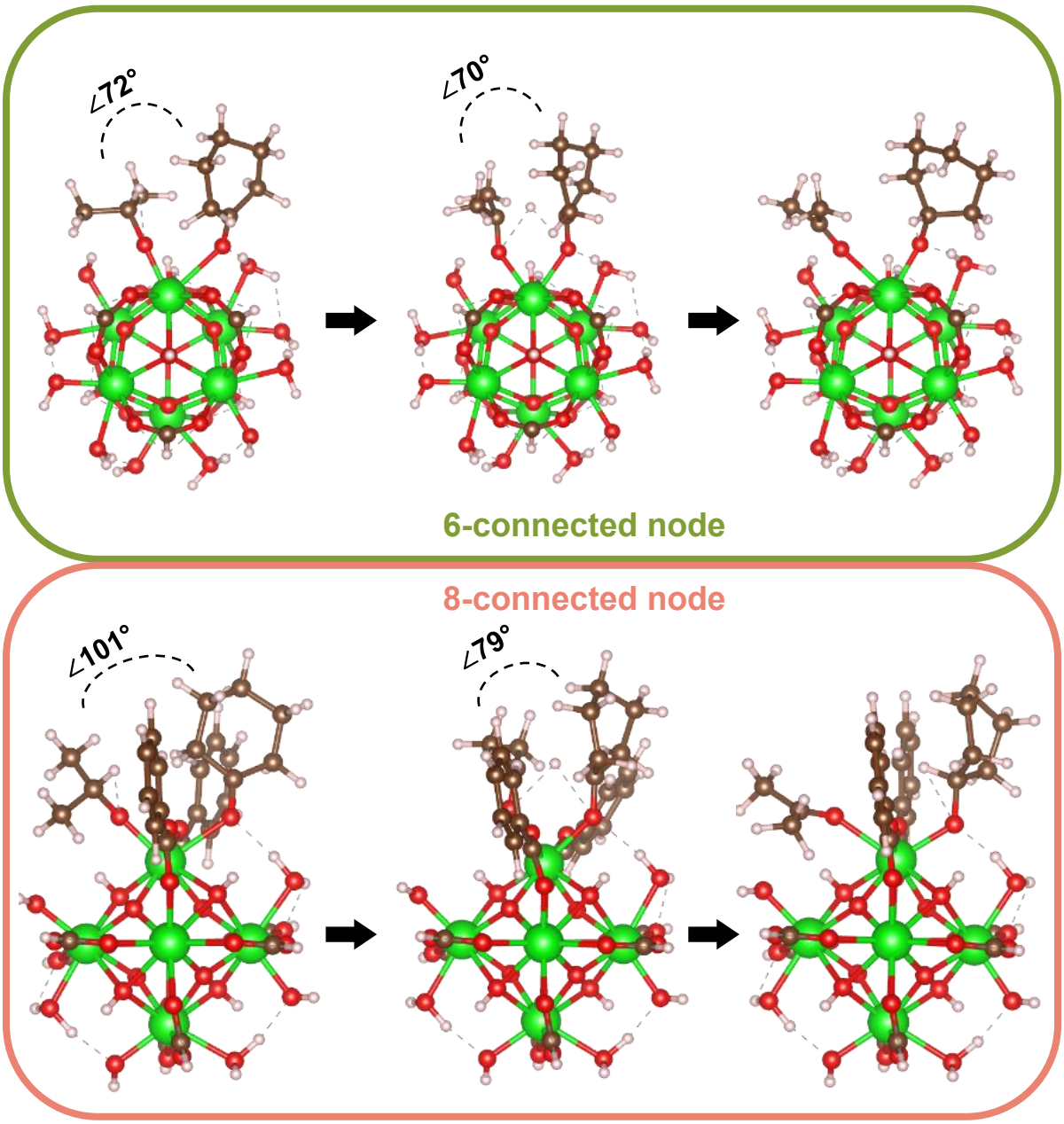

Figure 5.3.3.2. Reactants, transition states, and products of MPV reduction (from left to right) calculated for 6- and 8-connected nodes. Zr–O–Zr bond angles are emphasized for reactants and transition states for clarity.

When examining the pathway of substrate adsorption at adjacent Lewis acid sites, followed by the formation of an 8-membered ring transition state, we see a significantly lower barrier for the 8-connected cluster of 67 kJ/mol. This 2-site barrier is over 30 kJ/mol lower than the calculated 1-site barrier for MPV on 8-connected nodes, suggesting adjacent, 2-site pathways are much more favorable and predominately active in 8-connected MOFs. However, this barrier is also 6 kJ/mol higher than the 1-site barrier calculated for the 6-connected node of MOF-808, indicating MPV reduction is more favorable over 6-connected nodes, regardless of the mechanistic pathway over 8-connected nodes.

While calculations for 2-site pathways over 6-connected nodes are still ongoing, these preliminary results help to provide a fuller understanding of catalytic data for MPV reduction in 6 and 8-connected MOFs. In NU-1000 and other 8-connected MOFs, the significantly most favored pathway is hydride transfer across two adjacent Lewis acid sites. In the more geometrically restrictive node connectivity, this leaves only one viable neighboring Lewis acid site for fruitful reactivity, as hydride transfer using *cis* adsorption sites is highly disfavored. This thereby limits the number of productive configurations of substrates to 1. In contrast, hydride transfer is likely favorable between substrates at both *cis* **and** adjacent adsorption sites in the 6-connected topology of MOF-808, consistent with other mechanistic studies in Zr-MOFs.[240, 242] This suggests that parallel kinetic pathways are occurring for MPV reduction on the 6-connected node, and for every adsorbed ketone, there are 3 neighboring hydride donors, increasing the number of productive configurations and the likelihood of catalytic activity. (**Scheme 5.3.3.1.)** We propose that this increased configurational entropy in reactant intermediates on six connected nodes compounded with differences in the intrinsic barriers of reactivity for each material and pathway likely result in the observed orders of magnitude differences in catalytic yields.

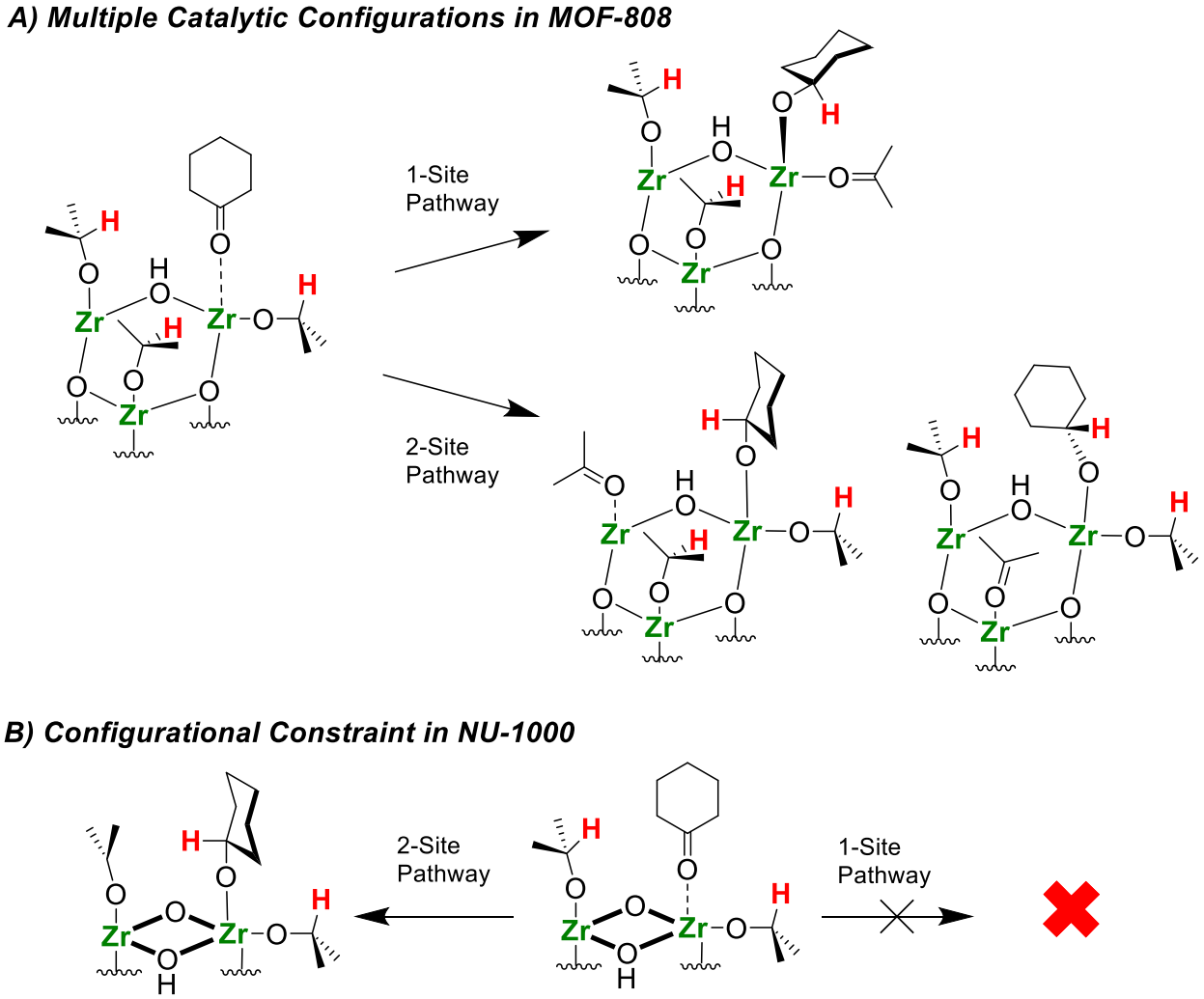

Scheme 5.3.3.1. Schematic representation of substrates for MPV reduction of cyclohexanone, adsorbed on 6- (top, A) and 8-connected (bottom, B) clusters. Clusters are truncated, and linkers and some bridging oxo/hydroxyl ligands are omitted for visual clarity. In the case of MOF-808, multiple hydride donors can coordinate near and access cyclohexanone from neighboring atoms on the same face of the Zr_6 octahedron, or at the same Zr atom vertex. In contrast, hydride donors can only adsorb and access cyclohexanone from one neighboring Zr, along the octahedron edge, leading to fewer productive pathways for MPV reduction.

5.4. Conclusions and Outlook

Overall, computational and experimental results together show that MOF-topology, which dictates linker connectivity around the Zr_6O_8 node, significantly affects the catalytic behavior of structural defects and coordination sites through control over orientation with which substrates adsorb. While lower cluster connectivity for 6-connected MOFs results in higher catalytic yields

and activity on a per site basis, 8-connected MOFs appear to exert more steric influence over product selectivity. Additionally, added structural motifs appear to have influence over other aspects of catalytic performance for MPV reduction, e.g., framework flexibility and linker rotation influencing the steric environment of the reaction. These results provide additional structural parameters when considering or designing potential MOF-based MPV reduction catalysts, in addition to the established parameters of active site Lewis acidity and defect quantity.

Next steps in this work could involve expansion of these studies to alternate but related topologies, such as *kgd*, which is 6-connected, but with inverted linker connectivity and adsorption sites, relative to the *spn* topology of MOF-808. Additionally, in terms of influencing product selectivity, channels in zeolites have shown greater influence over 4-*tert*-butylcyclohexanone selectivity. Given this, one could target Zr-chain MOFs in the MIL-140 series, which possess channels of various sizes, that might have greater influence over transition state selectivity. Finally, calculations are still underway for the 8-membered ring transition state barrier in MOF-808. While they will not be available in time to make it into this document, they will likely provide additional insight into this preliminary work, bolstering present conclusions, and/or adding nuance to understanding of structural effects on MPV activity. Those results will most likely be available with this research when published in an academic journal.

5.5. Additional information.

5.5.1. Experimental Details

Catalyst Synthesis

All MOFs (NU-1000, NU-901, NU-1200, UiO-66, UiO-67, MOF-808, and Hf-MOF-808) were synthesized, washed, and activated according to reported literature procedures.[94, 98, 117, 184, 215, 248, 250, 251] In the case of NU-1000, UiO-66, UiO-67, and MOF-808, due to scalability of procedures,

MOFs were made on 2-5 g scales to reduce batch to batch variability. Hf-MOF-808 was made on a 250 mg scale, and NU-901 and NU-1200 were made in parallel, small 20 mg batches, which were combined into larger batches for each respective MOF.

Catalytic Experimentation

In all experiments comparing MOF catalysts, fresh stock solutions of substrates were made to predetermined concentrations in isopropanol, and reactions were done in parallel 1.5-dram vials on the same shaker plate. This was done in order to avoid differences in variability between MOFs due to variability in stock solution concentration, moisture levels, temperature controlling, and other factors. All reactions were done at 80°C with a shaker plate rotation set to 500 rpm. Shaker plate was also preheated to reaction temperature before adding samples. Additionally, 5-6 mg of catalyst were added to each vial.

When collecting reaction time points or other data, vials were removed from the shaker plate, allowed to cool to touch, and then reaction solutions were filtered using glass fiber syringe filters. Liquid contents were then placed in GC vials and then sampled via GC-FID. Products and reactants were quantified using o-xylene as internal standard.

T.O.N. for MOFs were calculated via molecular weights for each material, calculated using linker to node ratios via crystal structure formulas, or ratios obtained from thermogravimetric analysis, in the case of UiO-66 and UiO-67. Additionally, when normalizing to accessible Zr atoms, rates were divided by crystallographically or experimentally determined values. In the case of ZrO_2, values were calculated according to methods reported in Gonell et al.[237]

Computational methodology

DFT calculations were performed with Gaussian 16, Rev. C03 software[185] using M06-L exchange-correlation functional[186] and def2-TZVP basis set[187] for all elements (with ECP for Zr). D3 dispersion correction was applied to account for long-range van der Waals interactions.[252] The Zr_6O_8 clusters were cleaved from the experimental structures of NU-1000 (8-connected node) and MOF-808 (6-connected node). The linkers' sites were capped by formate modulators for simplicity, except for 2 sites adjacent to the reaction site for the 8-connected node, which are capped by benzoate to mimic the presence of tetratopic aromatic linker. The rest of the acid Zr sites not participating in the reaction are capped with OH H_2O pairs (1 OH and 1 H_2O per 1 Zr site) following the most thermodynamically stable mix-S proton topology.[89] The reactions were modeled in the closed-shell singlet states. The transition states were obtained with the Berny optimization algorithm with the initial guess obtained from 'soft scan' calculations where the proton was iteratively translated between alcohol and ketone with the optimization of all other degrees of freedom. Both stationary and transition states were confirmed with vibrational frequency (0 and 1 imaginary frequencies, respectively). Thermodynamic functions were calculated at 298 K and 1 atm with GoodVibes (version 3.2).[23] The frequencies were scaled by the factor of 0.976[190] and the frequency cutoff of 100 cm^{-1} was applied.

5.5.2. Characterization

UiO-66 Synthesis

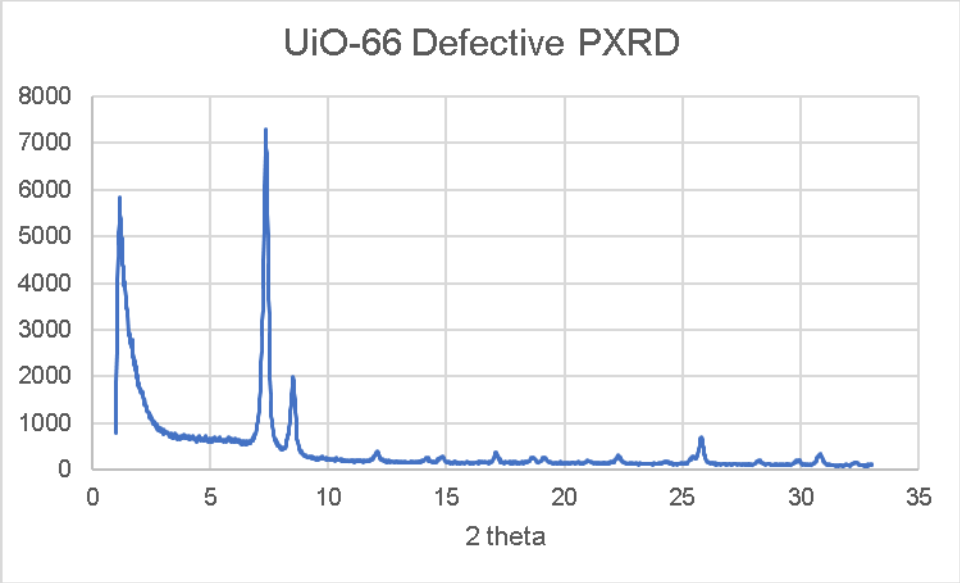

Figure 5.5.2.1. Powder X-Ray Diffraction pattern for defective UiO-66.

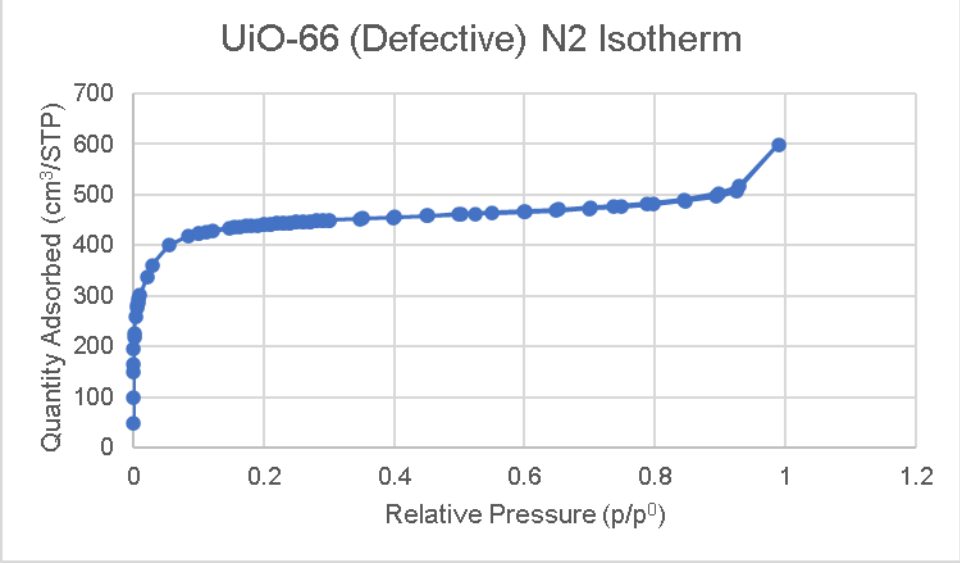

Figure 5.5.2.2. N_2 adsorption isotherm for defective UiO-66 at 77 K.

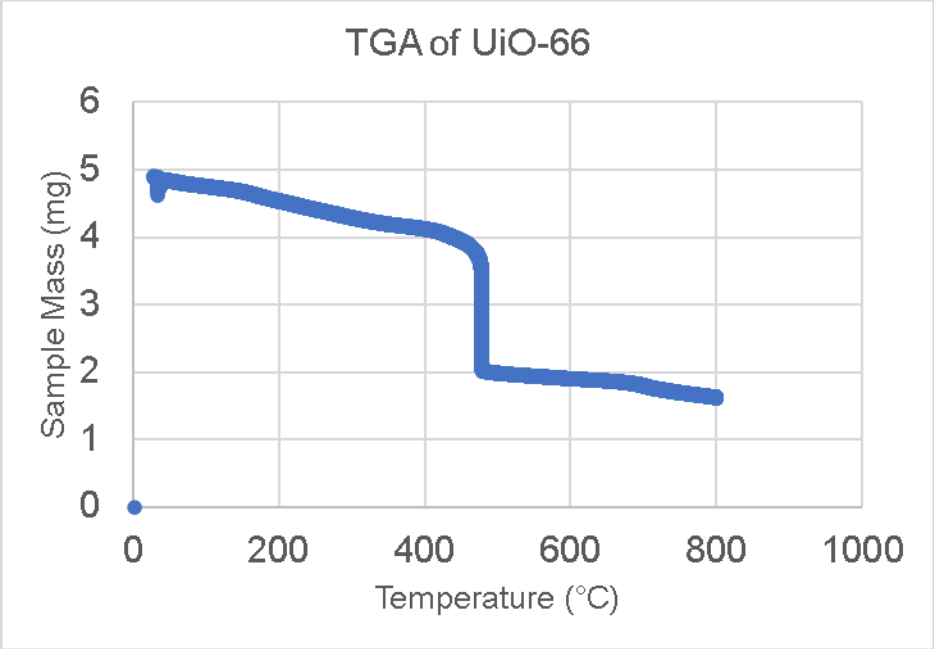

Figure 5.5.2.3. Thermogravimetric analysis of defectively synthesized UiO-66. Linker-to-node ratio calculated to be 3.7 based on mass differences. (1.8 mg linker, 2 mg node)

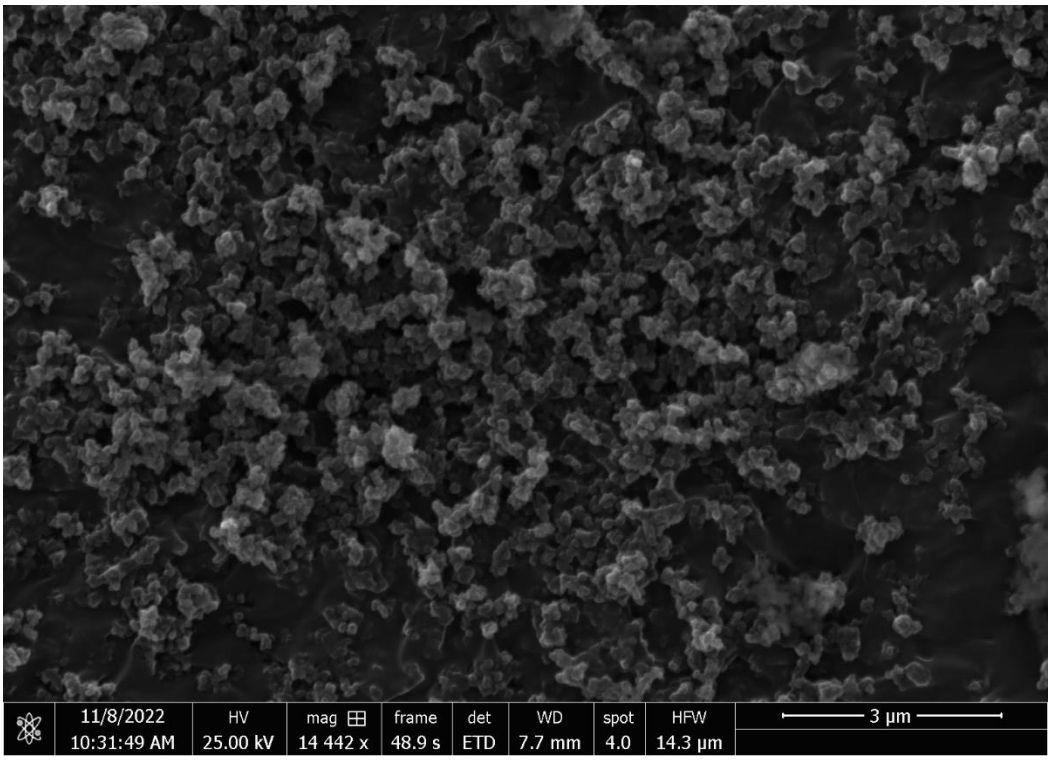

Figure 5.5.2.4. Scanning Electron Microscopy image of defective UiO-66, showing crystallites around 200 nm in size. In some cases, crystallites are agglomerated into larger particles.

NU-1000 Synthesis

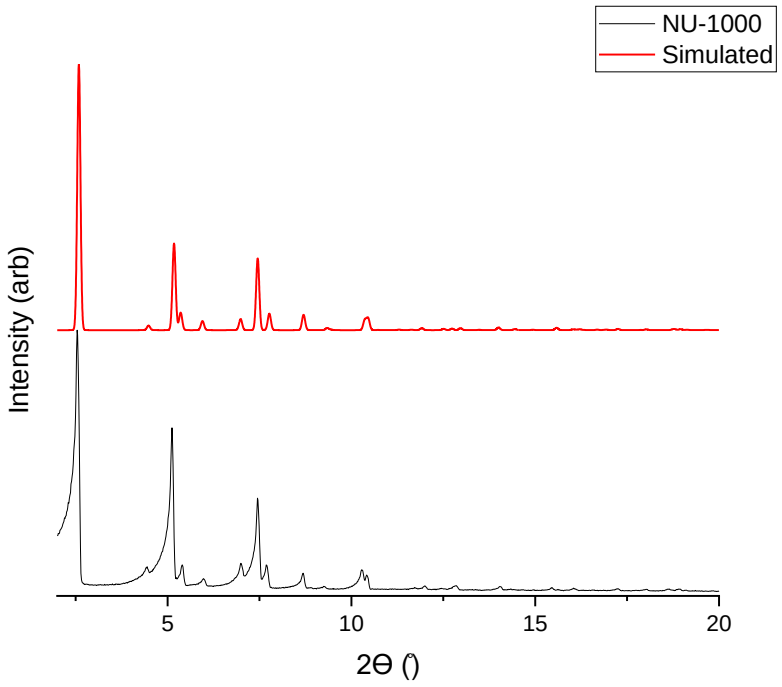

Figure 5.5.2.5. Powder X-ray Diffraction pattern of NU-1000 (black) and simulated pattern from NU-1000 crystal structure (red).

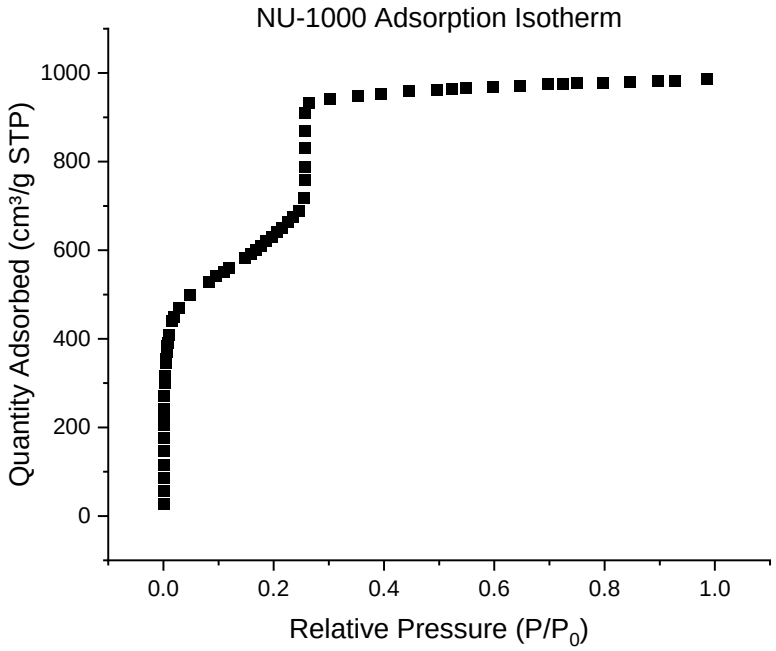

Figure 5.5.2.6. N_2 adsorption isotherm of NU-1000 at 77 K.

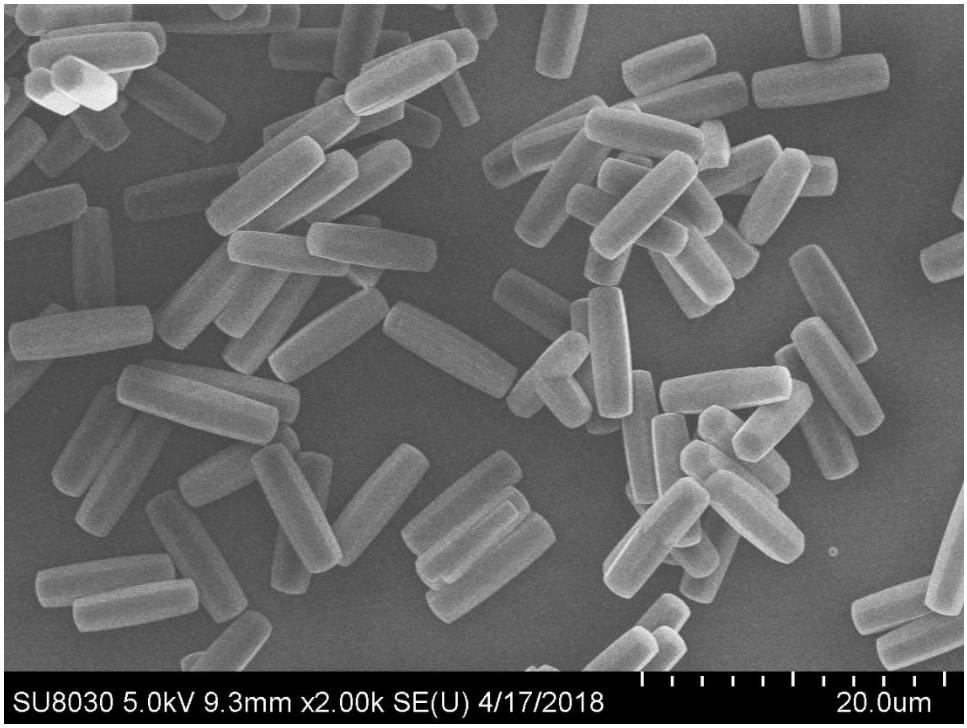

Figure 5.5.2.7. SEM of NU-1000 Crystallites. Particles are approximately 9 μm long and 2.5 μm wide.

NU-901

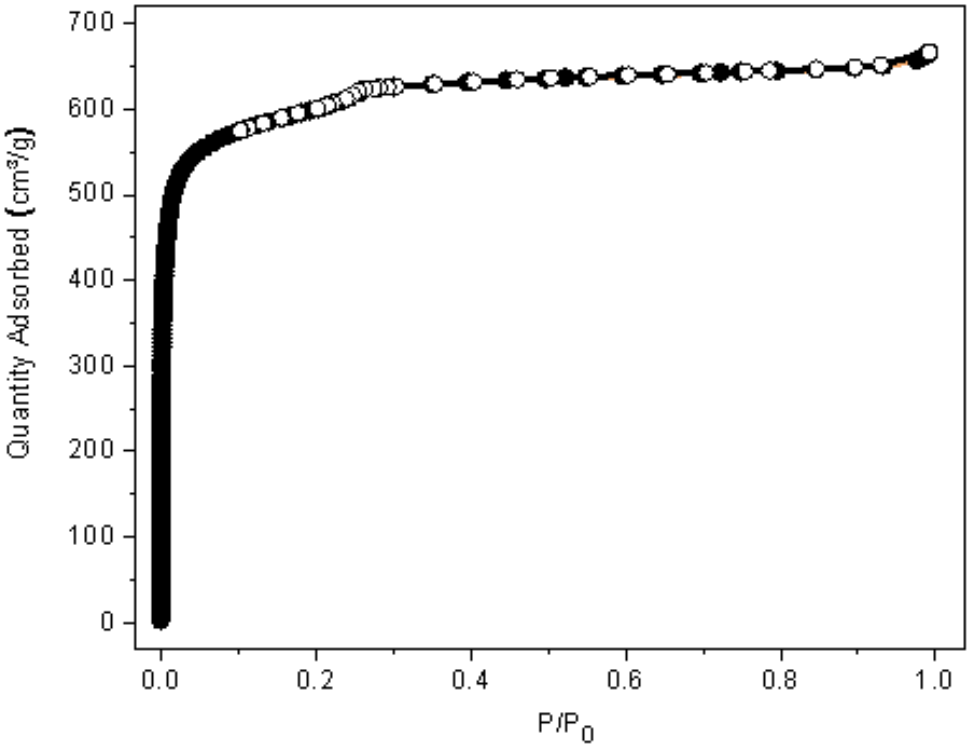

Figure 5.5.2.8. N_2 adsorption isotherm of NU-901 at 77 K.

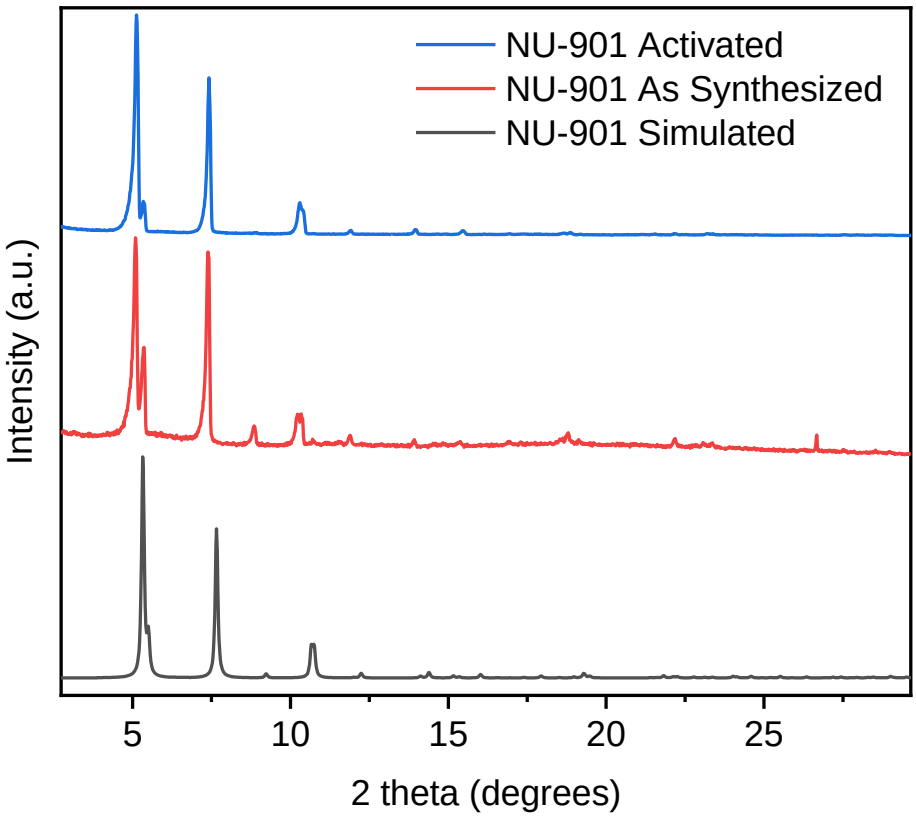

Figure 5.5.2.9. Powder X-ray Diffraction pattern of NU-901, simulated (black), as-synthesized pattern (red), and after thermal activation (blue).

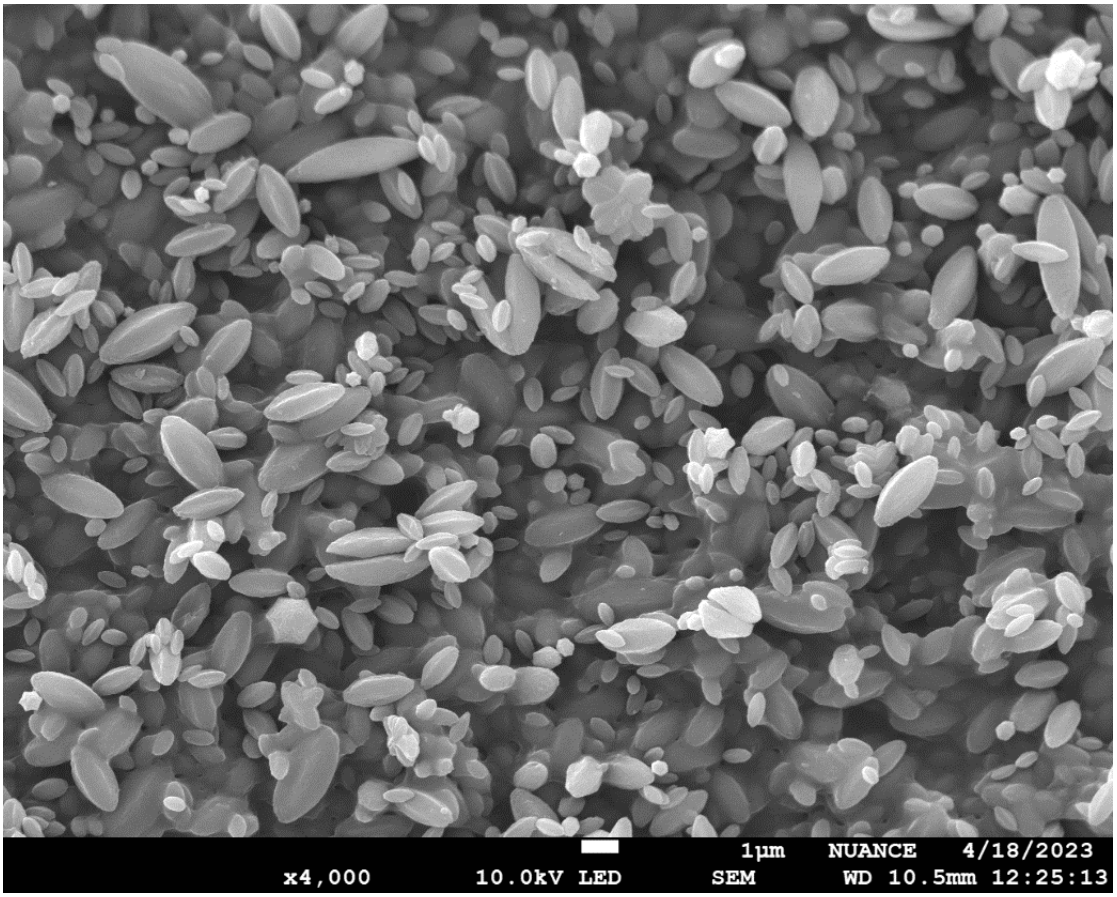

Figure 5.5.2.10. SEM Image of NU-901. Particles of varying size are observed due to mixing of synthetic batches.

MOF-808-OH

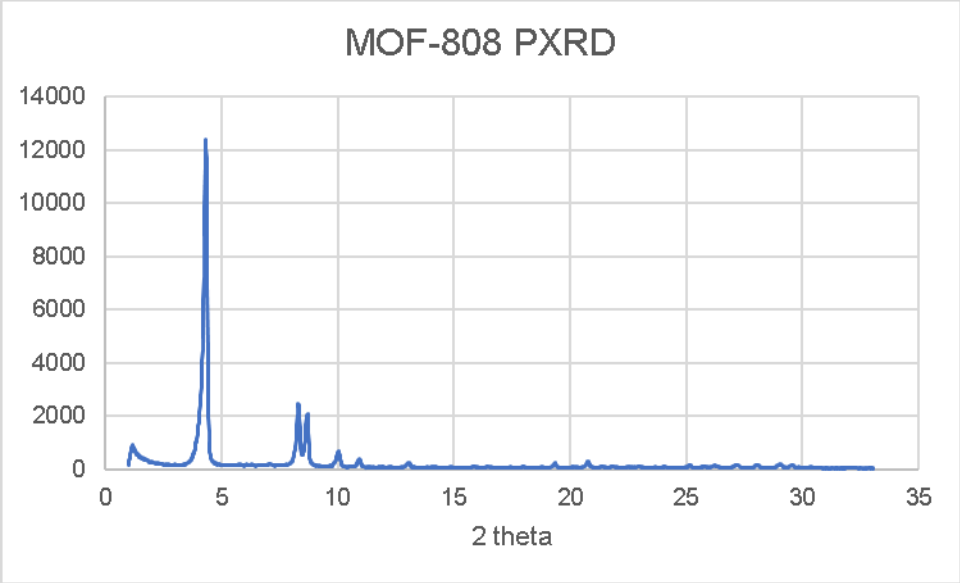

Figure 5.5.2.11. Powder X-Ray Diffraction pattern MOF-808-OH.

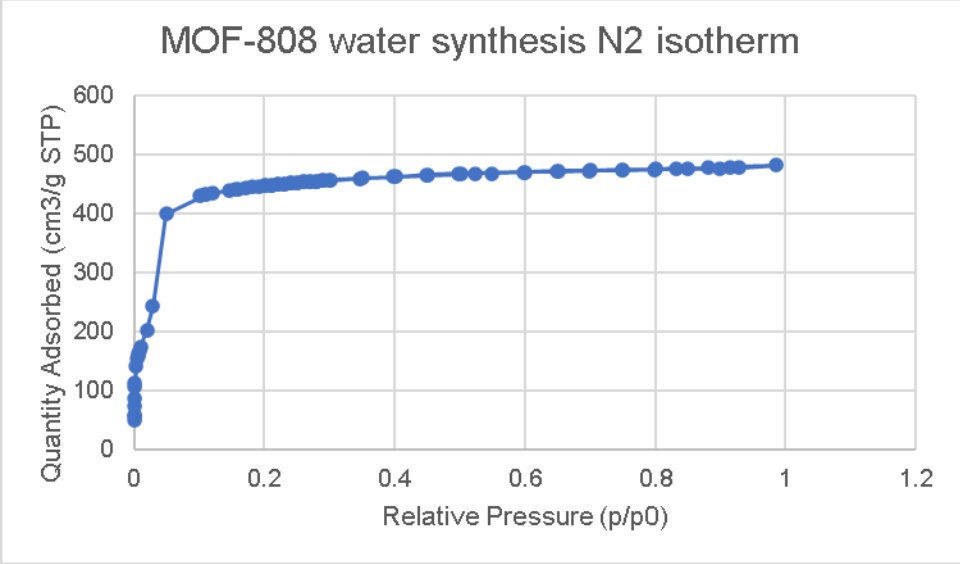

Figure 5.5.2.12. N_2 adsorption isotherm of MOF-808-OH at 77 K

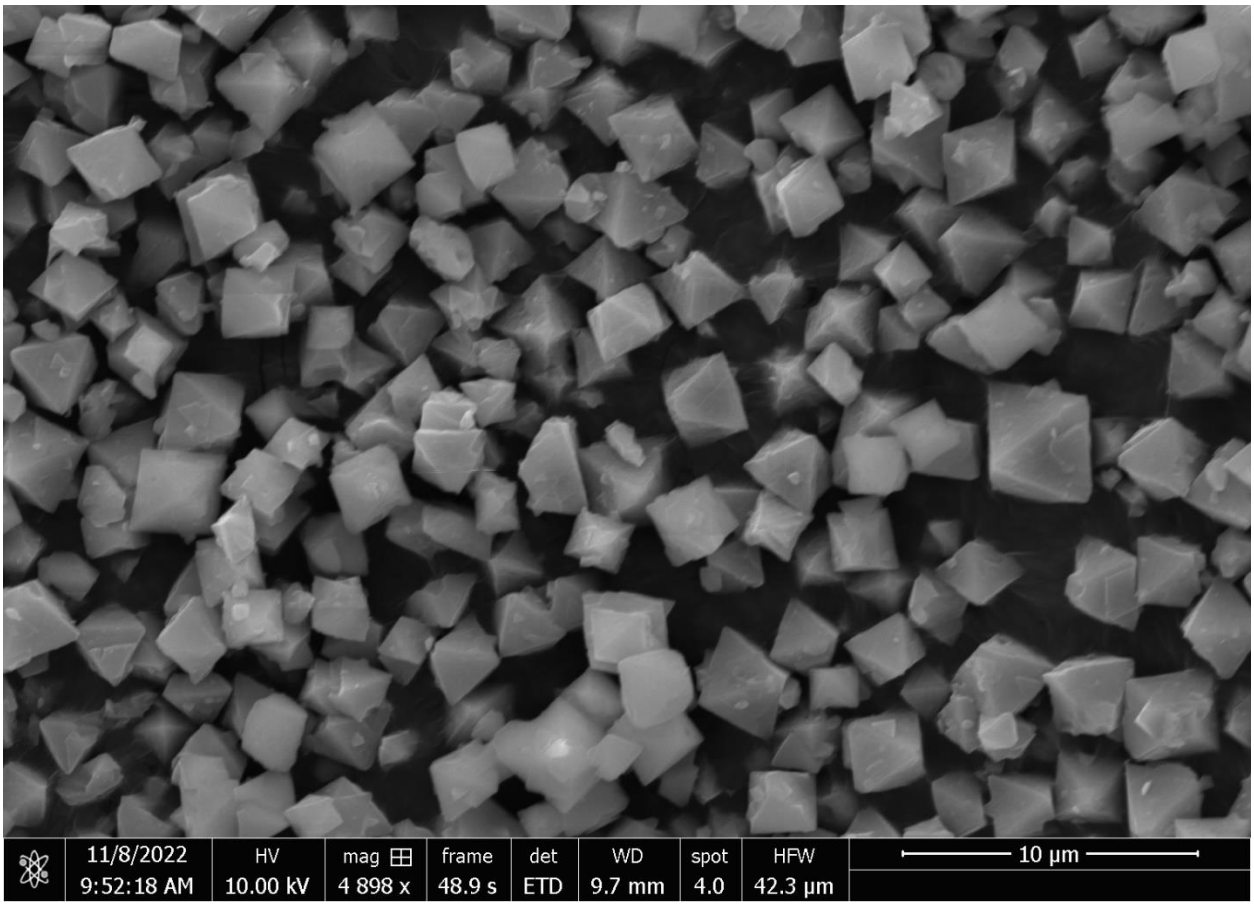

Figure 5.5.2.13. SEM image of MOF-808 OH. Particles ranging from 2-10 µm are observed.

MOF-808-F

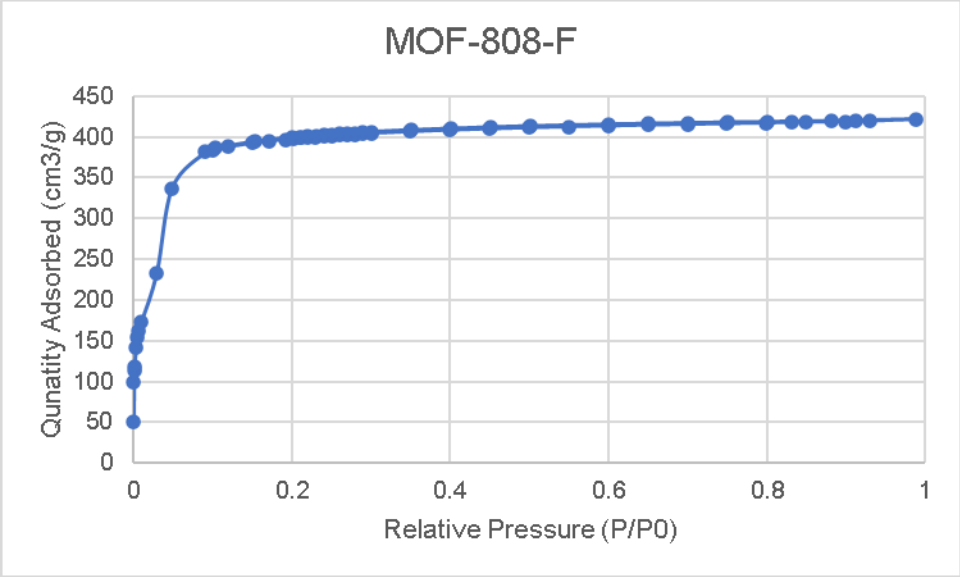

Figure 5.5.2.14. N_2 adsorption isotherm of MOF-808-F at 77 K

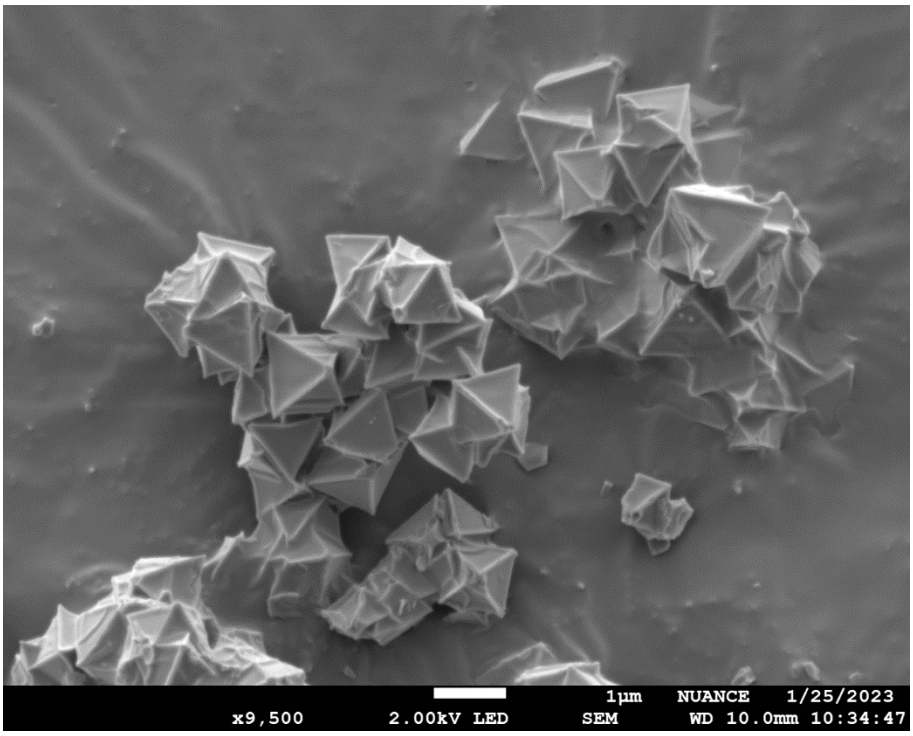

Figure 5.5.2.15. SEM Image of MOF-808-F. Parke sizes are around 1-2 µm in diameter.

Hf-MOF-808-F

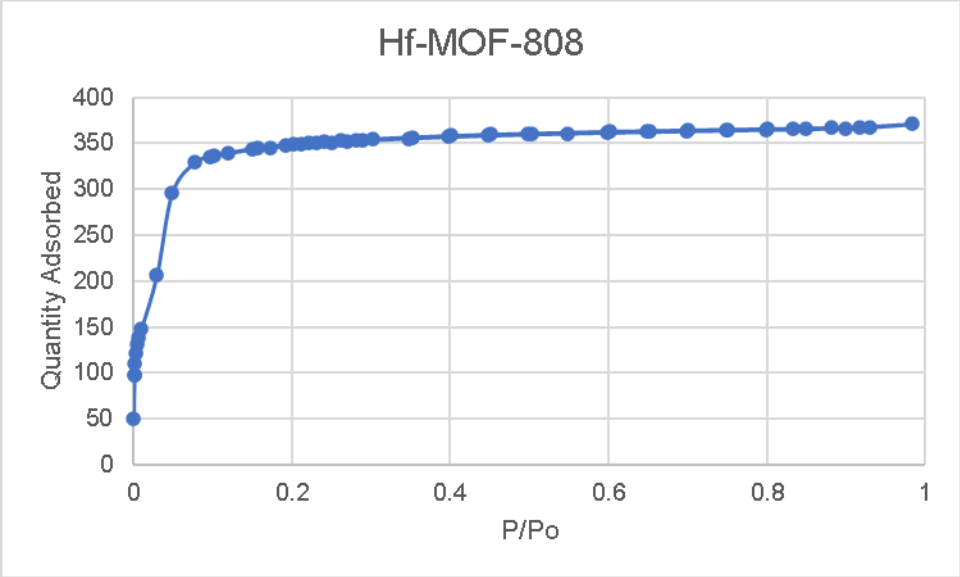

Figure 5.5.2.16. N_2 adsorption isotherm of Hf-MOF-808-F at 77 K

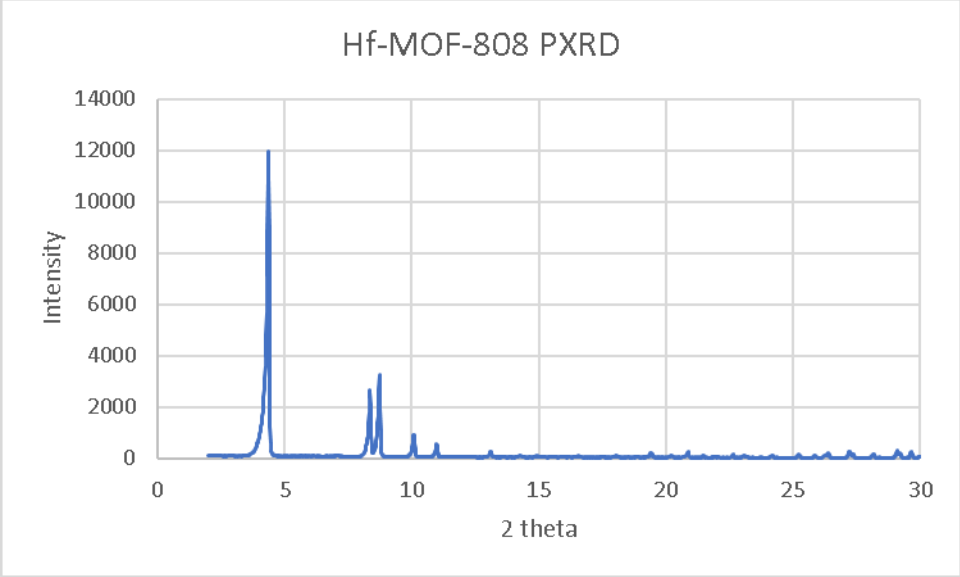

Figure 5.5.2.17. PXRD pattern for Hf-MOF-808-F.

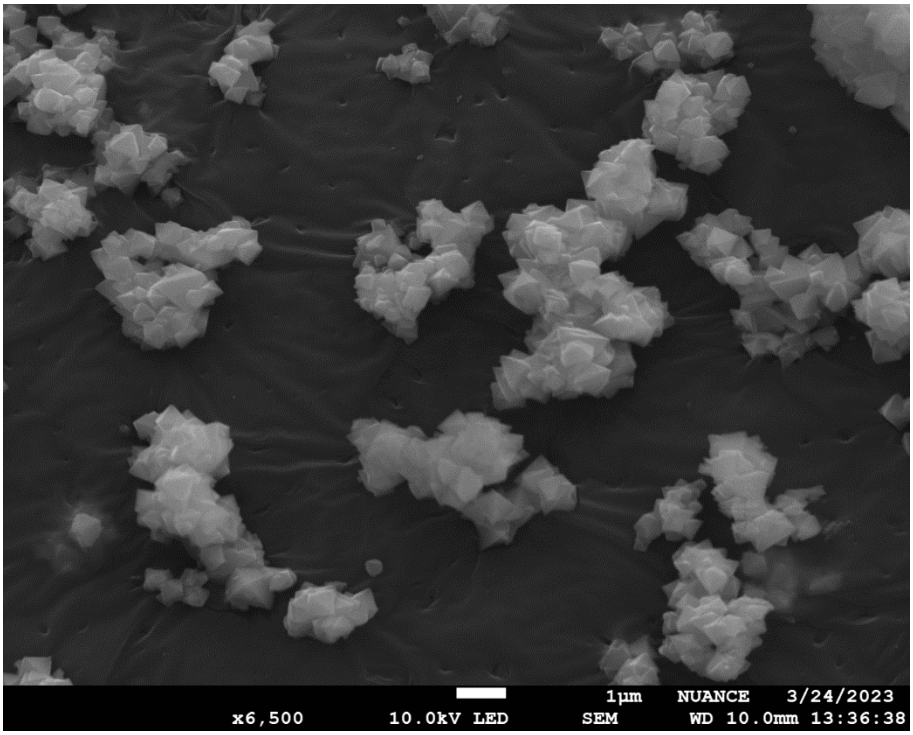

Figure 5.5.2.18. SEM of Hf-MOF-808-F. Crystallites are between 0.5-1 µm in size.

UiO-67

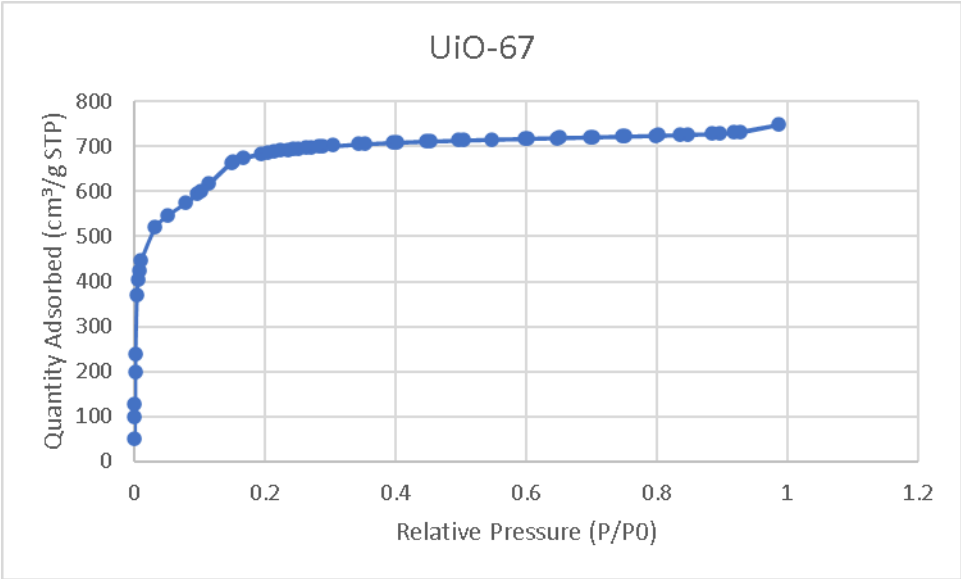

Figure 5.5.2.19. N_2 adsorption isotherm of defective UiO-67 at 77 K.

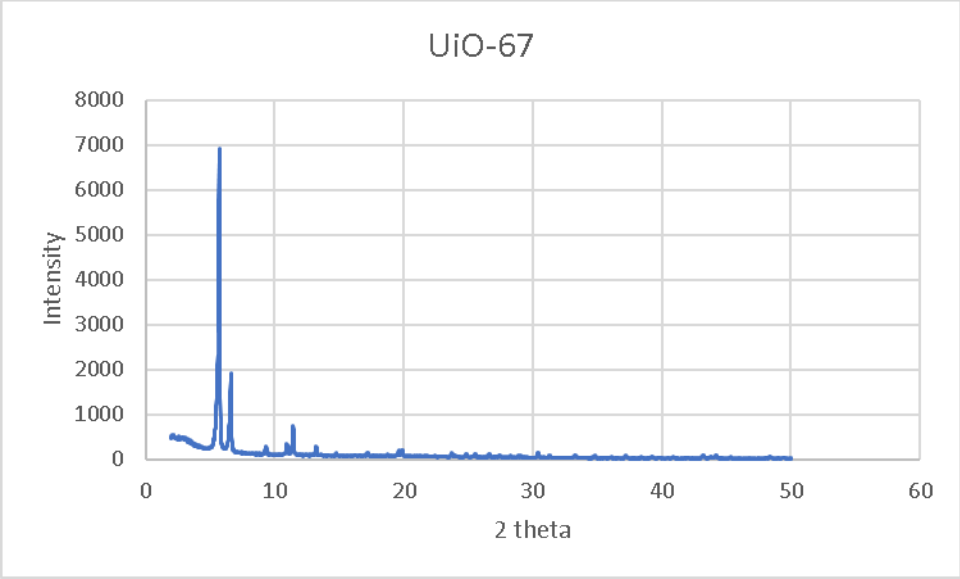

Figure 5.5.2.20. PXRD pattern for UiO-67.

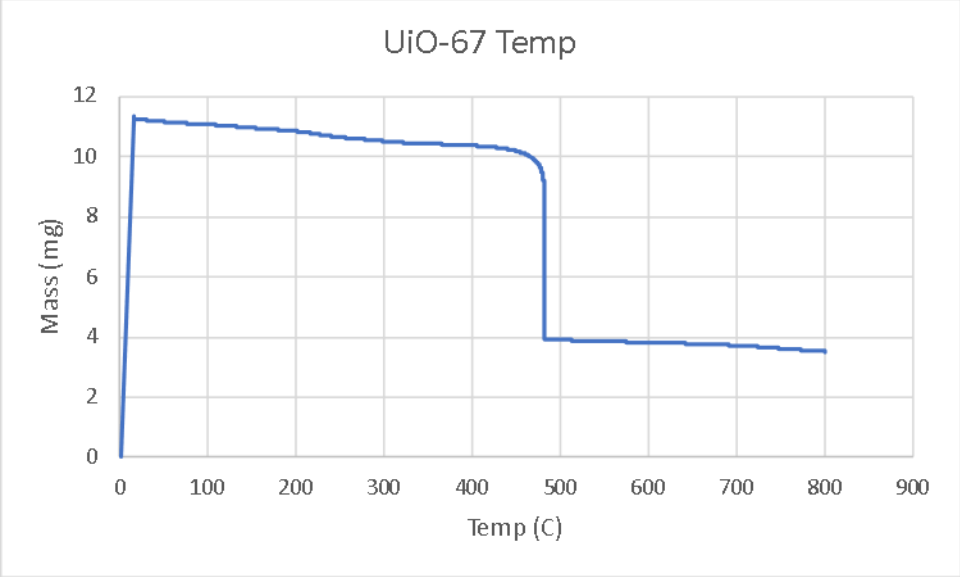

	(approx mass)		mass%	MW	mg*mol/g	linker/nod
linker	10	6	0.6	240.214	0.024978	4.21709
node	4		0.4	675.336	0.005923	

Figure 5.5.2.21. Thermogravimetric analysis of defectively synthesized UiO-67. Linker-to-node ratio calculated to be 4.2 based on mass differences. (6 mg linker, 4 mg node)

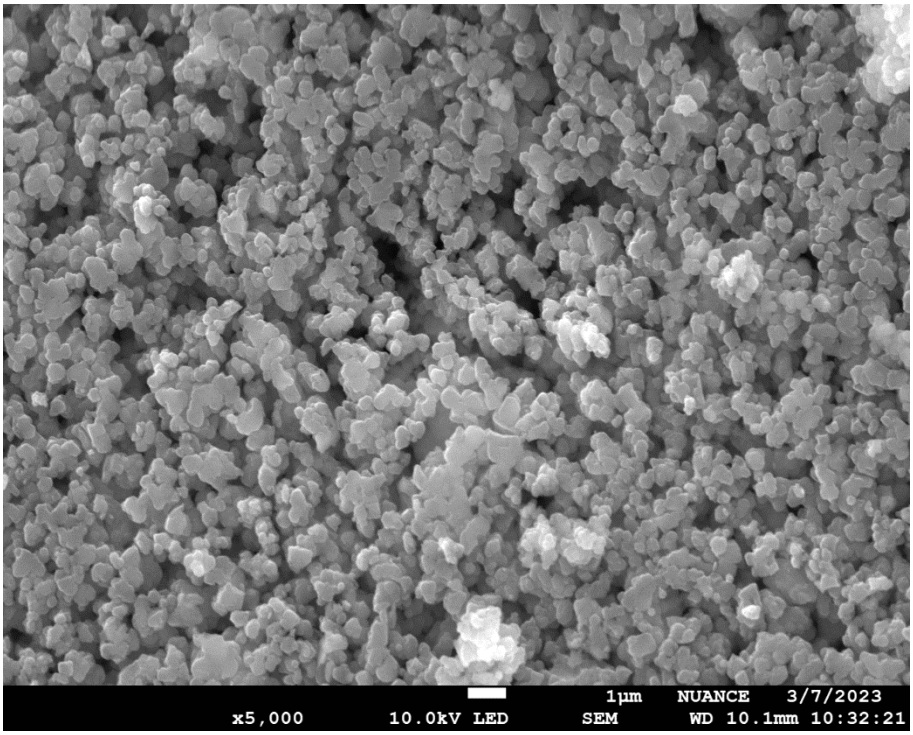

Figure 5.5.2.22. SEM of UiO-67. Crystallites are between 0.5-1 µm in diameter.

NU-1200

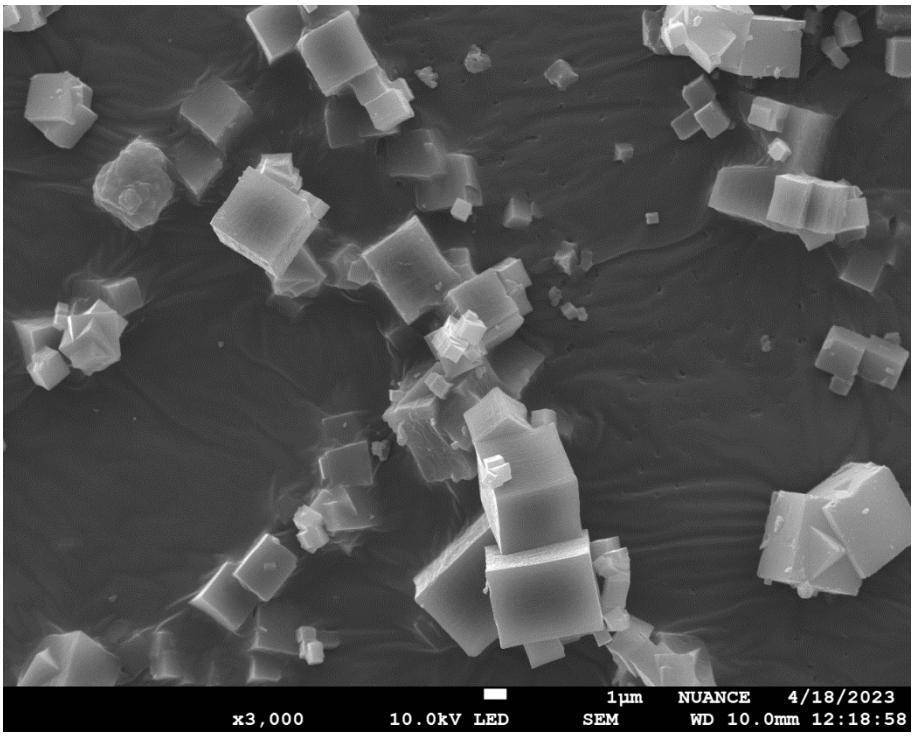

Figure 5.5.2.23. SEM of NU-1200. Crystallites are between 1-5 µm in diameter.

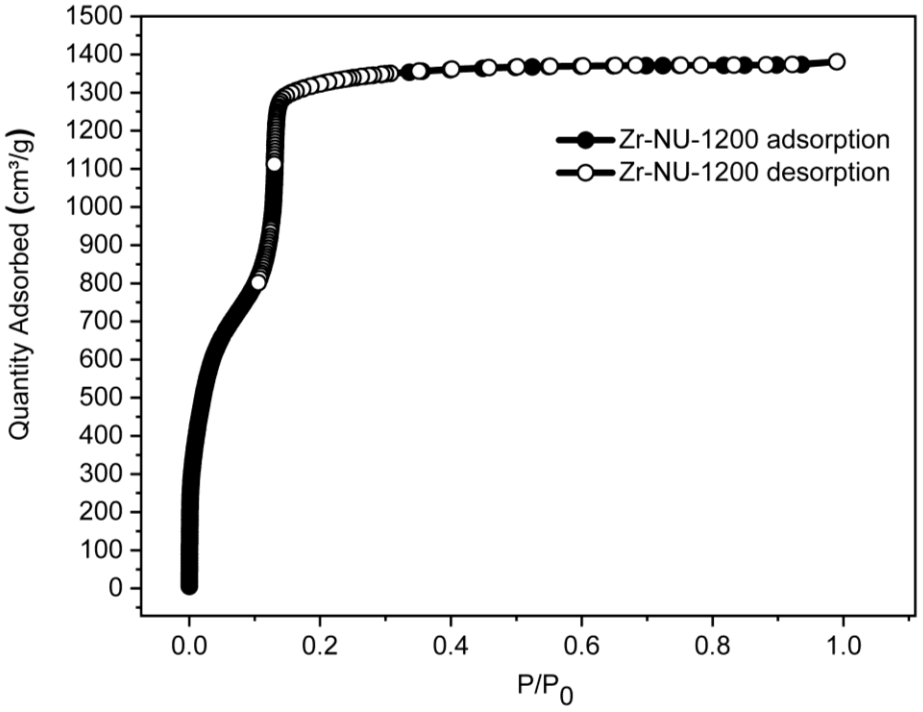

Figure 5.5.2.24. N_2 adsorption isotherm of defective NU-1200 at 77 K.

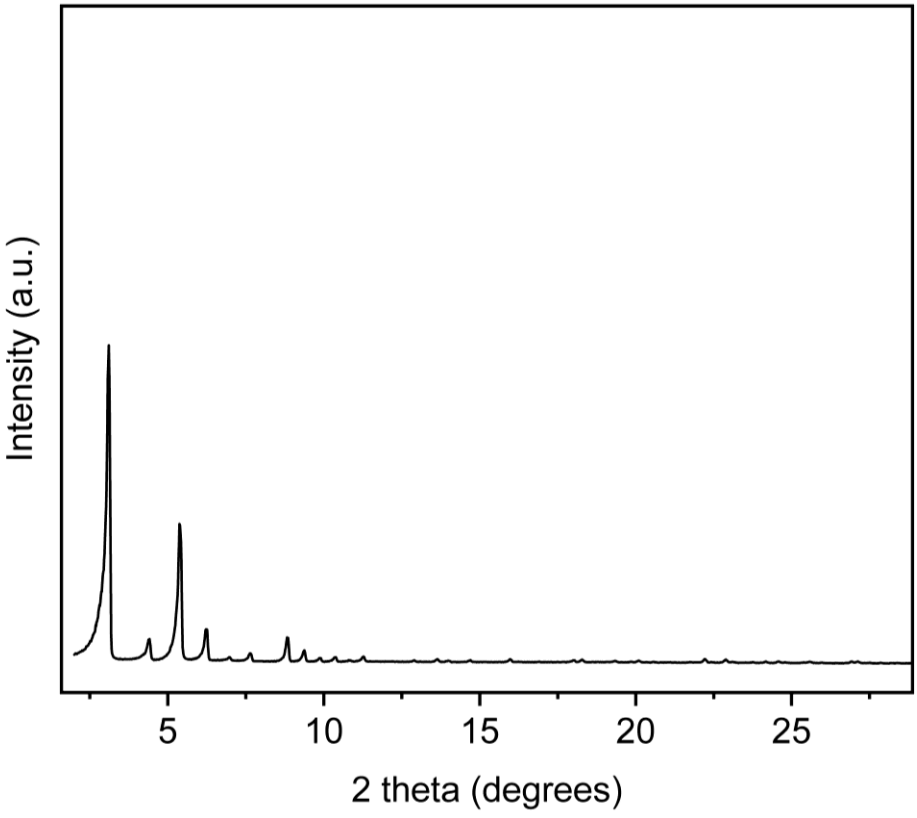

Figure 5.5.2.25. PXRD pattern for NU-1200.

5.5.3. Post Catalysis Analysis of Formate Containing MOFs

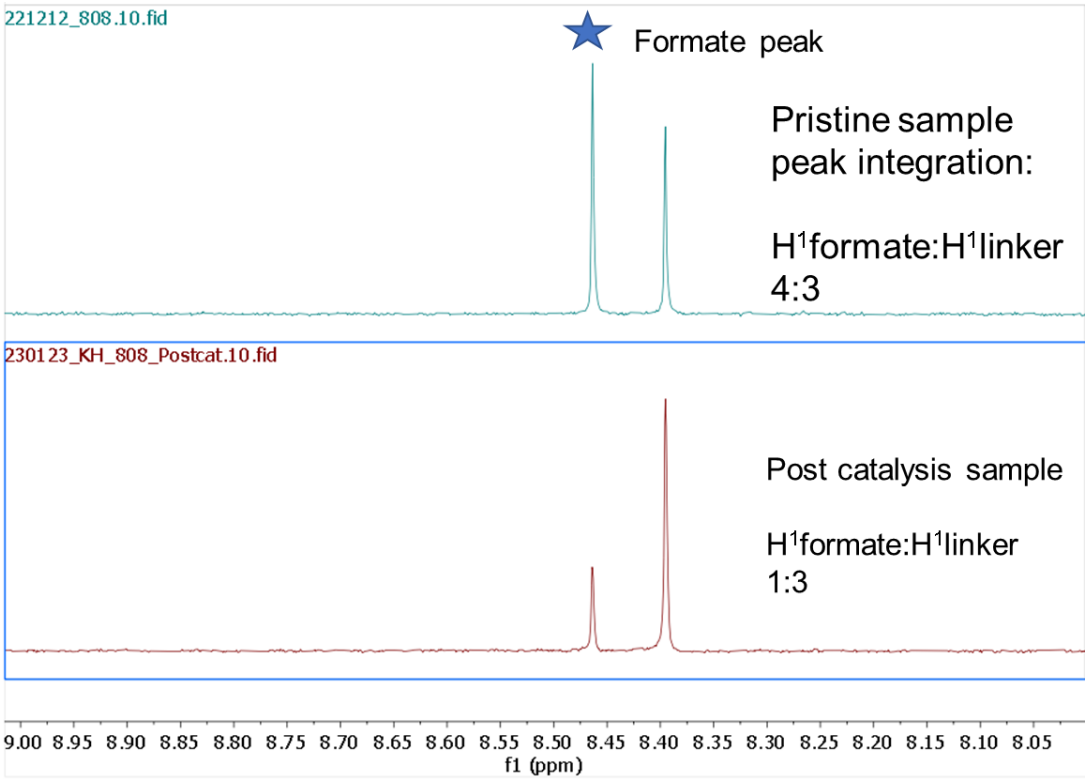

Figure 5.5.3.1 Post catalysis ^{1}H NMR of MOF-808-F.

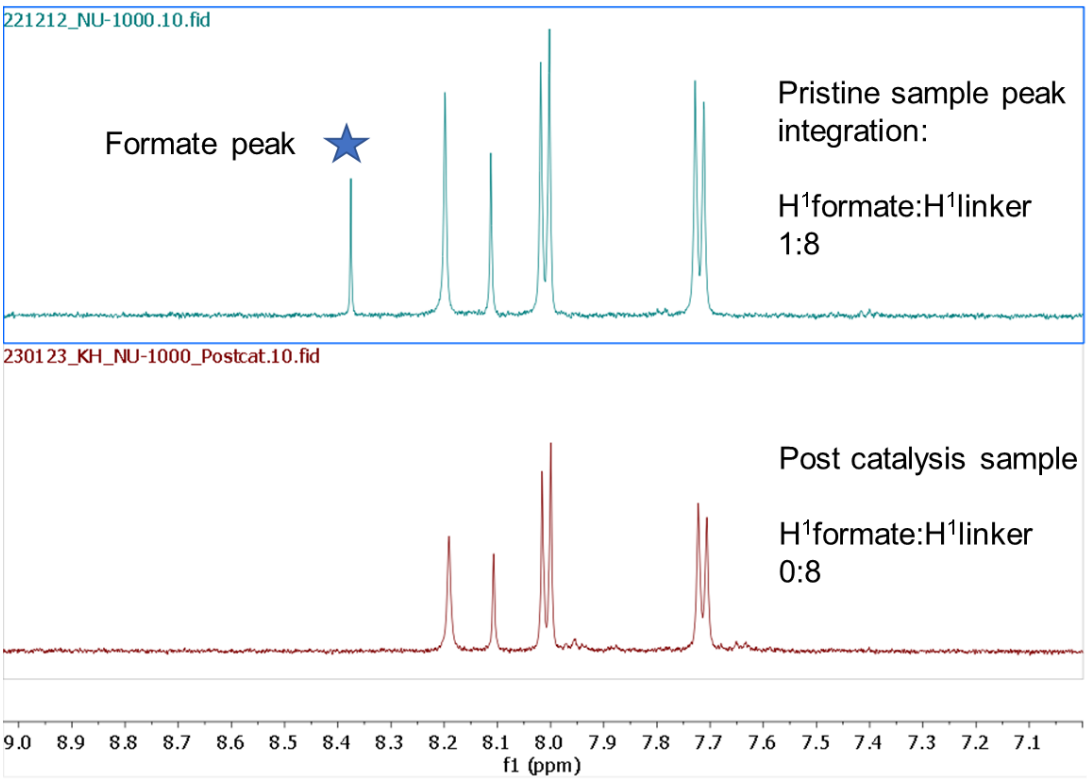

Figure 5.5.3.2. Post catalysis ^{1}H NMR of NU-1000.

REFERENCES

1. Levi, P. G.; Cullen, J. M. Mapping Global Flows of Chemicals: From Fossil Fuel Feedstocks to Chemical Products. *Environmental Science & Technology* **2018**, *52* (4), 1725-1734. DOI: 10.1021/acs.est.7b04573.
2. Hess, J.; Bednarz, D.; Bae, J.; Pierce, J. Petroleum and Health Care: Evaluating and Managing Health Care's Vulnerability to Petroleum Supply Shifts. *American Journal of Public Health* **2011**, *101* (9), 1568-1579. DOI: 10.2105/ajph.2011.300233.
3. Copéret, C.; Allouche, F.; Chan, K. W.; Conley, M. P.; Delley, M. F.; Fedorov, A.; Moroz, I. B.; Mougel, V.; Pucino, M.; Searles, K.; et al. Bridging the Gap between Industrial and Well-Defined Supported Catalysts. *Angewandte Chemie International Edition* **2018**, *57* (22), 6398-6440. DOI: 10.1002/anie.201702387.
4. Pelletier, J. D. A.; Basset, J.-M. Catalysis by Design: Well-Defined Single-Site Heterogeneous Catalysts. *Accounts of Chemical Research* **2016**, *49* (4), 664-677. DOI: 10.1021/acs.accounts.5b00518.
5. Védrine, J. C. Metal Oxides in Heterogeneous Oxidation Catalysis: State of the Art and Challenges for a More Sustainable World. *ChemSusChem* **2019**, *12* (3), 577-588. DOI: 10.1002/cssc.201802248.
6. Copéret, C.; Comas-Vives, A.; Conley, M. P.; Estes, D. P.; Fedorov, A.; Mougel, V.; Nagae, H.; Núñez-Zarur, F.; Zhizhko, P. A. Surface Organometallic and Coordination Chemistry toward Single-Site Heterogeneous Catalysts: Strategies, Methods, Structures, and Activities. *Chemical Reviews* **2016**, *116* (2), 323-421. DOI: 10.1021/acs.chemrev.5b00373.
7. Busca, G. The surface acidity of solid oxides and its characterization by IR spectroscopic methods. An attempt at systematization. *Physical Chemistry Chemical Physics* **1999**, *1* (5), 723-736, 10.1039/A808366E. DOI: 10.1039/A808366E.
8. Rascón, F.; Wischert, R.; Copéret, C. Molecular nature of support effects in single-site heterogeneous catalysts: silicavs.alumina. *Chemical Science* **2011**, *2* (8), 1449-1456, 10.1039/C1SC00073J. DOI: 10.1039/C1SC00073J.
9. Gajan, D.; Copéret, C. Silica-supported single-site catalysts: to be or not to be? A conjecture on silica surfaces. *New Journal of Chemistry* **2011**, *35* (11), 2403-2408, 10.1039/C1NJ20506D. DOI: 10.1039/C1NJ20506D.
10. Amakawa, K.; Sun, L.; Guo, C.; Hävecker, M.; Kube, P.; Wachs, I. E.; Lwin, S.; Frenkel, A. I.; Patlolla, A.; Hermann, K.; et al. How Strain Affects the Reactivity of Surface Metal Oxide Catalysts. *Angewandte Chemie International Edition* **2013**, *52* (51), 13553-13557. DOI: https://doi.org/10.1002/anie.201306620.
11. Sattler, J. J. H. B.; Ruiz-Martinez, J.; Santillan-Jimenez, E.; Weckhuysen, B. M. Catalytic Dehydrogenation of Light Alkanes on Metals and Metal Oxides. *Chemical Reviews* **2014**, *114* (20), 10613-10653. DOI: 10.1021/cr5002436.
12. Yang, D.; Babucci, M.; Casey, W. H.; Gates, B. C. The Surface Chemistry of Metal Oxide Clusters: From Metal–Organic Frameworks to Minerals. *ACS Central Science* **2020**, *6* (9), 1523-1533. DOI: 10.1021/acscentsci.0c00803.
13. Ogba, O. M.; Warner, N. C.; O'Leary, D. J.; Grubbs, R. H. Recent advances in ruthenium-based olefin metathesis. *Chemical Society Reviews* **2018**, *47* (12), 4510-4544, 10.1039/C8CS00027A. DOI: 10.1039/C8CS00027A.

14. Fernandes, R. A.; Jha, A. K.; Kumar, P. Recent advances in Wacker oxidation: from conventional to modern variants and applications. *Catalysis Science & Technology* **2020**, *10* (22), 7448-7470, 10.1039/D0CY01820A. DOI: 10.1039/D0CY01820A.
15. McGuinness, D. S. Olefin Oligomerization via Metallacycles: Dimerization, Trimerization, Tetramerization, and Beyond. *Chemical Reviews* **2011**, *111* (3), 2321-2341. DOI: 10.1021/cr100217q.
16. Sydora, O. L. Selective Ethylene Oligomerization. *Organometallics* **2019**, *38* (5), 997-1010. DOI: 10.1021/acs.organomet.8b00799.
17. Wasson, M. C.; Buru, C. T.; Chen, Z.; Islamoglu, T.; Farha, O. K. Metal–organic frameworks: A tunable platform to access single-site heterogeneous catalysts. *Applied Catalysis A: General* **2019**, *586*, 117214. DOI: https://doi.org/10.1016/j.apcata.2019.117214.
18. Syed, Z. H.; Chen, Z.; Idrees, K. B.; Goetjen, T. A.; Wegener, E. C.; Zhang, X.; Chapman, K. W.; Kaphan, D. M.; Delferro, M.; Farha, O. K. Mechanistic Insights into C–H Borylation of Arenes with Organoiridium Catalysts Embedded in a Microporous Metal–Organic Framework. *Organometallics* **2020**, *39* (7), 1123-1133. DOI: 10.1021/acs.organomet.9b00874.
19. Bavykina, A.; Kolobov, N.; Khan, I. S.; Bau, J. A.; Ramirez, A.; Gascon, J. Metal-Organic Frameworks in Heterogeneous Catalysis: Recent Progress, New Trends, and Future Perspectives. *Chem Rev* **2020**, *120* (16), 8468-8535. DOI: 10.1021/acs.chemrev.9b00685.
20. Trunschke, A.; Hoang, D. L.; Lieske, H. In situ FTIR studies of high-temperature adsorption of hydrogen on zirconia. *Journal of the Chemical Society, Faraday Transactions* **1995**, *91* (24), 4441-4444, 10.1039/FT9959104441. DOI: 10.1039/FT9959104441.
21. Platero-Prats, A. E.; Mavrandonakis, A.; Gallington, L. C.; Liu, Y.; Hupp, J. T.; Farha, O. K.; Cramer, C. J.; Chapman, K. W. Structural Transitions of the Metal-Oxide Nodes within Metal–Organic Frameworks: On the Local Structures of NU-1000 and UiO-66. *Journal of the American Chemical Society* **2016**, *138* (12), 4178-4185. DOI: 10.1021/jacs.6b00069.
22. Shabbir, H.; Pellizzeri, S.; Ferrandon, M.; Kim, I. S.; Vermeulen, N. A.; Farha, O. K.; Delferro, M.; Martinson, A. B. F.; Getman, R. B. Influence of spin state and electron configuration on the active site and mechanism for catalytic hydrogenation on metal cation catalysts supported on NU-1000: insights from experiments and microkinetic modeling. *Catalysis Science & Technology* **2020**, *10* (11), 3594-3602, 10.1039/D0CY00394H. DOI: 10.1039/d0cy00394h.
23. Luchini, G.; Alegre-Requena, J.; Funes-Ardoiz, I.; Paton, R. GoodVibes: automated thermochemistry for heterogeneous computational chemistry data. F1000Res: 2020.
24. Li, Y.-P.; Gomes, J.; Mallikarjun Sharada, S.; Bell, A. T.; Head-Gordon, M. Improved Force-Field Parameters for QM/MM Simulations of the Energies of Adsorption for Molecules in Zeolites and a Free Rotor Correction to the Rigid Rotor Harmonic Oscillator Model for Adsorption Enthalpies. *The Journal of Physical Chemistry C* **2015**, *119* (4), 1840-1850. DOI: 10.1021/jp509921r.
25. Böhm, L. L. The Ethylene Polymerization with Ziegler Catalysts: Fifty Years after the Discovery. *Angewandte Chemie International Edition* **2003**, *42* (41), 5010-5030. DOI: https://doi.org/10.1002/anie.200300580.
26. Gordon, C. P.; Engler, H.; Tragl, A. S.; Plodinec, M.; Lunkenbein, T.; Berkessel, A.; Teles, J. H.; Parvulescu, A.-N.; Copéret, C. Efficient epoxidation over dinuclear sites in titanium silicalite-1. *Nature* **2020**, *586* (7831), 708-713. DOI: 10.1038/s41586-020-2826-3.

27. Lane, G. S.; Modica, F. S.; Miller, J. T. Platinum/zeolite catalyst for reforming n-hexane: Kinetic and mechanistic considerations. *Journal of Catalysis* **1991**, *129* (1), 145-158. DOI: https://doi.org/10.1016/0021-9517(91)90018-Y.
28. Tanabe, K.; Hölderich, W. F. Industrial application of solid acid–base catalysts. *Applied Catalysis A: General* **1999**, *181* (2), 399-434. DOI: https://doi.org/10.1016/S0926-860X(98)00397-4.
29. Allendorf, M. D.; Stavila, V.; Witman, M.; Brozek, C. K.; Hendon, C. H. What Lies beneath a Metal–Organic Framework Crystal Structure? New Design Principles from Unexpected Behaviors. *Journal of the American Chemical Society* **2021**, *143* (18), 6705-6723. DOI: 10.1021/jacs.0c10777.
30. Bai, Y.; Dou, Y.; Xie, L.-H.; Rutledge, W.; Li, J.-R.; Zhou, H.-C. Zr-based metal–organic frameworks: design, synthesis, structure, and applications. *Chemical Society Reviews* **2016**, *45* (8), 2327-2367, 10.1039/C5CS00837A. DOI: 10.1039/C5CS00837A.
31. Corma, A.; García, H.; Llabrés i Xamena, F. X. Engineering Metal Organic Frameworks for Heterogeneous Catalysis. *Chemical Reviews* **2010**, *110* (8), 4606-4655. DOI: 10.1021/cr9003924.
32. El-Sayed, E.-S. M.; Yuan, Y. D.; Zhao, D.; Yuan, D. Zirconium Metal–Organic Cages: Synthesis and Applications. *Accounts of Chemical Research* **2022**, *55* (11), 1546-1560. DOI: 10.1021/acs.accounts.1c00654.
33. Dhakshinamoorthy, A.; Opanasenko, M.; Čejka, J.; Garcia, H. Metal organic frameworks as heterogeneous catalysts for the production of fine chemicals. *Catalysis Science & Technology* **2013**, *3* (10), 2509-2540, 10.1039/C3CY00350G. DOI: 10.1039/C3CY00350G.
34. Syed, Z. H.; Sha, F.; Zhang, X.; Kaphan, D. M.; Delferro, M.; Farha, O. K. Metal–Organic Framework Nodes as a Supporting Platform for Tailoring the Activity of Metal Catalysts. *ACS Catalysis* **2020**, *10* (19), 11556-11566. DOI: 10.1021/acscatal.0c03056.
35. Yang, D.; Gates, B. C. Catalysis by Metal Organic Frameworks: Perspective and Suggestions for Future Research. *ACS Catalysis* **2019**, *9* (3), 1779-1798. DOI: 10.1021/acscatal.8b04515.
36. Pascanu, V.; González Miera, G.; Inge, A. K.; Martín-Matute, B. Metal–Organic Frameworks as Catalysts for Organic Synthesis: A Critical Perspective. *Journal of the American Chemical Society* **2019**. DOI: 10.1021/jacs.9b00733.
37. O'Neill, B. J.; Jackson, D. H. K.; Lee, J.; Canlas, C.; Stair, P. C.; Marshall, C. L.; Elam, J. W.; Kuech, T. F.; Dumesic, J. A.; Huber, G. W. Catalyst Design with Atomic Layer Deposition. *ACS Catalysis* **2015**, *5* (3), 1804-1825. DOI: 10.1021/cs501862h.
38. Ardagh, M. A.; Bo, Z.; Nauert, S. L.; Notestein, J. M. Depositing SiO2 on Al2O3: a Route to Tunable Brønsted Acid Catalysts. *ACS Catalysis* **2016**, *6* (9), 6156-6164. DOI: 10.1021/acscatal.6b01077.
39. Lwin, S.; Wachs, I. E. Catalyst Activation and Kinetics for Propylene Metathesis by Supported WOx/SiO2 Catalysts. *ACS Catalysis* **2017**, *7* (1), 573-580. DOI: 10.1021/acscatal.6b03097.
40. Altvater, N. R.; Dorn, R. W.; Cendejas, M. C.; McDermott, W. P.; Thomas, B.; Rossini, A. J.; Hermans, I. B-MWW Zeolite: The Case Against Single-Site Catalysis. *Angewandte Chemie International Edition* **2020**, *59* (16), 6546-6550. DOI: 10.1002/anie.201914696 (acccessed 2020/10/27).
41. Hensen, E. J. M.; Poduval, D. G.; Degirmenci, V.; Ligthart, D. A. J. M.; Chen, W.; Maugé, F.; Rigutto, M. S.; Veen, J. A. R. v. Acidity Characterization of Amorphous Silica–

Alumina. *The Journal of Physical Chemistry C* **2012**, *116* (40), 21416-21429. DOI: 10.1021/jp309182f.
42. Zhu, Y.; Zheng, J.; Ye, J.; Cui, Y.; Koh, K.; Kovarik, L.; Camaioni, D. M.; Fulton, J. L.; Truhlar, D. G.; Neurock, M.; et al. Copper-zirconia interfaces in UiO-66 enable selective catalytic hydrogenation of CO2 to methanol. *Nature Communications* **2020**, *11* (1), 5849. DOI: 10.1038/s41467-020-19438-w.
43. Love, A. M.; Carrero, C. A.; Chieregato, A.; Grant, J. T.; Conrad, S.; Verel, R.; Hermans, I. Elucidation of Anchoring and Restructuring Steps during Synthesis of Silica-Supported Vanadium Oxide Catalysts. *Chemistry of Materials* **2016**, *28* (15), 5495-5504. DOI: 10.1021/acs.chemmater.6b02118.
44. Praveen, C. S.; Borosy, A. P.; Copéret, C.; Comas-Vives, A. Strain in Silica-Supported Ga(III) Sites: Neither Too Much nor Too Little for Propane Dehydrogenation Catalytic Activity. *Inorganic Chemistry* **2021**, *60* (10), 6865-6874. DOI: 10.1021/acs.inorgchem.0c03135.
45. Li, K.; Chen, J. G. CO2 Hydrogenation to Methanol over ZrO2-Containing Catalysts: Insights into ZrO2 Induced Synergy. *ACS Catalysis* **2019**, *9* (9), 7840-7861. DOI: 10.1021/acscatal.9b01943.
46. Prins, R. Hydrogen Spillover. Facts and Fiction. *Chemical Reviews* **2012**, *112* (5), 2714-2738. DOI: 10.1021/cr200346z.
47. Wolek, A. T. Y.; Ardagh, M. A.; Pham, H. N.; Alayoglu, S.; Datye, A. K.; Notestein, J. M. Creating Brønsted acidity at the SiO2-Nb2O5 interface. *Journal of Catalysis* **2021**, *394*, 387-396. DOI: https://doi.org/10.1016/j.jcat.2020.10.027.
48. Yan, H.; He, K.; Samek, I. A.; Jing, D.; Nanda, M. G.; Stair, P. C.; Notestein, J. M. Tandem In_2O_3-Pt/Al_2O_3 catalyst for coupling of propane dehydrogenation to selective H_2 combustion. *Science* **2021**, *371* (6535), 1257-1260. DOI: doi:10.1126/science.abd4441.
49. Vidal, V.; Théolier, A.; Thivolle-Cazat, J.; Basset, J.-M. Metathesis of Alkanes Catalyzed by Silica-Supported Transition Metal Hydrides. *Science* **1997**, *276* (5309), 99-102. DOI: 10.1126/science.276.5309.99.
50. Weisz, P. B. Molecular shape selective catalysis. *Pure and Applied Chemistry* **1980**, *52* (9), 2091-2103. DOI: doi:10.1351/pac198052092091 (acccessed 2023-04-30).
51. Fraenkel, D.; Gates, B. C. Shape-selective Fischer-Tropsch synthesis catalyzed by zeolite-entrapped cobalt clusters. *Journal of the American Chemical Society* **1980**, *102* (7), 2478-2480. DOI: 10.1021/ja00527a067.
52. van der Waal, J. C.; Creyghton, E. J.; Kunkeler, P. J.; Tan, K.; van Bekkum, H. Beta–type zeolites as selective and regenerable catalysts in the Meerwein–Ponndorf–Verley reduction of carbonyl compounds. *Topics in Catalysis* **1997**, *4* (3), 261-268. DOI: 10.1023/A:1019160827175.
53. Huybrechts, W.; Vanbutsele, G.; Houthoofd, K. J.; Bertinchamps, F.; Laxmi Narasimhan, C. S.; Gaigneaux, E. M.; Thybaut, J. W.; Marin, G. B.; Denayer, J. F. M.; Baron, G. V.; et al. Skeletal isomerization of octadecane on bifunctional ZSM-23 zeolite catalyst. *Catalysis Letters* **2005**, *100* (3), 235-242. DOI: 10.1007/s10562-004-3461-6.
54. Schenk, M.; Calero, S.; Maesen, T. L. M.; Vlugt, T. J. H.; van Benthem, L. L.; Verbeek, M. G.; Schnell, B.; Smit, B. Shape selectivity through entropy. *Journal of Catalysis* **2003**, *214* (1), 88-99. DOI: https://doi.org/10.1016/S0021-9517(03)00023-X.
55. Ahn, S.; Nauert, S. L.; Buru, C. T.; Rimoldi, M.; Choi, H.; Schweitzer, N. M.; Hupp, J. T.; Farha, O. K.; Notestein, J. M. Pushing the Limits on Metal–Organic Frameworks as a Catalyst Support: NU-1000 Supported Tungsten Catalysts for o-Xylene Isomerization and

Disproportionation. *Journal of the American Chemical Society* **2018**, *140* (27), 8535-8543. DOI: 10.1021/jacs.8b04059.
56. Zhang, W.; Lu, G.; Cui, C.; Liu, Y.; Li, S.; Yan, W.; Xing, C.; Chi, Y. R.; Yang, Y.; Huo, F. A Family of Metal-Organic Frameworks Exhibiting Size-Selective Catalysis with Encapsulated Noble-Metal Nanoparticles. *Advanced Materials* **2014**, *26* (24), 4056-4060. DOI: 10.1002/adma.201400620.
57. Taoufik, M.; Roux, E. L.; Thivolle-Cazat, J.; Copéret, C.; Basset, J.-M.; Maunders, B.; Sunley, G. J. Alumina supported tungsten hydrides, new efficient catalysts for alkane metathesis. *Topics in Catalysis* **2006**, *40* (1), 65-70, journal article. DOI: 10.1007/s11244-006-0108-4.
58. Samantaray, M. K.; Kavitake, S.; Morlanés, N.; Abou-Hamad, E.; Hamieh, A.; Dey, R.; Basset, J.-M. Unearthing a Well-Defined Highly Active Bimetallic W/Ti Precatalyst Anchored on a Single Silica Surface for Metathesis of Propane. *Journal of the American Chemical Society* **2017**, *139* (9), 3522-3527. DOI: 10.1021/jacs.6b12970.
59. Samantaray, M. K.; Dey, R.; Kavitake, S.; Abou-Hamad, E.; Bendjeriou-Sedjerari, A.; Hamieh, A.; Basset, J.-M. Synergy between Two Metal Catalysts: A Highly Active Silica-Supported Bimetallic W/Zr Catalyst for Metathesis of n-Decane. *Journal of the American Chemical Society* **2016**, *138* (27), 8595-8602. DOI: 10.1021/jacs.6b04307.
60. Samantaray, M. K.; Dey, R.; Abou-Hamad, E.; Hamieh, A.; Basset, J.-M. Effect of Support on Metathesis of n-Decane: Drastic Improvement in Alkane Metathesis with WMe5 Linked to Silica–Alumina. *Chemistry – A European Journal* **2015**, *21* (16), 6100-6106. DOI: 10.1002/chem.201406033.
61. Rataboul, F.; Copéret, C.; Lefort, L.; de Mallmann, A.; Thivolle-Cazat, J.; Basset, J.-M. Synthesis, characterization and propane metathesis activity of a tantalum-hydride prepared on high surface area "silica supported zirconium hydroxide". *Dalton Transactions* **2007**, (9), 923-927, 10.1039/B616921J. DOI: 10.1039/B616921J.
62. Zhao, H.; Song, H.; Chou, L.; Zhao, J.; Yang, J.; Yan, L. Insight into the structure and molybdenum species in mesoporous molybdena–alumina catalysts for isobutane dehydrogenation. *Catalysis Science & Technology* **2017**, *7* (15), 3258-3267, 10.1039/C7CY00975E. DOI: 10.1039/C7CY00975E.
63. Wang, L.; Agnew, D. W.; Yu, X.; Figueroa, J. S.; Cohen, S. M. A Metal–Organic Framework with Exceptional Activity for C−H Bond Amination. *Angewandte Chemie International Edition* **2018**, *57* (2), 511-515. DOI: 10.1002/anie.201709420.
64. Noh, H.; Cui, Y.; Peters, A. W.; Pahls, D. R.; Ortuño, M. A.; Vermeulen, N. A.; Cramer, C. J.; Gagliardi, L.; Hupp, J. T.; Farha, O. K. An Exceptionally Stable Metal–Organic Framework Supported Molybdenum(VI) Oxide Catalyst for Cyclohexene Epoxidation. *Journal of the American Chemical Society* **2016**, *138* (44), 14720-14726. DOI: 10.1021/jacs.6b08898.
65. Li, Z.; Schweitzer, N. M.; League, A. B.; Bernales, V.; Peters, A. W.; Getsoian, A. B.; Wang, T. C.; Miller, J. T.; Vjunov, A.; Fulton, J. L.; et al. Sintering-Resistant Single-Site Nickel Catalyst Supported by Metal–Organic Framework. *Journal of the American Chemical Society* **2016**, *138* (6), 1977-1982. DOI: 10.1021/jacs.5b12515.
66. Klet, R. C.; Tussupbayev, S.; Borycz, J.; Gallagher, J. R.; Stalzer, M. M.; Miller, J. T.; Gagliardi, L.; Hupp, J. T.; Marks, T. J.; Cramer, C. J.; et al. Single-Site Organozirconium Catalyst Embedded in a Metal–Organic Framework. *Journal of the American Chemical Society* **2015**, *137* (50), 15680-15683. DOI: 10.1021/jacs.5b11350.
67. Ahn, S.; Thornburg, N. E.; Li, Z.; Wang, T. C.; Gallington, L. C.; Chapman, K. W.; Notestein, J. M.; Hupp, J. T.; Farha, O. K. Stable Metal–Organic Framework-Supported

Niobium Catalysts. *Inorganic Chemistry* **2016**, *55* (22), 11954-11961. DOI: 10.1021/acs.inorgchem.6b02103.
68. Zhang, X.; Huang, Z.; Ferrandon, M.; Yang, D.; Robison, L.; Li, P.; Wang, T. C.; Delferro, M.; Farha, O. K. Catalytic chemoselective functionalization of methane in a metal−organic framework. *Nature Catalysis* **2018**, *1* (5), 356-362. DOI: 10.1038/s41929-018-0069-6.
69. Xia, Q.; Li, Z.; Tan, C.; Liu, Y.; Gong, W.; Cui, Y. Multivariate Metal–Organic Frameworks as Multifunctional Heterogeneous Asymmetric Catalysts for Sequential Reactions. *Journal of the American Chemical Society* **2017**, *139* (24), 8259-8266. DOI: 10.1021/jacs.7b03113.
70. Chan, K. W.; Mance, D.; Safonova, O. V.; Copéret, C. Well-Defined Silica-Supported Tungsten(IV)–Oxo Complex: Olefin Metathesis Activity, Initiation, and Role of Brønsted Acid Sites. *Journal of the American Chemical Society* **2019**, *141* (45), 18286-18292. DOI: 10.1021/jacs.9b09493.
71. Le Roux, E.; Chabanas, M.; Baudouin, A.; de Mallmann, A.; Copéret, C.; Quadrelli, E. A.; Thivolle-Cazat, J.; Basset, J.-M.; Lukens, W.; Lesage, A.; et al. Detailed Structural Investigation of the Grafting of [Ta(CHtBu)(CH2tBu)3] and [Cp*TaMe4] on Silica Partially Dehydroxylated at 700 °C and the Activity of the Grafted Complexes toward Alkane Metathesis. *Journal of the American Chemical Society* **2004**, *126* (41), 13391-13399. DOI: 10.1021/ja046486r.
72. Chen, Y.; Abou-hamad, E.; Hamieh, A.; Hamzaoui, B.; Emsley, L.; Basset, J.-M. Alkane Metathesis with the Tantalum Methylidene [(≡SiO)Ta(═CH2)Me2]/[(≡SiO)2Ta(═CH2)Me] Generated from Well-Defined Surface Organometallic Complex [(≡SiO)TaVMe4]. *Journal of the American Chemical Society* **2015**, *137* (2), 588-591. DOI: 10.1021/ja5113468.
73. Basset, J.-M.; Coperet, C.; Soulivong, D.; Taoufik, M.; Cazat, J. T. Metathesis of Alkanes and Related Reactions. *Accounts of Chemical Research* **2010**, *43* (2), 323-334. DOI: 10.1021/ar900203a.
74. Goldman, A. S.; Roy, A. H.; Huang, Z.; Ahuja, R.; Schinski, W.; Brookhart, M. Catalytic Alkane Metathesis by Tandem Alkane Dehydrogenation-Olefin Metathesis. *Science* **2006**, *312* (5771), 257-261. DOI: doi:10.1126/science.1123787.
75. Haibach, M. C.; Kundu, S.; Brookhart, M.; Goldman, A. S. Alkane Metathesis by Tandem Alkane-Dehydrogenation–Olefin-Metathesis Catalysis and Related Chemistry. *Accounts of Chemical Research* **2012**, *45* (6), 947-958. DOI: 10.1021/ar3000713.
76. Tanabe, K. K.; Siladke, N. A.; Broderick, E. M.; Kobayashi, T.; Goldston, J. F.; Weston, M. H.; Farha, O. K.; Hupp, J. T.; Pruski, M.; Mader, E. A.; et al. Stabilizing unstable species through single-site isolation: a catalytically active TaV trialkyl in a porous organic polymer. *Chemical Science* **2013**, *4* (6), 2483-2489, 10.1039/C3SC22268C. DOI: 10.1039/C3SC22268C.
77. Morlanés, N.; Kavitake, S. G.; Rosenfeld, D. C.; Basset, J.-M. Alkane Cross-Metathesis Reaction between Light and Heavy Linear Alkanes, on a Silica Supported Well-Defined Single-Site Catalyst. *ACS Catalysis* **2019**, *9* (2), 1274-1282. DOI: 10.1021/acscatal.8b02472.
78. Soulivong, D.; Norsic, S.; Taoufik, M.; Coperet, C.; Thivolle-Cazat, J.; Chakka, S.; Basset, J.-M. Non-Oxidative Coupling Reaction of Methane to Ethane and Hydrogen Catalyzed by the Silica-Supported Tantalum Hydride: (≡SiO)2Ta−H. *Journal of the American Chemical Society* **2008**, *130* (15), 5044-5045. DOI: 10.1021/ja800863x.
79. Riache, N.; Callens, E.; Samantaray, M. K.; Kharbatia, N. M.; Atiqullah, M.; Basset, J.-M. Cyclooctane Metathesis Catalyzed by Silica-Supported Tungsten Pentamethyl

[(□SiO)W(Me)5]: Distribution of Macrocyclic Alkanes. *Chemistry – A European Journal* **2014**, *20* (46), 15089-15094. DOI: 10.1002/chem.201403704.
80. Thiam, Z.; Abou-Hamad, E.; Dereli, B.; Liu, L.; Emwas, A.-H.; Ahmad, R.; Jiang, H.; Isah, A. A.; Ndiaye, P. B.; Taoufik, M.; et al. Extension of Surface Organometallic Chemistry to Metal–Organic Frameworks: Development of a Well-Defined Single Site [(≡Zr–O−)W(═O)(CH2tBu)3] Olefin Metathesis Catalyst. *Journal of the American Chemical Society* **2020**, *142* (39), 16690-16703. DOI: 10.1021/jacs.0c06925.
81. Chatterjee, A. K.; Choi, T.-L.; Sanders, D. P.; Grubbs, R. H. A General Model for Selectivity in Olefin Cross Metathesis. *Journal of the American Chemical Society* **2003**, *125* (37), 11360-11370. DOI: 10.1021/ja0214882.
82. Zhang, Y.; Diver, S. T. A Macrocyclic Ruthenium Carbene for Size-Selective Alkene Metathesis. *Journal of the American Chemical Society* **2020**, *142* (7), 3371-3374. DOI: 10.1021/jacs.0c00081.
83. Schrock, R. R.; Fellmann, J. D. Multiple metal-carbon bonds. 8. Preparation, characterization, and mechanism of formation of the tantalum and niobium neopentylidene complexes, M(CH2CMe3)3(CHCMe3). *Journal of the American Chemical Society* **1978**, *100* (11), 3359-3370. DOI: 10.1021/ja00479a019.
84. Cohen, S. M. The Postsynthetic Renaissance in Porous Solids. *Journal of the American Chemical Society* **2017**, *139* (8), 2855-2863. DOI: 10.1021/jacs.6b11259.
85. Li, Z.; Peters, A. W.; Platero-Prats, A. E.; Liu, J.; Kung, C.-W.; Noh, H.; DeStefano, M. R.; Schweitzer, N. M.; Chapman, K. W.; Hupp, J. T.; et al. Fine-Tuning the Activity of Metal–Organic Framework-Supported Cobalt Catalysts for the Oxidative Dehydrogenation of Propane. *Journal of the American Chemical Society* **2017**, *139* (42), 15251-15258. DOI: 10.1021/jacs.7b09365.
86. Peters, A. W.; Otake, K.; Platero-Prats, A. E.; Li, Z.; DeStefano, M. R.; Chapman, K. W.; Farha, O. K.; Hupp, J. T. Site-Directed Synthesis of Cobalt Oxide Clusters in a Metal–Organic Framework. *ACS Applied Materials & Interfaces* **2018**, *10* (17), 15073-15078. DOI: 10.1021/acsami.8b02825.
87. Mondloch, J. E.; Bury, W.; Fairen-Jimenez, D.; Kwon, S.; DeMarco, E. J.; Weston, M. H.; Sarjeant, A. A.; Nguyen, S. T.; Stair, P. C.; Snurr, R. Q.; et al. Vapor-Phase Metalation by Atomic Layer Deposition in a Metal–Organic Framework. *Journal of the American Chemical Society* **2013**, *135* (28), 10294-10297. DOI: 10.1021/ja4050828.
88. Yuan, S.; Qin, J.-S.; Lollar, C. T.; Zhou, H.-C. Stable Metal–Organic Frameworks with Group 4 Metals: Current Status and Trends. *ACS Central Science* **2018**, *4* (4), 440-450. DOI: 10.1021/acscentsci.8b00073.
89. Planas, N.; Mondloch, J. E.; Tussupbayev, S.; Borycz, J.; Gagliardi, L.; Hupp, J. T.; Farha, O. K.; Cramer, C. J. Defining the Proton Topology of the Zr6-Based Metal–Organic Framework NU-1000. *The Journal of Physical Chemistry Letters* **2014**, *5* (21), 3716-3723. DOI: 10.1021/jz501899j.
90. Klet, R. C.; Liu, Y.; Wang, T. C.; Hupp, J. T.; Farha, O. K. Evaluation of Brønsted acidity and proton topology in Zr- and Hf-based metal–organic frameworks using potentiometric acid–base titration. *Journal of Materials Chemistry A* **2016**, *4* (4), 1479-1485, 10.1039/C5TA07687K. DOI: 10.1039/C5TA07687K.
91. Yang, D.; Gates, B. C. Elucidating and Tuning Catalytic Sites on Zirconium- and Aluminum-Containing Nodes of Stable Metal–Organic Frameworks. *Accounts of Chemical Research* **2021**, *54* (8), 1982-1991. DOI: 10.1021/acs.accounts.1c00029.

92. Lu, Z.; Liu, J.; Zhang, X.; Liao, Y.; Wang, R.; Zhang, K.; Lyu, J.; Farha, O. K.; Hupp, J. T. Node-Accessible Zirconium MOFs. *Journal of the American Chemical Society* **2020**, *142* (50), 21110-21121. DOI: 10.1021/jacs.0c09782.
93. Liu, J.; Lu, Z.; Chen, Z.; Rimoldi, M.; Howarth, A. J.; Chen, H.; Alayoglu, S.; Snurr, R. Q.; Farha, O. K.; Hupp, J. T. Ammonia Capture within Zirconium Metal–Organic Frameworks: Reversible and Irreversible Uptake. *ACS Applied Materials & Interfaces* **2021**, *13* (17), 20081-20093. DOI: 10.1021/acsami.1c02370.
94. Liu, X.; Kirlikovali, K. O.; Chen, Z.; Ma, K.; Idrees, K. B.; Cao, R.; Zhang, X.; Islamoglu, T.; Liu, Y.; Farha, O. K. Small Molecules, Big Effects: Tuning Adsorption and Catalytic Properties of Metal–Organic Frameworks. *Chemistry of Materials* **2021**, *33* (4), 1444-1454. DOI: 10.1021/acs.chemmater.0c04675.
95. Kirlikovali, K. O.; Chen, Z.; Islamoglu, T.; Hupp, J. T.; Farha, O. K. Zirconium-Based Metal–Organic Frameworks for the Catalytic Hydrolysis of Organophosphorus Nerve Agents. *ACS Applied Materials & Interfaces* **2020**, *12* (13), 14702-14720. DOI: 10.1021/acsami.9b20154.
96. Mondloch, J. E.; Katz, M. J.; Isley Iii, W. C.; Ghosh, P.; Liao, P.; Bury, W.; Wagner, G. W.; Hall, M. G.; DeCoste, J. B.; Peterson, G. W.; et al. Destruction of chemical warfare agents using metal–organic frameworks. *Nature Materials* **2015**, *14* (5), 512-516. DOI: 10.1038/nmat4238.
97. Yang, D.; Bernales, V.; Islamoglu, T.; Farha, O. K.; Hupp, J. T.; Cramer, C. J.; Gagliardi, L.; Gates, B. C. Tuning the Surface Chemistry of Metal Organic Framework Nodes: Proton Topology of the Metal-Oxide-Like Zr6 Nodes of UiO-66 and NU-1000. *Journal of the American Chemical Society* **2016**, *138* (46), 15189-15196. DOI: 10.1021/jacs.6b08273.
98. Wang, T. C.; Vermeulen, N. A.; Kim, I. S.; Martinson, A. B. F.; Stoddart, J. F.; Hupp, J. T.; Farha, O. K. Scalable synthesis and post-modification of a mesoporous metal-organic framework called NU-1000. *Nature Protocols* **2015**, *11*, 149. DOI: 10.1038/nprot.2016.001.
99. Yang, D.; Ortuño, M. A.; Bernales, V.; Cramer, C. J.; Gagliardi, L.; Gates, B. C. Structure and Dynamics of Zr6O8 Metal–Organic Framework Node Surfaces Probed with Ethanol Dehydration as a Catalytic Test Reaction. *Journal of the American Chemical Society* **2018**, *140* (10), 3751-3759. DOI: 10.1021/jacs.7b13330.
100. Chen, Y.; Credendino, R.; Callens, E.; Atiqullah, M.; Al-Harthi, M. A.; Cavallo, L.; Basset, J.-M. Understanding Tantalum-Catalyzed Ethylene Trimerization: When Things Go Wrong. *ACS Catalysis* **2013**, *3* (6), 1360-1364. DOI: 10.1021/cs400349p.
101. Ahn, H.; Marks, T. J. High-Resolution Solid-State 13C NMR Studies of Chemisorbed Organometallics. Chemisorptive Formation of Cation-like and Alkylidene Organotantalum Complexes on High Surface Area Inorganic Oxides. *Journal of the American Chemical Society* **2002**, *124* (24), 7103-7110. DOI: 10.1021/ja0123204.
102. Platero-Prats, A. E.; League, A. B.; Bernales, V.; Ye, J.; Gallington, L. C.; Vjunov, A.; Schweitzer, N. M.; Li, Z.; Zheng, J.; Mehdi, B. L.; et al. Bridging Zirconia Nodes within a Metal–Organic Framework via Catalytic Ni-Hydroxo Clusters to Form Heterobimetallic Nanowires. *Journal of the American Chemical Society* **2017**, *139* (30), 10410-10418. DOI: 10.1021/jacs.7b04997.
103. Chabanas, M.; Quadrelli, E. A.; Fenet, B.; Copéret, C.; Thivolle-Cazat, J.; Basset, J.-M.; Lesage, A.; Emsley, L. Molecular Insight Into Surface Organometallic Chemistry Through the Combined Use of 2D HETCOR Solid-State NMR Spectroscopy and Silsesquioxane Analogues.

Angewandte Chemie International Edition **2001**, *40* (23), 4493-4496. DOI: 10.1002/1521-3773(20011203)40:23<4493::Aid-anie4493>3.0.Co;2-x.
104. Yamamoto, T.; Yoshizawa, M.; Mahmut, A.; Abe, M.; Kuroda, S.-i.; Imase, T.; Sasaki, S. Preparation of new π-conjugated polypyrroles by organometallic polycondensations. Synthesis of N-BOC (t-butoxycarbonyl) and N-phenylethynyl polymers, thermal deprotection of the BOC Group, and packing structure of the N-phenylethynyl polymer. *Journal of Polymer Science Part A: Polymer Chemistry* **2005**, *43* (24), 6223-6232. DOI: 10.1002/pola.21080.
105. Polshettiwar, V.; Thivolle-Cazat, J.; Taoufik, M.; Stoffelbach, F.; Norsic, S.; Basset, J.-M. "Hydro-metathesis" of Olefins: A Catalytic Reaction Using a Bifunctional Single-Site Tantalum Hydride Catalyst Supported on Fibrous Silica (KCC-1) Nanospheres. *Angewandte Chemie International Edition* **2011**, *50* (12), 2747-2751. DOI: https://doi.org/10.1002/anie.201007254.
106. Houžvička, J.; Ponec, V. Skeletal Isomerization of Butene: On the Role of the Bimolecular Mechanism. *Industrial & Engineering Chemistry Research* **1997**, *36* (5), 1424-1430. DOI: 10.1021/ie960588b.
107. Nakano, Y.; Iizuka, T.; Hattori, H.; Tanabe, K. Surface properties of zirconium oxide and its catalytic activity for isomerization of 1-butene. *Journal of Catalysis* **1979**, *57* (1), 1-10. DOI: https://doi.org/10.1016/0021-9517(79)90038-1.
108. Pajonk, G. M.; Tanany, A. E. Isomerization and hydrogenation of butene-1 on a zirconia aerogel catalyst. *Reaction Kinetics and Catalysis Letters* **1992**, *47* (2), 167-175. DOI: 10.1007/BF02137646.
109. Bilhou, J. L.; Basset, J. M.; Mutin, R.; Graydon, W. F. A stereochemical study of metathesis and cis-trans isomerization of 2-pentenes. *Journal of the American Chemical Society* **1977**, *99* (12), 4083-4090. DOI: 10.1021/ja00454a029.
110. Pascanu, V.; González Miera, G.; Inge, A. K.; Martín-Matute, B. Metal–Organic Frameworks as Catalysts for Organic Synthesis: A Critical Perspective. *Journal of the American Chemical Society* **2019**, *141* (18), 7223-7234. DOI: 10.1021/jacs.9b00733.
111. Bavykina, A.; Kolobov, N.; Khan, I. S.; Bau, J. A.; Ramirez, A.; Gascon, J. Metal–Organic Frameworks in Heterogeneous Catalysis: Recent Progress, New Trends, and Future Perspectives. *Chemical Reviews* **2020**, *120* (16), 8468-8535. DOI: 10.1021/acs.chemrev.9b00685.
112. Kim, M.; Cohen, S. M. Discovery, development, and functionalization of Zr(iv)-based metal–organic frameworks. *CrystEngComm* **2012**, *14* (12), 4096-4104, 10.1039/C2CE06491J. DOI: 10.1039/C2CE06491J.
113. Ding, M.; Cai, X.; Jiang, H.-L. Improving MOF stability: approaches and applications. *Chemical Science* **2019**, *10* (44), 10209-10230, 10.1039/C9SC03916C. DOI: 10.1039/C9SC03916C.
114. Valenzano, L.; Civalleri, B.; Chavan, S.; Bordiga, S.; Nilsen, M. H.; Jakobsen, S.; Lillerud, K. P.; Lamberti, C. Disclosing the Complex Structure of UiO-66 Metal Organic Framework: A Synergic Combination of Experiment and Theory. *Chemistry of Materials* **2011**, *23* (7), 1700-1718. DOI: 10.1021/cm1022882.
115. Bezrukov, A. A.; Törnroos, K. W.; Le Roux, E.; Dietzel, P. D. C. Incorporation of an intact dimeric Zr12 oxo cluster from a molecular precursor in a new zirconium metal–organic framework. *Chemical Communications* **2018**, *54* (22), 2735-2738, 10.1039/C8CC00507A. DOI: 10.1039/C8CC00507A.

116. Feng, D.; Jiang, H.-L.; Chen, Y.-P.; Gu, Z.-Y.; Wei, Z.; Zhou, H.-C. Metal–Organic Frameworks Based on Previously Unknown Zr8/Hf8 Cubic Clusters. *Inorganic Chemistry* **2013**, *52* (21), 12661-12667. DOI: 10.1021/ic4018536.
117. Katz, M. J.; Brown, Z. J.; Colón, Y. J.; Siu, P. W.; Scheidt, K. A.; Snurr, R. Q.; Hupp, J. T.; Farha, O. K. A facile synthesis of UiO-66, UiO-67 and their derivatives. *Chemical Communications* **2013**, *49* (82), 9449-9451, 10.1039/C3CC46105J. DOI: 10.1039/C3CC46105J.
118. Caratelli, C.; Hajek, J.; Cirujano, F. G.; Waroquier, M.; Llabrés i Xamena, F. X.; Van Speybroeck, V. Nature of active sites on UiO-66 and beneficial influence of water in the catalysis of Fischer esterification. *Journal of Catalysis* **2017**, *352*, 401-414. DOI: https://doi.org/10.1016/j.jcat.2017.06.014.
119. Ji, P.; Drake, T.; Murakami, A.; Oliveres, P.; Skone, J. H.; Lin, W. Tuning Lewis Acidity of Metal–Organic Frameworks via Perfluorination of Bridging Ligands: Spectroscopic, Theoretical, and Catalytic Studies. *Journal of the American Chemical Society* **2018**, *140* (33), 10553-10561. DOI: 10.1021/jacs.8b05765.
120. Chen, X.; Lyu, Y.; Wang, Z.; Qiao, X.; Gates, B. C.; Yang, D. Tuning Zr12O22 Node Defects as Catalytic Sites in the Metal–Organic Framework hcp UiO-66. *ACS Catalysis* **2020**, *10* (5), 2906-2914. DOI: 10.1021/acscatal.9b04905.
121. Cirujano, F. G.; Luz, I.; Soukri, M.; Van Goethem, C.; Vankelecom, I. F. J.; Lail, M.; De Vos, D. E. Boosting the Catalytic Performance of Metal–Organic Frameworks for Steroid Transformations by Confinement within a Mesoporous Scaffold. *Angewandte Chemie International Edition* **2017**, *56* (43), 13302-13306. DOI: 10.1002/anie.201706721.
122. Plessers, E.; Fu, G.; Tan, C. Y. X.; De Vos, D. E.; Roeffaers, M. B. J. Zr-Based MOF-808 as Meerwein–Ponndorf–Verley Reduction Catalyst for Challenging Carbonyl Compounds. *Catalysts* **2016**, *6* (7), 104.
123. Mishra, A. A.; Bhanage, B. M. Zirconium-MOF-catalysed selective synthesis of α-hydroxyamide via the transfer hydrogenation of α-ketoamide. *New Journal of Chemistry* **2019**, *43* (16), 6160-6167, 10.1039/C9NJ00900K. DOI: 10.1039/C9NJ00900K.
124. Desai, S. P.; Ye, J.; Zheng, J.; Ferrandon, M. S.; Webber, T. E.; Platero-Prats, A. E.; Duan, J.; Garcia-Holley, P.; Camaioni, D. M.; Chapman, K. W.; et al. Well-Defined Rhodium–Gallium Catalytic Sites in a Metal–Organic Framework: Promoter-Controlled Selectivity in Alkyne Semihydrogenation to E-Alkenes. *Journal of the American Chemical Society* **2018**, *140* (45), 15309-15318. DOI: 10.1021/jacs.8b08550.
125. Yang, D.; Odoh, S. O.; Wang, T. C.; Farha, O. K.; Hupp, J. T.; Cramer, C. J.; Gagliardi, L.; Gates, B. C. Metal–Organic Framework Nodes as Nearly Ideal Supports for Molecular Catalysts: NU-1000- and UiO-66-Supported Iridium Complexes. *Journal of the American Chemical Society* **2015**, *137* (23), 7391-7396. DOI: 10.1021/jacs.5b02956.
126. Rimoldi, M.; Hupp, J. T.; Farha, O. K. Atomic Layer Deposition of Rhenium–Aluminum Oxide Thin Films and ReOx Incorporation in a Metal–Organic Framework. *ACS Applied Materials & Interfaces* **2017**, *9* (40), 35067-35074. DOI: 10.1021/acsami.7b12303.
127. An, B.; Zhang, J.; Cheng, K.; Ji, P.; Wang, C.; Lin, W. Confinement of Ultrasmall Cu/ZnOx Nanoparticles in Metal–Organic Frameworks for Selective Methanol Synthesis from Catalytic Hydrogenation of CO2. *Journal of the American Chemical Society* **2017**, *139* (10), 3834-3840. DOI: 10.1021/jacs.7b00058.
128. Choe, K.; Zheng, F.; Wang, H.; Yuan, Y.; Zhao, W.; Xue, G.; Qiu, X.; Ri, M.; Shi, X.; Wang, Y.; et al. Fast and Selective Semihydrogenation of Alkynes by Palladium Nanoparticles

Sandwiched in Metal–Organic Frameworks. *Angewandte Chemie International Edition* **2020**, *59* (9), 3650-3657. DOI: 10.1002/anie.201913453.
129. Goetjen, T. A.; Zhang, X.; Liu, J.; Hupp, J. T.; Farha, O. K. Metal–Organic Framework Supported Single Site Chromium(III) Catalyst for Ethylene Oligomerization at Low Pressure and Temperature. *ACS Sustainable Chemistry & Engineering* **2019**, *7* (2), 2553-2557. DOI: 10.1021/acssuschemeng.8b05524.
130. Manna, K.; Ji, P.; Lin, Z.; Greene, F. X.; Urban, A.; Thacker, N. C.; Lin, W. Chemoselective single-site Earth-abundant metal catalysts at metal–organic framework nodes. *Nature Communications* **2016**, *7* (1), 12610. DOI: 10.1038/ncomms12610.
131. Cheng, E.; McCullough, L.; Noh, H.; Farha, O.; Hupp, J.; Notestein, J. Isobutane Dehydrogenation over Bulk and Supported Molybdenum Sulfide Catalysts. *Industrial & Engineering Chemistry Research* **2020**, *59* (3), 1113-1122. DOI: 10.1021/acs.iecr.9b05844.
132. Goswami, S.; Noh, H.; Redfern, L. R.; Otake, K.-i.; Kung, C.-W.; Cui, Y.; Chapman, K. W.; Farha, O. K.; Hupp, J. T. Pore-Templated Growth of Catalytically Active Gold Nanoparticles within a Metal–Organic Framework. *Chemistry of Materials* **2019**, *31* (5), 1485-1490. DOI: 10.1021/acs.chemmater.8b04983.
133. Gutterød, E. S.; Øien-Ødegaard, S.; Bossers, K.; Nieuwelink, A.-E.; Manzoli, M.; Braglia, L.; Lazzarini, A.; Borfecchia, E.; Ahmadigoltapeh, S.; Bouchevreau, B.; et al. CO2 Hydrogenation over Pt-Containing UiO-67 Zr-MOFs—The Base Case. *Industrial & Engineering Chemistry Research* **2017**, *56* (45), 13206-13218. DOI: 10.1021/acs.iecr.7b01457.
134. Ahn, S.; Nauert, S. L.; Hicks, K. E.; Ardagh, M. A.; Schweitzer, N. M.; Farha, O. K.; Notestein, J. M. Demonstrating the Critical Role of Solvation in Supported Ti and Nb Epoxidation Catalysts via Vapor-Phase Kinetics. *ACS Catalysis* **2020**, *10* (4), 2817-2825. DOI: 10.1021/acscatal.9b04906.
135. Korzyński, M. D.; Consoli, D. F.; Zhang, S.; Román-Leshkov, Y.; Dincă, M. Activation of Methyltrioxorhenium for Olefin Metathesis in a Zirconium-Based Metal–Organic Framework. *Journal of the American Chemical Society* **2018**, *140* (22), 6956-6960. DOI: 10.1021/jacs.8b02837.
136. Yang, Q.; Xu, Q.; Jiang, H.-L. Metal–organic frameworks meet metal nanoparticles: synergistic effect for enhanced catalysis. *Chemical Society Reviews* **2017**, *46* (15), 4774-4808, 10.1039/C6CS00724D. DOI: 10.1039/C6CS00724D.
137. Hydrogenation of Alkenes and Related Processes. In *Metal-Catalysed Reactions of Hydrocarbons*, Bond, G. C. Ed.; Springer US, 2005; pp 291-355.
138. Zhang, T.; Manna, K.; Lin, W. Metal–Organic Frameworks Stabilize Solution-Inaccessible Cobalt Catalysts for Highly Efficient Broad-Scope Organic Transformations. *Journal of the American Chemical Society* **2016**, *138* (9), 3241-3249. DOI: 10.1021/jacs.6b00849.
139. Sawano, T.; Lin, Z.; Boures, D.; An, B.; Wang, C.; Lin, W. Metal–Organic Frameworks Stabilize Mono(phosphine)–Metal Complexes for Broad-Scope Catalytic Reactions. *Journal of the American Chemical Society* **2016**, *138* (31), 9783-9786. DOI: 10.1021/jacs.6b06239.
140. Rimoldi, M.; Nakamura, A.; Vermeulen, N. A.; Henkelis, J. J.; Blackburn, A. K.; Hupp, J. T.; Stoddart, J. F.; Farha, O. K. A metal–organic framework immobilised iridium pincer complex. *Chemical Science* **2016**, *7* (8), 4980-4984, 10.1039/C6SC01376G. DOI: 10.1039/C6SC01376G.
141. Liu, J.; Li, Z.; Zhang, X.; Otake, K.-i.; Zhang, L.; Peters, A. W.; Young, M. J.; Bedford, N. M.; Letourneau, S. P.; Mandia, D. J.; et al. Introducing Nonstructural Ligands to Zirconia-like

Metal–Organic Framework Nodes To Tune the Activity of Node-Supported Nickel Catalysts for Ethylene Hydrogenation. *ACS Catalysis* **2019**, *9* (4), 3198-3207. DOI: 10.1021/acscatal.8b04828.
142. Falkowski, J. M.; Sawano, T.; Zhang, T.; Tsun, G.; Chen, Y.; Lockard, J. V.; Lin, W. Privileged Phosphine-Based Metal–Organic Frameworks for Broad-Scope Asymmetric Catalysis. *Journal of the American Chemical Society* **2014**, *136* (14), 5213-5216. DOI: 10.1021/ja500090y.
143. Bernales, V.; Yang, D.; Yu, J.; Gümüşlü, G.; Cramer, C. J.; Gates, B. C.; Gagliardi, L. Molecular Rhodium Complexes Supported on the Metal-Oxide-Like Nodes of Metal Organic Frameworks and on Zeolite HY: Catalysts for Ethylene Hydrogenation and Dimerization. *ACS Applied Materials & Interfaces* **2017**, *9* (39), 33511-33520. DOI: 10.1021/acsami.7b03858.
144. Manna, K.; Zhang, T.; Carboni, M.; Abney, C. W.; Lin, W. Salicylaldimine-Based Metal–Organic Framework Enabling Highly Active Olefin Hydrogenation with Iron and Cobalt Catalysts. *Journal of the American Chemical Society* **2014**, *136* (38), 13182-13185. DOI: 10.1021/ja507947d.
145. Thacker, N. C.; Lin, Z.; Zhang, T.; Gilhula, J. C.; Abney, C. W.; Lin, W. Robust and Porous β-Diketiminate-Functionalized Metal–Organic Frameworks for Earth-Abundant-Metal-Catalyzed C–H Amination and Hydrogenation. *Journal of the American Chemical Society* **2016**, *138* (10), 3501-3509. DOI: 10.1021/jacs.5b13394.
146. Ji, P.; Manna, K.; Lin, Z.; Urban, A.; Greene, F. X.; Lan, G.; Lin, W. Single-Site Cobalt Catalysts at New Zr8(μ2-O)8(μ2-OH)4 Metal-Organic Framework Nodes for Highly Active Hydrogenation of Alkenes, Imines, Carbonyls, and Heterocycles. *Journal of the American Chemical Society* **2016**, *138* (37), 12234-12242. DOI: 10.1021/jacs.6b06759.
147. Yang, D.; Gaggioli, C. A.; Conley, E.; Babucci, M.; Gagliardi, L.; Gates, B. C. Synthesis and characterization of tetrairidium clusters in the metal organic framework UiO-67: Catalyst for ethylene hydrogenation. *Journal of Catalysis* **2020**, *382*, 165-172. DOI: https://doi.org/10.1016/j.jcat.2019.11.031.
148. Platero-Prats, A. E.; Li, Z.; Gallington, L. C.; Peters, Aaron W.; Hupp, J. T.; Farha, O. K.; Chapman, K. W. Addressing the characterisation challenge to understand catalysis in MOFs: the case of nanoscale Cu supported in NU-1000. *Faraday Discussions* **2017**, *201* (0), 337-350, 10.1039/C7FD00110J. DOI: 10.1039/C7FD00110J.
149. Hester, P.; Xu, S.; Liang, W.; Al-Janabi, N.; Vakili, R.; Hill, P.; Muryn, C. A.; Chen, X.; Martin, P. A.; Fan, X. On thermal stability and catalytic reactivity of Zr-based metal–organic framework (UiO-67) encapsulated Pt catalysts. *Journal of Catalysis* **2016**, *340*, 85-94. DOI: https://doi.org/10.1016/j.jcat.2016.05.003.
150. Halder, A.; Lee, S.; Yang, B.; Pellin, M. J.; Vajda, S.; Li, Z.; Yang, Y.; Farha, O. K.; Hupp, J. T. Structural reversibility of Cu doped NU-1000 MOFs under hydrogenation conditions. *The Journal of Chemical Physics* **2020**, *152* (8), 084703. DOI: 10.1063/1.5130600.
151. Guo, Z.; Xiao, C.; Maligal-Ganesh, R. V.; Zhou, L.; Goh, T. W.; Li, X.; Tesfagaber, D.; Thiel, A.; Huang, W. Pt Nanoclusters Confined within Metal–Organic Framework Cavities for Chemoselective Cinnamaldehyde Hydrogenation. *ACS Catalysis* **2014**, *4* (5), 1340-1348. DOI: 10.1021/cs400982n.
152. Gole, B.; Sanyal, U.; Banerjee, R.; Mukherjee, P. S. High Loading of Pd Nanoparticles by Interior Functionalization of MOFs for Heterogeneous Catalysis. *Inorganic Chemistry* **2016**, *55* (5), 2345-2354. DOI: 10.1021/acs.inorgchem.5b02739.

153. Deng, Z.; Yu, H.; Wang, L.; Liu, J.; Shea, K. J. Ferrocene-based metal–organic framework nanosheets loaded with palladium as a super-high active hydrogenation catalyst. *Journal of Materials Chemistry A* **2019**, *7* (26), 15975-15980, 10.1039/C9TA03403J. DOI: 10.1039/C9TA03403J.
154. Noh, H.; Kung, C.-W.; Islamoglu, T.; Peters, A. W.; Liao, Y.; Li, P.; Garibay, S. J.; Zhang, X.; DeStefano, M. R.; Hupp, J. T.; et al. Room Temperature Synthesis of an 8-Connected Zr-Based Metal–Organic Framework for Top-Down Nanoparticle Encapsulation. *Chemistry of Materials* **2018**, *30* (7), 2193-2197. DOI: 10.1021/acs.chemmater.8b00449.
155. Luz, I.; Rösler, C.; Epp, K.; Llabrés i Xamena, F. X.; Fischer, R. A. Pd@UiO-66-Type MOFs Prepared by Chemical Vapor Infiltration as Shape-Selective Hydrogenation Catalysts. *European Journal of Inorganic Chemistry* **2015**, *2015* (23), 3904-3912. DOI: 10.1002/ejic.201500299.
156. Sheng, D.; Zhang, Y.; Song, Q.; Xu, G.; Peng, D.; Hou, H.; Xie, R.; Shan, D.; Liu, P. Isomerization of 1-Butene to 2-Butene Catalyzed by Metal–Organic Frameworks. *Organometallics* **2020**, *39* (1), 51-57. DOI: 10.1021/acs.organomet.9b00599.
157. Liu, P.; Redekop, E.; Gao, X.; Liu, W.-C.; Olsbye, U.; Somorjai, G. A. Oligomerization of Light Olefins Catalyzed by Brønsted-Acidic Metal–Organic Framework-808. *Journal of the American Chemical Society* **2019**, *141* (29), 11557-11564. DOI: 10.1021/jacs.9b03867.
158. Jiang, J.; Gándara, F.; Zhang, Y.-B.; Na, K.; Yaghi, O. M.; Klemperer, W. G. Superacidity in Sulfated Metal–Organic Framework-808. *Journal of the American Chemical Society* **2014**, *136* (37), 12844-12847. DOI: 10.1021/ja507119n.
159. Trickett, C. A.; Osborn Popp, T. M.; Su, J.; Yan, C.; Weisberg, J.; Huq, A.; Urban, P.; Jiang, J.; Kalmutzki, M. J.; Liu, Q.; et al. Identification of the strong Brønsted acid site in a metal–organic framework solid acid catalyst. *Nature Chemistry* **2019**, *11* (2), 170-176. DOI: 10.1038/s41557-018-0171-z.
160. Tanabe, K. Surface and catalytic properties of ZrO2. *Materials Chemistry and Physics* **1985**, *13* (3), 347-364. DOI: https://doi.org/10.1016/0254-0584(85)90064-1.
161. Kauppi, E. I.; Honkala, K.; Krause, A. O. I.; Kanervo, J. M.; Lefferts, L. ZrO2 Acting as a Redox Catalyst. *Topics in Catalysis* **2016**, *59* (8), 823-832. DOI: 10.1007/s11244-016-0556-4.
162. Tanabe, K.; Yamaguchi, T. Acid-base bifunctional catalysis by ZrO2 and its mixed oxides. *Catalysis Today* **1994**, *20* (2), 185-197. DOI: https://doi.org/10.1016/0920-5861(94)80002-2.
163. Bird, R.; Kemball, C.; Leach, H. F. Reactions of alkenes and the equilibration of hydrogen and deuterium on zirconia. *Journal of the Chemical Society, Faraday Transactions 1: Physical Chemistry in Condensed Phases* **1987**, *83* (9), 3069-3082, 10.1039/F19878303069. DOI: 10.1039/F19878303069.
164. Syzgantseva, O.; Calatayud, M.; Minot, C. Hydrogen Adsorption on Monoclinic ($\bar{1}11$) and ($\bar{1}01$) ZrO2 Surfaces: A Periodic ab Initio Study. *The Journal of Physical Chemistry C* **2010**, *114* (27), 11918-11923. DOI: 10.1021/jp103463s.
165. Syzgantseva, O. A.; Calatayud, M.; Minot, C. Revealing the Surface Reactivity of Zirconia by Periodic DFT Calculations. *The Journal of Physical Chemistry C* **2012**, *116* (11), 6636-6644. DOI: 10.1021/jp209898q.
166. Kondo, J.; Sakata, Y.; Domen, K.; Maruya, K.-i.; Onishi, T. Infrared study of hydrogen adsorbed on ZrO2. *Journal of the Chemical Society, Faraday Transactions* **1990**, *86* (2), 397-401, 10.1039/FT9908600397. DOI: 10.1039/FT9908600397.

167. Kondo, J.; Domen, K.; Maruya, K.-i.; Onishi, T. Infrared study of molecularly adsorbed H2 on ZrO2. *Chemical Physics Letters* **1992**, *188* (5), 443-445. DOI: https://doi.org/10.1016/0009-2614(92)80845-3.
168. Ouyang, F.; Kondo, J. N.; Maruya, K.-c.; Domen, K. Isotope-exchange reaction between hydrogen molecules and surface hydroxy groups on bare and modified ZrO2. *Journal of the Chemical Society, Faraday Transactions* **1996**, *92* (22), 4491-4495, 10.1039/FT9969204491. DOI: 10.1039/FT9969204491.
169. Onishi, T.; Abe, H.; Maruya, K.-i.; Domen, K. I.r. spectra of hydrogen adsorbed on ZrO2. *Journal of the Chemical Society, Chemical Communications* **1985**, (9), 617-618, 10.1039/C39850000617. DOI: 10.1039/C39850000617.
170. Jacob, K.-H.; Knözinger, E.; Benfer, S. Chemisorption of H2 and H2—O2 on polymorphic zirconia. *Journal of the Chemical Society, Faraday Transactions* **1994**, *90* (19), 2969-2975, 10.1039/FT9949002969. DOI: 10.1039/FT9949002969.
171. Sang-Chul, M.; Kouji, T.; Takaiki, N.; Masakazu, A. Selective Dimerization and Hydrogenation of Ethylene on Active Zirconium Oxide with Coordinatively Unsaturated Surface Sites. *Chemistry Letters* **1994**, *23* (12), 2241-2244. DOI: 10.1246/cl.1994.2241.
172. Zhivonitko, V. V.; Kovtunov, K. V.; Beck, I. E.; Ayupov, A. B.; Bukhtiyarov, V. I.; Koptyug, I. V. Role of Different Active Sites in Heterogeneous Alkene Hydrogenation on Platinum Catalysts Revealed by Means of Parahydrogen-Induced Polarization. *The Journal of Physical Chemistry C* **2011**, *115* (27), 13386-13391. DOI: 10.1021/jp203398j.
173. Coleto, I.; Roldán, R.; Jiménez-Sanchidrián, C.; Gómez, J. P.; Romero-Salguero, F. J. Valorization of α-olefins: Double bond shift and skeletal isomerization of 1-pentene and 1-hexene on zirconia-based catalysts. *Catalysis Today* **2010**, *149* (3), 275-280. DOI: https://doi.org/10.1016/j.cattod.2009.06.017.
174. Zhang, Y.; Zhao, Y.; Otroshchenko, T.; Lund, H.; Pohl, M.-M.; Rodemerck, U.; Linke, D.; Jiao, H.; Jiang, G.; Kondratenko, E. V. Control of coordinatively unsaturated Zr sites in ZrO2 for efficient C–H bond activation. *Nature Communications* **2018**, *9* (1), 3794. DOI: 10.1038/s41467-018-06174-5.
175. Kouva, S.; Honkala, K.; Lefferts, L.; Kanervo, J. Review: monoclinic zirconia, its surface sites and their interaction with carbon monoxide. *Catalysis Science & Technology* **2015**, *5* (7), 3473-3490, 10.1039/C5CY00330J. DOI: 10.1039/C5CY00330J.
176. Liu, J.; He, Y.; Yan, L.; Li, K.; Zhang, C.; Xiang, H.; Wen, X.; Li, Y. Nano-sized ZrO2 derived from metal–organic frameworks and their catalytic performance for aromatic synthesis from syngas. *Catalysis Science & Technology* **2019**, *9* (11), 2982-2992, 10.1039/C9CY00453J. DOI: 10.1039/C9CY00453J.
177. Hiroshi, A.; Ken-ichi, M.; Kazunari, D.; Takaharu, O. AN INFRARED SPECTROSCOPIC STUDY ON THE MECHANISM OF METHANOL FORMATION FROM CO AND H2 OVER ZIRCONIA. *Chemistry Letters* **1984**, *13* (11), 1875-1878. DOI: 10.1246/cl.1984.1875.
178. Kondo, J.; Abe, H.; Sakata, Y.; Maruya, K.-i.; Domen, K.; Onishi, T. Infrared studies of adsorbed species of H2, CO and CO2 over ZrO2. *Journal of the Chemical Society, Faraday Transactions 1: Physical Chemistry in Condensed Phases* **1988**, *84* (2), 511-519, 10.1039/F19888400511. DOI: 10.1039/F19888400511.
179. Wambach, J.; Baiker, A.; Wokaun, A. CO2 hydrogenation over metal/zirconia catalysts. *Physical Chemistry Chemical Physics* **1999**, *1* (22), 5071-5080, 10.1039/A904923A. DOI: 10.1039/A904923A.

180. Yan, G. X.; Wang, A.; Wachs, I. E.; Baltrusaitis, J. Critical review on the active site structure of sulfated zirconia catalysts and prospects in fuel production. *Applied Catalysis A: General* **2019**, *572*, 210-225. DOI: https://doi.org/10.1016/j.apcata.2018.12.012.
181. Olindo, R.; Li, X.; Lercher, J. A. Activation of Light Alkanes on Sulfated Zirconia. *Chemie Ingenieur Technik* **2006**, *78* (8), 1053-1060. DOI: 10.1002/cite.200600064.
182. Hino, M.; Arata, K. Synthesis of solid superacid of tungsten oxide supported on zirconia and its catalytic action for reactions of butane and pentane. *Journal of the Chemical Society, Chemical Communications* **1988**, (18), 1259-1260, 10.1039/C39880001259. DOI: 10.1039/C39880001259.
183. Wang, T. C.; Vermeulen, N. A.; Kim, I. S.; Martinson, A. B. F.; Stoddart, J. F.; Hupp, J. T.; Farha, O. K. Scalable synthesis and post-modification of a mesoporous metal-organic framework called NU-1000. *Nature Protocols* **2016**, *11* (1), 149-162. DOI: 10.1038/nprot.2016.001.
184. Islamoglu, T.; Otake, K.-i.; Li, P.; Buru, C. T.; Peters, A. W.; Akpinar, I.; Garibay, S. J.; Farha, O. K. Revisiting the structural homogeneity of NU-1000, a Zr-based metal–organic framework. *CrystEngComm* **2018**, *20* (39), 5913-5918, 10.1039/C8CE00455B. DOI: 10.1039/C8CE00455B.
185. *Gaussian 16 Rev. C.01*; Wallingford, CT, 2016. (accessed.
186. Zhao, Y.; Truhlar, D. G. A new local density functional for main-group thermochemistry, transition metal bonding, thermochemical kinetics, and noncovalent interactions. *The Journal of chemical physics* **2006**, *125* (19), 194101. DOI: 10.1063/1.2370993 PubMed.
187. Weigend, F.; Ahlrichs, R. Balanced basis sets of split valence, triple zeta valence and quadruple zeta valence quality for H to Rn: Design and assessment of accuracy. *Physical Chemistry Chemical Physics* **2005**, *7* (18), 3297-3305, 10.1039/B508541A. DOI: 10.1039/B508541A.
188. Martin, J. M. L.; Sundermann, A. Correlation consistent valence basis sets for use with the Stuttgart–Dresden–Bonn relativistic effective core potentials: The atoms Ga–Kr and In–Xe. *The Journal of Chemical Physics* **2001**, *114* (8), 3408-3420. DOI: 10.1063/1.1337864.
189. Alecu, I. M.; Zheng, J.; Zhao, Y.; Truhlar, D. G. Computational Thermochemistry: Scale Factor Databases and Scale Factors for Vibrational Frequencies Obtained from Electronic Model Chemistries. *Journal of Chemical Theory and Computation* **2010**, *6* (9), 2872-2887. DOI: 10.1021/ct100326h.
190. S. Kanchanakungwankul, J. L. B., J. Zheng, I. M. Alecu, B. J. Lynch, Y. Zhao, and D. G. Truhlar. *Database of Frequency Scale Factors for Electronic Model Chemistries – Version 4*. https://comp.chem.umn.edu/freqscale/190107_Database_of_Freq_Scale_Factors_v4.pdf (accessed.
191. Grimme, S. Supramolecular Binding Thermodynamics by Dispersion-Corrected Density Functional Theory. *Chemistry – A European Journal* **2012**, *18* (32), 9955-9964. DOI: 10.1002/chem.201200497.
192. Akimoto, H.; Sprung, J. L.; Pitts, J. N., Jr. Nitrogen dioxide catalyzed geometric isomerization of 3-butene and 2-pentene. Precise method for determining the enthalpies and entropies of geometric isomerizations. *J. Amer. Chem. Soc.* **1972**, *94* (14), 4850-4855, 10.1021/ja00769a009. DOI: 10.1021/ja00769a009.
193. Meyer, E. F.; Stroz, D. G. Thermodynamics of n-butene isomerization. *J. Amer. Chem. Soc.* **1972**, *94* (18), 6344-6347, 10.1021/ja00773a015. DOI: 10.1021/ja00773a015.

194. Kapteijn, F.; Steen, A. J. v. d.; Mol, J. C. Thermodynamics of the geometrical isomerization of 2-butene and 2-pentene. *The Journal of Chemical Thermodynamics* **1983**, *15* (2), 137-146. DOI: https://doi.org/10.1016/0021-9614(83)90152-0.
195. Schwartz, J.; Ward, M. D. Silica-supported zirconium hydrides as isomerization or hydrogenation catalysts for long-chain olefins. *Journal of Molecular Catalysis* **1980**, *8* (4), 465-469. DOI: https://doi.org/10.1016/0304-5102(80)80085-X.
196. Copéret, C.; Estes, D. P.; Larmier, K.; Searles, K. Isolated Surface Hydrides: Formation, Structure, and Reactivity. *Chemical Reviews* **2016**, *116* (15), 8463-8505. DOI: 10.1021/acs.chemrev.6b00082.
197. Schweitzer, N. M.; Hu, B.; Das, U.; Kim, H.; Greeley, J.; Curtiss, L. A.; Stair, P. C.; Miller, J. T.; Hock, A. S. Propylene Hydrogenation and Propane Dehydrogenation by a Single-Site Zn2+ on Silica Catalyst. *ACS Catalysis* **2014**, *4* (4), 1091-1098. DOI: 10.1021/cs401116p.
198. Kondo, J.; Domen, K.; Maruya, K.-i.; Onishi, T. Infrared studies of ethene hydrogenation over ZrO2. Part 1.—Ethene adsorption. *Journal of the Chemical Society, Faraday Transactions* **1990**, *86* (17), 3021-3026, 10.1039/FT9908603021. DOI: 10.1039/FT9908603021.
199. Kondo, J.; Domen, K.; Maruya, K.-i.; Onishi, T. Infrared studies of ethene hydrogenation over ZrO2. Part 3.—Reaction mechanism. *Journal of the Chemical Society, Faraday Transactions* **1992**, *88* (14), 2095-2099, 10.1039/FT9928802095. DOI: 10.1039/FT9928802095.
200. Wu, F.; Jordan, R. F. Sigma-Bond Metathesis Reactions of Zirconocene Alkyl Cations with Phenylsilane. *Organometallics* **2005**, *24* (11), 2688-2697. DOI: 10.1021/om049099z.
201. Jordan, R. F.; Taylor, D. F. Zirconium-catalyzed coupling of propene and .alpha.-picoline. *Journal of the American Chemical Society* **1989**, *111* (2), 778-779. DOI: 10.1021/ja00184a081.
202. Rungtaweevoranit, B.; Baek, J.; Araujo, J. R.; Archanjo, B. S.; Choi, K. M.; Yaghi, O. M.; Somorjai, G. A. Copper Nanocrystals Encapsulated in Zr-based Metal–Organic Frameworks for Highly Selective CO2 Hydrogenation to Methanol. *Nano Letters* **2016**, *16* (12), 7645-7649. DOI: 10.1021/acs.nanolett.6b03637.
203. Gutterød, E. S.; Lazzarini, A.; Fjermestad, T.; Kaur, G.; Manzoli, M.; Bordiga, S.; Svelle, S.; Lillerud, K. P.; Skúlason, E.; Øien-Ødegaard, S.; et al. Hydrogenation of CO2 to Methanol by Pt Nanoparticles Encapsulated in UiO-67: Deciphering the Role of the Metal–Organic Framework. *Journal of the American Chemical Society* **2020**, *142* (2), 999-1009. DOI: 10.1021/jacs.9b10873.
204. Gutterød, E. S.; Pulumati, S. H.; Kaur, G.; Lazzarini, A.; Solemsli, B. G.; Gunnæs, A. E.; Ahoba-Sam, C.; Kalyva, M. E.; Sannes, J. A.; Svelle, S.; et al. Influence of Defects and H2O on the Hydrogenation of CO2 to Methanol over Pt Nanoparticles in UiO-67 Metal–Organic Framework. *Journal of the American Chemical Society* **2020**, *142* (40), 17105-17118. DOI: 10.1021/jacs.0c07153.
205. Wei, R.; Gaggioli, C. A.; Li, G.; Islamoglu, T.; Zhang, Z.; Yu, P.; Farha, O. K.; Cramer, C. J.; Gagliardi, L.; Yang, D.; et al. Tuning the Properties of Zr6O8 Nodes in the Metal Organic Framework UiO-66 by Selection of Node-Bound Ligands and Linkers. *Chemistry of Materials* **2019**, *31* (5), 1655-1663. DOI: 10.1021/acs.chemmater.8b05037.
206. Du, Q.; Rao, R.; Bi, F.; Yang, Y.; Zhang, W.; Yang, Y.; Liu, N.; Zhang, X. Preparation of modified zirconium-based metal-organic frameworks (Zr-MOFs) supported metals and recent application in environment: A review and perspectives. *Surfaces and Interfaces* **2022**, *28*, 101647. DOI: https://doi.org/10.1016/j.surfin.2021.101647.

207. Rimoldi, M.; Howarth, A. J.; DeStefano, M. R.; Lin, L.; Goswami, S.; Li, P.; Hupp, J. T.; Farha, O. K. Catalytic Zirconium/Hafnium-Based Metal–Organic Frameworks. *ACS Catalysis* **2017**, *7* (2), 997-1014. DOI: 10.1021/acscatal.6b02923.
208. Wei, R.; Fan, J.; Qu, X.; Gao, L.; Wu, Y.; Zhang, Z.; Hu, F.; Xiao, G. Tuning the Catalytic Activity of UiO-66 via Modulated Synthesis: Esterification of Levulinic Acid as a Test Reaction. *European Journal of Inorganic Chemistry* **2020**, *2020* (10), 833-840. DOI: 10.1002/ejic.202000031.
209. Gutov, O. V.; Hevia, M. G.; Escudero-Adán, E. C.; Shafir, A. Metal–Organic Framework (MOF) Defects under Control: Insights into the Missing Linker Sites and Their Implication in the Reactivity of Zirconium-Based Frameworks. *Inorganic Chemistry* **2015**, *54* (17), 8396-8400. DOI: 10.1021/acs.inorgchem.5b01053.
210. Ji, P.; Feng, X.; Oliveres, P.; Li, Z.; Murakami, A.; Wang, C.; Lin, W. Strongly Lewis Acidic Metal–Organic Frameworks for Continuous Flow Catalysis. *Journal of the American Chemical Society* **2019**, *141* (37), 14878-14888. DOI: 10.1021/jacs.9b07891.
211. Simons, M. C.; Ortuño, M. A.; Bernales, V.; Gaggioli, C. A.; Cramer, C. J.; Bhan, A.; Gagliardi, L. C–H Bond Activation on Bimetallic Two-Atom Co-M Oxide Clusters Deposited on Zr-Based MOF Nodes: Effects of Doping at the Molecular Level. *ACS Catalysis* **2018**, *8* (4), 2864-2869. DOI: 10.1021/acscatal.8b00012.
212. Furukawa, H.; Gándara, F.; Zhang, Y.-B.; Jiang, J.; Queen, W. L.; Hudson, M. R.; Yaghi, O. M. Water Adsorption in Porous Metal–Organic Frameworks and Related Materials. *Journal of the American Chemical Society* **2014**, *136* (11), 4369-4381. DOI: 10.1021/ja500330a.
213. Øien, S.; Wragg, D.; Reinsch, H.; Svelle, S.; Bordiga, S.; Lamberti, C.; Lillerud, K. P. Detailed Structure Analysis of Atomic Positions and Defects in Zirconium Metal–Organic Frameworks. *Crystal Growth & Design* **2014**, *14* (11), 5370-5372. DOI: 10.1021/cg501386j.
214. Hicks, K. E.; Rosen, A. S.; Syed, Z. H.; Snurr, R. Q.; Farha, O. K.; Notestein, J. M. Zr6O8 Node-Catalyzed Butene Hydrogenation and Isomerization in the Metal–Organic Framework NU-1000. *ACS Catalysis* **2020**, *10* (24), 14959-14970. DOI: 10.1021/acscatal.0c03579.
215. Drout, R. J.; Howarth, A. J.; Otake, K.-i.; Islamoglu, T.; Farha, O. K. Efficient extraction of inorganic selenium from water by a Zr metal–organic framework: investigation of volumetric uptake capacity and binding motifs. *CrystEngComm* **2018**, *20* (40), 6140-6145, 10.1039/C8CE00992A. DOI: 10.1039/C8CE00992A.
216. Romero-Muñiz, I.; Romero-Muñiz, C.; del Castillo-Velilla, I.; Marini, C.; Calero, S.; Zamora, F.; Platero-Prats, A. E. Revisiting Vibrational Spectroscopy to Tackle the Chemistry of Zr6O8 Metal-Organic Framework Nodes. *ACS Applied Materials & Interfaces* **2022**, *14* (23), 27040-27047. DOI: 10.1021/acsami.2c04712.
217. Ouyang, F.; Nakayama, A.; Tabada, K.; Suzuki, E. Infrared Study of a Novel Acid−Base Site on ZrO2 by Adsorbed Probe Molecules. I. Pyridine, Carbon Dioxide, and Formic Acid Adsorption. *The Journal of Physical Chemistry B* **2000**, *104* (9), 2012-2018. DOI: 10.1021/jp992970i.
218. Chirik, P. J.; Bercaw, J. E. Cyclopentadienyl and Olefin Substituent Effects on Insertion and β-Hydrogen Elimination with Group 4 Metallocenes. Kinetics, Mechanism, and Thermodynamics for Zirconocene and Hafnocene Alkyl Hydride Derivatives. *Organometallics* **2005**, *24* (22), 5407-5423. DOI: 10.1021/om0580351.
219. Nakanishi, Y.; Ishida, Y.; Kawaguchi, H. Zirconium Hydride Complex Supported by a Tetradentate Carbon-Centered Tripodal Tris(aryloxide) Ligand: Synthesis, Structure, and

Reactivity. *Inorganic Chemistry* **2016**, *55* (8), 3967-3973. DOI: 10.1021/acs.inorgchem.6b00233.
220. Mautschke, H. H.; Drache, F.; Senkovska, I.; Kaskel, S.; Llabrés i Xamena, F. X. Catalytic properties of pristine and defect-engineered Zr-MOF-808 metal organic frameworks. *Catalysis Science & Technology* **2018**, *8* (14), 3610-3616, 10.1039/C8CY00742J. DOI: 10.1039/C8CY00742J.
221. Lu, Z.; Liu, J.; Zhang, X.; Liao, Y.; Wang, R.; Zhang, K.; Lyu, J.; Farha, O. K.; Hupp, J. T. Node-Accessible Zirconium MOFs. *Journal of the American Chemical Society* **2020**. DOI: 10.1021/jacs.0c09782.
222. Wang, Y.; Huang, J.; Lu, S.; Li, P.; Xia, X.; Li, C.; Li, F. Phosphorus-modified zirconium metal organic frameworks for catalytic transfer hydrogenation of furfural. *New Journal of Chemistry* **2020**, *44* (46), 20308-20315, 10.1039/D0NJ04285D. DOI: 10.1039/D0NJ04285D.
223. Syed, Z. H.; Mian, M. R.; Patel, R.; Xie, H.; Pengmei, Z.; Chen, Z.; Son, F. A.; Goetjen, T. A.; Chapovetsky, A.; Fahy, K. M.; et al. Sulfated Zirconium Metal–Organic Frameworks as Well-Defined Supports for Enhancing Organometallic Catalysis. *Journal of the American Chemical Society* **2022**, *144* (37), 16883-16897. DOI: 10.1021/jacs.2c05290.
224. Liu, F.; Xue, T.; Wu, C.; Yang, S. Coadsorption of CO and O over strained metal surfaces. *Chemical Physics Letters* **2019**, *722*, 18-25. DOI: https://doi.org/10.1016/j.cplett.2019.03.010.
225. Boronat, M.; Corma, A.; Renz, M. Mechanism of the Meerwein−Ponndorf−Verley−Oppenauer (MPVO) Redox Equilibrium on Sn− and Zr−Beta Zeolite Catalysts. *The Journal of Physical Chemistry B* **2006**, *110* (42), 21168-21174. DOI: 10.1021/jp063249x.
226. Komanoya, T.; Nakajima, K.; Kitano, M.; Hara, M. Synergistic Catalysis by Lewis Acid and Base Sites on ZrO2 for Meerwein–Ponndorf–Verley Reduction. *The Journal of Physical Chemistry C* **2015**, *119* (47), 26540-26546. DOI: 10.1021/acs.jpcc.5b08355.
227. Mattson, B.; Foster, W.; Greimann, J.; Hoette, T.; Le, N.; Mirich, A.; Wankum, S.; Cabri, A.; Reichenbacher, C.; Schwanke, E. Heterogeneous Catalysis: The Horiuti–Polanyi Mechanism and Alkene Hydrogenation. *Journal of Chemical Education* **2013**, *90* (5), 613-619. DOI: 10.1021/ed300437k.
228. Chen, Y.; Zhang, X.; Mian, M. R.; Son, F. A.; Zhang, K.; Cao, R.; Chen, Z.; Lee, S.-J.; Idrees, K. B.; Goetjen, T. A.; et al. Structural Diversity of Zirconium Metal–Organic Frameworks and Effect on Adsorption of Toxic Chemicals. *Journal of the American Chemical Society* **2020**, *142* (51), 21428-21438. DOI: 10.1021/jacs.0c10400.
229. Feng, X.; Song, Y.; Lin, W. Dimensional Reduction of Lewis Acidic Metal–Organic Frameworks for Multicomponent Reactions. *Journal of the American Chemical Society* **2021**, *143* (21), 8184-8192. DOI: 10.1021/jacs.1c03561.
230. Hicks, K. E.; Wolek, A. T. Y.; Farha, O. K.; Notestein, J. M. The Dependence of Olefin Hydrogenation and Isomerization Rates on Zirconium Metal–Organic Framework Structure. *ACS Catalysis* **2022**, *12* (21), 13671-13680. DOI: 10.1021/acscatal.2c04303.
231. Assary, R. S.; Curtiss, L. A.; Dumesic, J. A. Exploring Meerwein–Ponndorf–Verley Reduction Chemistry for Biomass Catalysis Using a First-Principles Approach. *ACS Catalysis* **2013**, *3* (12), 2694-2704. DOI: 10.1021/cs400479m.
232. Mariscal, R.; Maireles-Torres, P.; Ojeda, M.; Sádaba, I.; López Granados, M. Furfural: a renewable and versatile platform molecule for the synthesis of chemicals and fuels. *Energy &*

Environmental Science **2016**, *9* (4), 1144-1189, 10.1039/C5EE02666K. DOI: 10.1039/C5EE02666K.
233. Gilkey, M. J.; Xu, B. Heterogeneous Catalytic Transfer Hydrogenation as an Effective Pathway in Biomass Upgrading. *ACS Catalysis* **2016**, *6* (3), 1420-1436. DOI: 10.1021/acscatal.5b02171.
234. Plessers, E.; De Vos, D. E.; Roeffaers, M. B. J. Chemoselective reduction of α,β-unsaturated carbonyl compounds with UiO-66 materials. *Journal of Catalysis* **2016**, *340*, 136-143. DOI: https://doi.org/10.1016/j.jcat.2016.05.013.
235. Mautschke, H. H.; Llabrés i Xamena, F. X. One-Step Chemo-, Regio- and Stereoselective Reduction of Ketosteroids to Hydroxysteroids over Zr-Containing MOF-808 Metal-Organic Frameworks. *Chemistry – A European Journal* **2021**, *27* (41), 10766-10775, https://doi.org/10.1002/chem.202100967. DOI: https://doi.org/10.1002/chem.202100967 (acccessed 2022/09/12).
236. Nandi, P.; Solovyov, A.; Okrut, A.; Katz, A. AlIII–Calix[4]arene Catalysts for Asymmetric Meerwein–Ponndorf–Verley Reduction. *ACS Catalysis* **2014**, *4* (8), 2492-2495. DOI: 10.1021/cs5001976.
237. Gonell, F.; Boronat, M.; Corma, A. Structure–reactivity relationship in isolated Zr sites present in Zr-zeolite and ZrO2 for the Meerwein–Ponndorf–Verley reaction. *Catalysis Science & Technology* **2017**, *7* (13), 2865-2873, 10.1039/C7CY00567A. DOI: 10.1039/C7CY00567A.
238. Creyghton, E. J.; Ganeshie, S. D.; Downing, R. S.; van Bekkum, H. Stereoselective Meerwein–Ponndorf–Verley and Oppenauer reactions catalysed by zeolite BEA1Communication presented at the First Francqui Colloquium, Brussels, 19–20 February 1996.1. *Journal of Molecular Catalysis A: Chemical* **1997**, *115* (3), 457-472. DOI: https://doi.org/10.1016/S1381-1169(96)00351-2.
239. Vermoortele, F.; Bueken, B.; Le Bars, G.; Van de Voorde, B.; Vandichel, M.; Houthoofd, K.; Vimont, A.; Daturi, M.; Waroquier, M.; Van Speybroeck, V.; et al. Synthesis Modulation as a Tool To Increase the Catalytic Activity of Metal–Organic Frameworks: The Unique Case of UiO-66(Zr). *Journal of the American Chemical Society* **2013**, *135* (31), 11465-11468. DOI: 10.1021/ja405078u.
240. Agusta, K. D.; Miharja, M. F.; Sakti, A. W.; Arrozi, U. S. F.; Mukaromah, L.; Patah, A.; Hara, T.; Permana, Y. Zr-MOFs–catalyzed transfer hydrogenation of furfural to furfuryl alcohol: Unveiled performance of DUT-52. *Molecular Catalysis* **2022**, *524*, 112265. DOI: https://doi.org/10.1016/j.mcat.2022.112265.
241. Rahaman, M. S.; Tulaphol, S.; Hossain, M. A.; Mulvehill, M. C.; Spurgeon, J. M.; Maihom, T.; Sathitsuksanoh, N. Mechanism of transfer hydrogenation of carbonyl compounds by zirconium and hafnium-containing metal-organic frameworks. *Molecular Catalysis* **2022**, *522*, 112247. DOI: https://doi.org/10.1016/j.mcat.2022.112247.
242. Valekar, A. H.; Lee, M.; Yoon, J. W.; Kwak, J.; Hong, D.-Y.; Oh, K.-R.; Cha, G.-Y.; Kwon, Y.-U.; Jung, J.; Chang, J.-S.; et al. Catalytic Transfer Hydrogenation of Furfural to Furfuryl Alcohol under Mild Conditions over Zr-MOFs: Exploring the Role of Metal Node Coordination and Modification. *ACS Catalysis* **2020**, *10* (6), 3720-3732. DOI: 10.1021/acscatal.9b05085.
243. Vermoortele, F.; Vandichel, M.; Van de Voorde, B.; Ameloot, R.; Waroquier, M.; Van Speybroeck, V.; De Vos, D. E. Electronic Effects of Linker Substitution on Lewis Acid Catalysis with Metal–Organic Frameworks. *Angewandte Chemie International Edition* **2012**, *51* (20), 4887-4890. DOI: https://doi.org/10.1002/anie.201108565.

244. Haase, W. A. Walton, Molecular and crystal structure models, Ellis Horwood Ltd., Chichester, England, 1978. 201 Seiten, Preis:£ 9,—(vertrieben durch John Wiley). Wiley Online Library: 1981.
245. Wang, J.; Liu, L.; Chen, C.; Dong, X.; Wang, Q.; Alfilfil, L.; AlAlouni, M. R.; Yao, K.; Huang, J.; Zhang, D.; et al. Engineering effective structural defects of metal–organic frameworks to enhance their catalytic performances. *Journal of Materials Chemistry A* **2020**, *8* (8), 4464-4472, 10.1039/C9TA12230C. DOI: 10.1039/C9TA12230C.
246. Bakuru, V. R.; Churipard, S. R.; Maradur, S. P.; Kalidindi, S. B. Exploring the Brønsted acidity of UiO-66 (Zr, Ce, Hf) metal–organic frameworks for efficient solketal synthesis from glycerol acetalization. *Dalton Transactions* **2019**, *48* (3), 843-847, 10.1039/C8DT03512A. DOI: 10.1039/C8DT03512A.
247. Beyzavi, M. H.; Klet, R. C.; Tussupbayev, S.; Borycz, J.; Vermeulen, N. A.; Cramer, C. J.; Stoddart, J. F.; Hupp, J. T.; Farha, O. K. A Hafnium-Based Metal–Organic Framework as an Efficient and Multifunctional Catalyst for Facile CO2 Fixation and Regioselective and Enantioretentive Epoxide Activation. *Journal of the American Chemical Society* **2014**, *136* (45), 15861-15864. DOI: 10.1021/ja508626n.
248. Robison, L.; Drout, R. J.; Redfern, L. R.; Son, F. A.; Wasson, M. C.; Goswami, S.; Chen, Z.; Olszewski, A.; Idrees, K. B.; Islamoglu, T.; et al. Designing Porous Materials to Resist Compression: Mechanical Reinforcement of a Zr-MOF with Structural Linkers. *Chemistry of Materials* **2020**, *32* (8), 3545-3552. DOI: 10.1021/acs.chemmater.0c00634.
249. Liu, T.-F.; Vermeulen, N. A.; Howarth, A. J.; Li, P.; Sarjeant, A. A.; Hupp, J. T.; Farha, O. K. Adding to the Arsenal of Zirconium-Based Metal–Organic Frameworks: the Topology as a Platform for Solvent-Assisted Metal Incorporation. *European Journal of Inorganic Chemistry* **2016**, *2016* (27), 4349-4352, https://doi.org/10.1002/ejic.201600627. DOI: https://doi.org/10.1002/ejic.201600627 (acccessed 2023/01/31).
250. Webber, T. E.; Liu, W.-G.; Desai, S. P.; Lu, C. C.; Truhlar, D. G.; Penn, R. L. Role of a Modulator in the Synthesis of Phase-Pure NU-1000. *ACS Applied Materials & Interfaces* **2017**, *9* (45), 39342-39346. DOI: 10.1021/acsami.7b11348.
251. Islamoglu, T.; Ray, D.; Li, P.; Majewski, M. B.; Akpinar, I.; Zhang, X.; Cramer, C. J.; Gagliardi, L.; Farha, O. K. From Transition Metals to Lanthanides to Actinides: Metal-Mediated Tuning of Electronic Properties of Isostructural Metal–Organic Frameworks. *Inorganic Chemistry* **2018**, *57* (21), 13246-13251. DOI: 10.1021/acs.inorgchem.8b01748.
252. Grimme, S.; Antony, J.; Ehrlich, S.; Krieg, H. A consistent and accurate ab initio parametrization of density functional dispersion correction (DFT-D) for the 94 elements H-Pu. *The Journal of Chemical Physics* **2010**, *132* (15). DOI: 10.1063/1.3382344 (acccessed 4/30/2023).